Cutting Force Component-Based Rock Differentiation Utilising Machine Learning

_____

Faculty of Geosciences, Geotechnics and Mining

Institute of Mining and Special Civil Engineering

Chair of Surface Mining

Technical University Bergakademie Freiberg

_____

Accepted

Dissertation

To Obtain the Academic Degree of

Doctor of Engineering

Dr.-Ing.

Submitted by: Bruno Grafe

Born 18.04.1987 in Dresden

Freiberg, 08.06.2022

Reviewer:
Prof. Carsten Drebenstedt
Prof. Nikolaus A. Sifferlinger
Prof. Dragan Ignjatović

Awarded on: 09.12.2022

Declaration of Authorship

I hereby declare that I completed this work on my own without receiving any improper help from a third party and without using any aid other than those cited. All ideas derived directly or indirectly from other sources are identified as such.

I also confirm that I did not seek the help of a professional doctorate consultant and no persons received payment from me for any work done for me. Neither this thesis nor any parts thereof have been previously submitted for formal assessment in the same or a similar form at this university, nor any other.

Bruno Grafe
Freiberg, 08.06.2022

Acknowledgements

Abstract

<u>English Version</u>

This dissertation evaluates the possibilities and limitations of rock type identification in rock cutting with conical picks. For this, machine learning in conjunction with features derived from high frequency cutting force measurements is used. On the basis of linear cutting experiments, it is shown that boundary layers can be identified with a precision of less than 3.7 cm when using the developed programme routine. It is further shown that rocks weakened by cracks can be well identified and that anisotropic rock behaviour may be problematic to the classification success. In a case study, it is shown that the supervised algorithms artificial neural network and distributed random forest perform relatively well while unsupervised k-means clustering provides limited accuracies for complex situations. The 3d-results are visualised in a web app. The results suggest that a possible rock classification system can achieve good results—that are robust to changes in the cutting parameters when using the proposed evaluation methods.

<u>Deutsche Fassung</u>

Die Dissertation evaluiert Möglichkeiten und Grenzen der Gebirgserkennung bei der schneidenden Gewinnung von Festgesteinen mit Rundschaftmeißeln unter Nutzung maschinellen Lernens – in Verbindung mit aus hochaufgelösten Schnittkraftmessungen abgeleiteten Kennwerten. Es wird auf linearen Schneidversuchen aufbauend gezeigt, dass Schichtgrenzen mit Genauigkeiten unter 3,7 cm identifiziert werden können. Ferner wird gezeigt, dass durch Risse geschwächte Gesteine gut identifiziert werden können und dass anisotropes Gesteinsverhalten möglicherweise problematisch auf den Klassifizierungserfolg wirkt. In einer Fallstudie wird gezeigt, dass die überwachten Algorithmen Künstliches Neurales Netz und Distributed Random Forest teils sehr gute Ergebnisse erzielen und unüberwachtes k-means-Clustering begrenzte Genauigkeiten für komplexe Situationen liefert. Die Ergebnisse werden in einer Web-App visualisiert. Aus den Ergebnissen wird abgeleitet, dass ein mögliches Sensorsystem mit den vorgeschlagenen Auswerteroutinen gute Ergebnisse erzielen kann, die gleichzeitig robust gegen Änderungen der Schneidparameter sind.

Technical Summary

Although investigated since the 1970s, cutting force-based rock differentiation or classification systems have not yet reached market readiness for conical pick-based rock excavation. One of the reasons for this could be the high variability of the cutting parameters *cutting depth* and *spacing* during the excavation process. The variation of these parameters strongly influences the cutting forces during the cutting process. Moreover, sensor assemblies must exhibit considerable robustness, and high data acquisition rates to accurately measure the interaction between tool and rock. Additionally, standard practice in rock cutting research rarely incorporates statistical measures other than mean and peak values of the cutting forces to describe the process (owing to a lack of necessity until now). The result is limited published knowledge of other statistical measures that could be used for the purpose of rock classification.

This work aims to estimate the capabilities of a rock classification system based on cutting forces for conical picks, and to define the basic requirements for a possible cutting force sensor system utilising such an approach. The issue is addressed by investigating cutting force component ratios (FCR) as possible candidate features for material differentiation with machine learning methods during cutting. FCRs are abstractions of the angles at which a resulting force acts on the tool.

The FCRs are calculated on real-time data, which results in large datasets that need to be further summarised. A moving-window block model approach is used for this summary, which allows for a regional summary based on descriptive statistics. The resulting 3d-block model stores statistical parameters of the high-frequency FCR found in a given *search radius*. These parameters can then be used as features for machine learning algorithms to predict the rock type.
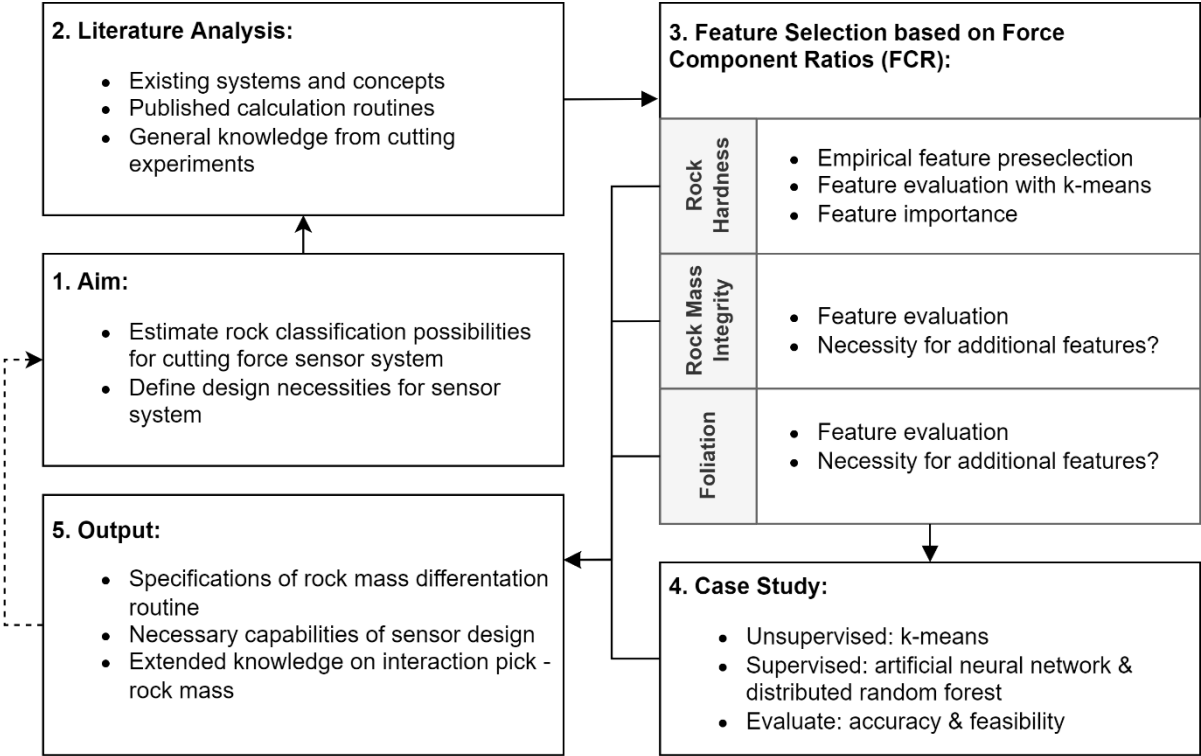
Figure A: Workflow of force component ratio feature selection and assessment

The workflow outlined in Figure A was carried out to achieve the objectives of this work and estimate the performance of the abovementioned methodology. Linear rock cutting experiments were conducted with different cutting parameters and on different rock types.

In total, four different experimental campaigns were conducted. The first, cutting experiments on concrete samples with varying hardness zones, resulted in an initial set of possible FCR-features. The set was chosen by a procedural selection algorithm combined with a k-means cluster analysis, a correlation analysis, and a distributed random forest (DRF)-based feature importance analysis. Furthermore, this experiment investigated the spatial precision of boundary layer detection between adjacent concrete zones based on k-means clustering.

The subsequent two experiments investigated an extension of the feature analysis with respect to two different rock mass conditions. These experiments investigated a cracked rock state using artificially damaged granite and a foliated rock—gneiss. These experiments resulted in a refined set of features. This is followed by a case study that tested machine learning classification algorithms using the previously selected features. These experiments investigated samples composed of concrete and natural ore pieces. The aim was to use three machine learning (ML) algorithms to distinguish between ore and concrete. Two of the algorithms are supervised: distributed random forest (DRF) and feedforward artificial neural network (ANN). One is an unsupervised algorithm: the k-means clustering algorithm.
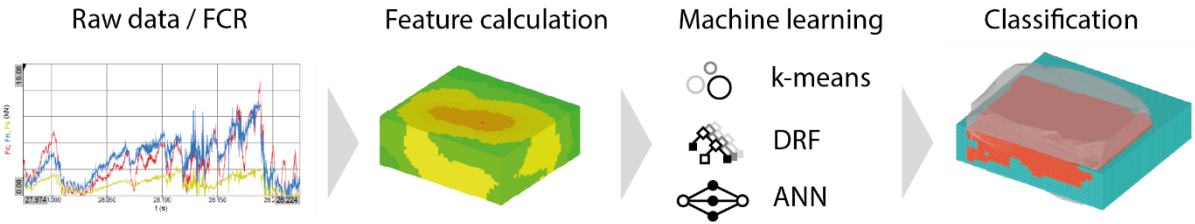
Figure B: Scheme of machine learning based rock classification

Figure B illustrates the machine learning workflow: From the raw cutting force data, real-time FCR were calculated. The moving-window algorithm extracted features from the FCR and coded them into a block model. The block model was then used for the machine learning which led to the evaluation of the classification success of the different learners.

Based on the k-means clustering with the concrete experiments, boundaries between rock types with differences as low as 7.7 MPa *uniaxial compressive strength (UCS)* could be identified from the cutting data. The mean spatial precision to identify a boundary between two adjacent types of concrete ranged between 2.4 and 3.7 cm. Seven FCR-based features were selected from these first experiments to serve in the case study.

The investigation of the cracked rock resulted in the finding that cracked rock states can be identified relatively clearly. Even larger single cracks could be identified and located. The results of the gneiss suggested that anisotropy can be a problematic error source for the classification process as it significantly influences the interaction between pick and rock depending on the angle between foliation and the movement vector of the pick. As a result of the two additional experiments, an additional feature, *contact ratio,* was formulated, and introduced as an eighth feature. It is derived from the behaviour of the *normal force* and serves as an indicator of how consistent the contact between pick and rock is.

In the case study, the three machine learning algorithms (learners) were trained on 3d-block models that were populated with the previously selected features. The learners trained on eight different situations consisting of different rock types. These situations involved either concrete + fluorite-barite ore samples

(FBA), concrete + galena-sphalerite ore samples (PB), or even multiple samples. The learners from each training case were then applied to classify the whole dataset of which they only saw a part during training. The learners were also applied to the seven other situations they were not trained with. As a result of this methodology, the main performance parameter—*accuracy*—is displayed as *self-accuracy* respectively *cross-accuracy* in this work.

For the two supervised learners, a high *self-accuracy* between 92% and 97% was recorded. The c*ross-accuracy* varied strongly, depending on the training situation. Generally, the FBA samples were very heterogeneous, which yielded lower *cross-accuracies* than for the relatively uniform PB samples. At the same time, the unsupervised k-means algorithm showed much lower *self-accuracies* between 32% and 82%. Also, the cross-accuracy was lower than for the supervised algorithms.

Additionally, the required amount of data that the supervised learners, need to provide performant results was investigated. It shows that acceptable results can be obtained with as little as 2-5% of the total data while an optimum lies between 20–40%.

Summarizing the comparison between the three algorithms, the two supervised learners provided similar results—with the ANN showing slightly better generalisation behaviour, the DRF showing faster computation speeds and easy setup of the algorithm. The k-means showed lower *accuracy* but very fast calculation speeds and does not require labelled data.

However, the biggest unknown is the geologic diversity encountered in an excavation situation. This was shown by the poor *cross-accuracy* among the fluorite-barite samples, which were all sampled at the same spot of a narrow hydrothermal vein deposit, but consisted of varying proportions of quartz, fluorite, barite, and altered gneiss. The problematic *cross-accuracy* occurred to a lesser extent on the PB samples because they showed a more homogenous composure.

In summary, FCR-based features in conjunction with a contact indicator such as the *contact ratio*, can provide accurate results for classifying different rock types. However, any learner must have experienced the possible range of behaviour during cutting to be able to identify rock zones correctly. Extrapolation is possible only to a limited extent. A training process over a wider spatial range appears essential. For unknown situations, unsupervised k-means clustering can be a flexible tool to classify untrained lithologies or serve as a support for supervised methods.

In order to provide the features researched here, a sensor system must be able to measure at least the cutting component and the normal component of the cutting force. A 3d-force sensor system could potentially achieve the highest performance. The block model-based approach used in this work significantly reduces the amount of data in the early data processing chain while retaining the necessary information level. It reduces noise and feature variance and potentially makes subsequent data processing computationally less expensive. As such, the combination of force component ratios, 3d-block model feature computation, and machine learning-based rock classification has the potential to usher in the applicability of cutting force-based automation and rock classification systems during rock cutting.

Table of Contents

Annexes

Large parts of the Annexes N to P are located on the accompanying CD. A description of the data can be found on the respective pages in this work.

List of Figures

List of Tables

List of Variables

A	Cross section area	[mm²]
A and B	Random variables for calculation of R	
A_c	Chipping cross-section area	[mm²]
α_a	Attack angle	[°]
α_c	Clearance angle	[°]
α_r	Rake angle	[°]
α_s	Slant angle	[°]
α_t	Tilt angle	[°]
α_w	Wedge angle	[°]
α_{xres}	Angle between F_x and F_{res}	[°]
$\alpha_{yx} / \alpha^*_{yx}$	Angle between F_x and F_{res} / complementary angle to α_{yx}	[°]
α_{yres}	Angle between F_y and F_{res}	[°]
α_{zres}	Angle between F_z and F_{res}	[°]
$\alpha_{zx} / \alpha^*_{zx}$	Angle between F_z and F_x / complementary angle to α_{zx}	[°]
$\alpha_{zy} / \alpha^*_{zy}$	Angle between F_z and F_y / complementary angle to α_{zy}	[°]
b_1	brittleness index	[1]
BTS	Brazilian tensile strength	[MPa]
β	Rotation angle of the cutter head	[°]
$c_0,...,c_i$	Regression parameters	
C_{rel}	Relative contribution	[%]
CR	Contact ratio	[1]
CAI	Cerchar abrasivity index	[1]
$cUCS$	Cubic uniaxial compressive strength	[MPa]
d	Cutting depth	[mm]
d_E	Squared Euclidean distance	
d_s	Diameter of sample	[mm]
d_β	Instantaneous cutting depth depending on rotation angle β	[mm]
d_{max}	Maximum cutting depth	[mm]
dr	Difference between two ranks	
E	Energy, general	[kWh]
E_{sp}	Specific energy	[kWh/m³]
E_{sp-n}	Normalised specific energy	[kWh/(m³*MPa)]
E_{st}	Static elasticity modulus	[N/m²]
E_{dyn}	Dynamic elasticity modulus	[N/m²]
EF	Error function	
F	Force, general	[kN]
F_{max}	Peak force	[kN]
F_{res}	Resulting force	[kN]
F_x	Cutting force	[kN]
$F_{x,ch}$	Chipping force	[kN]
F_{x-n}	Normalised cutting force	[kN/(mm*MPa)]
F_y	Side force	[kN]
F_z	Normal force	[kN]
g	Activation function	[1]
h_{io}	Input-output pair	
h_o	Output node	
IQR	Interquartile range	
k_c	Conversion factor	[1]
k	Number of clusters for k-means	[1]
l	Way or length, general	[m]
L	Length of a sample	[m]
l_c	Length of cut	[mm]

l_s	Length of sample	[mm]
ls_{50}	Point load strength for a 50 mm diameter sample	[MPa]
m	Selected features for DRF training	
$m_{1...}m_k$	Cluster centres 1 to k	
μ	Friction coefficient	[1]
n	Number, general	[1]
N	Number of cases in a data set	[1]
n_{dp}	Number of data points within a search radius SR	[1]
o	Predicted value	
p	p-value	[1]
P	Set of parameters, general	
PC_i	Number of observations predicted to belong to a class i	[1]
P_{rock}	Rock parameters at a certain position	
PP_{x0}	Amount of data points where $F_x < 0$ kN	[1]
PP_{z05}	Amount of data points where $F_z < 0.5$ kN	[1]
$Q_{0.05}/Q_{0.95}$	0.05-quantile/0.95-quantile	
$Q_{25}/Q_{50}/Q_{75}$	Lower, central, and upper quartile	
R	Pearson correlation coefficient	[1]
R^2	Coefficient of determination	[1]
RC_i	Number of total observations belonging class i	[1]
R_N/R_{NR}	Schmidt hammer rebound value for N-type and NR-type hammer	[1]
R_s	Spearman correlation coefficient	[1]
s	Spacing between cuts	[mm]
σ	Standard deviation	
σ^2	Variance	
SE	Standard error	
SR	Search radius	[mm]
TC_i	Number of true predictions for a given class i	[1]
TS	(Direct) tensile strength	[MPa]
UCS	Uniaxial compressive strength	[MPa]
v_c	Cutting speed	[m/s]
V_{exc}	Volume of excavation	[m³]
v_p	Acoustic p-wave velocity	[m/s]
w_o	Weight of intercept neuron	
w_i	Weight of input neuron	
X	Position on x-axis	[mm]
$\bar{x}$ / mean()	Mean	
$\tilde{x}$	Median	
x_c	Instantaneous position of the pick during a cut	[mm]
$\bar{x}_{geom}$	Geometric mean	
x_i	Random sample / single observation	
x_{is}	Standardised value of observation	
y	True value	
Y	Position on y-axis	[mm]
z	Output of neuron	
z_0	Value of intercept neuron	
z_i	Value of input neuron	
Z	Position on z-axis	[mm]

List of Abbreviations

ADC	Analogue digital converter
ANN	Artificial neural network
API	Application programming interface
CO	Concrete experiments in this work
CSM	Continuous surface miner
CV	Cross-validation
DAQ	Data acquisition
FBA	Experiments on fluorite-barite ore and concrete composite samples in this work
F-Ba	Fluorite-barite ore
FC	Force component
FCR	Force component ratio
FFT	Fast Fourier transformation
GN	Gneiss experiments in this work
KG	Knowledge gap
ML	Machine learning
MT	Main task
MWC	Measure-while-cutting
MWD	Measure-while-drilling
MW	Moving-window
OEM	Original equipment manufacturer
PB	Experiments on lead-zinc ore and concrete composite samples in this work
Pb-Zn	Lead-zinc ore
PLT	Point load test
RQ	Research question
TBM	Tunnel boring machine
TU BAF	Technical University Bergakademie Freiberg
WC	Tungsten carbide

List of Machine Learning Termini

Terminus	Explanation
Application programming interface	Application programming interfaces are software intermediaries that allow software to communicate and exchange data with each other. In the context of this work, the H2O-API was used to connect the H2O-framework to the R-Studio programming interface
Artificial neural network	A machine learning algorithm that is inspired by biological neuronal networks. Artificial neurons are connected and evaluate a problem by passing signals through the connections. All inputs are modified by a weight and summed. A visualisation can be found at: https://playground.tensorflow.org/
Distributed random forest	A supervised machine learning algorithm, which uses a larger number of single decision trees. Each of the trees is only trained with a part of the data and, as such, has limited but generalised knowledge. During prediction, the ensemble of individual trees then votes for a classification result. The method is fast in computation and can be robust against overfitting.
Ensemble learners	Are collections of multiple learners that classify the same problem and then vote for the best result.
Feature	Regarding machine learning, features or covariates are the input parameters for a machine learning algorithm that conducts, e.g., the classification. A general rule of thumb is to use as few features as possible that hold a maximum of information. This leads to the necessity that the features should—in theory—be uncorrelated. Feature selection is a complex and diverse process, and much of this work revolves around it.
Hyperparameters	The parameters that define the classification behaviour of a learner are called hyperparameters. Examples are the number of neurons or activation function of an artificial neural network.
K-means algorithm	Algorithm for clustering multidimensional data into a number of clusters (k) using Euclidean distances along the dimensions. Extensions for automated estimation of k exist. Depending on the uncorrelatedness of the data, it can suffer the curse of dimensionality for higher dimensions, which in this case can mean that differences between data become less visible.
Machine learning	Machine learning concentrates on algorithms that improve automatically (often iteratively) by using data. Usually, algorithms are trained on training data with the aim of making predictions or decisions. The field combines many methods. In this work, machine learning algorithms are used exclusively for classification purposes. K-means, distributed random forest (DRF), and neural network (NN) algorithms are used.
Test set	Dataset that is not part of the immediate training/validation. Usually, it focusses on how well the machine learning algorithm performs on data that it has not seen before. Therefore, performance measures are estimated using a separate test set of data than the one used for the training of the machine learner.
Training set	Part of a dataset that is used to train the actual machine learning algorithm.
Validation set	Part of a dataset similar to the training data but not used for the actual training. Instead, it is withheld and used to estimate the performance of the machine learning classifier, mainly during hyperparameter variation.

1 Introduction

<u>Background</u>

The mining industry faces lower grades and operations in greater depth as deposits that are "easy" to access and process become depleted. This results in lower ore grades and more material to be processed. The result of this leads to higher energy demand. During the processing of mineral raw materials, between 50 and 90% of the total energy required in the process chain from excavation to pre-concentrate is consumed in the final process steps [1–3]. On the side of geopolitics, a development toward politics of austerity and rising supply risks for specific materials arise. The European Commission has coined the term "Critical Raw Material", which defines resources that are of high economic interest and whose production is concentrated nationally [4]. The EU aims to diversify the supply of these critical materials not only through trade policy but also through domestic production [5]. The supply-and-demand disruptions that followed in the wake of the global pandemic and rising conflicts in multiple parts of the world only put an exclamation mark on the developments that had led to this point.

Furthermore, demand for certain critical materials related to the disruptions of rising electromobility, the intended decarbonisation of the energy sector, and the fourth industrial revolution are on the rise. Supply for these future resource needs cannot be sated at the current levels of production [6, 7]. At the same time, growing environmental and safety standards and acceptance issues must be met under a rising not-in-my-backyard sentiment in societies [8]. All of this puts mining companies under ever-rising innovation pressure.

A major jigsaw in mining innovation is advanced automation and process optimisation, often referred to as *"Mining 4.0"*. In adjunction to Industry 4.0, it describes whole-process-integrated automation systems with a high level of autonomous machines. Several large mining companies started programs to achieve the innovation necessary to remain competitive [9]. At the same time, advances in the field of mechanical excavation machines take place and new cutting machine designs emerge [10]. New tool materials, especially polycrystalline diamond coatings, become more competitive to regular tungsten-cobalt-based tools [11–13]. These developments bring (semi-)autonomous mechanical excavation machines—that could play a major role in modern minimal-invasive mining—closer to the horizon.

Mechanical excavation is an alternative to drilling and blasting. Drilling and blasting is associated with disturbance of the surrounding rock mass, blasting gases, noise and vibration, and safety issues due to flyrock or rockfall. Additionally, it requires cyclical operation with a diverse machine park [14]. Mechanical, also called cutting excavation machines, operate continuously, are highly automatable and produce precise and smooth profiles [15]. Although being restricted in their application by maximum rock hardness and abrasiveness, the aforementioned technical developments broaden the applicability of cutting machines prospectively. As of recent, while requiring higher investment, the overall mining cost can already be lower [16].

Cutting machines that use conical picks are widely used and appear in different machine types comprising roadheaders, continuous (surface) miners, shearer loaders, or special machines for shaft sinking. Their automation potential and the industry's need for more integrated automation concepts pose significant synergy effects. This automation potential includes the strategic possibility of fully autonomous operation. To reap these automation potentials, novel sensor concepts are needed, since there will be no machine driver that directly *"feels"* the machine's behaviour.

One of such concepts is the measure-while-cutting (MWC) concept examined in this work. It is an analogy to measure-while-drilling (MWD) technologies. For MWD, the machine's working parameters

are constantly logged and interpreted to allow for a interpretation of the rock. Together with the spatial information from the drill hole trace, a spatial model of the parameters can be derived to identify changes in rock quality or type, and log boundaries between the different rock zones [17–20]. Similar effects could be achieved with the MWC technology.

One possible effect of MWC is a possible autonomous separation of ore and waste rock, as shown in Figure 1 a). This would allow for a significant reduction of waste rock in the entire processing chain. The result would be a potential reduction in the overall processing cost and cost for environmental management—since less material has to be hauled, processed, and dumped per ton of run-of-mine ore. A second effect could be an automated warning if the rock mass conditions change unfavourably as seen in Figure 1 b). This would improve roof safety and increase overall operations efficiency.
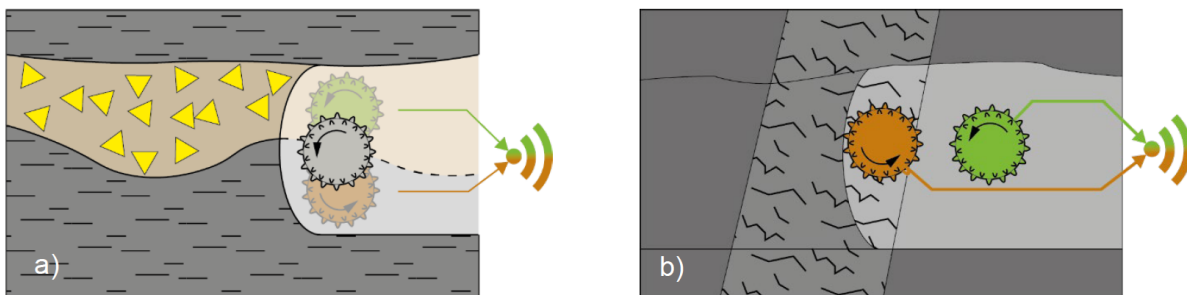
Figure 1: Basic working principle of MWC technology, a) identification of different ore types, b) identification of changing rock mass conditions

The functionality of MWD systems has been proven in the field. MWC systems, however, are in a less sophisticated state of development. The actual state of the art utilises the power consumption of the cutter drive, the slewing or marching speed, and the position of the cutter head to optimise excavation rates. However, this does not allow for detailed information on the rock mass. Utilising parameters such as cutter head torque or power consumption results in a loss of precision. A higher precision could be achieved by incorporating near-tool sensors (NTS) to measure indicatives of the reaction between tool and rock.

In soft rock for bucket wheel excavators, Drebenstedt et al. (2005) analysed this to optimise the excavation volume of the excavator depending on soil type [21]. For hard rock, a field test was published by Entacher et al. (2012)—however, for tunnel boring machines [22]. For application with conical picks, sensor concepts have been patented since the 1970s to distinguish between hard coal and the surrounding rock mass, with the latest patent coming from Sandvik [23]. However, these concepts are mainly in an experimental state that has never reached market readiness [24–26]. To date, no exact methodology of how acquired data are utilised further, and also no field experiences are described.

This work focuses on filling this gap by estimating the possibilities of using near-tool sensors for MWC purposes. Therefore, this work attempts to contribute towards a change from the old German miners saying, *"All is dark ahead of the pick"* towards *"The pick lights the way"*.

Approach

A near-tool MWC system should provide information about the changing state of the rock mass and the boundaries between different rock masses. This happens by measuring indicatives of the forces on the tools during excavation. These indicatives characterise the interaction between tool and rock.

However, this interaction is defined not only by the rock mass but also by the cutting parameters that depend on the machine itself. Most cutting machines that apply conical picks use rotating drums on

which the picks are mounted. Due to the rotational movement of the overlay of the cutter head with a slewing, sumping, or advancing movement, the picks describe a crescent shape cut as they move through the rock. This results in a change in the *cutting depth* of the pick during a cut. A changing *cutting depth* correlates with changing cutting forces and, as such, alters the force indicatives [27]. Apart from the *cutting depth*, as shown in Table 1, other parameters influence the interaction between tool and rock. These varying parameters from the side of the machine act as disturbances for rock characterisation and their influence needs to be minimised.

Table 1: Parameters influencing the interaction between rock and tool
(s: static, v: variable during operation)

Rock	Tool	Cutting parameters
Mechanical parameters (v)	State of tool/wear (v)	Cutting depth (v)
Quality, joints, cracks (v)	Tool geometry (s)	Spacing (s)
Foliation (v)		Cutting speed (v)
Alteration state (v)		Attack angle (s)
		Tilt angle (s)

To accurately define the knowledge gaps, a literature research on the state of application and patenting of MWC and related technologies is performed. This literature review is complemented by a semi-quantitative overview of the reporting standard in rock cutting research.

Based on the identified knowledge gaps, the aforementioned force component ratios are investigated as a way to approach the problem of the changing *cutting depth* during cutting. These FCRs are calculated from real-time data rather than from mean values. Furthermore, the FCRs as robust indicators for the rock type are used as input variables (features) for the training of three different machine learning algorithms.

Rather than proposing a new sensor concept, this work takes a step back and contributes towards defining the features that an MWC system would have to extract in order to provide a robust yet accurate classification of different rock masses. This leads to an explorative data analysis approach which allows deriving general requirements that a robust measurement system should meet. The general workflow of this work is shown in Figure 2.
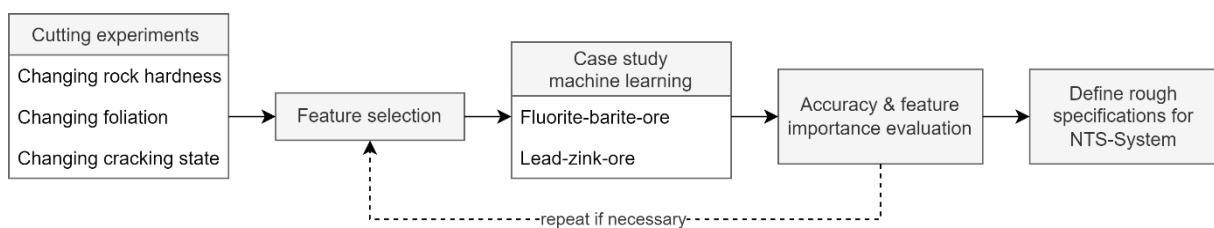
Figure 2: General workflow of this work

First, cutting experiments are conducted on concrete samples with varying hardness zones to identify an initial set of features. Here, a procedural selection algorithm is designed that preselects features from a pool of 72 possible candidate features. Based on this, k-means clustering is used to estimate the precision of boundary layer detection. In addition, two variations of this initial set are tested along with two sets of features that use "normal" cutting forces. A final set of features is then chosen from these five feature sets.

In addition, a first estimate of the precision of boundary layer detection is performed. This analysis is complemented by a correlation analysis and a feature importance analysis based on a distributed random forest classification.

Subsequently, an extension of the feature analysis with respect to two different rock mass conditions is carried out in the next two experiments. These experiments investigate a cracked rock state using artificially damaged granite and a foliated rock—gneiss. The result is a refined set of features that is further used in the machine learning case study.

In the case study, three machine learning classification algorithms that use the previously selected features are tested. Five larger samples, composed of two different materials, are each cut with two different cutting parameter combinations. Two samples consist of lead-zinc ore in the centre and concrete on the outside, and three consist of fluorite-barite ore and concrete. The data from cutting these samples are then used to test the classification behaviour of three different machine learning algorithms: k-means clustering, feedforward neural network, and distributed random forest. The first is unsupervised, and the latter two are supervised learners. The performance of these algorithms is measured in terms of classification accuracy. For the supervised algorithms, the necessary training data are also estimated. Furthermore, additional observations are considered, such as feature importance and computation time.

On the basis of the results of these experiments, the performance of a near-tool measure-while-cutting system using force component ratios can be approximated. Furthermore, the basic performance requirements can be stated for such a system.

2 Cutting Excavation with Conical Picks

This chapter presents the foundations of cutting with conical picks, also called point-attack picks, and lays the theoretical foundations for this work.

There are multiple machines available on the market that utilise conical picks. The most important types are shown in Figure 3. Roadheader type machines are used in tunnelling and development, to an extent also in production mining. Other types are continuous miner and continuous surface miner types. They are used mainly in production mining, the latter also being of importance in the construction industry—with applications in softer to medium-hard rocks such as coal, salts, trona, gypsum, limestone and even kimberlites [28]. The last type is the shearer loader, which finds application in the underground mining of seam-like deposits, primarily in coal and potash operations. A more detailed description of the different types of these cutting machines is presented in Annex A.

They all follow a common basic principle, where a rotating cutting head or cutting drum carries multiple conical picks (marked orange in the figure). These picks carry out the actual rock excavation. Cutting forces occur as responses of the cutting process, and the cutting process itself is the interaction of the conical pick with the rock during excavation. The application of conical pick-based machines ranges to a maximum of 120 MPa *uniaxial compressive strength* (*UCS*) [28].

Figure 3: Different excavation machines that utilise conical picks [29, 30][1]

Figure 4 shows the general working principle for the cutting drum of a surface miner. The tool holders on the drum house the actual cutting tools, the conical picks. These picks cut grooves into the rock. The actual penetrative movement of the pick through the rock mass is achieved by an overlay of a directional movement of the cutterhead as it rotates.

As such, the tools describe an advancing spiral movement through the rock mass. Each individual pick excavates a crescent-shaped groove during its passthrough [31]. As a result, a penetration, or *normal force*, a *cutting force,* and a *side force* are exerted on the picks. The material in the cutting trajectory/grooves is removed in this manner. In addition, the material between these grooves breaks

---

[1] Virtual models: by courtesy of Element Six (UK) Ltd.;
Photo: by courtesy of Wirtgen GmbH

out. The tools are usually arranged in a helix, double helix, or similar pattern. This is for multiple reasons:

a) It ensures that the tools are evenly distributed over the circumference of the drum. By this, reaction forces on the drum and the drive are more evenly distributed.

b) Adjacent picks will penetrate the rock in successive order, as indicated by the 1.–3. in Figure 4. By this, the material loosened through the succeeding tool breaks out towards the already created groove of the preceding tool. This is called semi-relieved cutting and results in reduced cutting forces compared to unrelieved cutting, where the material has no free face to break out to (for further details see Chapter 2.1)

c) Additionally, by breaking out towards the preceding groove, the material is already transported in that direction. The sequence of cuts is usually designed in such a way that the material flow goes towards the loading unit—this aids in the loading process of the material.
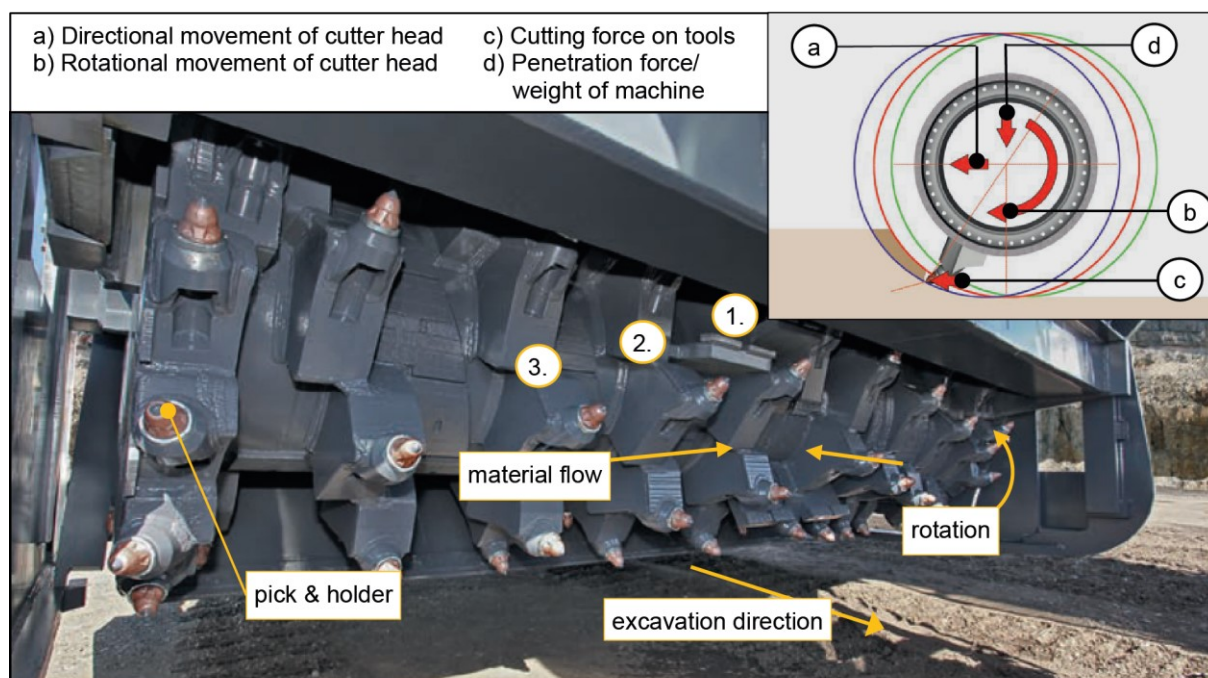
Figure 4: Working principle of the cutting drum of a surface miner, after [28][2]

There are several subtypes of this working principle. Although they vary in certain aspects, the general working principle is always based on the overlay of rotation with directional movement. One exemption from this rule is the coal plough. Here a non-rotating machine body holds the tools, and the excavation is conducted by linear movement of the whole plough body through/over the rock. Ploughs are limited in their application to coal operations underground and are not the focus of this work. However, a transfer of the findings to non-rotating cutting elements is possible.

As shown in Figure 5 on the next page, the interaction between tool and rock is influenced by multiple parameters that can be divided into influences of the rock mass and influences from the side of the machine and cutting tools. The rock mass is a combination of rock materials with different mechanical properties that is intersected by discontinuities. It can be characterised by its microscopic and macroscopic state. The former is defined by the rock-forming minerals' composition and structure; the rock mass' integrity defines the latter on a larger scale (e.g., the face of an excavation). The microscopic

---

[2] by courtesy of Wirtgen GmbH

properties can either be directly described, or the mechanical results, the rock mechanical parameters, can be measured. The latter usually happens on drill core segments in the laboratory.

The macroscopic properties of the rock mass describe the occurrence and characteristics of discontinuities (cracks and joints) and translate them into a numerical or discrete scale. The rock mechanical properties mainly define the strength of the intact rock on a smaller scale. The rock mass properties the rock mass alter, usually weaken, this rock mechanical strength on a larger scale. In a mining operation, the rock mass quality is often summarised into groups such as: "intact", "medium-fractured" or "fractured". These classes can then be associated with respective safety measures.

On the other side stand the influences of the excavation machine. The parameters of the excavation machine are defined by the general design of the machine, the working regimen, and the design of the tool and the cutter head. The shape of the cutter head, the lacing, and the geometric arrangement, together with the working regimen, define the shape of the cuts and the instantaneous cutting parameters during cutting. Of those cutting parameters, *cutting depth* (*d*) and *spacing* (*s*) which are underlined in the figure, significantly affect the cutting forces and are the main parameters investigated in this work. Other parameters are defined by the shape of the tool in conjunction with the geometric arrangement of the tool. While the geometric arrangement of the tool is fixed, the shape of the tool changes as it wears down. As such, some parameters change due to wear—marked (w) in the figure.

Possible output parameters that describe this interaction between tool and rock are the cutting forces that act on the tool during excavation, alongside other parameters like *specific energy* consumption or advance rate. In the scope of this work, the focus lies on the cutting forces. The cutting forces are the immediate response that describes the interaction between tool and rock.

Since this work aims to identify changes in rock types or rock mass during cutting, it is crucial to understand the important parameters that influence and describe this interaction. Hence, they are laid out in the following sub-chapters.
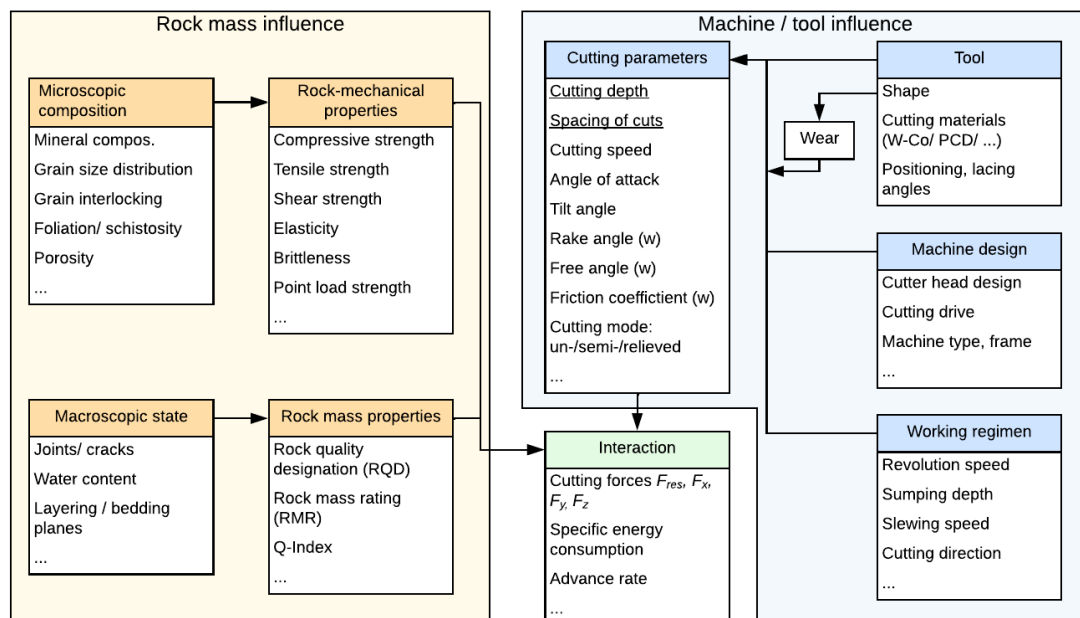
Figure 5: Parameters influencing the interaction between tool and rock during mechanical excavation, (w) – cutting parameters that change due to wear; compiled after [31–40]

2.1 Cutting Process

As the pick moves through the rock during excavation, it is subject to the resulting cutting resistance force F_{res}. This force can be described as the force vector $\overrightarrow{F_{res}}$. As such, it is the vector sum of its three (Cartesian) spatial components $\overrightarrow{F_x}$, $\overrightarrow{F_y}$ and $\overrightarrow{F_z}$ as shown in Figure 6. In cutting force measurement practice, the values of the components F_x, F_y, and F_z are usually measured, since their direction is strictly defined by the measurement device. The value of F_{res} can then be calculated after Formula (1).

$$\left|\overrightarrow{F_{res}}\right| = \sqrt{\left|\overrightarrow{F_x}\right|^2 + \left|\overrightarrow{F_y}\right|^2 + \left|\overrightarrow{F_z}\right|^2} \qquad (1)$$

Where F_x – drag force along the cutting direction, the *cutting force*; F_z – the penetration, or *normal force*; F_y – *side force*. Hereby, F_x is collinear with the movement direction of the pick.

The three force components are associated with the three Cartesian axes:

F_x	x-axis
F_y	y-axis
F_z	z-axis

In this context three planes can be defined:

x-y	chipping plane
x-z	cutting plane
y-z	normal plane
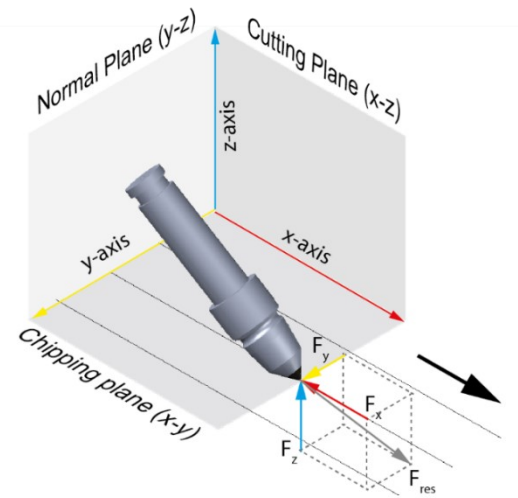
Figure 6: Definitions of forces, axes and planes on the pick, black arrow – cutting direction; after [41]

The nomenclature in cutting research is not defined uniformly and depends both on the language background of the authors and the application context of the work. This work uses the definitions with context to linear rock cutting experiments and the rock cutting test stand at TU Bergakademie Freiberg (TU BAF). Here, the x-axis denotes the cutting direction. Each cut is set with a *cutting depth* along the z-axis. Subsequent cuts (thin lines in the figure) are spaced with *spacing* along the y-axis.

The chipping process is a highly instationary process. The process is shown in Figure 7. It takes place in the following manner: the pick creates a zone of crushed material (1). The crushed material from Zone 1 is usually released as dust. Here, the rock is mainly subject to compression-based failure. Rostamsowlat et al. (2018) show that for a very small *cutting depth* (<0.7 mm), the mean pressure to excavate the material in the crushed zone is similar to the *UCS* [42]. During this phase, the components of the *cutting force* build up and a deformation field is induced in the rock resulting in elastic deformation (2). The tensor and elastic deformation grow as the pick moves forward. The *cutting force* increases until a local maximum is reached at the point where a shear chip is released by the pressure of the bit (3). This chipping is mainly subject to shear and tensile failure. With the release of the chip (4), the *cutting force* components are almost zero and increase again until the next chip is lifted off [43].
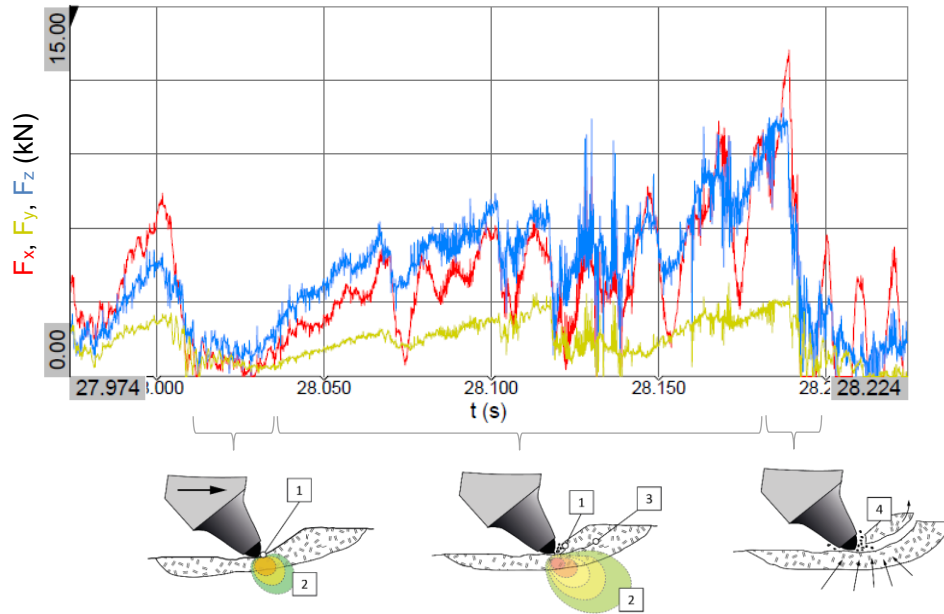
Figure 7: Diagram of cutting force components acting on the cutting tool during chipping process and chipping process with conical picks (explanations in text), after [43]

Due to the instationarity of the cutting process, Equation (1) can be reformulated as:

$$\left|\overrightarrow{F_{res}(P)}\right| = \sqrt{\left|\overrightarrow{F_c(P)}\right|^2 + \left|\overrightarrow{F_s(P)}\right|^2 + \left|\overrightarrow{F_n(P)}\right|^2} \; with \; x_c \in P \tag{2}$$

Hereby, x_c is the position of the tip of the pick along its trajectory, which is an element of the set of all parameters P that influence the cutting forces. This means that instantaneous cutting forces depend on the position of the pick with respect to its previous position, as well as the specific rock properties at this position.

Cutting Force F_x

As mentioned, the *cutting force* is necessary for the actual chipping process and colinear with the trajectory of the pick. This means that the *cutting force* usually has to be overcome by the cutter head drive of an excavation machine. F_x consists of the force necessary for the actual chipping and a friction part [27]:

$$x_c = F_{x,ch} + \mu * F_z \tag{3}$$

Where $F_{x,ch}$ is the part of F_x defined by the actual chipping, μ is the *friction coefficient*, and F_z is the *normal force*. The *cutting force* is an essential indicator of the torque that the cutter head drive must provide.

Normal Force F_z

The *normal force* acts perpendicular to the trajectory of movement of the pick and the surface of the rock. The *normal force* has to be overcome/provided by the excavation machine to keep the pick in the cutting groove and allow the actual excavation. The *cutting depth* and excavation efficiency will decrease if the *normal force* cannot be provided, because the pick will not stay in its groove anymore.

9

Side Force F_y

The *side force* acts perpendicular to the trajectory of the tool and lies on the surface plane (x-y plane) of the rock. The *side force* acts as a result of an asymmetric outbreak of material. The material outbreak occurs mainly towards the preceding cut in regular, semi-relieved cutting.

Interrelation of Cutting Force Components

Resulting from their trigonometric relationships, the ratios of the *cutting force* components can be formulated as shown in Figure 8 and Equations (4)–(9). Therefore, the *cutting force* ratios indirectly describe the angles at which the *resulting force* acts on the tip of the tool. The cotangent of two force components describes the angle on which F_{res} acts on the plane that these two vectors span. Furthermore, the enclosed angle between F_{res} and the respective force components F_x, F_y, and F_z describes not only the angle between those two vectors but also the proportional contribution of the respective force component to F_{res}.
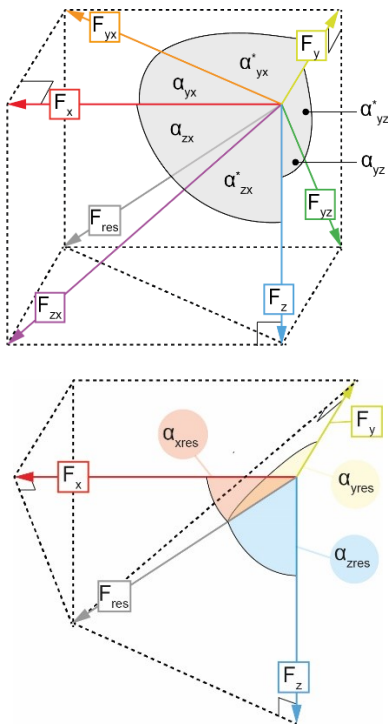
$$\tan(\alpha_{yx}) = \frac{F_y}{F_x}; \ \cot(\alpha_{yx}^*) = \frac{F_y}{F_x} \tag{4}$$

$$\tan(\alpha_{zy}) = \frac{F_z}{F_y}; \ \cot(\alpha_{zy}^*) = \frac{F_z}{F_y}; \tag{5}$$

$$\tan(\alpha_{zx}) = \frac{F_z}{F_x}; \cot(\alpha_{zx}^*) = \frac{F_z}{F_x} \tag{6}$$

$$\cos(\alpha_{xres}) = \frac{F_x}{F_{res}} \tag{7}$$

$$\cos(\alpha_{yres}) = \frac{F_y}{F_{res}} \tag{8}$$

$$\cos(\alpha_{zres}) = \frac{F_z}{F_{res}} \tag{9}$$

Figure 8: Angular relations of cutting force components

Where the angles α_{ij} represent the angle enclosed by the two force vectors indicated in the subscript—F_x, F_y, F_z, respectively F_{res}. The * denotes the respective complementary angle.

Specific Energy

The *specific energy* (E_{sp}) is defined as how much energy is necessary to excavate one m³ of rock. In rock cutting, the unit kWh/m³ is usually used. It is an often-used parameter to investigate the effectiveness of an excavation process [44]. The *specific energy* consumption is influenced by, and correlates to a multidate of factors—both from the side of the machine and from the side of the rock. The *Energy* (E), necessary for the excavation, can generally be written as the integral of a *force* (F) over the *way* (l) from the *starting point* (l_1) to the *endpoint* (l_2).

$$E = \int_{\vec{l}_1}^{\vec{l}_2} \vec{F}(\vec{l}) * d\vec{l} \tag{10}$$

In the context of cutting experiments, E_{sp} it is calculated as:

$$E_{sp} = \frac{E}{V_{exc}} = \frac{mean(F_x) * l_c}{3600 * V_{exc}} \left[\frac{kWh}{m^3}\right] \qquad (11)$$

For full-scale measurements on excavation machines, the electrical power consumption is usually measured directly to calculate E. For laboratory cutting experiments, $mean(F_x)$, the mean value of the *cutting force*, is measured, l_c is the total *length of the cut*, and V_{exc} is the *volume of excavated material*. V_{exc} can be measured in different ways, as such comparing results from different authors must be performed with caution. Additional information about different measuring methods for V_{exc} is located in Annex B.1.

Generally, it can be said that the harder and tougher the rock, and the more intact the rock mass is, the higher the *specific energy* consumption. Furthermore, the higher the chipping parameters s and d, the lower the *specific energy* consumption. This can be seen in Figure 9. There, the chipping area A_c, which forms as the product of d and s, is compared to the mean of E_{sp} and the mean of F_c. For detailed information on chipping parameters, see Chapter 2.1.2. Furthermore, E_{sp} correlates with the grain size of the cut material. Quang (2007 & 2009) reports a correlation of dust occurrence with *specific energy* consumption [45, 46].
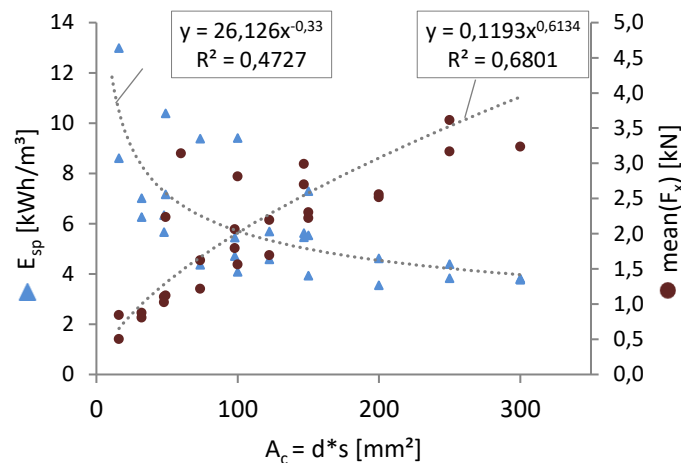
Figure 9: Relation of chipping area to specific energy and mean cutting force, recalculated after [47]

2.1.2 Cutting Parameters

The design of the excavation machine comprising machine type, cutter head type and design, transmission, and most importantly—pick design, arrangement, and lacing—they all define the cutting parameters together with the machine's working regimen [31]. While some parameters remain static during the excavation process, others change over time or during a single passthrough. The cutting parameters define the cutting process from the side of the machine and as such the cutting force measurement. It is essential to understand their influence if one aims to utilise cutting force measurements to identify rock types.

<u>Angles on the Pick</u>

During the cut, the pick is oriented with an *attack angle* (α_a), a *slant angle* (α_s), and a *tilt angle* (α_t). The tool geometry defines the *wedge angle* (α_w), which defines the opening angle of the cutting tip. Together with the *attack angle*, the *wedge angle* results in the *clearance angle* (α_c) and the *rake angle* (α_r). The

geometric conditions are shown in Figure 10. The black arrow indicates the cutting direction. All angles are not actively changed during excavation. However, the *wedge*, *clearance*, and *rake angle* are subject to wear and change as the tool wears down.
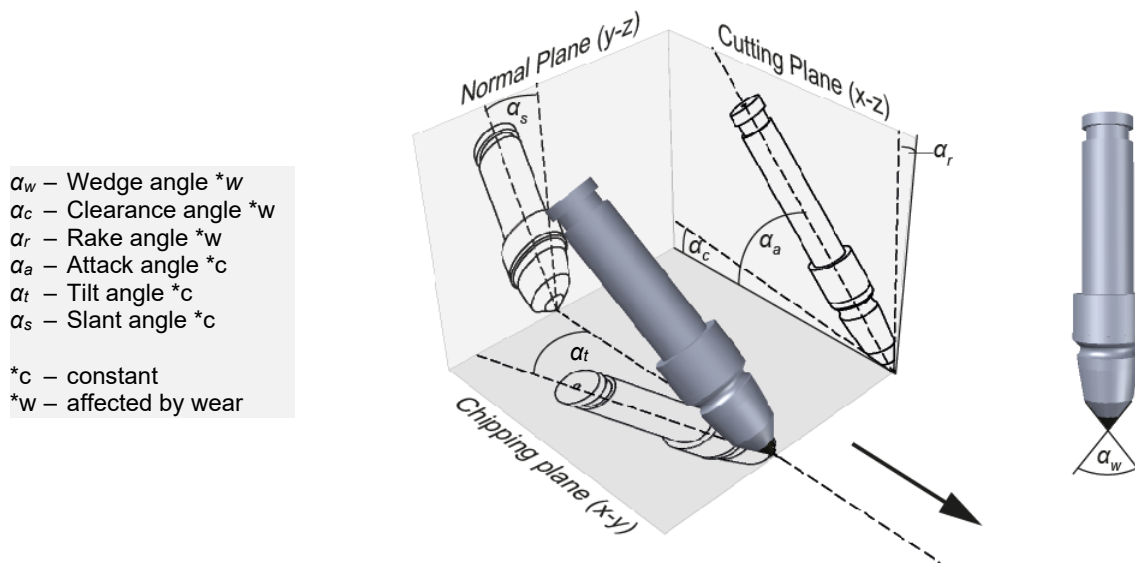
Figure 10: Angles on the pick, after [48]

α_w – Wedge angle *w
α_c – Clearance angle *w
α_r – Rake angle *w
α_a – Attack angle *c
α_t – Tilt angle *c
α_s – Slant angle *c

*c – constant
*w – affected by wear

Wedge Angle α_w

The *wedge angle* is the opening angle of the tip. Generally, a sharper *wedge angle* allows the bit to penetrate the rock more easily and reduces the *specific energy* requirement for excavation. However, it also increases the probability of a total failure of the bit due to breakage of the carbide pin. *Wedge angles* of 70 to 90° are common [31]. Zhou (2020) and Quang (2007) report that the *wedge angle* affects the generation of respirable dust. A higher *wedge angle* increases the *specific energy* consumption and the dust generation. [45, 49]. The *wedge angle*, together with the *attack angle*, and to a minor extent, the *tilt* and *slewing angles* define the *clearance angle*.

Clearance Angle α_c

A higher *clearance angle* reduces the contact area between the pick and the rock surface. Therefore, the *clearance angle* has a direct effect on the required *normal force*. An increase in the *normal force* increases frictional resistance and as such the *specific energy*. An increase in the *clearance angle* up to about 10° reduces the *specific energy* requirement. A larger *clearance angle* also increases the risk of tip failure, mainly because higher *clearance angles* are usually achieved using picks with smaller *wedge angles*. Additionally, the *clearance angle* decreases as the wear condition of the tool increases. Then, a wear flat develops, increasing friction between tool and rock. [50, 51]

Rake Angle α_r

The *rake angle* determines the type of load on the upper side of the pick's tip. If the *rake angle* is positive, the tool's tip is subjected to compressive stress, and if it is negative, it is increasingly subjected to tensile stress. The tool tips are generally made of tungsten carbide, while the tool's head is made of quenched and tempered steel. Although tungsten carbide has high compressive strength and hardness, unlike steel, it is relatively brittle and has a lower tensile strength. As a result, negative *rake angles* can lead to critical tensile stresses in the carbide pin and thus to a total failure of the pick [50, 51]. Additionally, Quang (2007 & 2009) states the influence of a high *rake angle* on higher dust generation [45, 46].

<u>Tilt and Slant Angle α_t / α_s</u>

The *tilt* and *slant angle* are closely connected. The *tilt angle* is the angle set by turning the tool holder around the z-axis [41]. The *slant angle* is the angle between the pick axis and the normal direction of the chipping plane. Sun and Li (2018) argue that while the *tilt angle* is set during machine design, the *slant angle* may be different for different picks depending on their position on a cutting drum—resulting in different forces on the tools [48].

<u>Attack Angle α_a</u>

The *attack angle* and the *wedge angle* determine the *clearance* and *rake angle* and thus represent a possibility of optimising the excavation process. Depending on the *wedge angle* and the desired *clearance* and *rake angles*, the *attack angle* is between 40° and 60° [27, 31, 50]. Optimising the *attack angle* means optimising the *rake* and *clearance angle* indirectly. The *attack angle* is defined by the tool holder's design, and as such, it is constant during cutting.

<u>Cutting Speed v_c</u>

The effect of the *cutting speed* (v_c) on the excavation process is rather complex and its influence on the cutting forces is reported ambiguously. Some sources report a slight increase in cutting forces with increasing *cutting speed*; others report no significant increase in cutting forces. Theoretical models do not consider the influence of the *cutting speed* [52–55]. Verhoef (1997) states various sources that showed ambiguous effects of the *cutting speed* on the cutting forces. He also presents a chain of causalities explaining a possible increase in cutting forces due to reaching a critical cutting speed, which causes spontaneous wear and, in return, increases the cutting forces [56][3]. Due to translation errors and nonstandard nomenclature, *cutting speed* sometimes can be mistaken for *advance rate* (e.g. [36]).
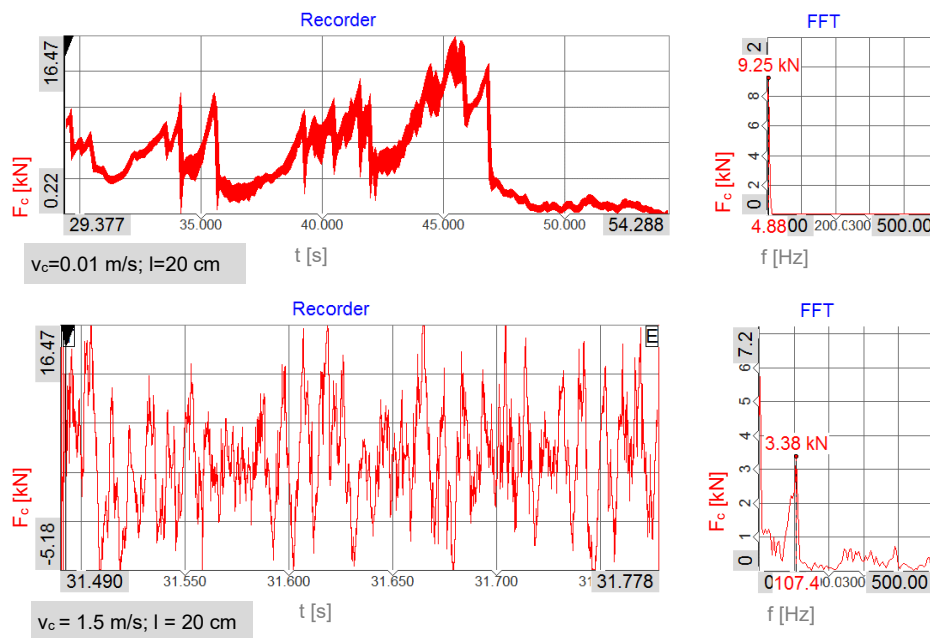
Figure 11: Exemplary force-time diagrams and FFT-analysis for slow (top) and fast (bottom) cutting speeds; other cutting parameters are constant

---

[3]Yadav (2018) [54] cites Menezes (2014) [55] who cites Verhoef (1997) [56]. Both Yadav (2018) and Menezes (2014) however only cite that the cutting speed has no influence on the forces, which Verhoef later in his work relativizes.

Own experiments show that an indirect relationship between cutting forces and *cutting speed* might occur. At higher cutting forces, the cutting test rig of TU BAF shows a dynamic and swinging behaviour around 94–110 Hz. This behaviour results in an oscillating overlay on F_x, which influences the distribution of F_x.

Figure 11 shows an example of this effect. Top, a slow cut ($v_c = 0.01$ m/s) is presented; bottom, a fast cut with $v_c = 1.5$ m/s. The build-up of the *cutting force* and sudden release upon breaking of the chip is well visible at the top. During fast cutting, the forces fall partially into negative territory due to the oscillation, while they do not during slow cutting. Also visible is the oscillation of the forces at 107.4 Hz during fast cutting. The maximum forces were 17 kN during slow cutting, while the maximum forces reached 24 kN during fast cutting. Entacher et al. (2012) support these findings with the experience-based statement that the *cutting speed* and the dynamic machine behaviour influence each other and the cutting process [57].

From previous experiments conducted at TU BAF, Keller (2016 & 2017) reports that the ratio of *normal* to *cutting force* increases for faster *cutting speeds* [58, 59]. Vorona's comparative literature review from 2012 can be summarised as follows: with increasing cutting speed, the tool temperature increases; furthermore, each tool/machine/rock combination has its own critical *cutting speed*. It usually lies at ca. 1.5 m/s for regular tungsten carbide (WC) conical picks. From there, the wear increases drastically. This is attributed to a local exceeding of a critical temperature that causes a change in the molecular matrix [27]. Shao et al. (2018) report that increasing the *cutting speed* increases the temperature at the tip of the pick as well as F_x and F_z. The maximum temperature measured was ca. 1100 °C for a *cutting speed* of 1.5 m/s and $d = 10$ mm, unrelieved cut [60]. For the cutting process during drilling, Loui and Karanam (2005) show a relationship between *cutting speed* and tool temperature [61].

Quang (2007 & 2009) reports that the *cutting speed* can influence dust emission [45, 46]. Since dust emission correlates with *specific energy* consumption, it can be stated that *cutting speed* influences the *specific energy* consumption. Complementary, Restner (2015) reports that a low *cutting speed* can positively influence the production rate in rock masses with a low integrity rating [62].

Although in-depth research on this topic was not conducted, it is suspected that swinging behaviour should not influence the mean forces. However, the peak forces and distribution measures are affected by this. This behaviour is always related to the exact design, shape, and material composition of the machine, which defines its dynamic behaviour. Since the *cutting speed* is usually static in the industrial environment, it is considered an unproblematic factor for the determination of cutting forces as long as no cross-comparison between different machines and sites is conducted.

Cutting Depth *d* and Spacing *s*

The *cutting depth* defines the depth, the tool indents the rock while cutting, and the *spacing* defines the distance between two neighbouring cuts, as shown in Figure 12. These parameters have a considerable influence on the *specific energy* required for extraction.

The greater the realisable *cutting depth*, the lower the *specific energy* requirement. However, the greater the *cutting depth*, the greater the cutting forces in general [30]. Due to the stability of the cutting picks and the available drive power of the cutting machine, the maximum *cutting depth* is limited.
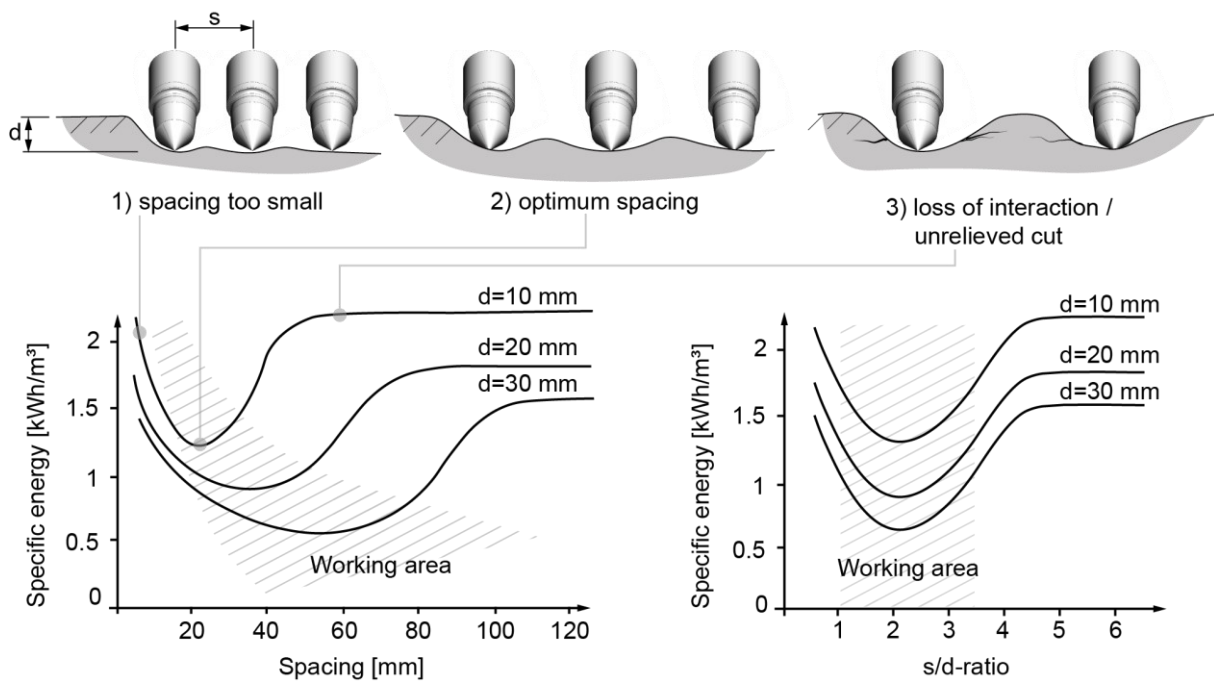
Figure 12: Relationship between specific energy, cutting spacing and cutting depth, after [31]

Due to cracks propagating from the cutting path, the resulting cracks of two cuts overlap each other. Subsequently, the material between adjacent cuts breaks out. This means that if two adjacent cuts are placed at a distance and the cracks barely overlap, a maximum of material breaks out between the two cuts—shown in Marking 1) in Figure 12. It is possible to determine an optimal cutting *spacing* between adjacent cuts. If *s* is smaller than this optimal distance, the material in between breaks away, but more cuts have to be made compared to the optimal cutting distance to break out the same volume (Marking 2). When the material between two cuts breaks out, it is called <u>semi-relieved cutting mode</u>. If *s* between the cutting lines is too large, ribs are formed due to the lack of crack overlap (Marking 3). This is connected to additional energy consumption because the conditions of confinement are less favourable due to the lack of a free face. This is also called (fully) blocked or <u>unrelieved cutting mode</u>.

There are two additional cutting modes. The first, the relieved cutting mode, defines a situation where there are free faces on two sides—resulting in the low cutting forces. However, it only applies to a few picks on a drum and is therefore not focused on in this work. The second one, (groove)-deepening cuts, refers to a method where multiple unrelieved cuts follow in the same groove, deepening the groove until a major material outbreak occurs. This method is associated with increased wear and reduced effectivity [36]. It is also not considered further in this work.

<u>Ratio *s/d*</u>

With greater *cutting depth*, the cracks spread further around the cut. This means that the distance between the cutting lines can be greater, so that the *specific energy* consumption can be further reduced. A ratio *s/d* can be defined as the ratio of *cutting spacing* to *cutting depth*. It is also called rib breaking factor, chipping modulus, or cutting modulus. It can be seen as the ratio of *distance* to the free face to the *cutting depth*. As shown in Figure 12, an optimum *s/d* exists independently of the actual *cutting depth*. At this optimum, the *specific energy* consumption is minimal due to the optimum outbreak of material in-between the cuts. The *s/d*-ratio depends mainly on the brittleness of the rock and is specific to each rock and tool combination. With increasing brittleness, the value of the optimum *s/d*-ratio increases [31].

Cutting Parameters During Regular Excavation

The *spacing* between the picks is defined by the arrangement of the picks on the cutter head. The fact that d increases following a sine function during the revolution of the drum results in a change of the *s/d*-ratio during one revolution of the cutting drum, as depicted in Figure 13 [27, 63, 64]. According to Pajer et al. (1971), the dependency of the *cutting depth* from the rotational angle of a cutting tool can be approximated by:

$$d_\beta \approx d_{max} * \sin \beta \tag{12}$$

Where d_β – *instantaneous cutting depth, d_{max} – maximum cutting depth, β – rotational angle of the pick on the cutting drum* [65].
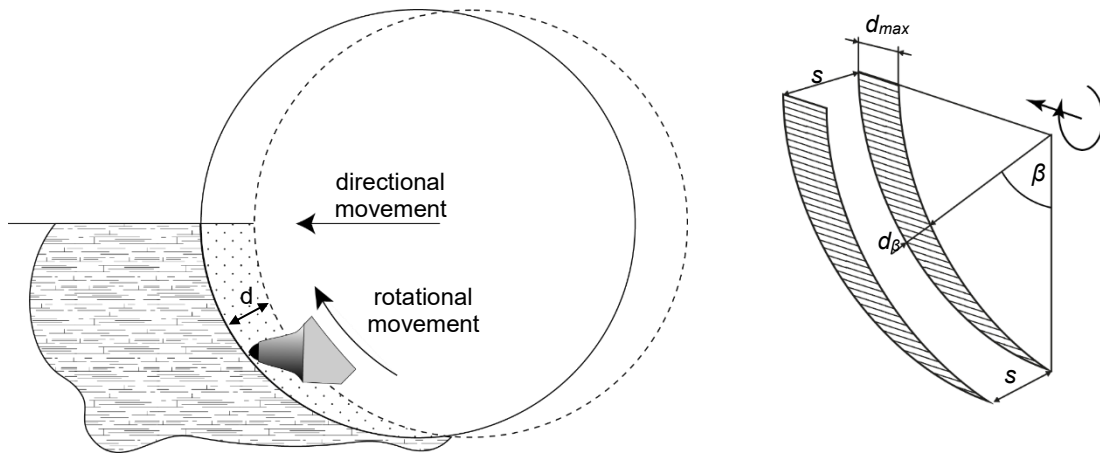
Figure 13: Scheme of cutting depth as a function of advance rate and rotational angle

The fact that the optimal *s/d*-ratio is independent of the *spacing* also means that during cutting with a rotary cutter head, *s/d* cannot be maintained at an optimum.

Both parameters, the *cutting depth* and *s/d* influence the cutting forces [27, 37, 66]. An increasing d correlates positively with F_x. A decreasing *s/d* correlates positively with F_x, but negatively with F_y [47, 67, 68]. For the utilisation of data derived from the cutting forces with the aim of rock characterisation, it is crucial to reduce or even eliminate the influence of those cutting parameters that vary during operation of the cutting machine. For this, two general approaches are possible:

    a) comparing the forces in relation to the pick's current position, hence the cutting parameters, or
    b) limiting the influence of the *cutting depth* on derived data.

Case b) is evaluated in this work. It follows the presumption that while the absolute force levels may vary, the ratios between the components of the cutting forces do not vary to such an extent and are mainly governed by the rock type. This presumption is derived from the works of multiple authors starting with Roxborough (1981)—where with a higher *cutting depth*, a proportional increase of F_x and F_z is reported. Vorona (2014) and Sarwary (2016) also report that this optimal *s/d* is dependent on material type [27, 60, 64, 69].

2.1.3 Influences of Rock Mechanical Properties

The mechanical behaviour of rock is mainly governed by mineral composition, grain sizes and shapes, state of interlocking in-between the crystals, and the orientation of the grains and porosity [70]. For engineering applications, the rock mechanical properties characterise the outcome of these composition parameters regarding the rock mechanical properties. This chapter focuses on important rock mechanical properties and shows their influence on the interaction between rock and tool.

Uniaxial Compressive Strength

The *uniaxial compressive strength* (*UCS)* is one of the basic parameters in rock engineering. In the US, the ASTM D2930 standard or the recommendation of the ISRM (International Society for Rock Mechanics) is used. The norm EN 1926:2006 is used as a standard in the European sphere.

After EN 1926, a cube or drill core with a height and diameter of 70±5 or 50±5 mm should be used. Its top and bottom surfaces must be parallel and levelled. The largest grain size must be less than 1/10 of the diameter of the sample. Otherwise, a higher sample number should be tested. The core is then put under uniaxial load from the top and bottom of the sample with a constant rate of 1±0.5 MPa/s until the sample fails. The *UCS* is then calculated after Equation (13).

$$UCS = \frac{F_{max}}{A} \tag{13}$$

Where *UCS – uniaxial compressive strength*, F_{max} *– force at which the sample failed, A – cross-section area of the sample*.

The *UCS* can be considered a general characterising property and is used for stability calculations or estimations of the efficiency of an excavation process. The cutting forces F_x and F_z scale positively with the *UCS*. A regression (s. Figure 14) for this scaling has been shown by Bilgin et al. (2006) [32]. Naeimpour et al. (2018) correlated *UCS* and *BTS* to the results of a micro scratch test which utilises a micro disc with a diameter of ca. 22 mm [71]. For concrete, *UCS* tests are often performed on cast cubes of 15 cm side length. In this work, the cube *UCS* is called *cUCS*. The *cUCS* can be up to 20% higher than *UCS*, depending on the concrete type, preparation and sampling conditions [72].
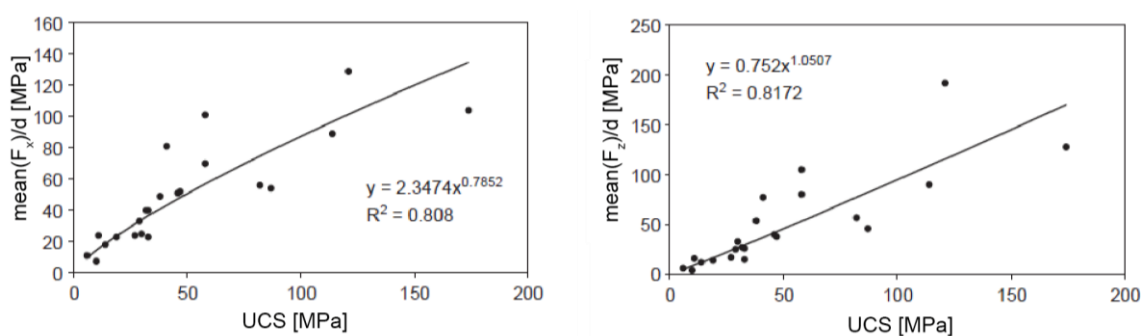
Figure 14: Ratio of mean cutting force (left) and mean normal force (right) to cutting depth vs. uniaxial compressive strength for semi-relieved cutting mode [32].[4]

---

[4] Reprinted with minor adjustments from International Journal of Rock Mechanics and Mining Sciences, Volume 43, Issue 1, N. Bilgin, M.A. Demircin, H. Copur, C. Balci, H. Tuncdemir, N. Akcin, Dominant rock properties affecting the performance of conical picks and the comparison of some experimental and theoretical results, pp. 139–156, Copyright © 2006, with permission from Elsevier

Tensile Strength and Brazilian Tensile Strength

While the *tensile strength* test is a direct test, the *Brazilian tensile strength* test is an indirect method to determine the tensile strength of a specimen. The direct tensile test follows Equation (14), which is the same principle as for *UCS*, but in a tensile manner.

$$TS = \frac{F_{max}}{A} \qquad (14)$$

Where *TS – direct tensile strength*, F_{max} *– peak pull force, A – cross-section area of the sample*. The direct tensile requires relatively high efforts for sample preparation and is rather expensive.

As an alternative, the Brazilian tensile test can be conducted as an indirect measure of the tensile strength of a rock sample. It follows the ASTM D3967 or ISRM norms for the anglophone area and the EN 12390-6 for Europe. A slice of a drilling core with a ratio of 0.5 for *length* to *diameter* is used for the test. The sample is then loaded using half-spheres. By that, a diametral loading scenario can be ensured. The compressive loading then results in a tensile loading at the centre of the core. Since the tensile strength is around 1/10 of the compressive strength for most rocks, cracks will occur due to tensile failure and will result in total failure of the sample. The Brazilian tensile strength is calculated using the following equation.

$$BTS = \frac{2F_{max}}{\pi * l_s * d_s} \qquad (15)$$

Where *BTS – Brazilian tensile strength*, F_{max} *– peak force, l_s – length of the sample, d_s – diameter of the sample*.

Compared to the regular tensile test, the Brazilian tensile test is faster, simpler, and more cost-effective to conduct. *BTS*, like *UCS* correlates directly with the forces F_x and F_z as shown in Figure 15.
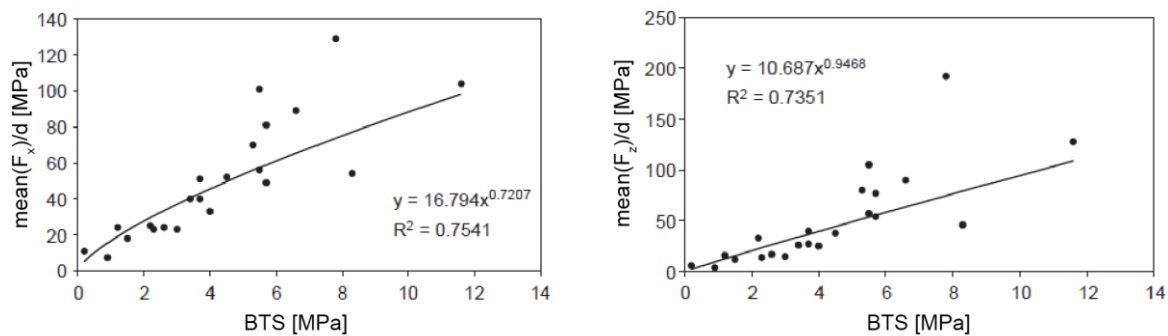
Figure 15: Ratio of mean cutting force (left) and mean normal force (right) to cutting depth vs. Brazilian tensile strength for semi-relieved cutting mode [32][5]

[5] Reprinted with minor adjustments from International Journal of Rock Mechanics and Mining Sciences, Volume 43, Issue 1, N. Bilgin, M.A. Demircin, H. Copur, C. Balci, H. Tuncdemir, N. Akcin, Dominant rock properties affecting the performance of conical picks and the comparison of some experimental and theoretical results, pp. 139–156, Copyright © 2006, with permission from Elsevier.

Point Load Strength

The point load test (PLT) is widespread due to its simplicity. Here, a rock sample is loaded between two diametral cones, and the peak pressure at failure of the sample is recorded. The point load strength scales linearly with *UCS*. As a conversion formula, the following is given [73]:

$$UCS = k_c * Is_{50}$$
(16)

Where *UCS – the uniaxial compression strength*, *Is$_{50}$ – the point load strength for a 50 mm diameter sample*, *k$_c$ – conversion factor*.

After EN 1926:2006, a value of 22 for k_c is taken. In the American area, a factor of 21 is common [73–75]. Thuro (2010) notes that a conversion between *Is$_{50}$* and *UCS* should only be conducted if the conversion factor could be experimentally defined at some samples [76]. Rusnak and Mark (2000) show a selection of studies that defined k_c experimentally. The values can deviate from 21/22 by up to 40% in some cases [73].

As Hoek (1977) pointed out, the mechanics of the point load test actually cause the rock to fail due to tension. Therefore, the PLT's *accuracy* in predicting the *UCS* depends on the relationship between *UCS* and *TS*. For most rocks, the ratio is approximately 10. For softer rocks like mudstones and claystones that quickly show plastic deformation, the PLT has to be used with care. There, the ratio may be closer to 5. This implies that PLT results might have to be interpreted differently for the weakest rocks [73, 75]. As the *Is$_{50}$* correlates with *UCS* and *BTS*, it also correlates positively with the cutting forces. Tiryaki and Dikmen (2006) established a linear correlation of *Is$_{50}$* to *specific energy* consumption [77].

Brittleness

The brittleness of rock is in the context of mining is typically used to describe how brittle or ductile a material behaves under load. In the context of excavation, it is related to the excavatability of a given rock. However, there is no general definition of brittleness. Ai et al. (2016) [78] and Dursun et al. (2016) [79] review a total 16 methods to define brittleness indices and present their own approaches for calculation [79]. Table 2 summarises the physical parameters used in these formulas to calculate these different brittleness indices. Of these 18 formulas, eight implement the peak compressive strength in some way. Annex B.2 shows details of these formulas.

Table 2: Summary of physical indicators used to calculate different brittleness indices, after [78–80]

Number of formulas	Physical parameters utilised in the formula
2	Ratio of volumetric content of brittle minerals to all minerals
8	Ratios of different components of stress (like *UCS*, *BTS*)
1	Elastic modulus and Poisson ratio
2	Different components of strain
2	Ratios of *energy* required for different stages of the breakage process (e.g., elastic deformation, cracking, etc.)
2	Penetration during pin penetration tests
2	Amount of fine-grain obtained during the impact of a mass

The definitions vary widely according to the aim and background of the calculation; e it an accurate rock mechanical description of failure during *UCS* tests or estimation of *specific energy* consumption of an excavation machine. In the context of rock cutting, the basic form of the brittleness index as presented by Goktan (2005), Wirtgen (2017) and Yasar (2020) is often used [28, 81, 82].

$$b_1 = \frac{UCS}{TS} \qquad\qquad (17)$$

With: b_1 – *brittleness index*, *UCS* – *uniaxial compressive strength*, *TS* – *tensile strength*.

In order to assess the effect of brittleness on the cutting process, Goktan (2005) uses the *normalised specific energy* consumption after Equation (18). This coefficient allows comparing the effectiveness of the cutting process normalised to both the *cutting depth* and compressive strength. Furthermore, this approach can be extended to the *cutting force*.

$$E_{sp-n} = \frac{E_{sp}}{d * UCS}; \; F_{x-n} = \frac{F_x}{d * UCS} \qquad\qquad (18)$$

Where: E_{sp-n} and F_{x-n} – *normalised specific energy* and *cutting force* respectively, d – *cutting depth*, *UCS* – *uniaxial compressive strength*.

Figure 16, Panel a) shows the relationship for E_{sp-n} to b_1 for drag bits in arenaceous rocks. It can be seen that E_{sp-n} decreases with increasing brittleness [82]. Panel b) shows the relation of F_{x-n} to b_1, recalculated after Yasar (2020) [81]. Expectedly, similar behaviour is shown. Both relationships may be described by a logarithmic relation. For E_{sp-n} this relation can explain 71% of the variation; for F_{x-n}, only 35% of the variation is explained. However, the dataset used is more extensive and incorporates different authors and cutting equipment[6].
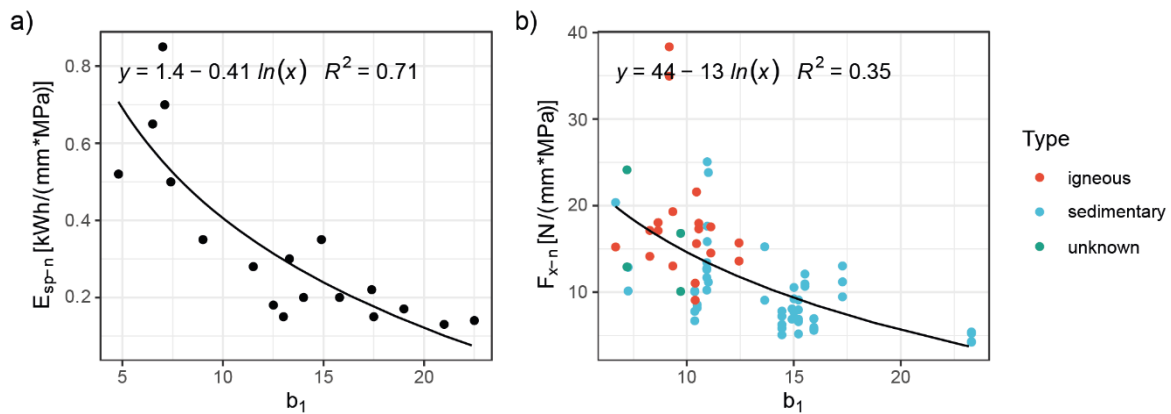
Figure 16: Relationship between: a) normalised specific energy after [82] and b) normalised cutting force to brittleness index, recalculated after [81]

In total, the results of these calculations indicate that, given the same compressive strength, a more brittle material shows a smaller cutting resistance than a more ductile material. In this regard, Restner (2002) proposes a correction factor of ±25% to the cutting rate based on the brittleness index of the rock mass [83].

Schmidt Rebound Value

The Schmidt rebound hammer is an easy-to-use and low-cost tool for estimating rock hardness. It is one of the few testing methodologies that act without destroying the sample. Initially, it was designated as a testing device to identify weakness zones and relative structural integrity of concrete-based buildings.

---

[6] For the recalculation from the data compiled by Yasar (2020) only results with similar cutting conditions were used: $\alpha_a = 55\,°$ and $\alpha_w = 80°$. Also, two outliers with b1 > 30 where disregarded. Data are located in Annex B.

20

There are different types of Schmidt hammers such as N-, NR-, or L-type. The rebound values are called R_N, R_{NR}, and R_L, respectively. The hammer measures the rebound hardness of the surface. Therefore, a spring accelerates a metal bolt onto the rock face. As the kinetic energy of the bolt acts on the material, a part of this energy is converted for the deformation of the rock material, another part is transformed into elastic deformation of both the bolt and the rock. This elastic deformation then causes the bolt to rebound from the rock face. The harder the rock, the more energy is kept in the cycle: kinetic energy, elastic deformation, kinetic energy. The *Schmidt rebound value* correlates with the compressive strength of the rock. Since elastic behaviour plays a significant role in this process, the elasticity modulus of the material influences the results as well.

The test is performed after ISRM or ASTM D5873 for the English sphere. For Europe, DIN EN 12504-2:2012-12 describes the determination of the rebound number of a surface of hardened concrete using a rebound hammer. According to the standard, the primary purpose is to identify the uniformity of in-situ concrete and to show areas or surfaces of low quality or for damaged concrete in structures. However, Note 2 of the norm allows the assessment of the strength of in-situ concrete to be estimated by a suitable correlation [31, 84].

Research has been undertaken to identify the relationships of Schmidt hammer values with *UCS* outside of calibrated areas. Kazemi et al. (2019) calibrated Schmidt hammer tests to *UCS* for recycled aggregate concretes [85]. Rinder and Reinhardt (2000) identified that the Schmidt hammer can be well used for high-performance concrete and that the results show conservative results for very hard concrete [86]. Aydin & Basu (2005) review a larger literature base and summarise 21 calibration curves for *UCS* and 14 for *Young's modulus*. They also propose a calibration curve for granite [87]. Bolla and Praonuzzi (2021) propose a combined calibration curve that incorporates the manufacturer's calibration curve and the Aydin and Basu's calibration curve for harder rocks, as shown in Figure 17, left [88]. Several authors incorporate machine learning approaches to estimate *UCS* from other rock parameters, including the Schmidt hammer test [89–93].
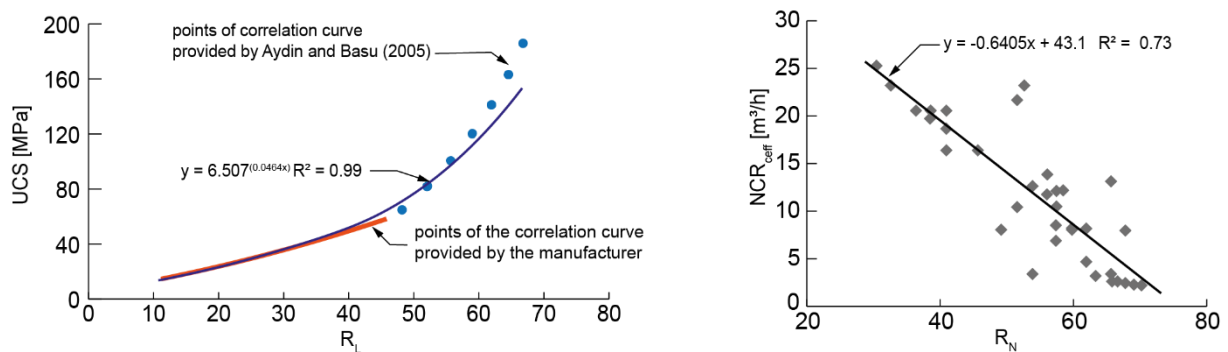
Figure 17: Correlation for L-type Schmidt hammer (left), after [88]; comparison of efficient net cutting rate and Schmidt rebound value (right), after [82]

Regarding cutting efficiency, Goktan (2005) compared the *efficient net cutting rate NCR_{eff}* of a 90 kW Herrenknecht roadheader for different sedimentary rocks during the construction of tunnels for the Istanbul sewerage system. He established a negative correlation of the rebound value with the net cutting rate, as shown in Figure 17, right side [82]. Tiryaki (2006) established a positive correlation between Schmidt hardness and *specific energy* consumption [77]. Yasar (2014) compared Schmidt tests with cutting resistance for a micro-cutting device that cuts with *d = 5 mm*. He found exponential relationships of F_x and F_z with the Schmidt hammer results [94].

Other Parameters

The list of measurable parameters that influence the interaction between tool and rock is extensible to a large degree. For brevity, additional parameters are mentioned briefly as follows:

- Young's modulus describes the elastic behaviour of the rock. It also influences the mechanical energy that a rock can absorb before breaking, which influences the cutting forces during excavation [77].
- P-wave-velocity describes the velocity of ultrasonic p-waves through a rock. It is influenced by the material composition, porosity, density, and crack occurrence [95].
- Density, as one of the most basic and common material parameters is used in some models to predict the cutting process [53].
- Cone intender hardness measures the resistance of a sample against the penetration of a WC-cone [96].
- Shore hardness is measured by the shore hardness scleroscope and is used for non-destructive measurement by a diamond-tipped hammer which is manually dropped vertically and freely from a rested height onto a horizontal, polished test surface [97].

Influence of Anisotropic Behaviour

Schistosity and foliation as anisotropic rock characteristics can influence the strength parameters depending on the direction in which they are measured. Figure 18 shows loading scenarios perpendicular and parallel to the foliation of a rock sample for *UCS* and *BTS* tests. Basu et al. (2013) present a comprehensive study of rock failure modes for *UCS*, *BTS*, and point load tests. Hereby, depending on the direction, different orientation-specific failure modes occurred. A failure along schistosity was associated with a lower rock strength for *UCS*, BTS, and *Is$_{50}$* because an opening of the contact surfaces occurred more often. More isotropic granite and sandstone samples did not show such behaviour [98].
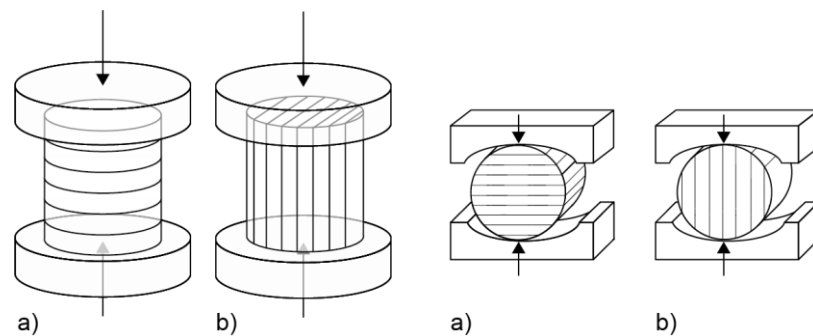
Figure 18: Loading scenarios for uniaxial compressive test and Brazilian tensile test a) parallel to bedding and b) perpendicular to bedding, after [31]

Concerning the interaction between rock and excavation tool, these associations are reported as well. Entacher (2012 & 2018), in a comparison between *BTS* tests and linear cutting tests with disc cutters, shows that cutting forces and *BTS* positively correlate with the angle of load toward foliation. This is shown in Figure 19, Panel b) for the *scaled rolling force* ($F_{R,scaled}$). There, the *rolling force* was scaled to the minimal value of all experiments to show the percentual increase in rolling forces with respect to the minimum [99, 100]. Little is directly published on the angular dependency of cutting forces for conical picks. However, Thuro (2002) reports that the excavation capacity falls to 60% during excavation with roadheaders if the bedding plane orientation is parallel to the tunnelling direction (Figure 19 a). The results are based on experiences during the excavation of a wastewater tunnel in Thuringia, Germany. Here, faults resulted in sudden changes in bedding plane orientation. However,

Thuro does not mention whether the results are based on a roadheader with an axial or radial cutter head [43].
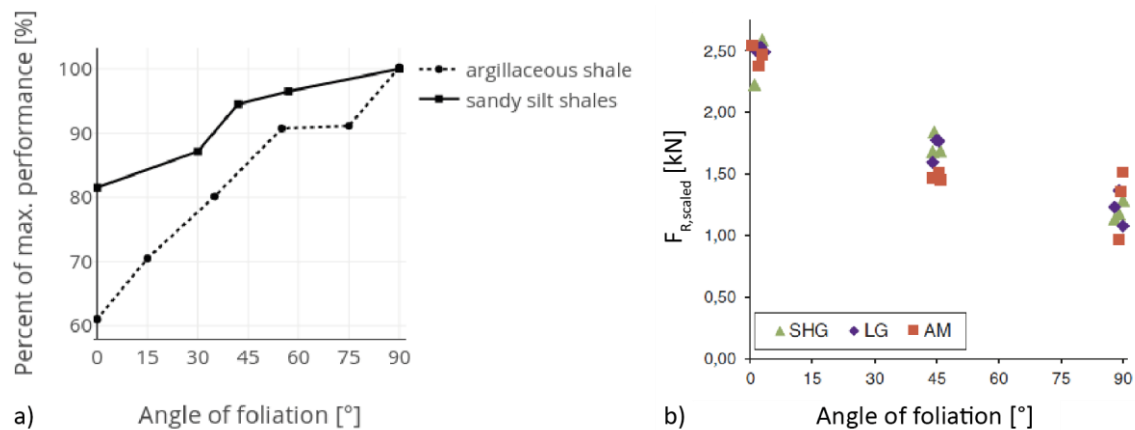
Figure 19: a) Dependency of excavation capacity during drifting with roadheader in anisotropic rock conditions, after [43]; b) average rolling forces for three rock types relative to foliation angle as relative values [100][7]

2.1.4 Influences of the Rock Mass

While foliation is an anisotropic property of intact rock, joints and other discontinuities are rock mass parameters. In addition to the rock mechanical properties, these rock mass properties influence the outcome of the mechanical excavation process as well. The state of the rock mass is defined by macroscopic properties like layering, bedding planes, joint occurrence, joint density, state of the joints, as well as water flow. It can be described by parameters such as rock mass rating (RMR), rock quality designation (RQD), mining rock mass rating, geological strength index after Hoek (GSI), or Q-index [32, 101, 102].

Entacher et al. (2019) state that the assessment of the influence of joints on the excavation process is problematic as the influence is:

1) *"not monotonic, meaning that it changes at different angles"* and
2) *"it is also a function of the joint spacing, and thus a strong cross correlation with [joint spacing] makes it very difficult to capture"* [103].

However, empirical knowledge generally suggests that a worse rock mass increases the excavation speed. Thuro (2002) reports that the excavation capacity can increase to up to 300% for joint spacings below 0.6 cm. Generally, he reports that below a joint spacing of ca. 6.3 cm, the cutting process changes more into a ripping process and hence the advance rate increases significantly [43].

Hartlieb et al. (2018) [53] estimate the effect of a weakening rock on mechanical excavation in a theoretical assessment based on the cutting prediction model for roadheaders by Restner et al. (2002 & 2015) [83, 104]. To assess the influence of the state of rock mass, Restner et al. use the ratio of the efficient net cutting rate to the theoretical cutting rate to describe the relative efficiency of the cutting machine. The cutting rate can be increased by a factor of up to 8 for rock masses in very poor conditions. In own works, it was shown that the state of the rock mass influences both mean values and maximum cutting forces [105–107].

---

[7] Reprinted from Tunnelling and Underground Space Technology, Volume 71, M. Entacher, E. Schuller, *Angular dependence of rock cutting forces due to foliation*, pp. 215–222, Copyright © 2018, with permission from Elsevier.

Entacher et al. (2018) show that the occurrence of joints alters the ratio of peak to average penetration forces (Figure 20). While these results are obtained for artificial rocks with disc cutters in linear cutting experiments, the results coincide with own results [106, 107]. The ratio of peak forces to mean forces increases with deteriorating rock mass integrity. This is based on the following facts:

A) the mean forces reduce due to easily breaking portions of the rock while
B) the peak forces stay similar to those that occur during the cutting of intact rock. Because even in a fractured rock mass, parts of high integrity still exist.

Figure 20 a) shows peak rolling forces to mean rolling forces during excavation. While this analysis compares a mean value with one only extreme value (maximum), it supports statements A) and B) above. A typical histogram on Panel b) of the figure also shows this effect; peak forces appear on a similar level when comparing homogeneous and jointed rock. At the same time, the modus of the distribution is shifted towards lower forces for the jointed block.
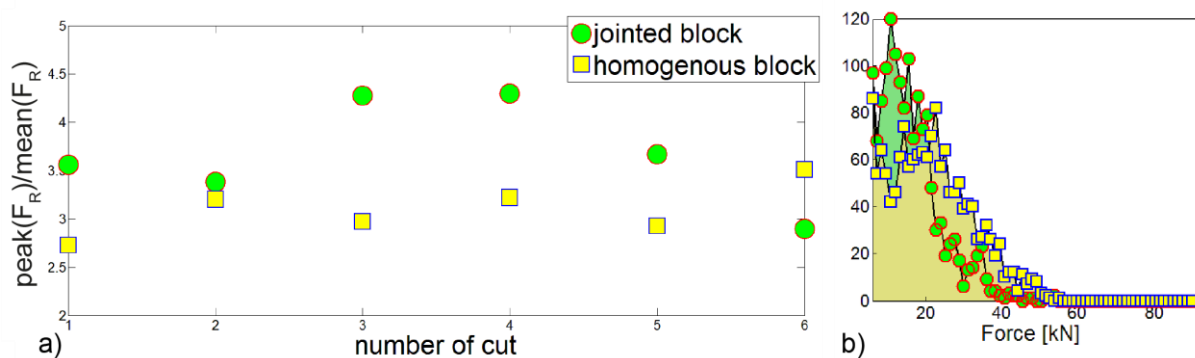
Figure 20: a) Ratio of peak rolling force and average rolling force for disc cutter experiment; b) histogram of rolling force of jointed and homogenous rock [57][8]

2.2 Ratios of Cutting Force Components

After Equation (1), the three spatial components F_x, F_y, and F_z define F_{res}. It is also known that the different components of the *resulting cutting force* play different roles in the cutting process. As such, the ratio of cutting forces toward each other can be investigated. Wang et al. (2017), in a meta-study, show that:

a) For a specific rock type, the cutting force components F_x and F_z follow a linear trend. This means that a ratio between the two can be formulated. This can be seen in Figure 21 a). The linear trends between these two force components are associated to the rock type.
b) The average ratio F_z/F_x correlates with the *UCS*. Hereby, the correlation shows an exponential trend, visible in Figure 21 b) [108].

---

[8] Reprinted from GeoCongress 2012, M. Entacher, E. Schuller, *Analysis of Force Path Diagrams of Linear Cutting Machine – Tests regarding Geotechnical Parameters*, Copyright © 2012, with permission from ASCE.
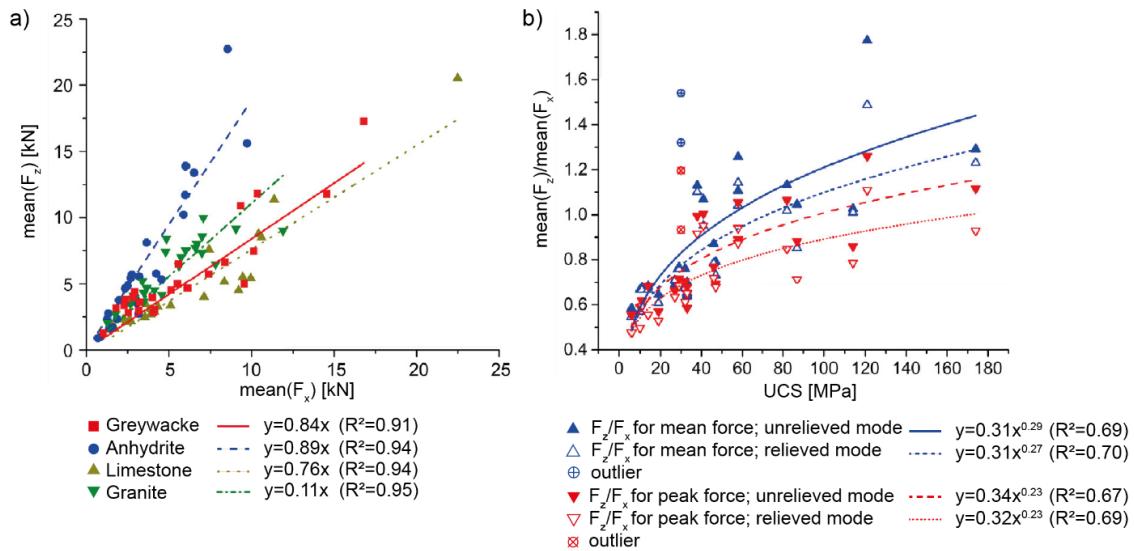
Figure 21: a) Linear regression for normal to cutting force for three different rock types; b) ratio of normal to cutting force in relation to UCS for mean and peak forces [108][9]

Similar results were described in a limited form as early as 1981 by Roxborough [64]. As F_z/F_x is influenced by the rock type and correlates with the *UCS*, it can be assumed to correlate with other rock-mechanical properties as well. To explore this, Figure 22 (next page) shows a part of the often-cited dataset from Copur et al. (2003) where *attack angle* = 55°, *wedge angle* = 80°, and cutting mode is unrelieved [109].

The figure shows a pairwise comparison of the mean of F_z/F_x to nine rock mechanical properties. The *cutting depth* is shown as shape of the data points. Linear regressions between the covariates are added and the *Pearson correlation coefficient (R)*, the *coefficient of determination (R²)*, and the *p-value (p)* are calculated. For the calculation of *R*, see Chapter □.

The correlation behaviour is generally weak to moderate (after Taylor (1990) [110]). The only exception is the *static elasticity modulus E_{st}*, showing a moderate to high correlation coefficient. However, only 48% of the variation is explained by this linear relationship. The d*ensity*, *Schmidt hammer rebound value (R_N)*, and *brittleness (b_1)* show moderate correlations. For these properties, the *p-values* are comparably low—indicating a relatively high statistical confidence in these correlations. The other parameters, *dynamic elasticity modulus (E_{dyn})*, *acoustic p-wave velocity (v_p)*, and *Cerchar abrasivity index (CAI)* show low correlations. These low correlations are expected, given the complexity of the cutting process.

This work aims to use FCRs to distinguish between different rock types. Since different rock types show different rock-mechanical properties, a correlation between the rock-mechanical properties and F_z/F_x would speak for its general suitability to distinguish between rock types. Although linear regression shows limited accuracy given the diversity of the dataset, it illustrates the broader picture that force component ratios could be utilised for rock differentiation.

---

[9] Reprinted from Tunnelling and Underground Space Technology, Volume 62, X. Wang, Y. Liang, Q. Wang, Z. Zhang, *Empirical models for tool forces prediction of drag-typed picks based on principal component regression and ridge regression methods*, pp. 75–95, Copyright © 2016, with permission from Elsevier
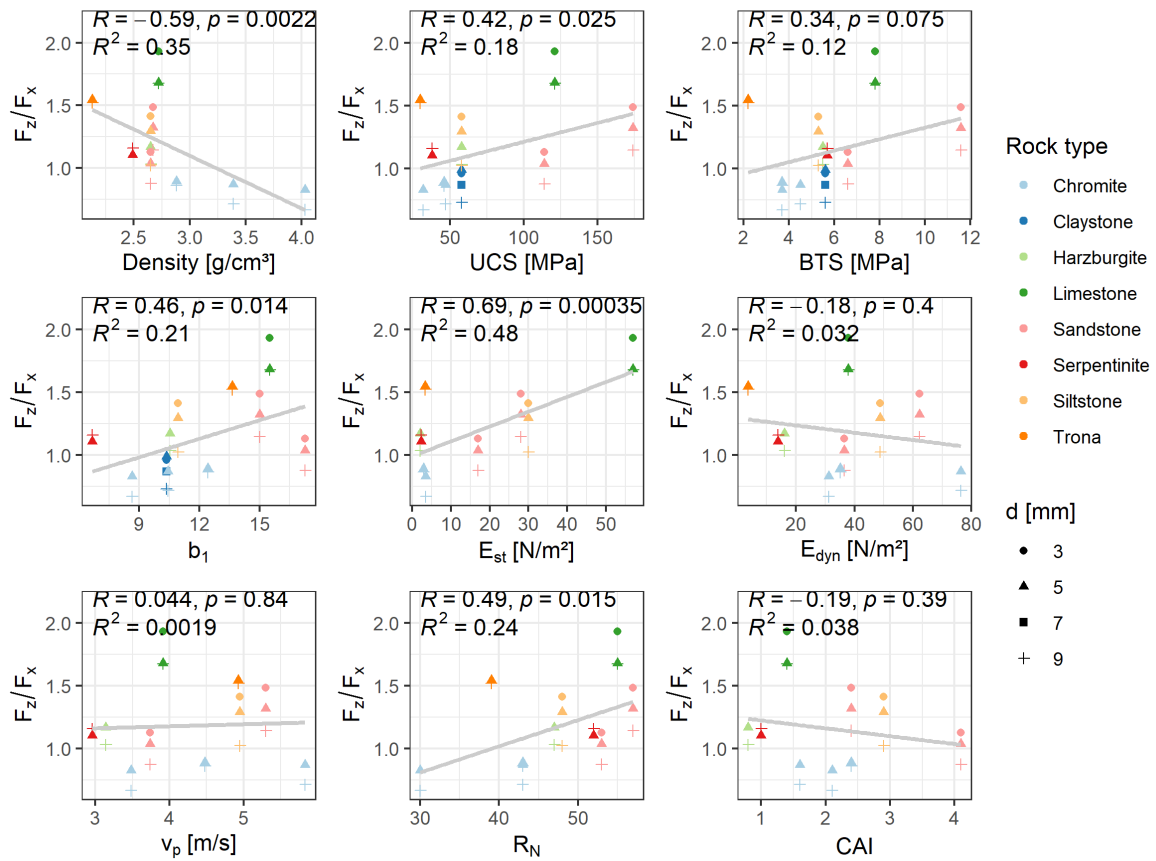
Figure 22: Correlation of F_z/F_x with different rock mechanical parameters, recalculated from [109], only data used where: attack angle = 55°, wedge angle = 80°, and unrelieved cutting mode

Figure 23 a) shows the results calculated after the measurements of Demou et al. (1983) [111]. There, F_z/F_x is less receptive to changes in *cutting depth* but influenced by the pick shape and rock type. Vorona (2012) additionally stated that the ratio between normal and *cutting force* increases when picks wear and become blunter [27].
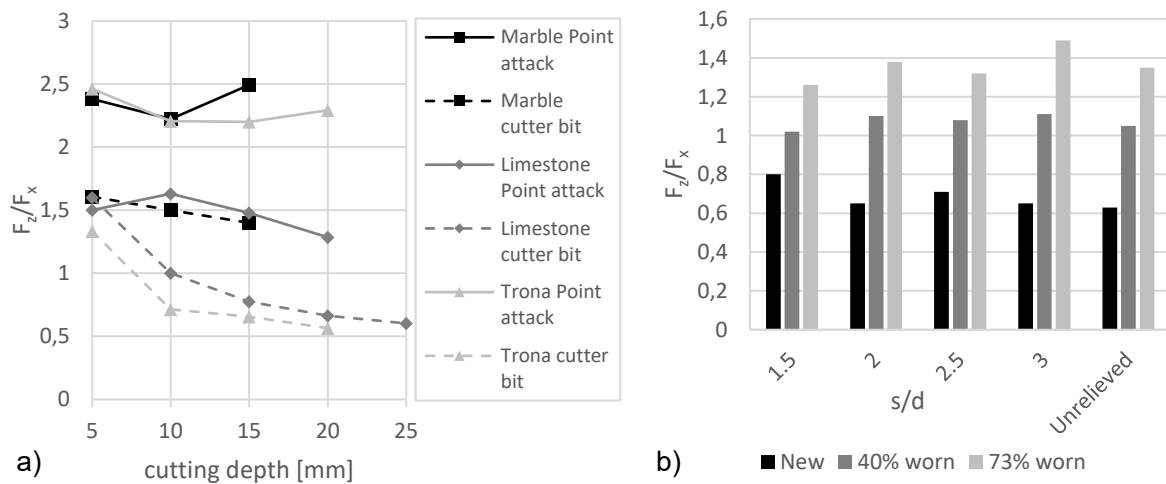
Figure 23: a) F_z/F_x for different rock types and pick geometries, recalculated after [111]; b) F_z/F_x as pick wears for cutting with conical picks in potash salt [27]

This can be seen in Figure 23 b). He used custom conical picks made of aluminium that wore faster than usual and conducted linear cutting experiments with concrete mixtures. The results suggest that F_z/F_x is less influenced by the actual cutting parameters but mainly by the wear state of the picks. This is also supported by older observations from Frenyo and Lang (1993) and Frenyo and Hanneke (1997), who state that F_z/F_x ranges between 1 for soft and brittle materials and 3 for hard and ductile materials. They also correlated harder materials to a higher *specific energy* consumption [112, 113].

Keller (2017 & 2020), regarding linear cutting experiments on the cutting test rig of TU BAF, reported that F_z/F_x is material-specific and independent of the *cutting depth* for unrelieved cuts (Figure 24). However, he noted that when the *cutting speed* increases, the dynamic behaviour of the cutting test rig influences the measurement. Subsequently, F_z/F_x changes for the harder rocks. The *normal force* rises substantially when the cutting process leads to a harmonic oscillation of the cutting machine. The *cutting force* starts to oscillate but stays at mean levels similar to those when no dynamic behaviour occurs. At the same time, F_z increases. This leads to a significant alteration of the force component ratios [41, 59].
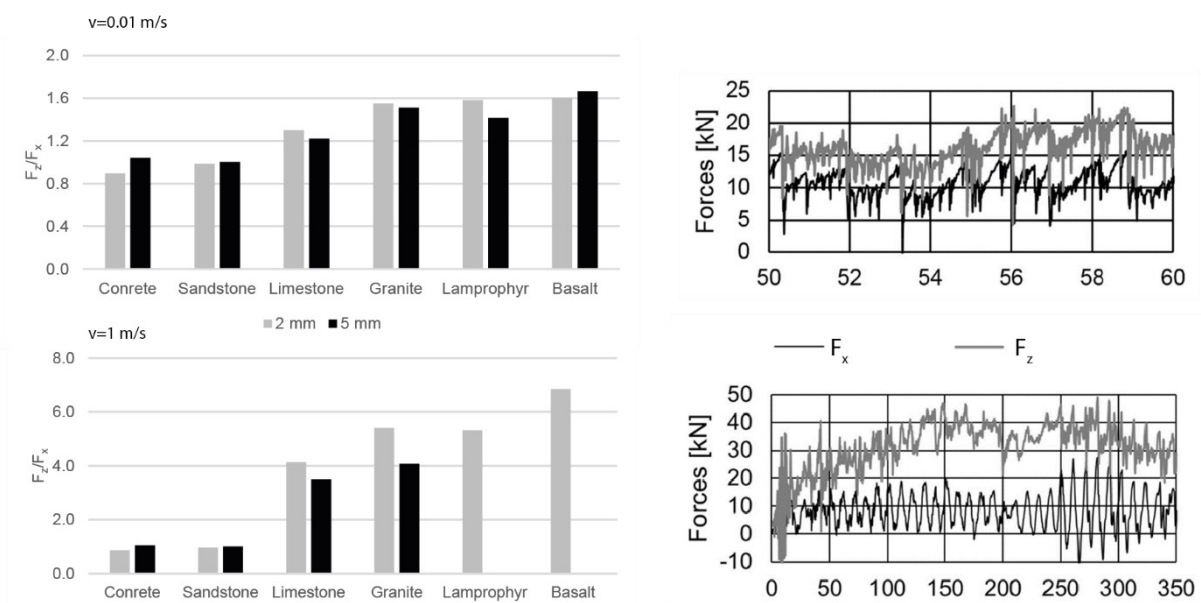
Figure 24: Ratio of normal to cutting force for low (top) and high (bot.) cutting velocities [41][10]

Figure 25 shows the regression lines that Bilgin et al. (2006) established between *UCS* respective *BTS* and F_z/d respective F_x/d. The reporting form of *Force/d* allows a *cutting depth*-independent view on the cutting forces. From these regression lines, F_z/F_x is calculated. It shows that with varying *UCS* respective *BTS*, the ratios change between 0.66–1.35 (*UCS*) and 0.87–0.96 (*BTS*). As a result, with increasing *UCS and BTS*, the ratio F_z/F_x increases [32]. These regressions were not explicitly tailored towards insights of F_z/F_x but still show the same general tendencies as other stated sources and as such confirm the assumption that the force component ratio F_z/F_x might be a suitable parameter to distinguish different rock types form cutting force measurements.

---

[10]Figure: Andreas Keller, CC BY 4.0, via qucosa.de
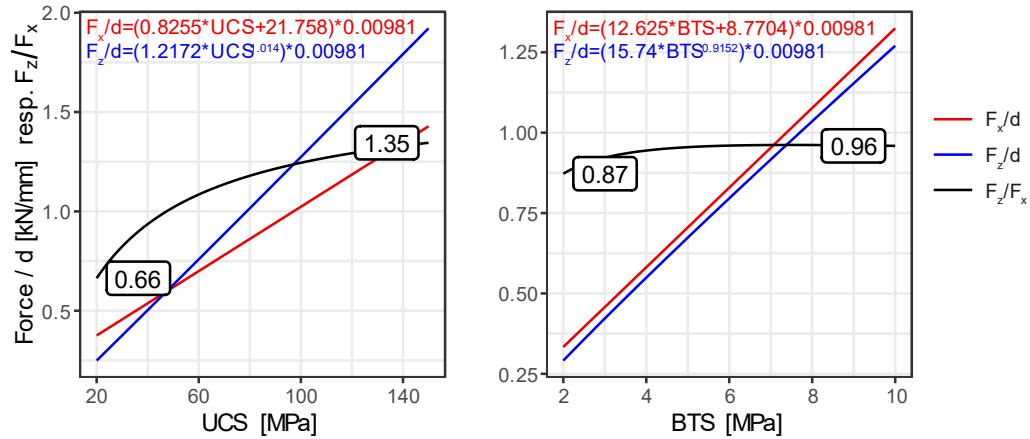
Figure 25: Cutting forces and ratio F_x/F_z vs. UCS (left) and BTS (right), after [32]

The values for F_z/F_x can range from ca. 0.7 to up to usually 1.8; in some cases, above 2. It must be considered that while typically F_z/F_x is presented as a ratio, physically, it represents the angle of the vector of F_{zx} between the vectors F_z and F_x. It follows the mathematical behaviour of a tangent function as shown in Figure 26. There, the angle α_{zx} as a result of Equation (6) is plotted; the inlay shows the typical range of values. The labels show α_{zx} for $F_z/F_x = 0.7$ and 1.8, respectively. This equals an angular range of 55° to 29.1°. Although this behaviour is considered in this work, in further analysis, the canonical reporting form as a force ratio is employed to allow comparability with other works.
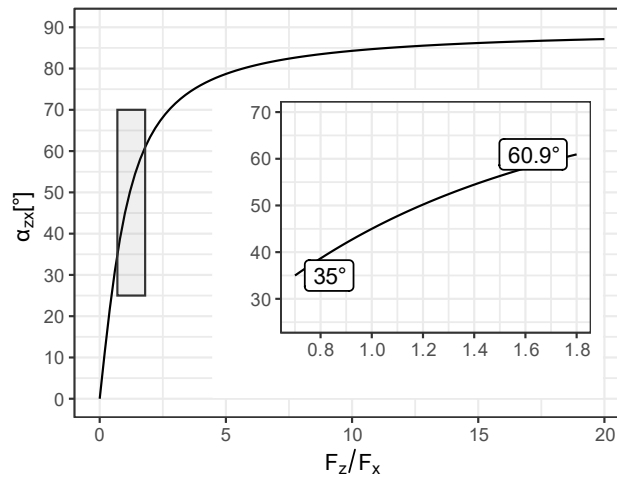
Figure 26: Plot of function $\alpha_{zx} = arctan(F_z/F_x)$, plot inset shows the normal range for F_z/F_x reported by literature

Chapter Summary

F_z/F_x ...

- ... is influenced by the rock properties,
- ... is influenced by wear and the pick geometry,
- ... appears influenced by cutting speed on a machine specific way,
- ... is not, or to a minimal extend influenced by *spacing* and *cutting depth*.

→   These findings might be extended to other force component ratios.

3 State of the Art

This chapter gives an overview of both the state of the art in laboratory rock cutting research and the existing systems used for rock classification during excavation. The former is necessary to understand the knowledge gaps. The latter shows the gaps in application. Since pick-based near tool sensors have not yet reached market readiness, a comparison to neighbouring application fields is shown.

3.1 Data Analysis in Rock Cutting Research

This chapter investigates the general state of the art in analysis techniques in hard rock cutting experiments. The aim is to provide a semi-quantitative overview of which analytical foci are laid out in this field. In total, 58 works were included in this analysis. Figure 27 shows a summary of these works. The vast majority of the works analysed were published since 2010, and 60% of the works were published in the time between 2017 and 2021. The oldest works included in the analysis are the works of Roxborough (1981) and Sobek (1987) [51, 64]. Since this work focuses on conical picks, 41 of the 58 works also focus on conical picks, 15 more focus on cutting force measurement with disc cutters, and five cannot be attributed to one group. These mainly include experiments on a smaller scale, such as cutting edges or micro-cutters. The groups do not add up to 58 because some papers can be attributed to two groups. Details of the classification can be found in Annex C.
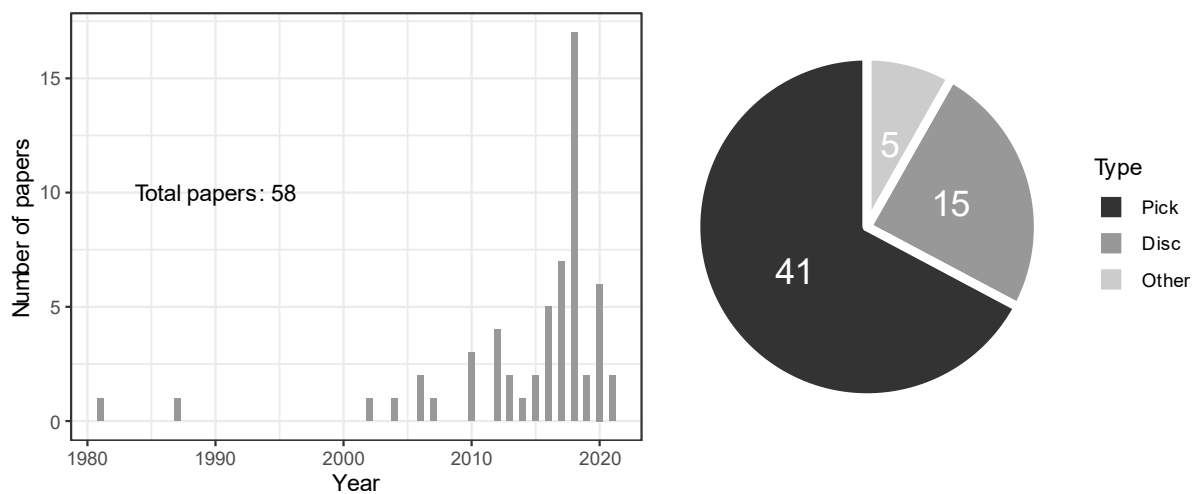
Figure 27: Overview of classified papers; left – publication dates, right – covered tool types

The papers were classified whether they cover the following topics:

States mean: Describes the standard approach to identify the results of rock cutting experiments. Mean cutting forces are stated in almost every paper.

More than one FC shown: In most papers, F_x is analysed. However, many papers also analyse F_z, some even F_y. This allows an assessment of FCR. If more than one force component is presented, the ratios of the force components could be calculated manually by third parties, as was done in Chapter 2.2.

F/t or F/l: Describes whether a Force-time- or Force-way-diagram was shown. Raw data are usually measured on an F-t-basis. The position of the tool can then be calculated with the speed of the tool. These diagrams are usually given for a broader understanding of the processes and, therefore, are often presented.

Specific energy: Describes whether cutting parameters or forces have been related to *specific energy* during the excavation process. As described in Chapter 2.1, Specific Energy, p. 10, there are several possibilities to calculate the *specific energy* that depend on the analysis' context. This means that a direct comparison between different sources must be taken cautiously. *Specific energy* can be used to evaluate the effectiveness of the excavation process and it provides indicators for relative changes in the advance rate.

Peak forces: Describes whether absolute peak forces or an algorithm to identify peak forces was used to characterise the cutting process with respect to the cutting forces. The calculation of peak forces differs between different authors. One method is to take one maximum value per cut, another takes three, and others use an algorithm to extract maximum values. Another possibility is the use of quantiles (such as the 0.95-quantile) as a peak force indicator. As such, comparing maximum forces between authors and different testing schemes requires caution. Additionally, the dynamic behaviour of the cutting machine can influence the results.

FCR mentioned: Describes whether, in addition to presenting the results of more than one force component, force component ratios are calculated, analysed, or even just qualitatively mentioned.

Grain size/shape analysis: Identifies whether any analysis or evaluation of the outbroken material in relation to the cutting parameters was conducted qualitatively or quantitatively.

Spatial relation of force mentioned: Describes whether the cutting force results were analysed or mentioned in relation to the position of the tool in any way. This mainly applies to works from Entacher et al. (and own works which are not included in this analysis).

Other measures of distribution: Identifies whether any descriptive statistics parameter was used to characterise the measured forces other than by calculating the arithmetic mean or stating peak forces. These descriptors, for example, can be standard deviation, variation coefficient, histograms, quantiles, IQR, or similar.

Frequency analysis describes whether the raw results were classified or characterised on a frequency-based approach. Here, only a discrete-Fourier-transformation-analysis [22] and empirical mode decomposition [114] appear.

Figure 28 shows the results of the analysis. The orange bars mark the methods that are of particular interest for this work. The results are shown in order of frequency. Usually, the main focus lies on mean cutting forces (48 papers). This is not surprising given its explanatory power. The vast majority of papers also presented more than one force component, some even three (F_x, F_z, F_y). However, only few papers put the presented FCs in relation to each other. Although 43 articles showed multiple FCs, only eight of them quantified or characterised the relationship of the components to each other. This means that the behaviour of FCRs is less understood than the behaviour of the FCs themselves.
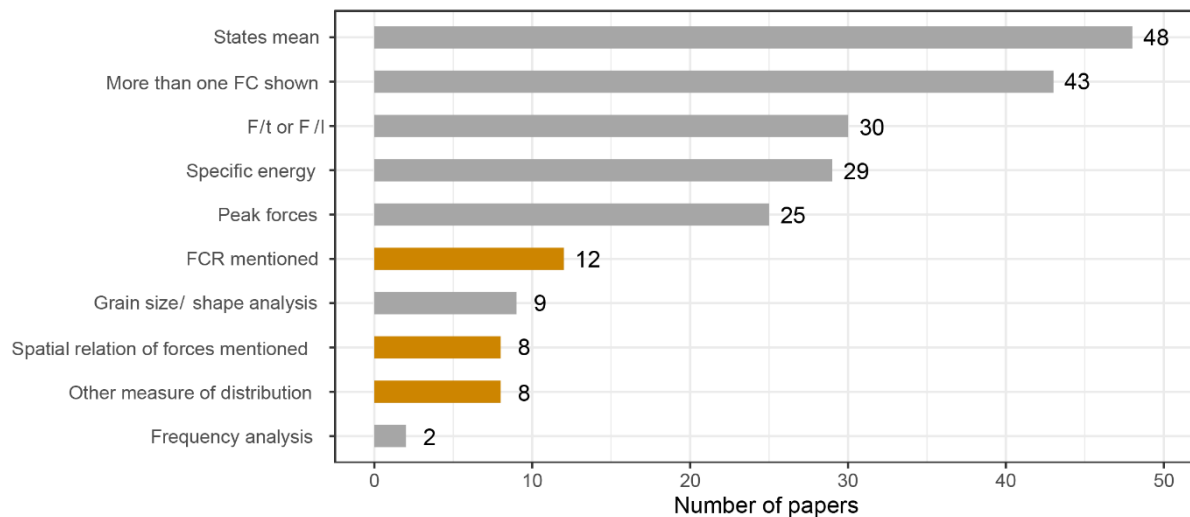
Figure 28: Covered topics in reporting for experimental rock cutting

Approximately 50% of the analysed papers use the *specific energy E_{sp}* for classifying the cutting process. The practical relevance of the value can explain this—it can be recalculated into required power of a possible cutter head, or if cutter drive power is fixed, into advance rate [41]. Grain size and shape analysis is a relatively rarely researched parameter. Here, correlations to the cutting parameters and the *specific energy* are usually analysed. While the grain size analysis and *specific energy* consumption are not part of this study, knowledge of these effects is required to understand the underlying processes.

More than half of all papers show characteristic F-t diagrams. These diagrams are often used to explain the cutting process itself. In addition to interpretation with mean values, analysis of the F-t behaviour often investigates peak forces (25 papers). In only eight studies, the authors use additional statistical parameters to describe the force behaviour of the cutting process. Partially, this can be explained by the fact that peak forces are indicatives of a spontaneous pick failure, while mean forces indicate the required cutter drive power/momentum. As such, from the viewpoint of application, the necessity for additional statistics is low. Some of these works state that the ratio of peak force to mean force is different for different materials and use it to characterise the cutting process—which is relevant for this work [32, 69, 108].

As an additional analysis to characterise the F-t behaviour, frequency analyses was only conducted twice in the reviewed set of articles, and it appears to be of limited interest for current research. Finally, an analysis of cutting forces in the spatial context occurred only in eight papers. These papers all focus on disc cutters. Apart from own studies, no papers were found that analyse cutting forces in relation to spatial changes of the rock. In summary, a knowledge gap can be noted in rock type related cutting force behaviour—especially focusing on spatial analysis.

Chapter Summary

A knowledge gap appears to exist with regards to:

- Spatial analysis of cutting forces, especially with conical picks.
- Deeper descriptive statistical analysis of cutting forces.
- Advanced use of FCR to describe the cutting process.

3.2 Rock Classification Systems

The following chapter gives an overview of technologies that are described or patented to do at least one of the following:

- identify rock type boundaries,
- identify zones of altering rock mass integrity,
- optimise the excavation process itself, based on cutting force data, or
- enable excavation machines to follow certain geometries.

In this work, these technologies are called measure-while-cutting-technologies (MWC), an analogy to measure-while-drilling-technologies (MWD). As far as possible, this analysis focuses on conical picks. However, the state of the art with a specific focus on conical pick-based machines is limited. Although sensor systems to measure forces during operation have been patented, to date, no complete concept for classifying rock mass during excavation with conical pick-based machines has been published. Hence, technological solutions that occur in neighbouring fields are presented as well to show the general state of application. Details of the accompanying patent analysis can be found in Annex D.

3.2.1 MWC – Measure-While-Cutting

The beginning of the evolution of cutting force-based automation started in coal seam mining in Germany and the United Kingdom around the 1970s. These developments focused on shearer-loaders. Here, the objective was to distinguish between coal seams and host rock. Usually, strain gauge assemblies were used as sensors. As such, they can be defined as the first MWC concepts.

Given that the computational possibilities were somewhat limited, simple and robust ideas emerged. The solutions were based on one or two picks, and no spatial correlation of the obtained results was performed. Later designs tried to avoid the influence of a varying *cutting depth* on the results; the following solutions were proposed:

A) Only peak forces were used for analysis.
B) Use of a special subsequent pick assembly. A succeeding pick followed the actual pick; this second pick cut with a low *cutting depth* (more scratching than cutting). As such, it maintained a nearly constant, shallow *cutting depth* [25, 26, 115, 116].

Apart from patents in coal mining, only few other patents for conical picks are published. The latest patents for conical picks are connected to the mining OEMs Sandvik and Famur. The Sandvik system is shown in Figure 29, Panel 1). Sensors located on the side of a tool-holding sleeve can measure bending (tangential) load. A central sensor can measure radial load. Measured signals are transferred to a data transmitter in the rear part of the assembly and sent to further processing via Wi-Fi [23]. Another recent patent for coal mining with shearer loaders comes from China and employs a piezoelectric sensor assembly to measure cutting forces [117].

The latest patent was submitted by Politechnika Ślaska in cooperation with Famur. This system (Figure 29, Panel 2) allows for a 3d-measurement of dynamic cutting forces and additionally claims a transformation of the data from a coordinate system related to the picks axis into a local coordinate system related to the cutting trajectory. This allows the interpretation of the measured data in the standard form of *cutting force*, *normal force*, and *side force.* Chelushka (2019) presented a case study in the context of this patent which implies that F_z/F_x shows a characteristic spread and is subject to the hardness of the excavated rock [118, 119].
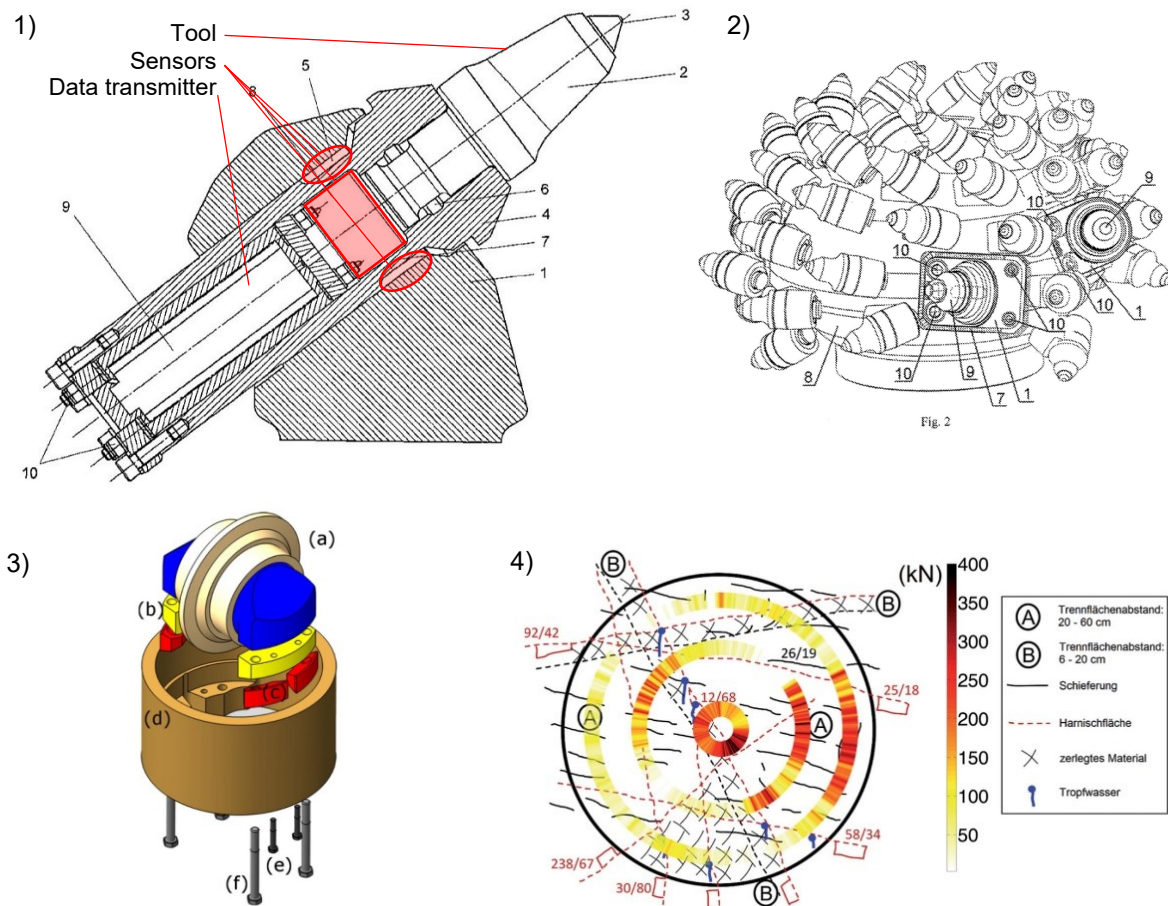
Figure 29: 1) Sandvik tool force measuring system [23]; 2) sensor concept from Politechnika Śląska and Famur [118]; 3) disc load measuring system by University of Leoben (right) [22][11]; 4) superimposition of measured disc normal forces averaged for three consecutive revolutions with geological documentation [120][12]

In the field of disc cutters, Entacher et al. published on this topic from 2013 onward. This research resulted in a force measurement system for disk cutters based on strain gauge bolts, shown in Figure 29 2), Marking (e). One element of their research was a qualitative analysis of measured cutting forces with respect to the mapped face of a tunnel [120, 121]. They found that the *normal forces* are related to geological features such as fractured zones and schistosity. These influences can be seen in Figure 29 4).

Entacher et al. also state that *"general statements that go beyond the analysis of a singular event should not be based on a single cut or a single revolution [of the cutter head]"* as *"subsequent cuts are dependent of each other"* [121]. In this case, the statement is limited to deepening cuts. This is extended to adjacent cuts in [122] and [99]. As shown in Figure 30, it is observed that for neighbouring cuts, where there was a force peak in the preceding cut, lower forces can be expected in the subsequent cut at the same spot. In [99], emphasis is also put on the necessity of a statistical evaluation of multiple events. The authors predict the possibility of identifying different rock masses based on cutting force analysis

---

[11] Reprinted from Tunnelling and Underground Space Technology, Vol 31, M. Entacher, G. Winter, T. Bumberger, K. Decker, I. Godor, R. Galler, Cutter force measurement on tunnel boring machines – System design, 97–106, Copyright © 2012, with permission from Elsevier

[12] Copyright © 2013 Ernst & Sohn Verlag für Architektur und technische Wissenschaften GmbH & Co. KG, Berlin

for TBMs. In [57], it is stated that the use of cutter forces for a correlation with *"geotechnical parameters can provide a strong aid for the geological and geotechnical interpretation of the tunnel face in mechanized tunnelling"*—given that the influences of the cutting machine and the cutter are understood thoroughly.
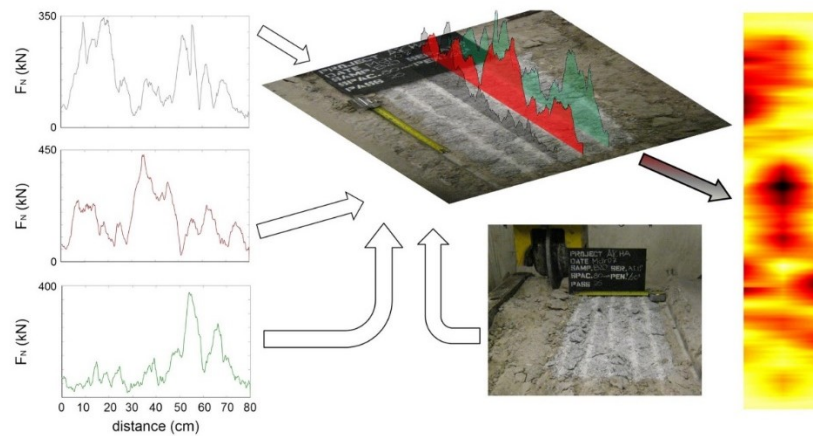
Figure 30: Visualisation of spatial analysis of cutting forces for linear cutting experiments with disc cutter [122][13]

For TBMs, the interpretation of cutting force data is less complex since the cutting parameters remain relatively constant during the cutting process. While these concepts allow precise force measurements, they neither explain the full potential of such systems nor the exact workflows to utilise the obtainable data.

In summary, until now, no complete system has been described in terms of how the measured data are processed and interpreted to classify the rock, neither for conical picks nor for disc cutters. For conical picks, no field experiences of the patented systems are known to the author.

3.2.2 MWD – Measuring-While-Drilling

Although MWC systems are still in early development, MWD systems are known in the drilling industry. The literature assessment here focuses on MWD-concepts for use in regular blast-hole drilling for production or tunnelling.

In terms of using acquired MWD-data, Gosh, Schunesson, van Eldert et al. published a series of articles from 1990 onwards with the aim to classify the rock mass quality and the extent of the excavation damage zone for blasting (Figure 31). The focus of these works was on tunnelling and production blasthole fan drilling. Fractured, macrocracked, faulty, or breccious rock can lead to problems when loading blastholes or when blasting. Van Eldert proposed to use MWD to classify the rock according to the RQD index and used this information for rock support design during tunnel excavation (left side in Figure 31) [17, 19, 123–127].

Furthermore, Liu et al. (2019) proposed solutions to use MWD data to recognise joints during roof bolting. Here, cumulative sum algorithms (CUSUM) combined with a moving-window approach were used to identify joints [128].

---

[13] Reprinted by permission from Springer Nature: Rock Mechanics and Rock Engineering, Rock Failure and Crack Propagation Beneath Disc Cutters, Martin Entacher et al., Copyright © 2014
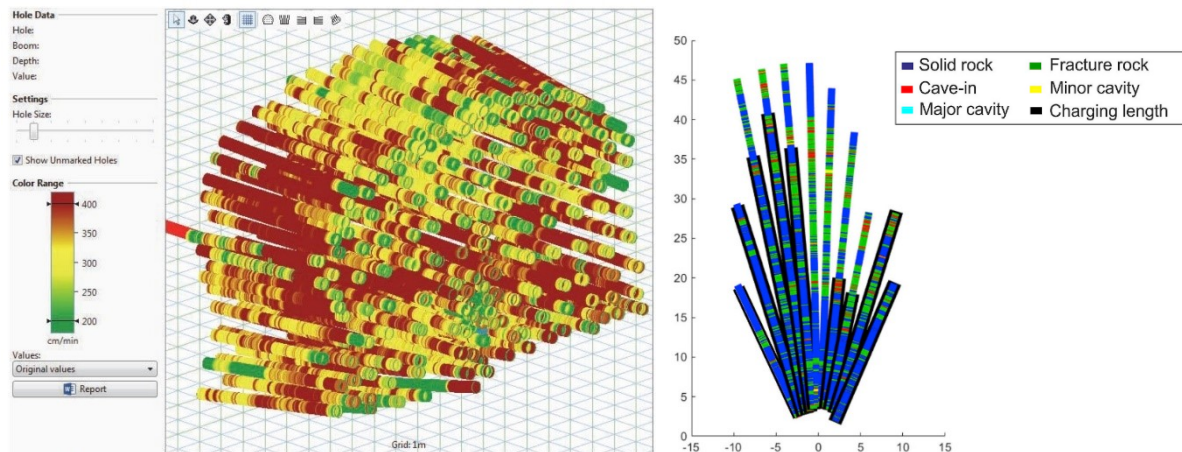
Figure 31: Penetration rate of one blast round in tunnelling (left) [18][14]; classification based on a ranking from first principal components interpretation (right) [126][15]

Clausen et al. (2019) used support vector machine algorithms for an MWD-application to predict the drilled rock's *UCS*, *BTS*, and *brittleness index*. It could be shown that the system can be used for boundary layer detection [129]. Ellefmo et al. (2020) used a mean- and variance-based changepoint analysis on the first principal component to detect fractured to solid marble changes in a quarry in Norway. The *accuracy* of the estimation model based on the changepoint analysis for the first principal component was 98%. This principal component was mainly defined by feed pressure, damping pressure, and rotation pressure [130]. Navarro et al. (2021) used a principal component-based analysis to characterise the rock mass and assess the strength properties on the one hand and the structural condition on the other [20].

Parallel to these developments, the mining original equipment manufacturers (OEM) Epiroc, Sandvik, and Bever Control have developed their own software as a tool to assess MWD-data. These tools provide integrated solutions, including 3d representations of hardness or fracturing indices [20].

3.2.3 Automated Profiling During Cutting

With increasing possibilities for automation and computation, MWC based technologies are flanked by several automation solutions based on general working parameters of the mining machine. These comprise hydraulic pressure, voltage, and current. These parameters indicate the total load to which the machine is subjected. This is flanked by possibilities of position measurement and control of the cutter head. With that, predefined profiles can be automatically followed. In addition, blockages and critical situations can be identified, and an appropriate reaction can be executed. For example, the slewing speed can be reduced when the cutter drive power draw exceeds critical levels [131–136]. Such systems also can store profiles for different rock types and then vary the slewing speed according to the toughness of the rock types [137]. There, however, the location of the rock types must be typed into the automation interface of the machine manually.

---

[14] Image: Jeroen van Eldert

[15] Reprinted from International Journal of Rock Mechanics and Mining Sciences, Juan Navarro, Håkan Schunnesson, Rajib Ghosh, Pablo Segarra, Daniel Johansson, José Ángel Sanchidrián, Application of drill-monitoring for chargeability assessment in sublevel caving, 180–192, Copyright © 2019, with permission from Elsevier

.

Additionally, for open-pit operations, such concepts can be extended to multi-machine systems that organise the movement and operation of multiple machines and take into consideration the respective advance rates and process information as patented by the former Atlas-Copco (now Epiroc)—until now only for drilling applications [138]. For continuous surface miners and dozers, automated GPS-based levelling systems are also on the market [28, 139].

3.2.4 Wear Monitoring

Another aspect is the use of systems that monitor the wear of mechanical excavation tools using various means. Wear and blunting of the tools are the main driver for impairing an excavation machine's advance rate since continuous check-ups and replacement of tools take considerable time. Restner (2016) mentioned as a general rule of thumb that a consumption of more than one pick per m³ of excavated material can be seen as a threshold for a feasible operation [140]. Methods include sensing general machine conditions such as vibration or power consumption behaviour or direct measurement of the state of wear of the tool, e.g., by laser scanning or inductive methods [135, 141–148]. Another method was patented by Lill and Freymann (1994), where a sensor-infused cover shoe is added to a pick holder. The sensors are thin wires that act as antennas at the same time. When the pick holder is damaged, it damages the cover shoe, which damages the antenna wires in return, making the pick location at which the damage occurs traceable [149].

3.3 Machine learning for Rock Classification

Although there are no direct rock classification systems from MWC, machine learning (ML) approaches for rock classification from other data are published. Excavation and mining project planning is usually based on rock mechanical tests that require significant financial resources. Especially the *UCS* test is relatively costly and time-consuming. The reliable prediction of *UCS* from cheaper tests results in overall savings in a project. Other applications include direct prediction of the excavation speed of a given excavation machine. Apart from the already mentioned approaches in rock classification from MWD-data, a broad overview of the vast field of utilising ML to estimate of rock parameters is given in the following.

Teryaki (2008) compared artificial neural nets, regression trees, and multiple nonlinear regression to estimate their suitability to predict the rock parameters *UCS* and E-modulus from the covariates quartz content, density, porosity, shore hardness, and cone indenter index [150]. Kaunda and Asbury (2016) used an artificial neural network (ANN) to predict the brittleness index from the punch penetration test based on a database of 20,000 rock property test results. The input data were: rock type (igneous, metamorphic, or sedimentary), unit weight, P-wave velocity, S-wave velocity, dynamic Poisson's ratio, dynamic Young's modulus, and Lame's constant [151]. Berzegar et al. (2020) estimated *UCS* of travertine with three different ensemble tree-based machine learning algorithms: random forest (RF), M5 model tree, and multivariate adaptive regression splines (MARS) [89]. Saeidi et al. (2014) used a fuzzy clustering-based ANN and multiple regression methods to estimate the rock mass digability index [152]. Aras et al. (2020) used ANN to predict the bond work index from rock mechanical properties [153]. Salimi et al. (2019) used classification and regression tree (CART) and genetic programming (GP) to predict TBM performance based on *UCS* and multiple rock quality ratings [154].

Liu et al. (2021) reported a method to identify rock hardness using cutter head drive current as input. An AdaBoost backpropagation artificial neural network was used with features extracted by utilising multi-scale permutation entropy [155].

Wang et al. (2020) used a multi-sensor approach, including a Dempster-Shafer multi-sensor fusion approach based on membership functions to predict the hardness of concrete during laboratory rock cutting tests. The signals used were: triaxial vibration, current, acoustic emission signal, and peak temperature at the contact between pick and rock measured by an infrared camera. One result of this study was that the parameter with the highest weight on prediction success was the maximum infrared temperature [156].

Vraetz (2018) used acoustic emission signals to classify the material flow during an in-line characterisation on a conveyor belt. Here, the material was falling against a hit-detection plate; as such, a constant data stream was received. The used features of this data stream were: number of values above a threshold, root-mean-square value, standard deviation, crest value, kurtosis, maximum, impulse, and area-under-the-curve of an impact burst. For the classification, a support-vector-machine algorithm was used [157].

4 Problem Statement and Justification of Topic

In summary of the previous chapters, the use of machine information for maintenance prediction, excavation optimisation, and following profiles is relatively well researched. The use of MWD is a well-known concept. On the other side, measure while cutting is a known idea—and first implementation attempts have been reported for disc cutters, to a limited extend also for conical picks.

However, no complete solution that describes the exact nature of the acquired data, how the data are used and evaluated, and how they can further be used for spatial rock classification has yet been presented for conical picks. The problem lies in the fact that the cutting process is highly instationary. This is a result of: the variation of d due to the crescent shape of the cut, the variation of s depending on the type and operation of the machine, the machine dynamics, as well as the general variability of the cutting process of brittle materials. Furthermore, the data volume required is relatively high, which means that the hardware of early generations was not capable of processing the data as required.

This high variability means that measurements have to be taken with a high frequency to capture the process adequately. Hence, treatment of the incoming data stream is of importance. On the other hand, the high variability necessitates complex evaluation methods. Both complex evaluation methods and big data streams became manageable just within the last decade through the increasing computation power of information technology. It is assumed by the author that the methods proposed and researched in this thesis are only unlocked by these recent developments.

From the literature review, the following knowledge gaps (KG) are summarised:

KG1	While being investigated since the 1970s, cutting force-based rock classification systems have not yet reached market readiness for conical pick assemblies.
KG2	The force responses strongly correlate with the *cutting depth* and the *spacing*. Literature points towards an understanding that the ratio of F_z/F_x correlates less with these two parameters, but more with the rock type. Hence, it might be utilised to characterise the rock for MWC purposes. How other force component ratios (F_y and F_{res}) act, is almost not reported.
KG3	Until now, the FCR F_z/F_x has been calculated from mean values of its force components, but only rarely from real-time cutting force data.
KG4	Until now, common practice in rock cutting research rarely incorporated statistics other than mean and peak values of F_x and F_z. Further statistical analysis is relatively rarely incorporated.
KG5	Machine learning has rarely been used with cutting force data to identify the rock type while cutting.

Consequently, this work aims to usher in unlocking MWC rock classification systems by further addressing these knowledge gaps. The potential of features derived from real-time cutting force component data in conjunction with ML for rock classification is investigated to achieve this.

In detail, the following research questions (RQ) are addressed:

RQ1	How suitable are features that describe the behaviour of real-time FCRs for rock classification—especially in combination with ML techniques?
RQ2	Are FCR-based features alone sufficient for rock classification, or are additional features advisable?
RQ3	Toughness, crack occurrence, and anisotropy are significant variables that define a rock type. How does a variation, respectively the presence of these parameters, affect FCR-based rock classification?
RQ4	Which classification accuracy and spatial precision can be expected?
RQ5	What basic requirements would an MWC sensor system have to meet?

The following main tasks (MT) are executed to answer the research questions:

MT1	Conduct experiments that assess the behaviour of real-time FCRs in different rock conditions (hardness, foliation, cracking state).
MT2	Design a methodology to select the features derived from the FCRs that are most significant for rock classification.
MT3	Design an algorithm that computes the selected features with spatial reference, from which it conducts a spatial rock classification using ML.
MT4	Test the algorithm with different ML techniques and assess the overall performance.
MT5	Give general recommendations towards sensor design.

5 Material and Methods

This section presents the research infrastructure used, the description of rock specimens tested, and the experimental routines followed.

5.1 Rock Cutting Equipment

All experiments were conducted on the cutting test rig HXS-1000-50 of TU BAF, shown in Figure 32, next page. The machine was constructed in 2008 as a special design by ASW Naumburg. While linear cutting test rigs are non-standardised, most cutting rigs follow a similar design. The concept is that the rock specimen (d) is placed on a table (e), and the table moves (g) against the actual cutting head (b). Normally, this motion is provided by hydraulic cylinders. The Freiberg testing machine shows a distinguishing feature. Two synchronised spindle drives provide the motion of the cutting table. Due to this, it can provide cutting speeds of up to 1.6 m/s. The second distinguishing feature lies in the use of piezoelectric force sensors (c), which provide higher stiffness and precision and can measure peak forces more precisely. Since the design is based on a CNC router, not only can forces be measured, but also the coordinates of the cutter head in relation to the cutting table. Subsequently, a traceback of the location of the pick during cutting is possible. In addition, the machine is equipped with a laser scanner. With the laser scanner, it is possible to scan the surface of the rock specimen. This allows a calculation of the volume of the outbroken material. The outbroken volume is used to estimate the *specific energy* consumption during excavation. The possibility to synchronise the force measurement data with the pick coordinates is a major prerequisite for the spatial analyses in this work.

The pick on the cutter head (b) is tiltable on the x-z-plane (*attack angle*) and the x-y-plane (*tilt angle*). The orientation of the machine's intrinsic coordinate system is also shown in the figure. The piezo force sensor system (c) is composed of a sandwich of four pre-tensioned sensors that have been jointly levelled and calibrated. The pretension is set to 75 kN. All four piezo sensors measure x-, y- and z-components with a maximum acquisition rate of 10 kHz. They are connected via a Wheatstone bridge circuit. This results in an equalisation of momenta independently of the actual lever length. Since the sensor package is pre-tensioned, it allows the measurement of positive and negative forces.

The general signal processing flow is shown in (j). The output signal is a charge difference. The four charge signals serve as input for a charge amplifier. The charge amplifier converts the signal into a ± 10 V signal. This analogue voltage signal is converted by analogue-to-digital converters (ADC) into a digital signal that can be further processed. The ADCs are housed in a DEWE5000 data acquisition (DAQ) computer (h). The computer houses seven ADCs, translating into seven simultaneous channels. The maximum DAQ rate of the ADCs lies at 100 kHz, which is higher than the maximum output frequency of the sensors (10 kHz). The seven channels comprise the x-, y-, and z-position of the cutter head as well as the x-, y- and z-component (F_x, F_y, F_z) of the cutting force; the last channel is used for the signal of the surface scanning laser.

For data acquisition, the Dewesoft software (i) is used. It allows the synchronisation of force measurements with high-speed video, real-time computation of derived signals, as well as automation of measurement and storage conditions. During the course of the experiments, an updated force sensor module was installed. The new sensor module is identical in geometric design but comprises a newer generation of sensors. As such, the measurable force limits were upgraded, as seen in Table 3.

(a) Portal
(b) Cutter head
(c) Load cells
(d) Specimen
(e) Specimen table
(f) Control Unit
(g) Cutting motion
(h) DAQ-computer
(i) DAQ-software
(j) DAQ-process
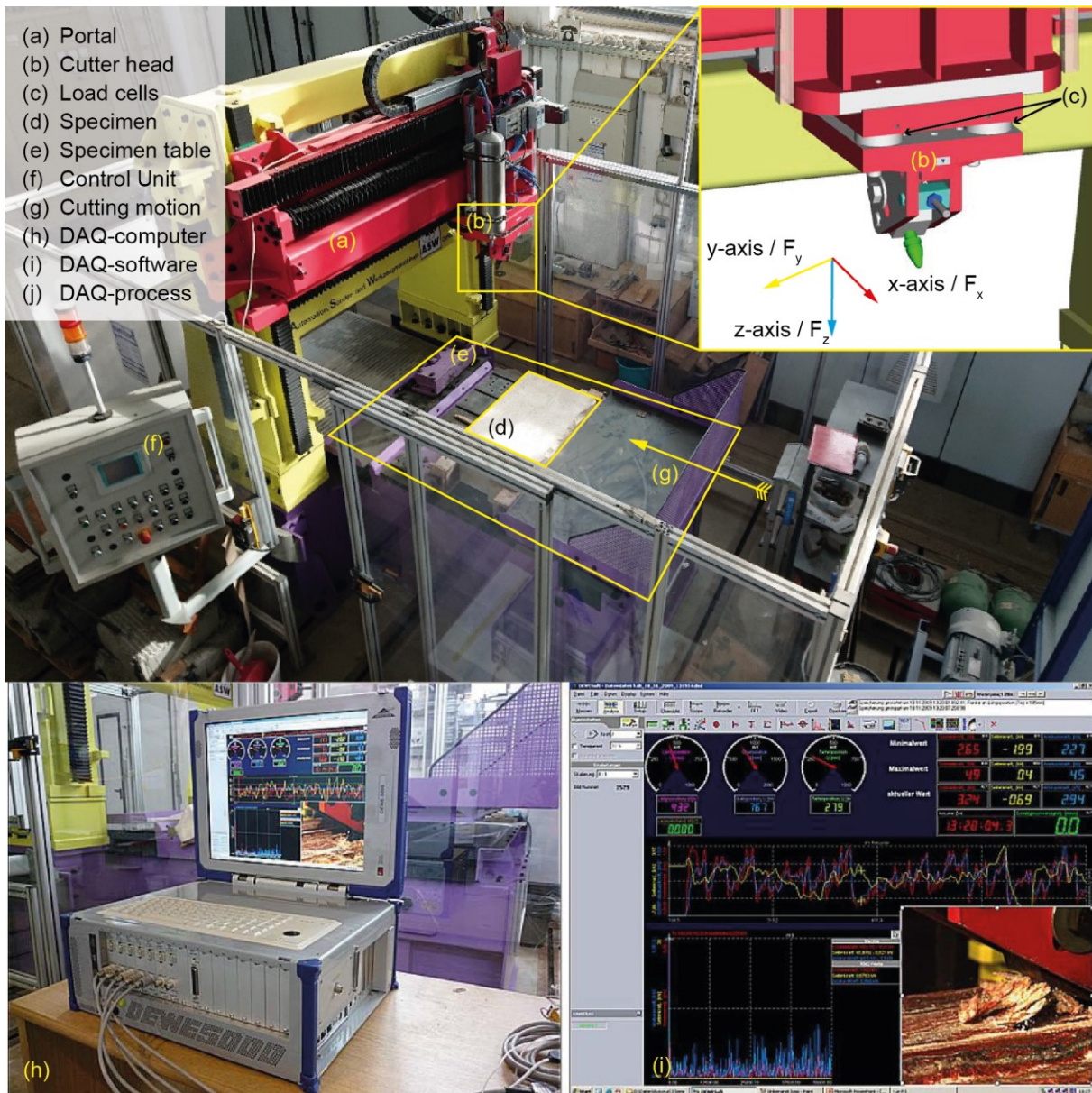
Figure 32: Linear rock cutting rig HXS-1000-50

Table 3: Main specifications of old and new sensor system compared

	F_x [kN]	F_y [kN]	F_z [kN]	Max. frequency [kHz]
Old system	50	30	50	10
New system (since 2019)	75	50	75	10

For all experiments, customised BETEK BSR112 picks were used (Figure 33). The picks were machined down to fit into the standard tool holder of the cutting test rig. A CAD drawing is shown in Annex F. The same pick was used for all experiments. These picks have a *wedge angle* of ca. 85°. During all experiments, the working angles remained unchanged. Moreover, the cutting speed remained static. These static parameters are as follows:

- *Attack angle*: 45°
- *Tilt angle*: 0°
- *Clearance angle*: 2.5°
- *Rake angle*: 2.5°
- *Cutting speed*: 0.1 m/s
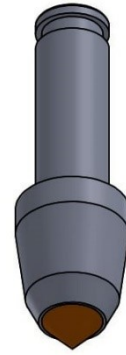
Figure 33: Customised BETEK BSR112

5.2 Software & PC

Several software packages were required and used for this study, as explained in the following Table 4. A regular desktop PC was used for all calculations: AMD Ryzen 7 CPU, Nvidea GeForce GTX 1060 6GB, 16 GB RAM.

Table 4: Software packages used for this work

Software Name	Short Description
Dewesoft	DAQ software by company DEWESOFT.
	Used for data acquisition, real-time calculation of additional parameters, and data export.
Weisang Flexpro	Measurement database software with an integrated scripting language.
	Used for the organisation of the measurement data for certain campaigns CO, FBA and PB, for error management and quality assurance of the data, as well as calculation of intermediate results.
R-Studio	Programming interface software for programming language R.
	Used for the main part of this work; for general descriptive statistics, procedural selection algorithm, correlation analysis, machine learning, and plotting of results. The scripts and code used are listed in Annex O.
Hexagon MinePlan	Mine planning software suite. Consists of multiple modules covering the mine planning process from drillhole management to deposit modelling/geostatistics, long-term planning, to production optimisation and short-term planning. Embedded in a CAD environment.
	Used for photographic modelling of ore boundaries during case study as well as visualisation of classification results in block models in conjunction with R-scripts.
Adobe Lightroom & Photoshop	Photo organising and processing softwares.
	Used for correction and orthorectification of photos to allow for photographic modelling in the case study.
Golden Software Surfer	2d geostatistics and mapping software.
	Used for visualisation of spatial cutting force distribution and partly orthorectification of photos.

5.3 Samples and Rock Cutting Parameters

This chapter describes the samples and the experimental routines. Five experiments based on linear rock cutting experiments were carried out, as shown in Table 5. Three preliminary Experiments CO, GN, and GR; followed by the case study Experiments PB and FBA. The main goal was to identify the perspective capabilities of machine learning-based rock classification with data that can be acquired by cutting force sensors. The five experiments follow a logical structure in which the output of the first three experiments leads to a case study that consists of the last two experiments.

Table 5: Summary of experiments

Name	Nr. of samples	Sample type	Sampling area	Main Task
CO	2	Different concrete layers	Artificial	Identify features for ML, and first prediction of ML-capabilities
GN	1	Foliated gneiss	Dörfel, Germany	Refine knowledge for foliation
GR	3	Uncracked and cracked granite	Neuhaus-Plöcking, Austria	Refine knowledge for crack occurrence
PB	2	Pb-Zn ore + concrete	Reiche Zeche Freiberg, Germany / artificial	Case study
FBA	3	F-Ba ore + concrete	Quarry Dörfel, Germany / artificial	Case study

The first campaign (CO) investigated the differences in the FCR responses for hybrid rocks with different hardness levels. This was done with concrete samples composed of up to three types of concrete. These concrete types comprised soft, medium, and tough concrete mixtures. The second experiment (GR) compared solid rock with cracked rock. Here, granite was used. Two samples were treated with high-power microwave radiation to induce a crack network, and one sample was left untreated to serve as a reference. The third experiment (GN) investigated the changes in the force behaviour during the cutting of foliated rock. Gneiss was used here. The sample was cut from different sides. As such, the cutting trajectory in relation to the foliation could be varied.

The last two experiments, PB and FBA, belong to a case study in which the possibilities of rock classification with the help of machine learning are explored in a 3d environment. Here, natural heterogeneous ore rocks, cast into a concrete block, were used. The concrete served as "host rock". The aim was to distinguish between the ore and the surrounding concrete. The PB experiment investigated samples comprising lead-zinc ore (Pb-Zn), and the FBA experiment comprised fluorite-barite ore (F-Ba).

5.3.1 Sample Sites

The granite for Experiment GR was acquired by the University of Leoben as part of a research cooperation. The granite was produced by Poschacher Natursteinwerk in Neuhaus-Plöcking, Austria.

The other specimens were sampled in Saxony, Germany. Figure 34 shows a geological map of Saxony with the sampling areas. The PB samples were taken from the Reiche Zeche underground mine (1) in Freiberg, which belongs to TU BAF and serves as a research and teaching mine. The samples were taken from the vein *"Wilhelm Stehender Nord"*. The area was freshly blasted, and boulders were taken from the blasting site. The samples for the FBA and GN experiments were extracted at the quarry Dörfel (2) in the Erzgebirge region of Saxony. The quarry is operated by the company Max Bögel. They were taken

from a hydrothermal vein that crosses the quarry. The vein is mainly composed of fluorite, barite, quartz, and altered gneiss. The host rock is gneiss, which forms the metamorphic basement in the area. Located close by (ca. 15 km) is one of the two currently operating German fluorspar mines, Niederschlag (3).
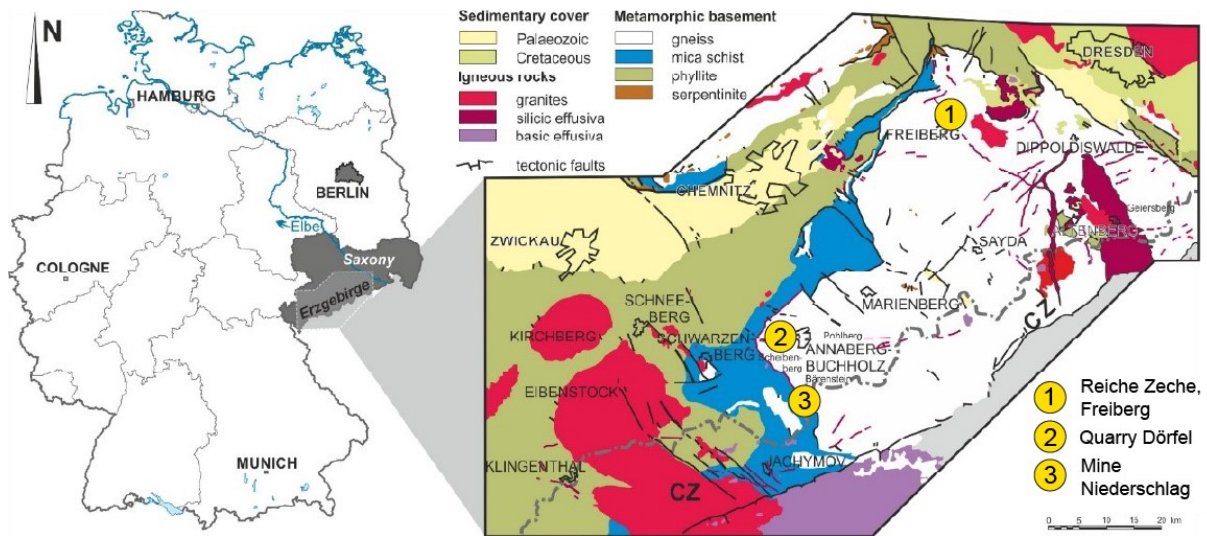
Figure 34: Geological map of Saxony with sampling locations (1 & 2) and the currently only operating fluorspar mine in Saxony (3) [158]

At the sampling point, the vein showed an inclination of ca. 70°. The thickness of the vein lay at ca. 1.5 m. The orange lines in Figure 35 a) sketch the approximate outlines of the vein. The quarry produces different gneiss products, therefore the vein material is not used for production. Because of this, the rock next to the vein was excavated, and the vein itself was left untouched. The sampling process can be seen in Figure 35, Panels a) to d). The samples were taken with the help of an excavator and transported to TU BAF. Lumps of up to 1.5 m in diameter could be extracted from the vein area.

Figure 35: Sampling of gneiss and fluorite-barite lumps at Dörfel quarry

5.3.2 Experiment CO – Zoned Concrete

For this experiment, linear cutting tests were conducted on two concrete blocks. The blocks consisted of different zones of ready-to-use concrete mixtures (Figure 36). The blocks were cast using a plywood casing of ca. 75 × 60 × 40 cm (inner measures). As shown in Figure 36, the casing was lined with a plastic layer to allow the removal of the casing after hardening. During casting, plastic sheets of ca. 0.5 cm thickness were inserted. These sheets separated the concrete mixtures during pouring. Immediately after casting the blocks, the plastic sheets were removed. This resulted in a defined vertical contact zone between the different concrete types and minimised the flow of concrete into the neighbouring zone. The blocks were removed from the casing after seven days.

Two blocks were cast. One block consisted of two different concrete mixtures (Block CO1); the second block consisted of three different zones (Block CO2). CO1 comprised medium and tough concrete; CO2 comprised weak, medium, and tough concrete. The main focus of this study lies on block CO2, consisting of 3 different zones. CO1 served as a failsafe and a more robust data foundation should the results of CO2 be too unreliable.

Figure 36: Zoning of test block during casting (left) and cutting (right)

Table 6 shows an overview of the concrete types used and their respective characteristics. The blocks were tested with a Schmidt hammer prior to cutting to approximate of the rock strength right before the actual cutting experiments were carried out. Schmidt tests are correlated with *UCS* and cutting resistance [85, 86, 159].

A Schmidt hammer of type NR with an impact energy of 2.207 Nm was used. Ten vertical repetition measurements were executed for each zone, and the arithmetic mean, and standard deviation were calculated. The tests were spaced at least 5 cm apart from each other. The *cube uniaxial compressive strength* was estimated with the calibration curve from the manufacturer of the hammer to allow comparison to the nominal rock strength from the datasheets of the concrete mixtures (Annex P on CD). The results are shown in Table 6. Generally, the *cUCS* of the cast blocks was lower than the nominal rock strength. Furthermore, the hardness of Zones 2 and 3 was lower in CO2 than in CO1.

*Table 6: Materials used for the construction of the test specimen; Schmidt hammer tests were conducted prior to cutting tests; * – extrapolated value*

Product	Name	cUCS (nominal) [MPa]	CO1 $R_{NR} \pm \sigma$	CO2 $R_{NR} \pm \sigma$	CO1 cUCS [MPa $\pm \sigma$]	CO2 cUCS [MPa $\pm \sigma$]
Kemmler Fertigbeton B25 (C25/30)	Zone 1	≥25	–	15,8 ± 3,5	–	12.0* ± 3.6
Maxit Ton 908 FB	Zone 2	≥ 45	34,9 ± 3,6	22,8 ± 3,9	34.9 ± 3.6	19.7 ± 4.5
PCI Repaflow® plus	Zone 3	≥ 85	46.5 ± 6.0	40.3 ± 3.3	57.0 ± 10.7	45.3 ± 5.8

Before cutting each layer, the surface of the blocks was levelled. The first cut of each test, which is an unrelieved cut, was not considered for the analysis. The subsequent were placed side by side, and as such were semi-relieved cuts.

Table 7 shows the chosen cutting parameters. The *cutting depth* and *s/d* ratio were varied on three levels. The *cutting depth* was varied at 6, 8 and 12 mm. The *s/d ratio* was varied in three levels: 2, 3 and 4. This resulted in seven levels for the *spacing*. The design causes three tests (Nr. 3, 5 and 6) to share a mutual absolute *spacing* of 24 mm. This mimics the crescent-circular movement of a pick during a passthrough with fixed *spacing*. The *cutting depth* levels of 6, 8 and 12 mm represent the rotation angle of a pick on a cutting drum of 30°, 42°, and 90°, respectively (for details to crescent cut, see Figure 13, p. 16).

*Table 7: Cutting parameters for the experiments; *: fixed spacing cuts*

Test Nr.	Depth of cut d [mm]	s/d-ratio	Spacing s [mm]	Represents rotational angle of [°]	Nr. of individual cuts
1	6	2	12		42
2	6	3	18		29
3	6	4	24*	30	21
4	8	2	16		33
5	8	3	24*	42	21
6	8	4	32		16
7	12	2	24*	90	21
8	12	3	36		14
9	12	4	48		10

A whole layer of the block's usable surface was cut for each test to obtain data that allowed for a spatial analysis. It also equalises extreme events in single cuts, the benefit of this is discussed in multiple works [33, 57, 122, 158]. While the entire surface of a layer was cut, safety strips were left at the edges (Figure 37). No measurements were made there. On the sides and the end of the block, they were ca. 10 cm wide. Also, the first 2 cm of a cut were omitted. This prevented measuring edge effects, where the cutting forces are lower because the confinement situation is different. The number of cuts ranged from 10 to 42 depending on the *spacing* and the width of the surface.
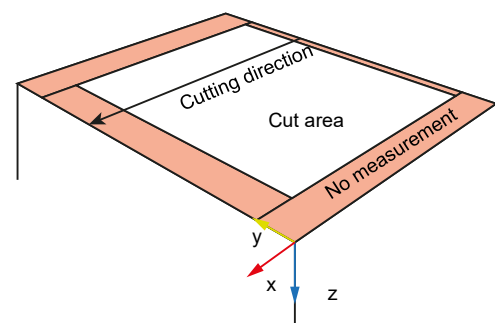
Figure 37: Scheme of omitting sides of the block surface from measurement

5.3.3 Experiment GN – Anisotropic Rock Gneiss

The gneiss from the Erzgebirge region shows a clear foliation. Due to this, its rock mechanical properties are highly anisotropic. As such, it was suited as a specimen for investigating the influence of anisotropy on FCRs. The rock mechanical properties of the gneiss have been tested at the Laboratory for Rock Mechanics at the Institute of Soil and Rock Mechanics of TU BAF.
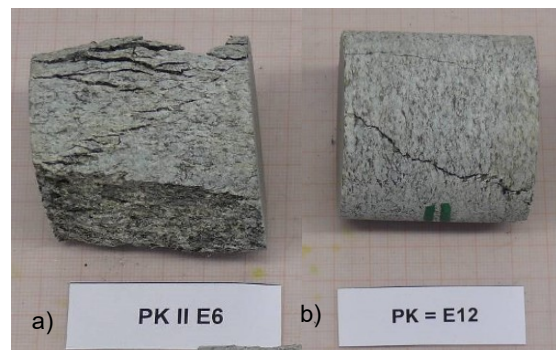
Figure 38: Gneiss samples, a) tested along foliation and b) normal to foliation

The *UCS* tests were conducted with core samples of ca. 50 × 50 mm (*d* × *l*). The *BTS* tests were conducted with samples of 50 × 25 mm. Figure 38 shows a *UCS* sample tested along (a), and a sample tested normal to the foliation (b). The different cracking behaviour is clearly visible. This results in a mean *UCS* of 175 MPa parallel to the foliation. The orthogonal *UCS* was only 84% of the parallel *UCS*. This result is relatively unusual. Normally, a loading along the bedding plane is reported to result in a lower *UCS* [160]. However, Hakala et al. (2007) reported a high *UCS* for low and high foliation angles (ca. 20° and 80°, respectively) and the lowest for ca. 45° foliation angle. Their experiments were conducted on Olkiluoto mica gneiss from Finland [161]. Cho et al. (2012) also report similar high *UCS* values for 0 and 90° foliation and the lowest for 45°–60°. However, they also received the highest variation for 0 and 90° foliation angles. Their experiments were carried out on Asan gneiss, Yeonchon schist, and Boryeong shale [162].

The values for the *BTS* follow the general expectations. A loading along the foliation axis results in the lowest strength values (load case B3 in Table 8)—the tensile stress acts orthogonal to the bedding planes. The values for B3 are ca. 55% compared to the other two bedding directions. The gneiss has a density of 2.72 t/m³. The documentation of the rock mechanical tests can be found in Annex P (on CD).

Table 8: Rock mechanical properties of gneiss specimen

	UCS		BTS		
Load Case	**U1**	**U2**	**B1**	**B2**	**B3**
Mean [MPa]	175.0	147.6	15.5	16.0	8.7
σ [MPa]	11.9	18.8	1.79	1.04	3.3
	E-modulus				
Mean [MPa]	35.4	26.5			
σ [MPa]	0.6	2.9			
Nr. of Samples	10	10	3	11	10

For the cutting experiments, two cuboid samples were prepared from natural lumps. Figure 39 b) on the next page shows a photo of a sample before preparation. A circular rock saw was used to cut the sample into shape (c). Three different cases were investigated concerning foliation. They were carried out on different sides of the same sample and are explained in Table 9.

Table 9: Cutting directions in relation to foliation planes

Case	Symbol	Explanation
A	⩾≣	Foliation along to the x-y-plane. Theoretically, this results in the heaving of layer-chips along the bedding plane.
B	⩾⦔	Foliation along y-z-plane. Higher forces expected since no heaving of chips should occur.
C	⩾⫔	Foliation along x-z-plane. Higher forces expected since no heaving of chips should occur.

Panel b) shows these three cases; the black arrow indicates the cutting direction. The cutting parameters that were used are shown in Table 10. The right side of the table shows the cutting pattern. One unrelieved cut for each test and three to four subsequent semi-relieved cuts were executed. Normally, a total cutting length of 2 m per test is recommended [41]. Due to the limited block size, only ca. 75 cm per set could be executed. The order of experiments was as follows: first, all unrelieved cuts for a layer were conducted. In the second step, the three semi-blocked cuts were added to the respective fully blocked cuts (Table 10, Cutting scheme). A safety distance of at least 5 cm was maintained between neighbouring sets to ensure that they did not influence each other. After the surface was fully consumed by the cuts, it was levelled for subsequent tests. This routine was executed for all three tested sides.

Table 10: Cutting parameters for Experiment GN and schematic of cutting pattern

Test Nr.	Cutting depth d [mm]	Spacing s [mm]	s/d-ratio	Foliation case	Cutting scheme
1	4	UR	UR	A	
2	4	8	2	A	
3	4	12	3	A	
4	4	16	4	A	
5	6	UR	UR	A	
6	6	8	1.33	A	
7	6	12	2	A	
8	6	16	2.67	A	
9	4	UR	UR	B	
10	4	8	2	B	
11	4	12	3	B	
12	4	16	4	B	
13	6	UR	UR	B	
14	6	8	1.33	B	
15	6	12	2	B	
16	6	16	2.67	B	
17	4	UR	UR	C	
18	4	8	2	C	
19	4	12	3	C	
20	4	16	4	C	
21	6	UR	UR	C	
22	6	8	1.33	C	
23	6	12	2	C	
24	6	16	2.67	C	

Red - unrelieved cut
Black - semi-relieved cut
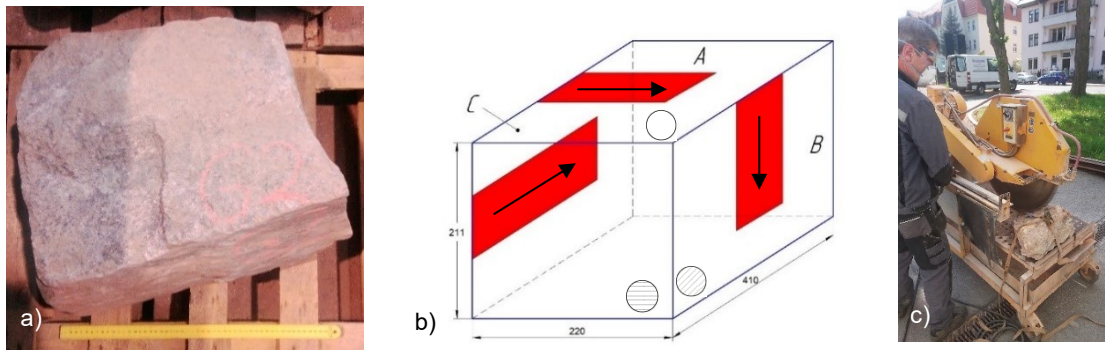
Figure 39: Gneiss specimen for Experiment GN

5.3.4 Experiment GR – Uncracked and Cracked Granite

Previous results of this experiment have been published in five publications [38, 105–107, 163] and further details can be found there. The focus of these works lay in examining the effect of microwave radiation on the excavatability of granite. In the present study, these results are extended to address the following questions:

- *How do the FCRs change with changing cracking state of the rock?*
- *Apart from FCRs, could additional features be feasible to identify a changing cracking state of the rock?*

For the experiments, three granite blocks with dimensions of $50 \times 50 \times 30$ cm were used for the cutting experiments. One surface of the first and second block was treated with microwave radiation in a "chessboard" spot pattern for 30 s and 45 s per spot, respectively. The distance between the spots was 90 mm. The third block was left untreated. The blocks were treated at the Sandvik research facility in Zeltweg, Austria, by MU Leoben as part of a cooperation between the University of Leoben and TU BAF. These blocks are called B30, B45, and B0, respectively. The described tests were performed with samples of *"Neuhauser Granite"*. This granite comprises 27% quartz, 53% feldspar, and 20% mica. Single minerals can be up to 4 mm in size. The texture is granular with some xenomorphic crystals. The rock shows the following parameters [106]:

- *UCS*: 210 MPa
- *Cerchar abrasivity Index*: 4.2
- *Density*: 2.67 t/m³

Microwave irradiation was performed with a 24 kW microwave source operating at a frequency of 2450 MHz with an open-ended waveguide directed at the rock surface (Figure 40 a). Corresponding to the size of the waveguide, these spots have dimensions of approximately 5 cm in diameter. Due to the microwave radiation, damaged and cracked zones occurred around the radiation spots. Here, the material showed partial minor spalling. Some spots showed small drops of molten rock in the centre of the radiation spots. Between the radiation spots, a network of larger cracks formed. The surface of the rock can be seen in Figure 40 b), and the crack network induced by the radiation (for B45) is shown in Panel c) of the figure. Further details on the irradiation effects can be found in [107].
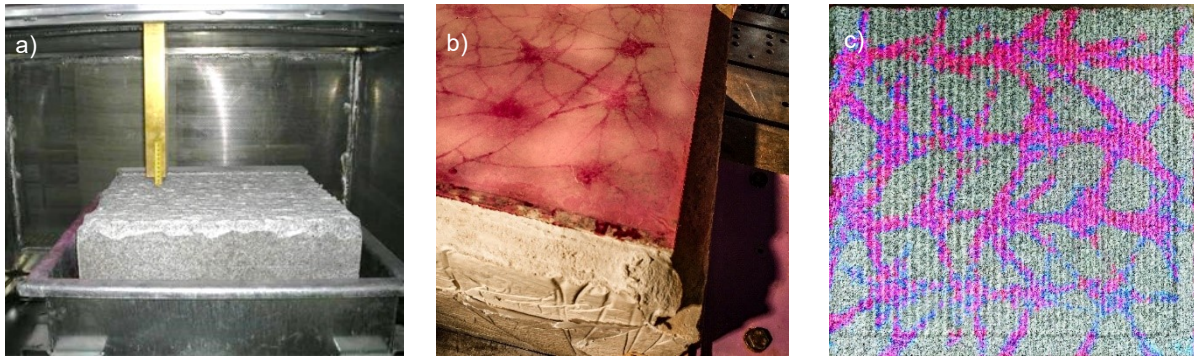
Figure 40: a) Microwave and waveguide [163]; b) detail of 30 s radiated block before cutting; c) crack marking fluid during the experiments (enhanced with Photoshop)

The following cutting parameters were chosen:

- *Spacing*: 8 / 12 mm
- *Cutting depth*: 4 mm

One half of the block was cut with $s = 8$ mm, the other with $s = 12$ mm. All other cutting parameters were constant. During the cutting of B45, the block failed while cutting the fifth layer. Because of this, only four layers could be analysed for B45. Figure 41 shows the failed block after cutting the fifth layer. In the figure, it can also be seen that due to the cracks, overbreak occurred where macrocracks were located (a). Also, the crack marking liquid is still visible (b), indicating a deeper penetration of the cracks into the rock mass.

Figure 41: Failed block B45 after cutting of 5th layer [163]

For the samples, the following number of layers was cut:

- B0　　　6
- B30　　8
- B45　　4

A new pick was used for each block to equalise the influence of the tool's wear. Subsequent layers were cut directly without levelling the surface and placed exactly over the cuts of the preceding layers.

5.3.5 Case Study PB and FBA – Lead-Zinc and Fluorite-Barite Ores

The sample preparation process of the last two experiments is similar. Hence, they are described together in this chapter. These samples consist of lumps of vein material cast into a surrounding concrete block. As a natural and heterogeneous material, the ore underlies relatively large variations. Three samples comprised a fluorite-barite ore (FBA1–FBA3), and two comprised a lead-zinc ore (PB1 and PB2). The FBA samples were obtained in the quarry Dörfel; the PB samples were obtained from the Reiche Zeche research and teaching mine, as described in Chapter 5.3.1.

Figure 42 shows all five samples. The lead-zinc ore consisted mainly of galena, sphalerite, to large portions of pyrite and a patch of altered gneiss. In smaller portions, chalcopyrite and arsenopyrite can be found in this ore [164]. Although no in-depth mineralogical analysis was performed, this is supported by handheld X-ray fluorescence analysis (XRFA) measurements on these samples [165]. Apart from the

patch of altered gneiss in PB1, the PB samples are comparably homogeneous and show no visible anisotropy, cracks, or cavities.

The FBA samples mainly consist of fluorite, barite, quartz, and altered gneiss. The samples show a certain oriented layering and are very heterogeneous. This includes larger zones where one mineral is dominant (either barite, fluorite, or altered gneiss) as well as cavities and quartz bands. As such, a very heterogeneous FCR behaviour is expected here. In terms of classification with ML, these samples serve as "complicated" samples, whereas the PB samples serve as "easier" samples.
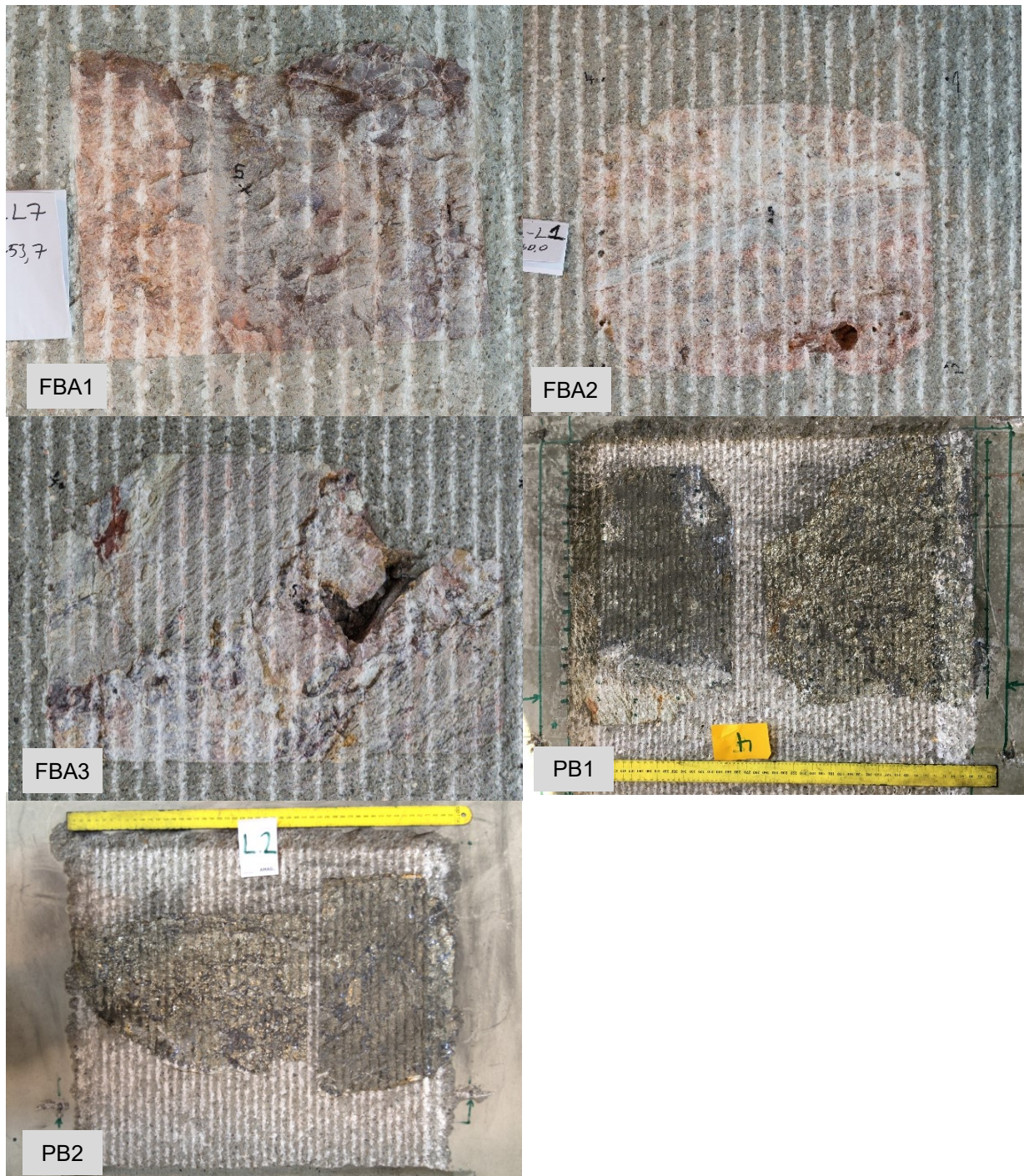
Figure 42: All samples of Experiments FBA and PB

Table 11 shows the rock mechanical properties of the FBA samples. The *UCS* along the layering is approximately 50% higher than the *UCS* perpendicular to the layering (120.1 resp. 81.1 MPa). Additionally, both sides show a relatively high *standard deviation*. The standard deviation for the tests along and perpendicular to the layering was 22.7 and 15.04 MPa, respectively. This underlines the heterogeneity of these samples.

Table 11: Rock mechanical properties of the fluorite-barite ore
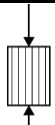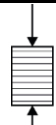
	UCS		BTS		
Load Case	U1	U2	B1	B2	B3
Mean [MPa]	120.1	81.1	5.3	4.9	5.1
σ [MPa]	22.7	15.04	2.1	0.4	3.2
	E-modulus				
Mean [MPa]	22.7	18.6			
σ [MPa]	4.2	2.7			
Nr. of Samples	10	11	4	4	3

Table 12 shows the rock mechanical results for the PB samples. Two samples were analysed with *UCS* tests, and nine samples were analysed with *BTS* tests. The tests were conducted at the Laboratory for Rock Mechanics at the Institute of Soil and Rock Mechanics of TU BAF. The two *UCS* tests showed values of 87.1 resp. 56.2 MPa *UCS*. The *BTS* was 5.3 MPa. For these samples, no layering orientation could be found.

*Table 12: Rock mechanical properties of the lead-zinc ore *since only two UCS tests could be conducted, the original values are given in brackets*

Lead-Zink ore	UCS [MPa]	E-modulus	BTS [MPa]
Mean	71.6* (87.1 / 56.2)	ca. 75	5.3
σ	-	-	2.1
Nr. Of Samples	2	2	9

Sample Block Preparation

The preparation of the samples was carried out "upside down" after the following sequence:

1. Cutting the ore specimen with the diamond circular saw so that at least one even surface is created.
2. Inserting the ore samples with the flat side facing down in the casting form.
3. Filling the casting form with PCI Repaflow mixture.
4. After seven days of hardening, removing of the casing and turning of the block so that the bottom side with the ore sample now faces up.
5. Levelling of the sample on the cutting test rig before the first experiment.

The same PCI Repaflow Plus concrete mixture as for Experiment CO was chosen, which shows a nominal compressive strength of 85 MPa after seven days (datasheet: see Annex P). The time until the samples were cut was approximately 30 days. The sizes of the samples can be seen in Table 13. In Figure 43 a), the position of a sample in the cast concrete block is shown. A upside-down prepared sample, right after casting is shown in Panel b).
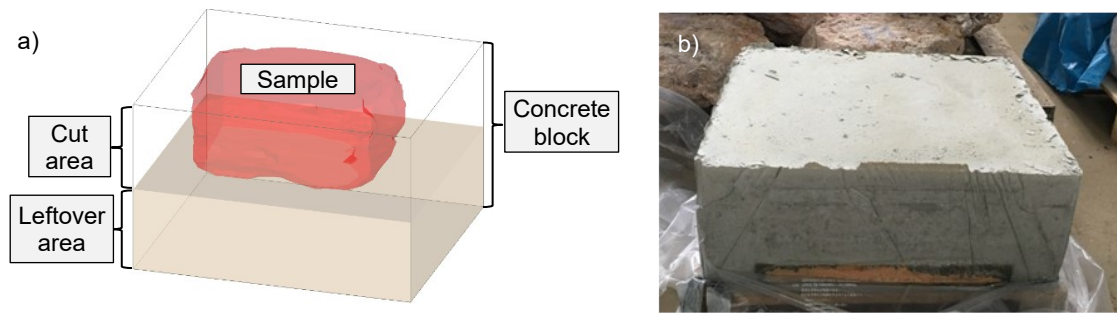
Figure 43: a) 3d-model of block FBA2, b) upside-down block after casting

Experimental Routine

Due to the required amount of data for 3d-modelling, only a limited cutting parameter variation could be selected. The samples for Experiment PB were cut using an approach where the *cutting depth* and the *spacing* were varied in three steps. For each block, only two parameter combinations were chosen. Since the *s/d*-ratio influences the results, it was also varied at two levels for this experiment. Details of the test plan can be seen in Table 13.

For Experiment FBA, a slightly modified testing plan was used. Following the assumption that the *spacing* is usually not variable during excavation, a fixed *spacing* was chosen. The *cutting depth* was varied on two levels. Originally, 7 and 14 mm were planned. The *s/d*-ratio should follow the levels 2 and 4, respectively. As such, the *spacing* of 28 mm was chosen. After the experiments on block FBA1, the testing plan had to be adjusted, since 14 mm *cutting depth* resulted in very large breakouts on the edges of the block. For the remaining two blocks, the *cutting depth* was lowered to 6 and 12 mm and the *spacing* was adjusted to 24 mm. This setup roughly follows the presumption of a pick position at 30° (half of maximum *cutting depth* reached) and 90° (maximum *cutting depth* reached) revolving angle with regards to the crescent cut (see Chapter 2.1.2, subsection Cutting Parameters During Regular Excavation).

Table 13: Block sizes and cutting parameters for experiment PB and FBA

Material	Block	Sample size (x × y × z) [cm]	Layer	Cutting depth [mm]	Spacing [mm]	s/d
PB	1	57 × 74 × 25	1–7	4	8	2
			8–12	6	12	3
	2	57 × 74 × 25	1–5	6	12	3
			6–9	8	16	2
FBA	1	45 × 50 × 28	1–9	7	28	4
			10–14	14	28	2
	2	45 × 50 × 28	1–10	6	24	4
			11–20	12	24	2
	3	50 × 60 × 30	1–8	6	24	4
			8–18	12	24	2

5.4 Data Processing

Figure 44 shows the data processing workflow followed, with all the respective outputs. Five experiments based on linear rock cutting experiments were carried out (i.e., three preliminary Experiments CO, GN and GR, followed by the case study PB and FBA). The main goal was to identify the perspective capabilities of machine learning-based rock classification with data that can be acquired

by cutting force sensors. The five experiments follow a logical structure where the output of the first three experiments leads to a case study that consists of the last two experiments.
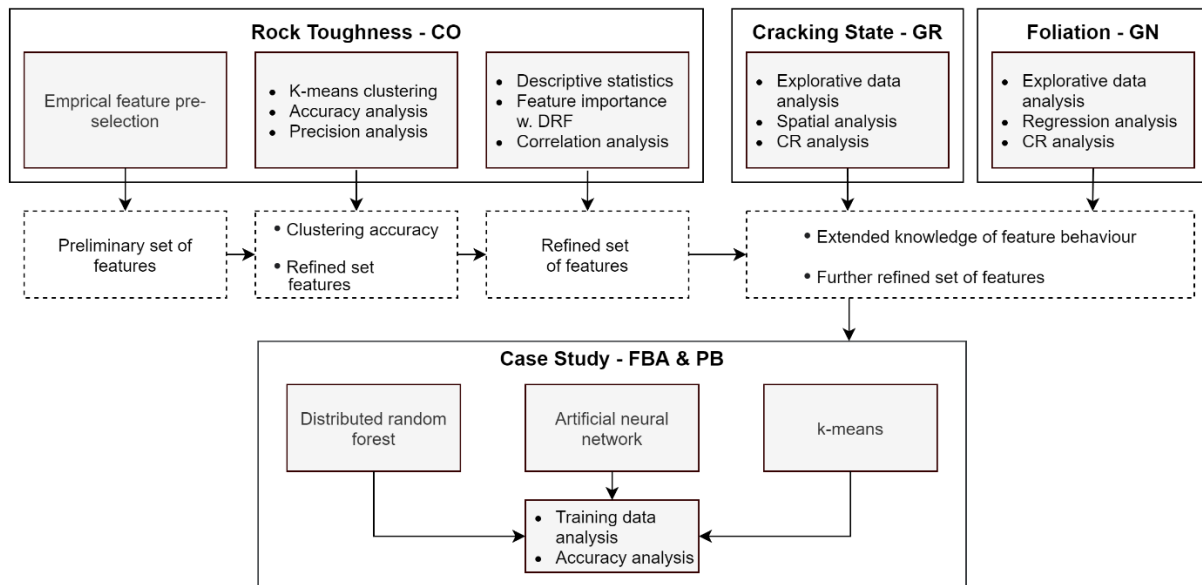
Figure 44: Logical structure of experimental routine

Generally, Experiment CO explored the behaviour and potential of ML on the example of composite concrete samples that comprise different toughness zones. The data received from CO were used to select a set of features based on FCR that can be further used. Based on this, k-means clustering was conducted, and the results were assessed in terms of classification *accuracy* and spatial *precision*. Further, the importance of all used features was examined based on a distributed random forest classification to identify redundancy. In addition, a correlation analysis was performed to verify the results. This led to a refined set of features. In order to extend the results of the first experiment to inhomogeneous rock states, the two Experiments GR and GN were conducted. GR explored the effects of crack occurrences, and GN explored the occurrence of anisotropic rock mechanical behaviour on the example of foliation in gneiss. This led to the addition of a new feature, the *contact ratio* (*CR)* to the set of features. The obtained findings were used to conduct the case study. Here, the chosen features were used to classify the five rock samples of type FBA and PB into ore and concrete. This allowed for a comparison of the *accuracy* and amount of data required for a reliable classification result. The specifics of the employed methods are explained in the following.

5.5 Force Component Ratio Calculation

To extend the knowledge that F_z/F_x can serve as an indicator for the rock being cut, the concept was extended to a) real-time data instead of mean values and b) to the other force components F_y and F_{res}. Various descriptive statistics characterise the real-time FCR data. These statistics serve as features— input variables—for the machine learning algorithms. This approach can be seen as a method of feature engineering. Feature engineering is an important part of the machine learning workflow that ensures the performance of these algorithms [166].

The ratios between the forces F_x, F_y, F_z, and F_{res} are calculated, resulting in 12 different ratio combinations including reciprocals. Table 14 shows all the possible combinations of FC to form a FCR as defined by Equation (19).

$$\frac{F_i}{F_j} = FCR\left(\frac{F_i}{F_j}\right) \tag{19}$$

Here, an $FCR(F_i/F_j)$ is defined as the ratio between two force components F_i and F_j. F_i and F_j can be F_x, F_y, F_z, and F_{res}.

Table 14: All force component ratios taken into consideration

Numerator i / Denominator j	F_x	F_y	F_z	F_{res}
F_x	1	F_y/F_x	F_z/F_x	F_{res}/F_x
F_y	F_x/F_y	1	F_z/F_y	F_{res}/F_y
F_z	F_x/F_z	F_y/F_z	1	F_{res}/F_z
F_{res}	F_x/F_{res}	F_y/F_{res}	F_z/F_{res}	1

As stated in Chapter 2.1.4, it is known that the state of the rock integrity and the rock type influence mean forces, maximum forces as well their ratio. As such, it is inferred that the FCR show a similar behaviour. Figure 45 shows two typical force diagrams from the cutting experiments of sample CO2.
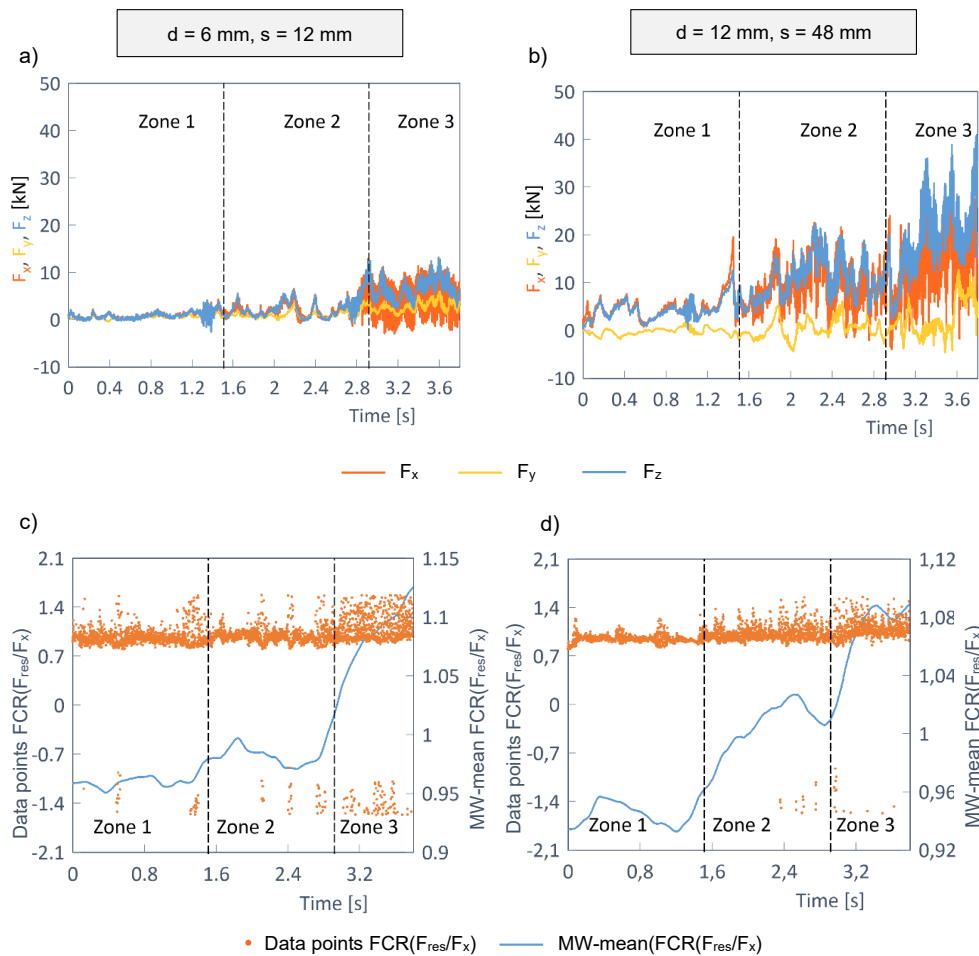
Figure 45: a) & b) Typical force diagrams for different cutting parameters; c) & d) real-time data and moving-window average of FCR(F_{res}/F_x)

The three different rock zones are marked in the diagrams. Panel a) shows a cut that was carried out with the smallest cutting parameters for this experiment ($d = 6$ mm, $s = 12$ mm). Panel b) shows a cut with the highest cutting parameters ($d = 12$ mm, $s = 48$ mm). One can see the different levels of the forces F_x, F_y, and F_z and their typical sawtooth-like behaviour. The magnitudes of F_x and F_z are roughly in the same range; F_y is minor to these two forces.

The diagram also illustrates that while the absolute magnitude of the force levels differs strongly between a) and b), similar behaviour can be seen with respect to the different rock zones. The cutting forces are lowest, and few peaks occur in Zone 1. In Zone 2, the general force levels are higher, and more peaks can be observed. In Zone 3, large oscillations of the forces can be seen; also, the general force levels are the highest. However, the differences between the two cutting parameter sets are higher than between the different concrete zones. As such, it would not be possible to trace the rock type based on the cutting forces when the cutting parameters are unknown.

The Panels c) and d) at the bottom of the figure show the nature of the FCR on the example of FCR(F_{res}/F_x). The real-time FCR data are shown as orange dots. A moving average smoothing of the raw data is shown as a blue line. It can be seen that the real-time data appear clustered in a band with a range of 0.8 to 1.1. Also, scatters of larger values up to ca. 1.5 and lower values up to -1.5 can be seen. These "outlier" scatters appear more often for Zone 3. The moving average shows that the values for this FCR are lowest in Zone 1, medium in Zone 2 and highest in Zone 3. Also, it can be seen that the values of $FCR(F_{res}/F_x)$ do not differ so much between the two cutting parameter sets as much as the raw force components do. Rather, $FCR(F_{res}/F_x)$ differs more in dependence of the zone number.

> *This behaviour is the cornerstone of the approach investigated in this work.*

Filtering and Truncation of Values

To calculate the real-time FCR, two filters were applied to improve data quality. The first one only lets data points where $F_z > 0.5$ kN pass. This serves as a filter to only take data where the pick was in contact with the rock. Filtering of $F_z > 0.5$ kN was not used to calculate the *contact ratio*.

The second filter truncates all FCR values < -20 and > 20. This is necessary because when the denominator of the FCR comes close to zero and the numerator does not, the FCR drifts to very high (infinite) values. This happens right after the breakout of a major chip when the pick swings freely for a short time or when cutting forces are generally on a low level—especially for F_x. Also, F_y tends to oscillate closer to 0 kN. To mitigate the influence of this, this truncation of the FCR was implemented. Ca. 95% of the FCR values lie in the range of up to ± 10, so only rare extreme values are truncated. Without truncation, values over $\pm 50,000$ have been recorded. Figure 46 shows this exemplarily. A plot of the distribution density for F_{res}/F_x is shown there. In the figure, a gap for values between ca. -1 and 1 can be seen. Its reason is not entirely clear, but it could appear due to filtering data points with $F_z < 0.5$ kN.
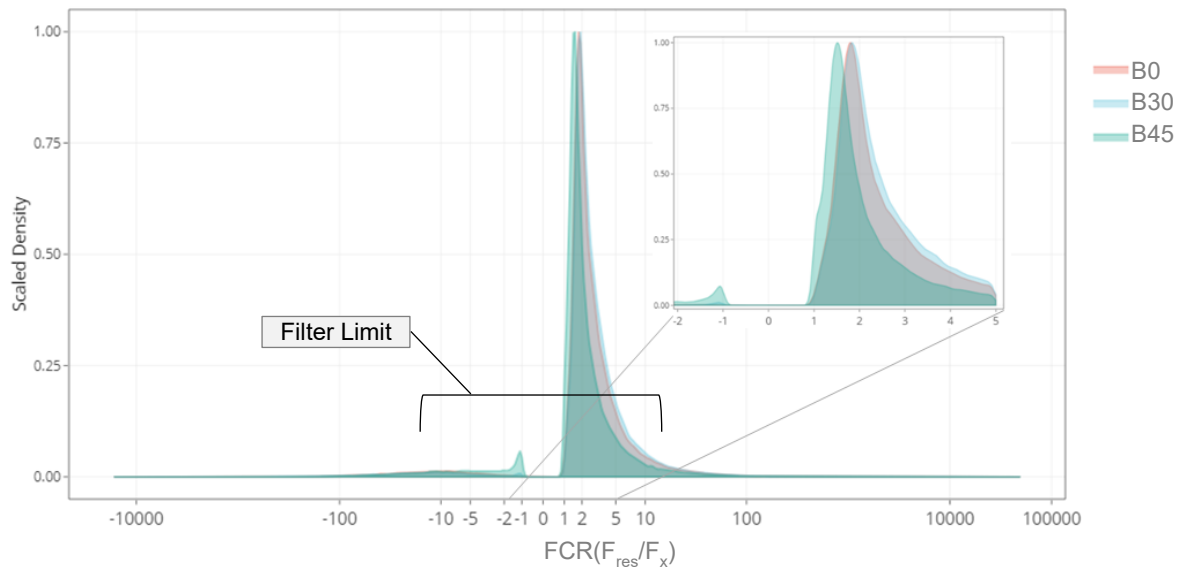
Figure 46: Raw distribution density curves for FCR(F_{res}/F_x) for Experiment GR

5.6 Procedural Selection of Features

For the training of machine learning algorithms, feature engineering is of crucial importance. In the following, the process of selecting the FCR-based features is outlined. The selected features were used further in the k-means analysis, where the set of features was refined and extended. This analysis was only conducted for Experiment CO.

Generally, cutting force data are noisy, high density data not suitable for direct interpretation. Following the experimental routine with a sampling rate of 1000 Hz, approximately 4000 data points were acquired per cut. Each measurement consists of eight channels: timestamp, F_x, F_y, F_z, F_{res}, x-, y- and z-position. For this analysis, the data of each set were sub-grouped according to the three Zones 1, 2, and 3 of experiment CO. The FCRs are calculated from the real-time data. Subsequently, descriptive statistics for the FCR are calculated. The following descriptive statistics were chosen to describe the behaviour of the FCR:

- $\bar{x}$ – arithmetic mean
- $\bar{x}_{geom}$ – geometric mean
- $\tilde{x}$ – median
- $Q_{0.95}$ – 0.95-quantile
- IQR – interquartile range
- v – variation coefficient

The geometric mean is reported to be useful for terms that are formed by a multiplication or division operation. It has also been a meaningful indicator for assessing differences in magnetic susceptibility between rock populations [167]. For the estimation of the 0.95-quantile and IQR, a type 7 estimation after Hyndman and Fan (1996) was employed [168]. It is the standard in the R language. Based on these descriptors, a procedural routine was designed to check whether an unambiguous assignment of the descriptors to the rock zones was possible <u>irrespective</u> of the cutting parameters.

Applying these descriptive statistics to the signals of the different FCRs led to 72 combinations of the six descriptive statistics describing the twelve FCRs. These features are encoded as in the following Table 15.

Table 15: Naming scheme of FCR features

		Statistical descriptor					
		$\bar{x}$	$\bar{x}_{geom}$	$\tilde{x}$	$Q_{0.95}$	IQR	v
		Statistical descriptor code					
		MEA	MED	GM	Q95	IQR	VAR
FCR	FCR-code	Feature codes					
F_x/F_z	XZ	XZMEA	XZMED	XZGM	XZQ95	XZIQR	XZVAR
F_z/F_x	ZX	ZXMEA	ZXMED	ZXGM	ZXQ95	ZXIQR	ZXVAR
F_x/F_{res}	XR	XRMEA	XRMED	XRGM	XRQ95	XRIQR	XRVAR
F_{res}/F_x	RX	RXMEA	RXMED	RXGM	RXQ95	RXIQR	RXVAR
F_z/F_{res}	ZR	ZRMEA	ZRMED	ZRGM	ZRQ95	ZRIQR	ZRVAR
F_{res}/F_z	RZ	RZMEA	RZMED	RZGM	RZQ95	RZIQR	RZVAR
F_y/F_x	YX	YXMEA	YXMED	YXGM	YXQ95	YXIQR	YXVAR
F_x/F_y	XY	XYMEA	XYMED	XYGM	XYQ95	XYIQR	XYVAR
F_y/F_z	YZ	YZMEA	YZMED	YZGM	YZQ95	YZIQR	YZVAR
F_z/F_y	ZY	ZYMEA	ZYMED	ZYGM	ZYQ95	ZYIQR	ZYVAR
F_y/F_{res}	YR	YRMEA	YRMED	YRGM	YRQ95	YRIQR	YRVAR
F_{res}/F_y	RY	RYMEA	RYMED	RYGM	RYQ95	RYIQR	RYVAR

Figure 47 shows the flowchart of the applied evaluation routine. The routine was implemented in R-Studio. The code can be accessed in Annex O. At first, the raw force data, grouped by cutting parameters, were imported. The force data were then grouped according to the zone. The signals for all the force component ratios were then computed for each zone.
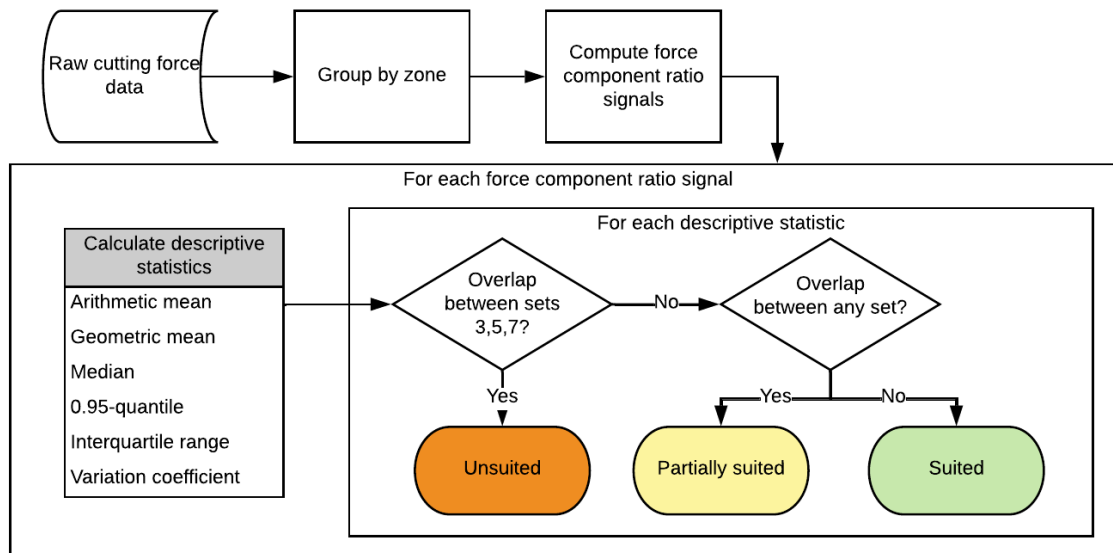
Figure 47: Flowchart for evaluation of material characterisation suitability of combinations of FCR and descriptive statistics

For each FCR signal, the six descriptive statistics mentioned above were calculated separately for each rock zone. The 72 resulting features were evaluated for their suitability for material classification. A combination of FCR and descriptive statistics is further called *FCR-feature*, as they serve as features for machine learning. For each given *FCR-feature*, a two-step check was carried out. In the first step, it was checked whether the calculated values formed unambiguous value ranges for each set, meaning that the values did not overlap between these individual zones. This situation can be seen in Figure 48 a) on the example of *FCR(F_{res}/F_x)–$Q_{0.95}$*. The $Q_{0.95}$ values form a band for each zone, and there is no overlap

between the values of the zones. This means that any of these values can be attributed precisely to one concrete zone—irrespective of the cutting parameters. If this condition was met, the combination of FCR and the descriptive statistic was classified as "suited".

The other two classification possibilities are shown in Panels b) and c) of Figure 48. Panel b) shows the situation where no such value corridor can be identified. Here, the values for $Q_{0.95}$ of $FCR(F_y/F_x)$ range from 0.39 to 1.01 for Zone 1, from 0.80 to 1.39 for Zone 2 and from 0.87 to 2.99 for Zone 3. It can be seen that the value corridors that are formed overlap. As such, no clear distinction between rock types irrespective of the cutting parameters is possible, and $Q_{0.95}$ of $FCR(F_y/F_x)$ would be classified "unsuited". However, as shown in Panel c), if only the three sets 3, 5 and 7 are considered, very clear value corridors are formed. Then the values range from 0.61 to 0.68 for Zone 1, from 1.03 to 1.08 for Zone 2 and from 1.59 to 1.66 for Zone 3. As described earlier, the three sets 3, 5 and 7 share the same *spacing* and, as such, would represent members of a perfect crescent cut at different *cutting depths*. Consequently, the algorithm classifies $Q_{0.95}$ of $FCR(F_y/F_x)$ as "partially suited" because the experiments that share the same *spacing* form a distinct value corridor.
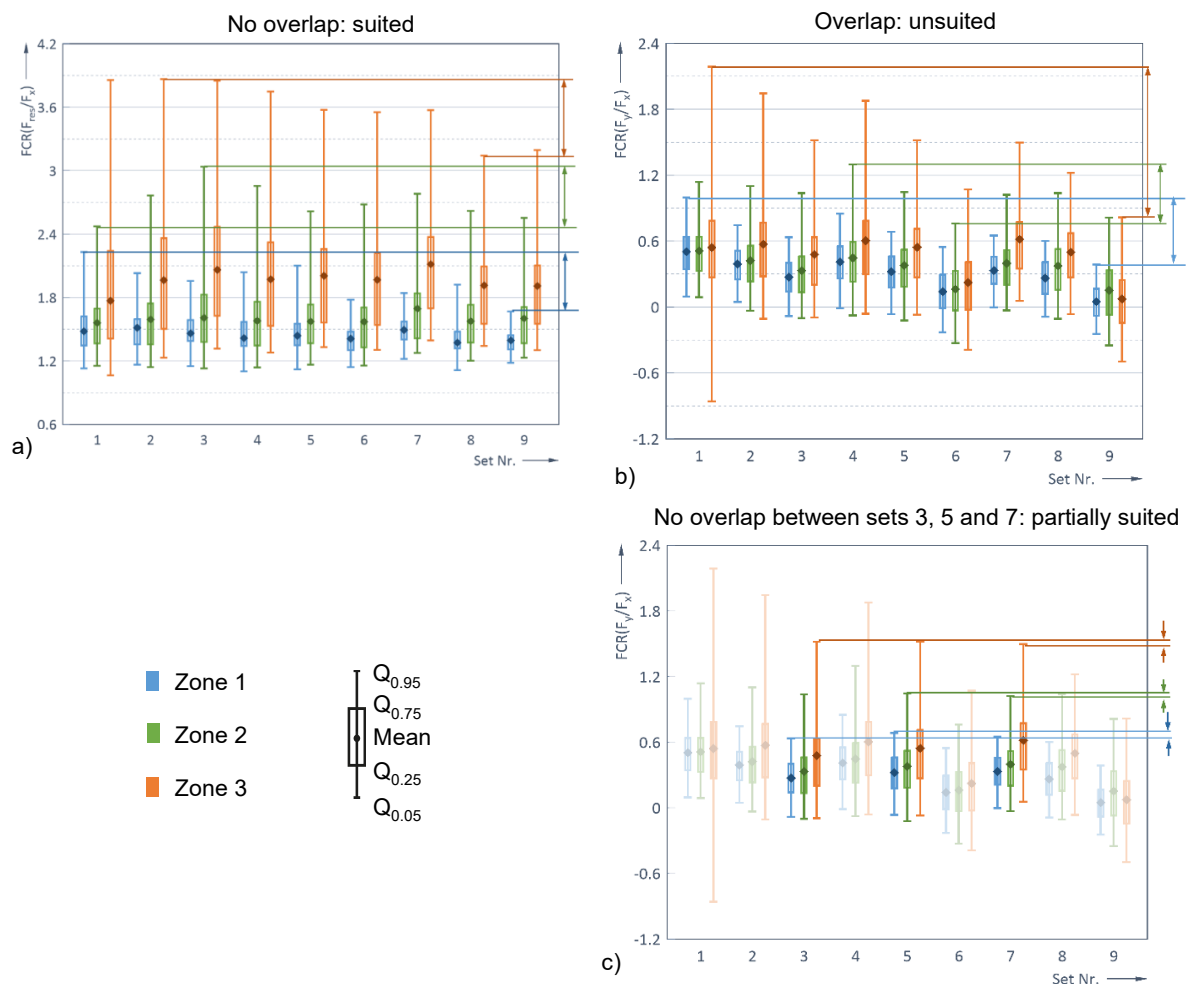
Figure 48: Exemplary results for a) FCR(F_{res}/F_x); b) and c) for FCR(F_y/F_x); horizontal lines show value corridors for $Q_{0.95}$

5.7 Image-Based Referencing and Rock Boundary Modelling

To compare the machine learning results with the real rock boundaries, the latter must be translated into the data environment of the block models. The workflow uses techniques derived from face mapping and cartography with orthophotos. An orthophoto usually is an aerial or satellite image geometrically corrected (orthorectified) such that the scale is uniform. It can be used to measure distances because it is an accurate representation of a surface, having been adjusted for topographic relief, lens distortion, and camera tilt [169, 170]. Here, the orthorectification process only included distortions of the lens and the perspective.

A digital photograph of the surface of the block was taken for each cut layer of the block. The images were manually taken at an angle close to 90° to the surface. Before a photo was taken, four reference points were painted with an Edding pen on the four corners of the block. The coordinates of these points were measured with reference to the tip of the pick (Figure 49). The images were orthorectified using either Adobe Lightroom, Photoshop, or Golden Software Surfer.

The pictures prepared in this way were then further processed in Hexagon MinePlan. First, empty layers were created on the z-coordinates of the cutting layers. The orthophotos were then draped onto these layers. Hereby, the four coordinate-referenced edge points were used to reference the photo. Then, boundaries between the two different rock types were digitised layer by layer. Finally, all digitised boundaries were connected to form a 3d-body. As such, the geometry of the rock boundaries could be translated into the intrinsic coordinate system of the rock cutting machine. Based on the resolution of the camera and the size of the sample, as well as optical inaccuracies, a total inaccuracy of up to 5 mm is suspected for the boundary digitisation. Additional information on digitisation accuracy is given in Annex H.
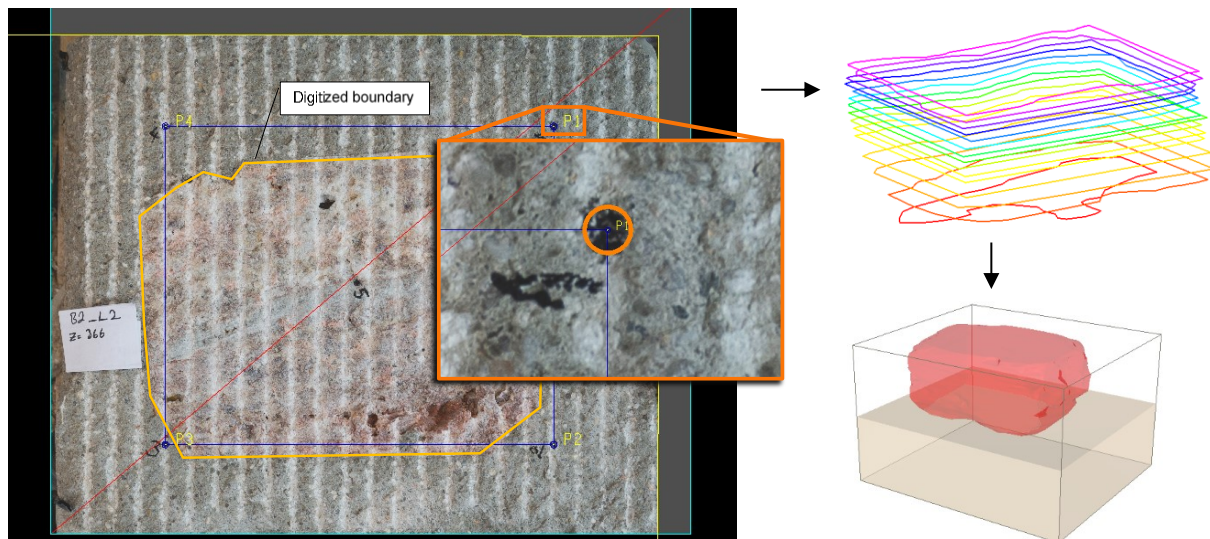
Figure 49: Workflow of modelling the 3d-boundaries of ore samples for the case study

The 3d-models created from the photos are shown in Figure 50. On the left, the FBA-samples are shown in red; on the right, the PB-samples are shown. The black box illustrates the region that was cut during the experiments; the brown area shows the leftover area that was not cut. The ore boundaries were coded into a regular MinePlan block model. This block model was then exported as a CSV file for further processing in R-Studio.
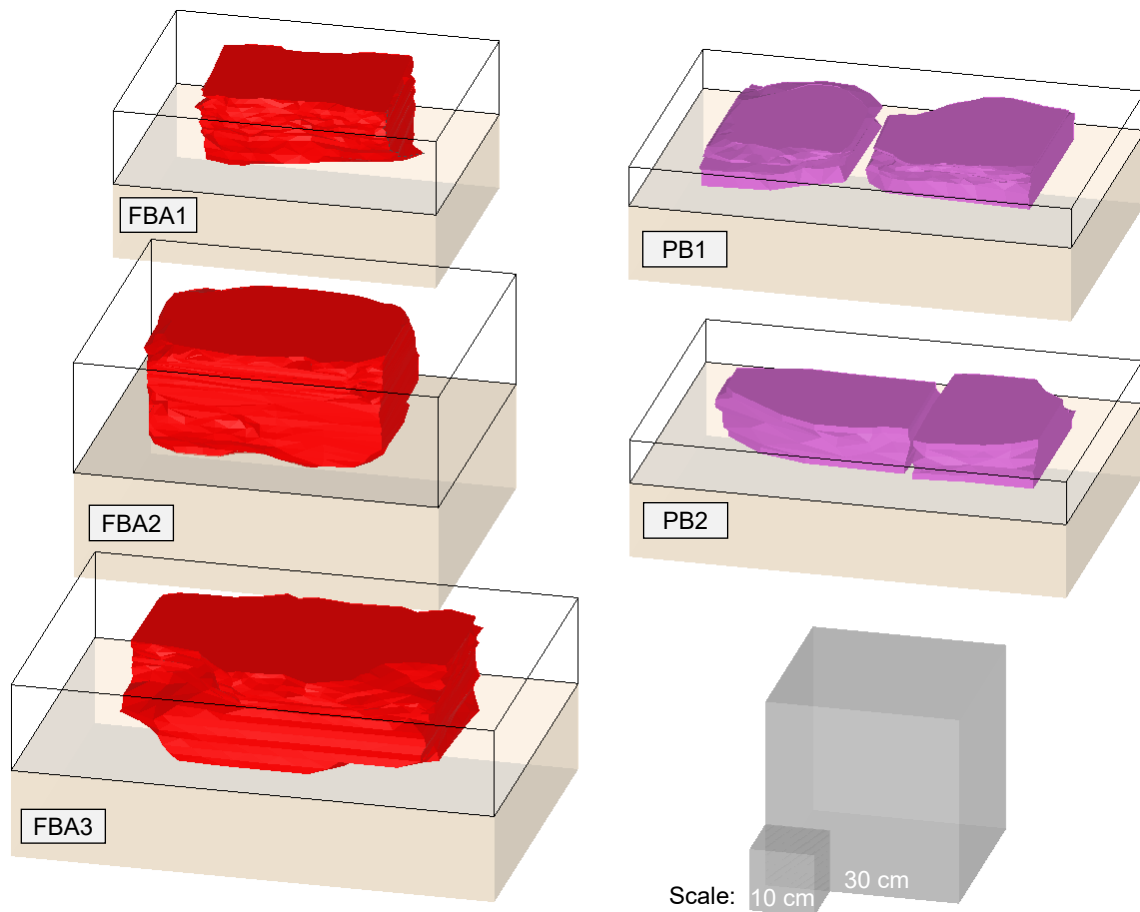
Figure 50: 3d-models of all specimens created from the photographic documentation, grey cubes for size reference

5.8 Block Modelling and Gridding

Block models are a core tool in mine planning. They represent a digitised simplification of the deposit model. In environmental sciences, similar techniques are used to create spatial models of, for example, toxicant distribution. In this work, a similar approach is used to model the spatial distribution of features for machine learning classification. Normally, the values stored in the block model are interpolated from sparse data (drill holes, sampling face sampling, etc.). Here, dense, continuous, but noisy information is available. Therefore, standard interpolation routines are not useful. Here, dense data must be simplified without losing the required information value. This is solved through a spatial moving search radius solution. Figure 51 shows a visualisation of the modelling process. Panel a) shows how the data of three subsequent cuts would lie in relation to the referenced images. Panel b) shows the same situation with the digitised rock boundaries.

Panel c) shows a block model laid over this situation. The block model already is coded with the rock types concrete (grey) and fluorite ore (brown). The blocks (also called grid nodes) are spaced 10 mm, both for 2d- and 3d-uses. The algorithm now calculates the descriptive statistics for all blocks from all input data points that are within the *search radius (SR)* of each respective block. An *SR* of 100 mm is used if not stated otherwise. This *search radius* is visualised by the teal sphere in the panel. A block model can have ca. 50,000 individual blocks; the algorithm performs the process for each block.
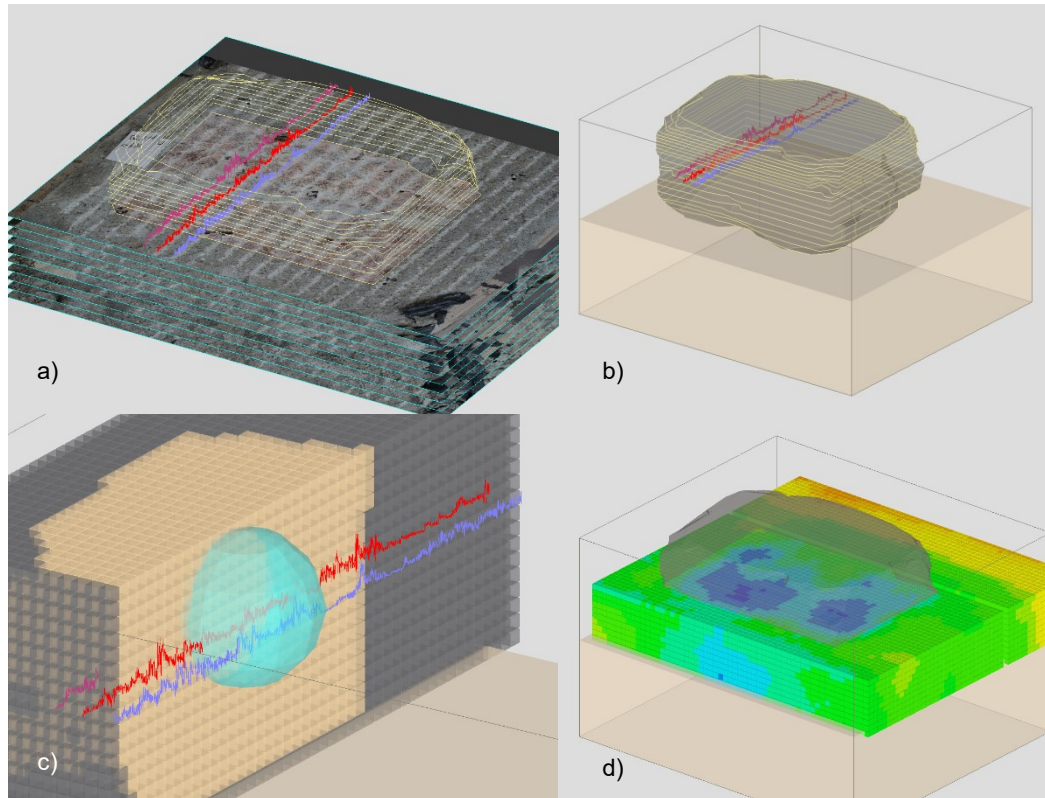
Figure 51: Visualisation of block modelling procedure, explanation in text

This means that the *search radii* of neighbouring grid points overlap each other. The result is a smoothed appearance of the gridded result, similar to a Gaussian filter used in digital image processing. The combination of grid spacing and *search radius* has been chosen as the result of three supervised theses related to this topic [165, 171, 172].

Additionally, a filter was applied to remove blocks that were too disturbed by the pick having only limited contact with the rock. As such, erroneous data were filtered out. For this filter, the *contact ratio* (*CR*) was formulated:

$$CR = \frac{n_{dp}(F_z < 0.5\ kN)}{n_{dp}} \qquad (20)$$

Where n_{dp} is the number of data points within the *search radius*; $n_{dp}(F_z < 0.5\ kN)$ denotes the number of data points within the *search radius* where F_z is less than 0.5 kN. During the creation of the feature block models, a filter of *CR* > 0.55 was used to filter out blocks that were highly disturbed by the pick being in the air. The used threshold of 0.55 was chosen by qualitative assessment among the values 0.45, 0.5, 0.55, 0.6 and 0.65.

A simple divide-and-conquer algorithm was used to calculate the features stored in the block model. Without this, the algorithm would have to calculate the 3d Euclidean distance of every grid point to every data point. For sample FBA3, this would be ca. 50,800 grid points and ca. 2.45 million data points. This would result in 125 billion combinations to compute. This process can take up to 4 h. The divide-and-conquer algorithm divides the spatial space into *n* subsets. Figure 52 illustrates this algorithm with a simple example. Given a regular grid of points with 38 × 40 points, we compute the number *n* of grid points within a *search radius* for each grid point. In this example, it would result in 2.3 million operations without divide-and-conquer. With divide-and-conquer, the area is divided into three equal parts along one axis. In the example, each subset now holds 1/3 of the total points. Each of the points now only has to be compared to the other points of the subset <u>plus</u> those points of the neighbouring

subset whose distance from the border of the subset along the dividing axis is smaller than the *search radius*. The example has a spacing of the grid points of four units and a *search radius* of ten units. This means that instead of calculating 2.3 million combinations, only 0.9 million combinations must be calculated.
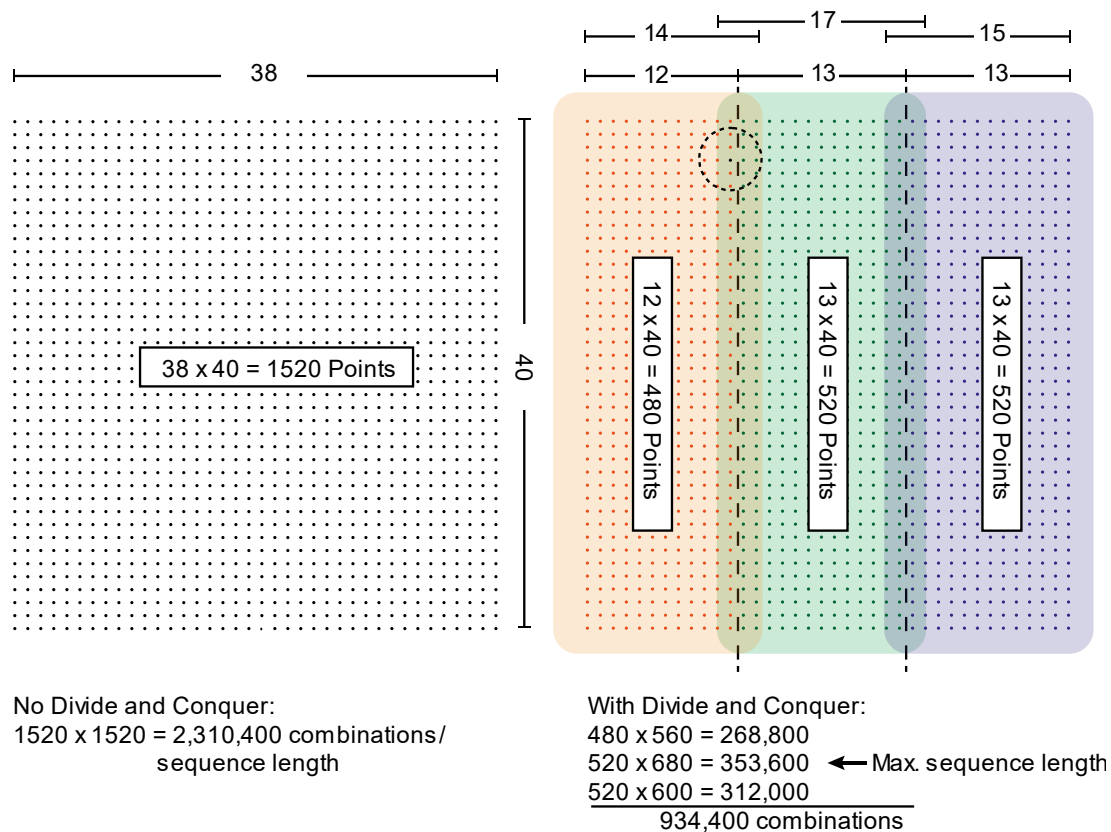
Figure 52: Principle of divide and conquer algorithm in this work, dotted circle – search radius

Furthermore, the calculations on the three subsets can be executed in parallel, which means that the number of calculations defining the computation time equals the maximum number of combinations in the subsets (353,600). This would reduce the computation time to ca. 15% compared to the standard algorithm.

In this work, the spatial space was divided into eight subsets along the x-axis, and calculations were carried out in eight parallel threads.

The block model was populated with the following data:

- Coordinates of the block (x-, y-, z-coordinates)
- FCR-features for material classification
- Contact Ratio
- True rock type
- Mean values of raw forces (F_x, F_y, F_z, F_{res}) if required

5.9 Correlation Analysis

Correlation analysis is a statistical method to evaluate the strength of a correlation between two variables. Hereby, high correlation means that two variables have a strong relationship with each other. A weak correlation means that the variables are hardly related [173]. Correlation analysis can be

conducted using either Pearson, Spearman, or Kendall algorithms. Pearson correlation analyses the correlation based on the assumption of a linear relationship. The Pearson correlation is used to explore the data correlation in Figure 22, p. 26. It is calculated with the following formula.

$$R = \frac{cov(A, B)}{\sigma_A \sigma_B} \tag{21}$$

Where: A and B are a pair of random variables; σ_A and σ_B is the standard deviation of A and B, respectively; cov is the covariance.

The other two correlation coefficients represent rank correlation analysis. As such, they calculate the correlation for a monotonous correlation function [174]. Due to their nature, they are resistant to outliers and do not require a linear relationship. For the main part of this work, the *Spearman correlation coefficient* (R_s) is used. It is calculated using the following formula:

$$R_s = 1 - 6 \frac{6 \sum dr_i^2}{n(n^2 - 1)} \tag{22}$$

Where dr is the difference between the two ranks of each observation and n is the number of observations. To test for statistical significance, the *p-value* was compared to the significance level of 0.01. All tests were performed using the statistical core functions and the package psyche of R [175]. The code can be found in Annex O.

5.10 Regression Analysis of Effect

Linear regression is performed to estimate the influence of the parameters s and d on the force levels for Experiment GN.

$$f(s, d) = b_0 + b_1 s + b_2 d \tag{23}$$

Hereby, $b_0, ..., b_2$ are the regression coefficients. For the regression, an intercept with the y-axis $b_0 \neq 0$ was allowed. This allows a minimum cutting resistance to occur when the cutting parameters are very small (<1 mm). This analysis is only possible for the special case investigated in this work where:

a) a linear relationship is assumed,
b) it is assumed that no interaction between s and d occurs, and
c) s and d share the same unit.

There, the coefficients b_1 and b_2 answer the question: "An increase of s or d by one mm increases $f(s, d)$ by how many kN when the other parameter remains fixed?" [176]. Then, the *relative contribution* (c_{rel}) of s and d can be calculated as follows:

$$s: c_{rel} = \frac{b_1}{b_1 + b_2} * 100 \; ; d: c_{rel} = \frac{b_2}{b_1 + b_2} * 100 \tag{24}$$

Note that b_0 is excluded for the calculation of c_{rel} because it does not influence the relative change of $f(s, d)$ when one of the parameters is varied. For this analysis, only the mean forces are analysed.

5.11 Machine Learning

This chapter describes the foundations and explains the specifications of the three used machine learning classification algorithms:

- unsupervised k-means (KM) algorithm, and the two supervised algorithms
- distributed random forest (DRF), and
- artificial neural network (ANN).

The R package "H2O" was used for the machine learning part. It implements an application programming interface (API) to the H2O software. H2O is a machine learning framework optimised for big-data applications that allows fast calculation speeds through parallelisation and in-memory computing while retaining a certain user-friendliness through the use of an API [166]. Its calculation speed is the reason it was preferred over the non-parallelised package Neuralnet that was used for the preliminary ANN analysis in Annex K. All codes for the algorithms were implemented using R-Studio and can be found in Annex O.

The first algorithm is part of the group of unsupervised clustering algorithms. It automatically assigns data points to a number of *k* clusters, where *k* can be defined by the user or approximated automatically. The assignment is performed by minimising Euclidean distances within the feature space.

The latter two algorithms belong to the group of supervised learners. Here, they are only used as classifiers, although they can also be used for regression problems. The distributed random forest is an extension of the decision tree algorithm. Where a regular decision tree algorithm finds one hierarchical set of rules to divide a dataset into classes, the DRF algorithm uses multiple less complex decision trees that form an ensemble and together decide on the class of a particular data point by majority voting.

Artificial neural networks, in general, are following the basic principles that biological neural networks also follow. A piece of information is passed as a signal between different neurons. At each neuron, the input signals are summed up with regard to their individual weights and integrated into an output signal that goes to further neurons. In this work, a feedforward ANN with backpropagation is used. There, the information flow is unidirectional from input to output. During training, the weights of the individual neurons are varied until the classification error is minimal.

The specifics of the three algorithms are explained in the following subsections. Other important parameters used are as follows.

Standardisation

All features were standardised before serving in the algorithms. Standardisation is the process of converting the features into a distribution space with a *mean* of 0 and *standard deviation* of 1 after the following formula:

$$x_{si} = \frac{x_i - \bar{x}}{\sigma} \tag{25}$$

With x_{si} – the standardised value of measurement; x_i – the individual measurement value; $\bar{x}$ – the empirical mean of values; σ – empirical standard deviation of values.

<u>Training and Validation Split</u>

For the training of supervised algorithms, the dataset has to be split into training and validation data to balance the overfitting and generalisation behaviour of an algorithm. The part of a dataset that is used to train the actual machine learning algorithm is called training split or training data.

The part of the original dataset used for evaluation of the training success is called validation data or validation split. It is withheld during training. The trained classifier is then applied to the validation data. The classification performance on the validation data is usually lower than on the training data, but the performance on the two data subsets should be similar. If the performance is much higher on the training data than on the validation data, then the classifier probably overfits. The training-validation split ratio can be varied to optimise the generalisation behaviour. This is investigated during the case study.

<u>N-Fold Training</u>

Normally, when training a machine learning classifier. The dataset is split into training and validation data. The learner is trained on the training data, but its performance is evaluated on the validation data to avoid overfitting. If the available data are limited, n-fold training and cross-validation can be used. Here, that dataset is split into n parts. In this work, $n = 5$ was used. Each of the five parts comprises 1/5 of the total data points. The training is then repeated five times. Each time with another of the five parts of the data.

Consequently, each of the five training results is validated on the other four $(n-1)$ parts that were not used for the training. This results in five trained models and validation results. The validation results are called cross-validation (CV) results. The algorithm then chooses the model with the lowest CV error.

5.11.2 K-Means Algorithm

Generally, k-means clustering calculates the Euclidian distance of each data point to each cluster and then assigns each point to the closest cluster. After the assignment, the centre of gravity for all points assigned to a cluster is calculated. These centres of gravity become the new cluster centres for which the Euclidian distance is calculated again. Hence, the process is an iterative process that stops when no further optimisation or change between subsequent iterations happens. An example where the *number of clusters (k)* equals three, and two features, can be seen in Figure 53 [177].
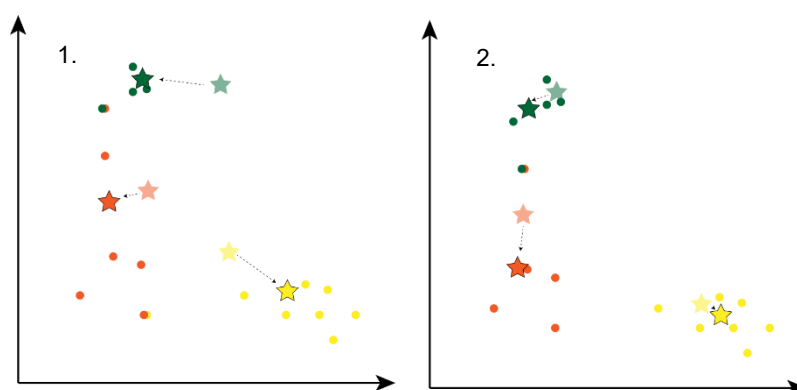
Figure 53: Visualisation of k-means clustering algorithm for two iterations

Before an iterative optimisation of the cluster positions can be done, the starting positions of the clusters must be chosen. In this work, the following approach was used. First, k is chosen and is usually equal to the number of expected rock types. The algorithm works as follows:

1. Choose one data point to be the *first cluster centre* (m_1) at random.
2. Calculate the difference between m_1 and each of the remaining $n-1$ observations.
3. Choose the next *cluster centre* (m_2) to be the data point with the maximum distance to m_1.
4. For the next *cluster centre* (m_3), the distance to all already chosen *cluster centres* is calculated and considered.
5. Repeat until all k centres have been chosen.
6. The algorithm calculates the difference between each observation x_i and each of the centres $m_1,...,m_k$, where difference is the squared Euclidean distance d_E taken over P parameters.

$$d_E(x_i, m_k) = \sum_{j=1}^{P}(x_{ij} - m_k)^2 = \|x_i - m_k\|^2 \qquad (26)$$

7. Next, all x_i are assigned to the cluster that minimises $d_E(x_i,m_k)$. When all observations x_i are assigned to a cluster, the mean of the points in the cluster is calculated as follows:

$$\bar{x}(k) = \left\{\overline{x_{\iota 1}}, ... \overline{x_{\iota p}}\right\} \qquad (27)$$

The term $\overline{x_{\iota 1}}, ... \overline{x_{\iota p}}$ is the mean for all observations for each of the respective parameters.

8. Lastly, $\bar{x}(k)$ is set as the new cluster centre m_k. The steps 6.–8. are repeated until the cluster assignments of the x_i are stable [166, 178].

For the case study, a variation of the initial assignment of clusters was implemented. Since the true rock types were known, the initial cluster positions m_k were set after Equation (27). Thereby $\overline{x_{\iota 1}}, ... \overline{x_{\iota p}}$ corresponded to the mean of the parameters for the rock types. This resulted in a variation of the k-means that could be defined as semi-supervised. However, the algorithm itself does not compare the true rock class to the cluster assignments.

5.11.3 Artificial Neural Networks

The authors of the Neuralnet package that was used for the preliminary assessment in Annex M define artificial neural networks as follows:

"In many situations, the functional relationship between covariates/[features] (also known as input variables) and response variables (also known as output variables) is of great interest. [...]. Artificial neural networks can be applied to approximate any complex functional relationship. [...]

They are in particular direct extensions of [generalised linear models] and can be applied in a similar manner. Observed data are used to train the neural network and the neural network learns an approximation of the relationship by iteratively adapting its parameters." [179]

Generally, an ANN, also called a multi-layer perceptron, is composed of artificial synapses. Its structure is similar to that of a biological neural net—but much simpler. The synapses are organised in layers that can be classified as in Figure 54 into:

- the input layer,
- the hidden layer(s),
- the output layer.

The synapses in the input layer (I) receive the input data, the features. The neurons in the output layer (O) calculate the final results. The synapses between input and output are called hidden layers, as they are not directly assessable. The majority of the calculations happens in the hidden neurons (H). The input data can be seen as signals passing through the neural net. A weight is attached to each of the hidden and output synapses, indicating the effect of the synapse. This weight is also called the intercept neuron (B). At each synapse, the signals are first processed by an integration function that combines all input signals. The activation function transforms this combined signal and passes it on to subsequent synapses or forms the output. The numbers in the grey boxes in Figure 54 denote the architecture of the respective neural net. The first number denominates the number of input neurons. In this example, eleven. It equals the number of features used. The last number defines the number of output layers. In this case, one, because the neural network only has to make one decision: "Concrete" or "Ore". The numbers in between define the hidden layers. In this work, each neuron is connected to all neurons of the subsequent layer.
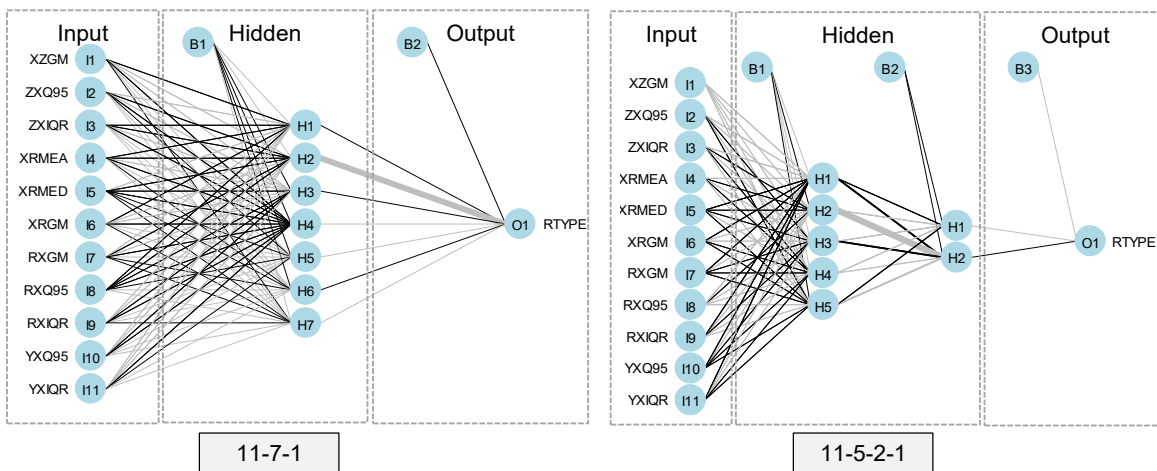
Figure 54: Visualisations of two neural networks used in this work; grey lines: negative connection weights, black lines: positive connection weights, line thickness: relative connection value

Each neuron calculates the integration function after Equation (28).

$$g(z) = w_0 z_0 + \sum_{i=1}^{k} w_i z_i \qquad (28)$$

Here, w_0 is the weight of the intercept neuron, z_0 is the value of the intercept neuron, w_i are the weights of the respective input neurons and z_i are their output values. As the activation function, a rectifier function was used:

$$z(g) = \max(0, g) \qquad (29)$$

Here, $z(g)$ denotes the output to be given to the next synapses, and g is the input after integrating the input with Equation (28). Rectifier functions show advantages over classic sigmoid- and tanh-activation functions in terms of training speed and are the most commonly used activation function as of 2018 [180, 181]. The ANN is fitted to the training data by varying the weights of the individual neurons and the static intercepts so that the error between prediction and model is minimised. To evaluate the error of the model during learning, an *error function EF* is calculated. For this, the sum of squared errors is calculated:

$$EF = \frac{1}{2} \sum_{h_{io}=1}^{H_{io}} \sum_{h_o=1}^{H_o} \left(o_{h_{io}h_o} - y_{h_{io}h_o} \right)^2 \qquad (30)$$

Here, $h_{io} = h_{io},...,H_{io}$ indexes the given input-output pairs and $h_o = h_o,...,H_o$ the output nodes; o and y denote predicted and true values, respectively.

The training of the neural network is an iterative process. After each iteration, the weights of the neurons are adjusted until EF reaches a stopping criterium. The stopping criterium used, was that EF does not improve anymore for at least 5 iterations.

As a learning algorithm, the stochastic gradient descent with backpropagation was used. It calculates the gradient of EF with respect to the weights *(dEF/dw)* as shown in Figure 55. Hereby a minimum is attempted to be found. When the derivative is negative, the *weight w_i* is increased for the next iteration *(w_{i+1})* and vice versa. As such, a local minimum of the error function can be found. The process modifies the weights until the stopping criterium is reached. As a prerequisite, the input data are standardised after Equation (26).
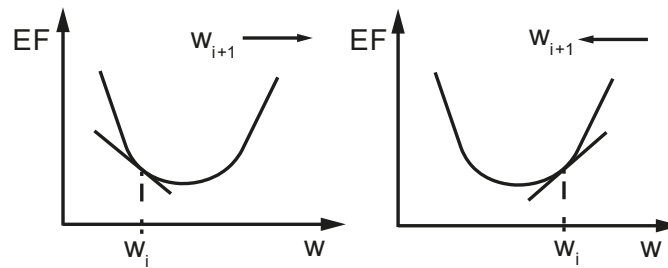
Figure 55: Principle of backpropagation algorithm for a univariate error function after [179]

Generally, the number of neurons and layers used depends on the complexity needed [179]. Adil et al. (2020) tested neuron amounts between 2 and 300 and 1, 2 and 3 hidden layer designs predicting the properties of different concrete mixtures. They obtained good results for two hidden layer designs. The best performing design was a 17-50-30-5 design ($R^2 = 0.98$), but also the 17-2-5 design provided an R^2 of 0.91 [182]. Olden (2004), in his study comparing his method of calculating the importance of covariates, received a 5-5-1 design as being optimal [183]. Tiryaki (2008) used a 3-3-2 network to predict *UCS* and *E-Modulus* from cone indenter, *density*, and *shore hardness* values [150]. For crack propagation in wood, Samarasinghe et al. (2007) obtained a 9-23-1 network to perform optimally [184]. Hecht-Nielson (1987) showed, based on Kolmogorov's mapping neural network existence theorem, that a number of hidden neurons of $2n+1$ in one hidden layer can implement any *n*-dimensional problem; where *n* is the number of input covariates [185]. Others, such as Kaunda (2016), followed this [151]. However, Hecht-Nielson's approach is based on the consideration that the covariates are independent of each other. A fact that is rarely given in the context of rock and material parameters. Heaton summarises multiple rules of thumb for a first approximation of the number of neurons in neural networks. They should a) be in between the size of the input layer and the size of the output layer, b) be around 2/3 the size of the input layer plus the size of the output layer, and c) be less than twice the size of the input layer [186].

Feature Importance

Neural networks are often seen as black boxes because the exact calculations within the neural net are complex to analyse. The main point of interest is the *feature importance* of the different input variables on the classification result. Multiple solutions to this problem exist: Garson's algorithm, further modified by Goh, the method of partial derivatives, input perturbation, sensitivity analysis after Lek, as well as Gedeon's method [183, 187]. The *H2O*-package uses Gedeon's method to calculate the *feature*

importance. This method considers the weights that connect the input features to the first two hidden layers [188]. As such, it is computationally fast while sacrificing some accuracy.

5.11.4 Distributed Random Forest

Distributed random forest is an effective classification and regression method that constructs a forest of classification or regression trees rather than a single tree. In this work, the method was used only for classification. Figure 56 shows a simple example for a single classification tree. The diagram on the left shows an example with two numerical features, *x* and *y*. The data points belong either to Class 1 or 2. The colour-shaded areas show the true (unknown) classes. Based on the sampled dataset, the decision tree splits the data into two groups in a way that minimises the misclassification error. In the example, three data points are misclassified (black circles). On the right side of Figure 56, the decision tree heuristic that corresponds to the classification on the left is shown.
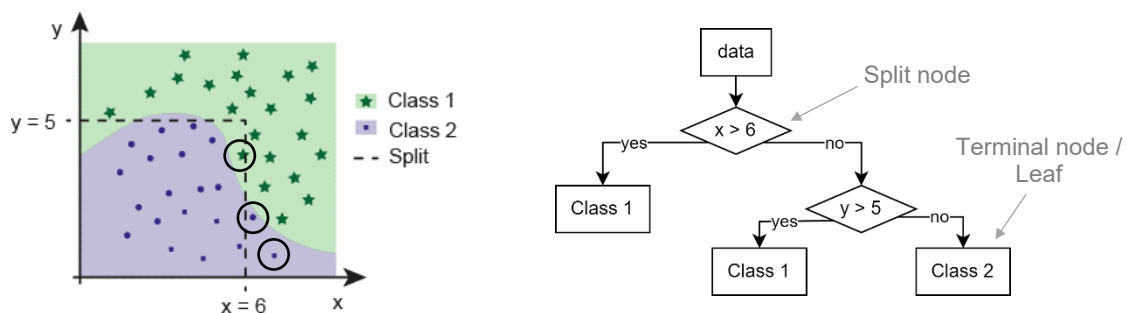
Figure 56: Simple example for decision tree

As shown in Figure 56, DRFs consist of split nodes that make the actual decision, and terminal nodes that define the final decision outcomes. Terminal nodes are also called leaves.

DRF avoid overclassification by incorporating many (weak) learners; hence belong to the group of ensemble learners. Another aspect is that all learners can be trained in parallel, adding to computational speed. The DRF trains a collection of decorrelated decision trees and obtains a class vote from each tree. It then uses the majority from all votes to generate a final prediction. The *variance* of the decision is reduced when more trees are constructed. DRF shows similar performance to gradient boosting (another extension of decision trees), but are simpler to train and tune. As such, they are widely used and are implemented in a variety of packages and softwares [166, 177, 189].

The distributed random forest algorithm works as follows [177]:

1. For each tree (*n=1,…,N*), do the following:
   a. Draw a bootstrap sample and create the first terminal node that contains all data.
   b. On the sample repeat the following procedure for each terminal node until a stopping criterion is reached:
      i. Select $m = \sqrt{P}$ features; with *P – Number of features*.
      ii. From all *m*, select the variable and the split-point that allows the best split.
      iii. Split the node according to ii. into two new terminal nodes.
2. Output the ensemble of the trees.

A more detailed description of the DRF algorithm can be found in Hastie et al. (2017), Chapter 15.2 [177].

The most important parameters of the used DRF algorithm are:

Number of trees:

Defines how many trees form the "forest". More trees reduce *variance* but increase calculation time. In this work, 100 is used.

Maximum tree depth:

The maximum number of split node levels that a tree can have. The deeper the tree, the more complex it is. This can increase *accuracy* but also overfitting behaviour.

In this work, 11 is used.

Sample rate:

Each tree is trained with a portion of the data. The default value of 0.632 was used.

Column sampling rate:

Defines the number of features from which can be chosen for each split. The standard value was used: the square root of the number of features.

Feature Importance

The *feature importance* is assessed by measuring the improvement in the split-criterion at each split for each tree and each variable. It is accumulated independently for each variable across all the trees in the forest. The importance values are then standardised. The result is called *standardised feature importance*.

5.11.5 Classification Success

To estimate the classification success of a classifier, multiple measures can be used. The most important parameters are *specificity*, *sensitivity*, *accuracy,* and *error rate*. Figure 16 shows these values on a confusion table. This table compares the *predicted class* (PC) to the *real class (RC)* to which a data point belongs. The example comprises three different classes.

Table 16: Example confusion matrix with three classes

		real class (RC)			
		A	**B**	**C**	
predicted class (PC)	**A**	AA (TC)	AB (FC)	AC (FC)	Specificity$_A$
	B	BA (FC)	BB (TC)	BC (FC)	Specificity$_B$
	C	CA (FC)	CB (FC)	CC (TC)	Specificity$_C$
		Sensitivity$_A$	Sensitivity$_B$	Sensitivity$_C$	Accuracy / Error

As shown in Equation (31), the *sensitivity* for a given class is defined as how many cases truly belonging to a class were identified correctly:

$$Sensitivity_i = \frac{TC_i}{RC_i} \tag{31}$$

Hereby, TC_i is the number of true classifications for a given class i, and RC_i is the number of total observations belonging to that class.

Opposing to this is the *specificity*, as shown in Equation (32). It is defined as the answer to the question: "From all classifications belonging to a class, how many do really belong to that class?"

$$Specificity_i = \frac{TC_i}{PC_i} \tag{32}$$

Here, TC_i is the number of true predictions for a given class i and PC_i is the number of total observations predicted as belonging to that class.

The *accuracy* then is a measure that summarises the overall performance across all classes after Equation (33).

$$Accuracy = \frac{\sum_1^i TC_i}{N}; \; Error = 1 - Accuracy \tag{33}$$

It is the sum of all true predictions TC_i across all classes divided by the total number of cases *N*. Vice versa, the error of the classifier is the opposing element to the *accuracy*.

As already mentioned in Section Training and Validation Split on p. 65, the *accuracy* can be related to the validation and the training data. It is then called *training accuracy* or *validation accuracy,* respectively. For n-fold training (s. Section N-Fold Training, p. 66), the *cross-validation accuracy*

(*CV-accuracy*) is computed. It defines the *accuracy* between the *n* training and validation sets during n-fold training.

For the case study, two nonstandard versions of the *accuracy* are used. When a learner is trained on a portion of a dataset and then classifies another dataset, it is called *cross-accuracy* in this work.

When the learner is trained on a fraction of a dataset and then used to classify this full dataset, including the training data, it is called *self-accuracy* in this work.

Although this is not a standard approach, it is used here because the objective is to show the spatial distribution of the classification results. If the training data were not used for classification, they would not appear in the spatial analysis. As such, *self-accuracy* represents the combination of *training* and *validation accuracy*. The case study shows that the difference between *self-accuracy* and *validation accuracy* can be estimated at 0.5%, which is considered negligible for the quality of the results. As such, this procedure is considered valid.

5.11.6 Boundary Layer Recognition Precision

For 2d-cases, the *precision* of the estimating the boundary between two rock types is evaluated. Figure 57 illustrates this method. For each row of y-coordinates, the maximum x-value for a zone is extracted. The x-coordinates of these points are then compared to the x-values of the real boundary. Then the absolute value of the x-deviation between the predictions and the true boundary is calculated. As a result, the row-wise deviation between classification and true rock type is obtained. Then the *mean* and *standard deviation* are calculated to quantify the *precision*. In the investigated cases, the maximum of the preceding zone is in contact with the minimum of the succeeding zone. Therefore, this approach is possible.
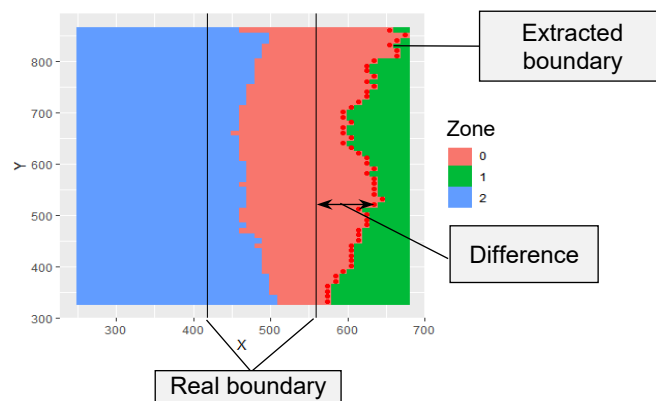
Figure 57: Scheme for estimation of boundary layer detection precision

5.12 Machine Learning Case Study

The workflow for the machine learning case study consists of twelve steps in total. These steps comprise methods that are explained in detail throughout Chapter 5. The workflow presented here summarises these methods and puts them into perspective. Figure 58 shows the workflow.

In the first step, photos are taken from each layer. The photos are then corrected (Nr. 2) and referenced to the coordinate system of the cutting machine. From these referenced photos, the lithology of the samples is reconstructed layer by layer. Steps 1–4 are described in detail in Chapter 5.7. Then, the rock types are coded into a block model (Nr. 5) which is exported into R-Studio (Chapter 5.8).

The cutting force data (Nr. 6) obtained from the experiments are organised in a Flexpro database (Nr. 7). There, a preliminary data integrity check is conducted (for details see Annex G). In the 8th step, the data are exported to R-Studio, filtered, and processed to obtain the raw real-time FCRs (Chapter 5.4).

In the 9th step, the raw FCRs from the 8th step are used to populate the block model from the 5th step with the features. The features are calculated with a spatial moving-window approach as described in Chapter 5.8. Also, the *contact ratio* is computed into the block model.

In the 10th step, the actual training is conducted with the three different machine learning classification algorithms. The results are stored for further reference (Nr. 11), and the classification success is evaluated as explained in Chapter 5.11.5.
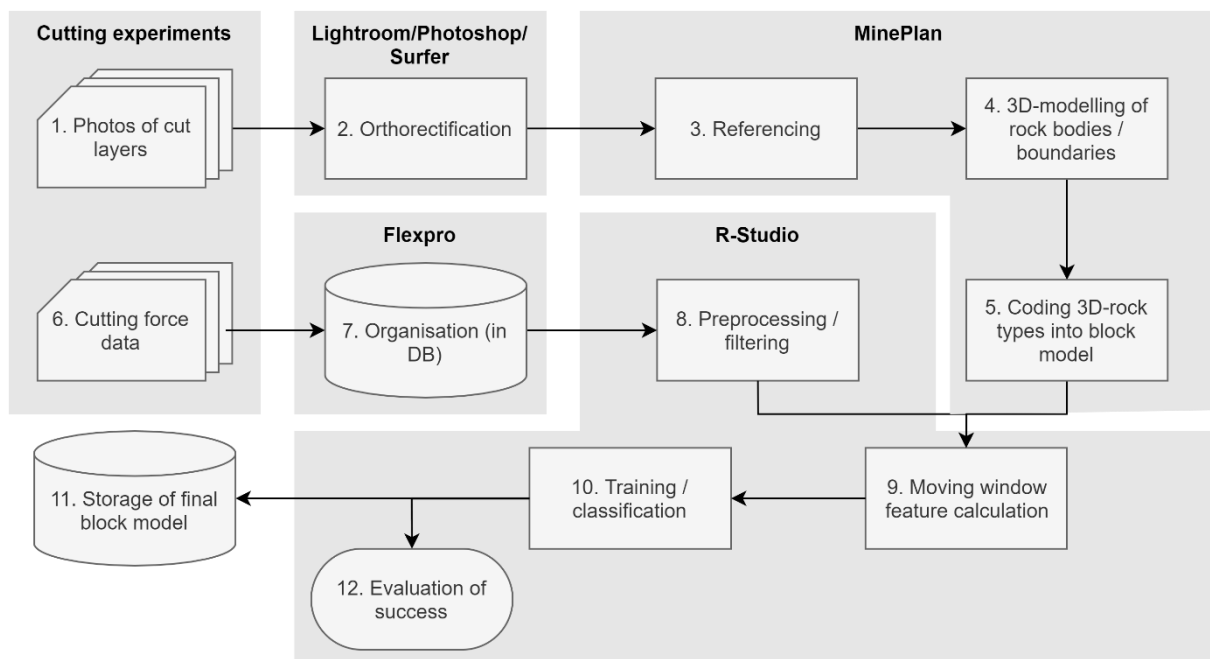
Figure 58: Workflow machine learning analysis (case study)

6 Results

This chapter shows the results of the five experiments. First, the results from the major Experiment CO are shown. There the influence of changing material toughness is investigated. In Experiment GN, the influence of directional anisotropy is investigated. In Experiment GR, the influence of cracks is shown. These findings lead to the final case study with the Experiments FBA and PB, where a machine learning case is used to differentiate between different rock types.

6.1 CO – Zoned Concrete

This chapter describes the results of Experiment CO. First, a qualitative assessment and descriptive statistics are presented to show the characteristics of the data. Based on the findings from the descriptive statistics, a procedural algorithm is presented to pre-classify all possible FCR-based features towards their prediction suitability. This is followed by a correlation analysis, which gives further insights into the results. From this, a k-means algorithm is used to classify the investigated rock mass with different sets of possible features. A precision evaluation of the different sets of features follows. To validate the findings from the k-means analysis, a feature importance analysis with a distributed random forest algorithm is conducted as a last step.

6.1.1 Descriptive Statistics

This section describes the basic aspects of the experiments. Figure 59 exemplarily shows a boxplot visualisation for sample CO2. The results for CO1 are located in Annex J.1.

The Panels a)–d) show the results for the forces F_x to F_{res}. The results for sets 1–9 are shown in each panel. The cutting parameters behind the sets are also stated in the figure. The results for each set are separated by the concrete zone in which they occurred. This allows an assessment of differences in the forces depending on cutting parameters and the concrete type. Unlike in standard boxplots, the whiskers show the quantiles $Q_{0.05}$ and $Q_{0.95}$.

It can be seen that with increasing zone toughness, all force components increase. Tendentially, a higher set number also coincides with higher forces. The exception to this is F_y for Sets 6 and 9. These sets show a *side force s*lightly above 0 kN. This follows expectation because the *side force* generally decreases as the *spacing* increases. The mean *side force* is theoretically 0 kN during the fully blocked cuts and only oscillates in both directions[16]. Irrespective of the cutting parameters, the mean forces for F_x vary from 1.03 to 4.91 kN for Zone 1, from 2.14 to 7.77 kN for Zone 2 and from 4.71 to 13.45 kN for Zone 3 over all cutting parameters. The behaviour of F_z and F_{res} is similar. It can be seen that as the mean forces increase, so does the variation and $Q_{0.95}$. Furthermore, the minimum values ($Q_{0.05}$) increase to a much lesser extend.

To summarise, the raw forces are influenced by the cutting parameters and the concrete zone. Because of that, a clear allocation of the forces to the concrete type—irrespective of the cutting parameters— seems not possible. As expected, descriptive statistics of raw force signals probably cannot be used to differentiate between adjacent concrete zones.

---

[16] When the pick is symmetrical and is arranged in a *tilt angle* of 0°
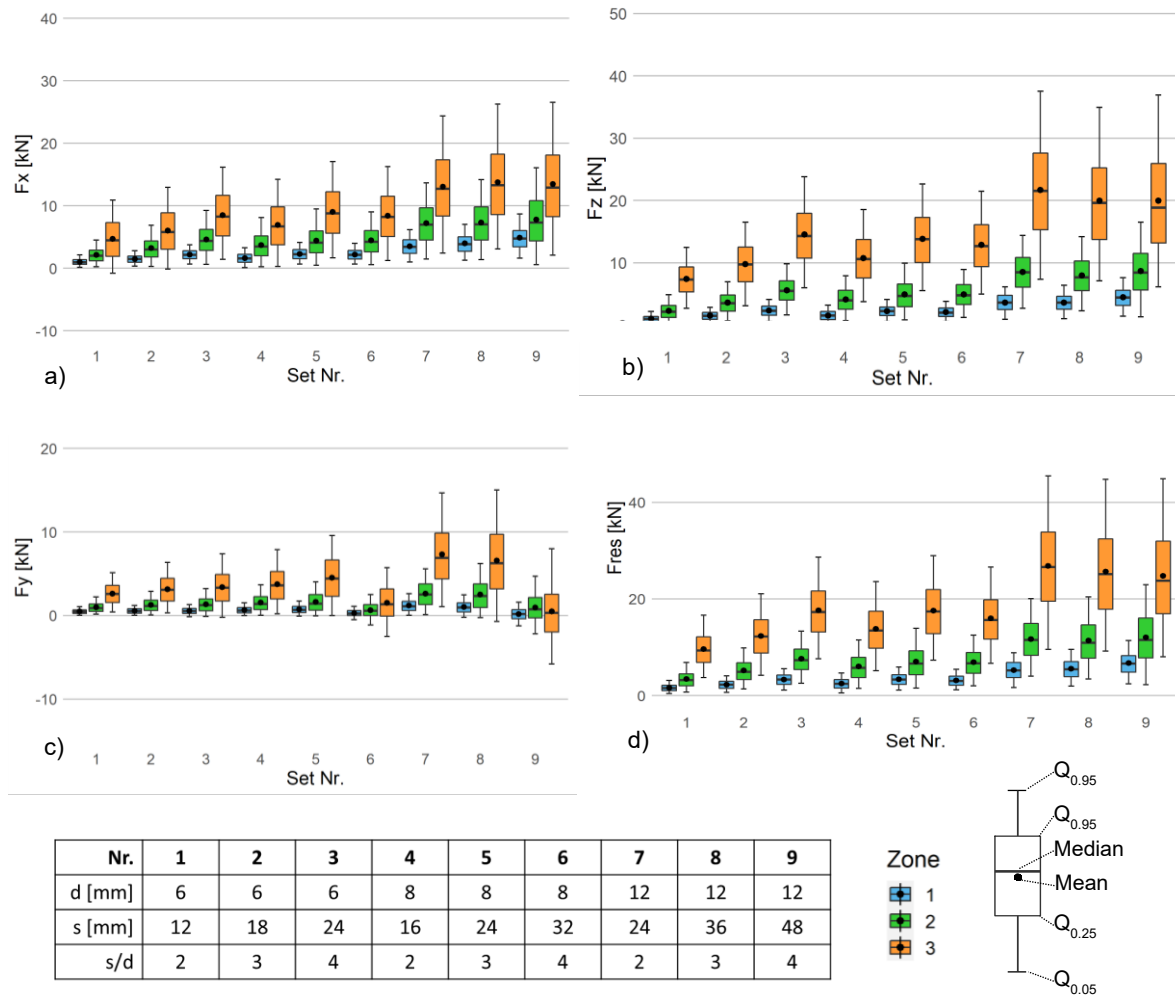
Figure 59: Boxplots of cutting force results of Experiment CO2

6.1.2 Procedural Evaluation

As described in Chapter 5.6, the differences between the value corridors for the concrete zones as formed by descriptive statistics of FCR are calculated. When the value corridors overlap, either the classification U – "unsuited" or P – "partially suited" is assigned. P is assigned if the value corridors of Sets 3, 5, and 7 do not overlap while the corridors for all sets overlap. S – "suited" is assigned when no overlap occurs at all. The numerical calculation results of the selection algorithms are located in Annex J.2.

Table 17 shows the evaluation results for the individual Blocks CO1 and CO2. It shows the combinations of the FCR and the respective statistical descriptors that were evaluated. For CO1, 17 parameters were classified as suited, and another 16 were classified as partially suited. The rest was classified as unsuited. For CO2, the individual results show a slightly different picture. Here, only 11 parameter combinations were suited. Another 12 were partially suited, and the rest was unsuited.

It can be seen that the general picture between CO1 and CO2 is similar. Since CO1 consists of only Zone 2 and 3, more parameters passed the overlap analysis algorithms. This is because a) only one zone difference occurred and b) the two zones differ relatively strongly in their toughness. For CO2, the limiting factor is the small difference in hardness between Zones 1 and 2 (7.7 MPa *cUCS*). As such, fewer features pass the assessment procedure for CO2.

Table 17: Results of the procedural feature selection algorithm for CO1 and CO2 separately

CO1

	F_x/F_z	F_z/F_x	F_x/F_{res}	F_{res}/F_x	F_z/F_{res}	F_{res}/F_z	F_y/F_x	F_x/F_y	F_y/F_z	F_z/F_y	F_y/F_{res}	F_{res}/F_y
$\bar{x}$	S	P	S	P	P	S	U	U	U	U	U	U
$\tilde{x}$	S	P	S	P	S	S	U	U	U	U	U	U
$\bar{x}_{geom}$	S	S	S	S	S	S	U	U	U	U	U	U
$Q_{0.95}$	P	S	P	S	U	P	P	U	U	U	U	U
IQR	U	S	P	S	U	P	P	U	P	U	U	U
v	U	U	U	U	P	P	U	U	U	P	U	U

CO2

	F_x/F_z	F_z/F_x	F_x/F_{res}	F_{res}/F_x	F_z/F_{res}	F_{res}/F_z	F_y/F_x	F_x/F_y	F_y/F_z	F_z/F_y	F_y/F_{res}	F_{res}/F_y
$\bar{x}$	P	P	S	S	P	U	P	U	U	U	U	U
$\tilde{x}$	P	U	S	P	U	U	U	U	U	U	U	U
$\bar{x}_{geom}$	S	P	S	S	U	U	U	U	U	U	U	U
$Q_{0.95}$	U	S	U	S	U	U	P	U	U	U	U	U
IQR	P	S	U	S	P	P	S	U	U	U	U	U
v	U	P	U	U	U	U	U	U	U	U	U	U

Table 18 shows the final classification results of the procedural analysis. For the assembly of this table, the worst result from both CO1 and CO2 were merged. As such, the results can be viewed as conservative. Nine criteria were suitable, and another twelve were classified as partially suitable; 51 criteria showed overlaps and were rejected.

Table 18: Results of the procedural feature selection algorithm for CO1 and CO2 together

	F_x/F_z	F_z/F_x	F_x/F_{res}	F_{res}/F_x	F_z/F_{res}	F_{res}/F_z	F_y/F_x	F_x/F_y	F_y/F_z	F_z/F_y	F_y/F_{res}	F_{res}/F_y
$\bar{x}$	P	P	S	P	P	U	U	U	U	U	U	U
$\tilde{x}$	P	U	S	P	U	U	U	U	U	U	U	U
$\bar{x}_{geom}$	S	P	S	S	U	U	U	U	U	U	U	U
$Q_{0.95}$	U	S	U	S	U	U	P	U	U	U	U	U
IQR	U	S	U	S	U	P	P	U	U	U	U	U
v	U	U	U	U	U	U	U	U	U	U	U	U

For $FCR(F_x/F_{res})$, the two *means* and the *median* received an S-rating. In absolute numbers, the differences for the *median* of $FCR(F_x/F_{res})$ vary between 0.07 for the transition between Zone 2 and 3 in CO1 and 0.0004 for the transition between Zones 1 and 2 for CO2. Although the results of CO1 for $Q_{0.95}$ and *IQR* of $FCR(F_x/F_{res})$ would allow for a P-rating. In CO2, there is an overlap for that potential feature. As such the rating "unsuited" is assigned.

In addition, features involving F_y only received two P-ratings. The two FCR involving F_{res} and F_z also received only two P-ratings. Moreover, all features involving the variance coefficient were unsuited.

Due to the necessity of filtering, the reciprocals do not show the exact same results as their counterparts; however, similar behaviour. The use of $\bar{x}_{geom}$ as a descriptor with three suitable ratings shows better results than the similar $\bar{x}$ or $\tilde{x}$ that only received one S-rating each. This picture becomes clearer in the CO1 results, with an S-rating for six FCR for $\bar{x}_{geom}$ and three respectively four for $\bar{x}$ and $\tilde{x}$.

In addition, using a relatively robust indicator for maxima, in this case, $Q_{0.95}$, instead of single maximum values, showed good results. The *IQR* exhibits similar behaviour as a measure of spread. Both descriptors were rated as "suited" twice each. The *IQR* was rated "partially suited" twice, $Q_{0.95}$ one time.

From the literature review, it was suspected that *FCR(F$_x$/F$_z$)* or *FCR(F$_z$/F$_x$)* would show good results; however, only *IQR* and $Q_{0.95}$ were classified as suitable for this FCR. Instead, FCRs involving F_{res} and F_x received in total six S-ratings.

6.1.3 Correlation of the Covariates

Figure 60 shows a heatmap of the spearman correlation of:

- the FCR-based features chosen in the pre-selection process,
- the mean values of the raw forces F_x, F_y, F_z and F_{res},
- the *cUCS* as an indicator for the rock hardness,
- and the cutting parameters.

In addition, the zone index is considered since it is ordered by the strength of the concrete. Positive correlations are mapped blue; negative correlations are mapped red. The hue indicates the strength of the Spearman correlation. Weak correlations < 0.3 are white. The results of the individual blocks and numeric values for Figure 60 are located Annex J.3.

The correlation of the FCR-based covariates is very high among each other (Marking a). It can be seen that the FCR-features show *correlation coefficients* between ±0.7 and 1 except those utilising F_y/F_x. This is expected. However, the correlations are not perfect. A perfect correlation would speak for redundancy in information value. *YXQ95* and *YXIQR* correlate less with the other features in their group. Additionally, they correlate slightly with *s*, A_c, and the ratio *s/d*. This can be attributed to the dependency of F_y on *s/d*.

Another aspect is seen in Marking d. The FCR-based features show almost no correlation with the cutting parameters s, *d*, A_c, and *s/d*, except for *YXQ95*. This is the desired behaviour using these features for rock classification irrespectively on the actual cutting parameters.

In addition, Marking c shows that the FCR-based features correlate stronger with the *cUCS* as a toughness indicator than the "classic" force-based features. This is also true for the zone index.

As seen in Marking b, the *mean* values of the cutting forces F_x, F_y, F_z, and F_{res} correlate weakly with the FCR-based covariates.

Marking e shows that the *means* of F_x, F_z, F_{res} show a weak correlation with the cutting parameters *d*, *s*, and the resulting A_c. This has already been suggested by the raw force analysis in Chapter 6.1.1. Additionally, the *mean* cutting forces correlate weaker with the zone index and *cUCS* than the FCR-based covariates do.
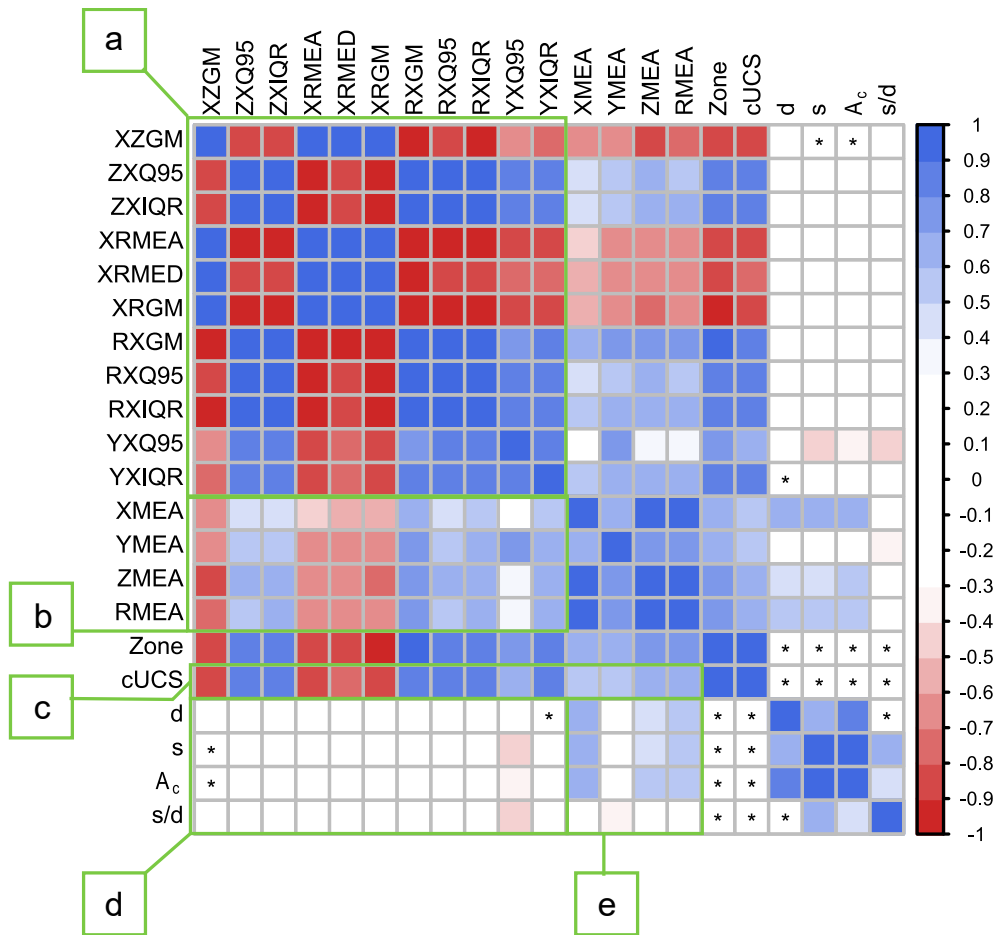
Figure 60: Correlogram for grid calculations of all Experiments CO1 and CO2 (both samples summarised); * – insignificant with significance level = 0.01

6.1.4 K-Means Cluster Analysis

The k-means cluster analysis is an unsupervised clustering algorithm. In this chapter, the algorithm is used to explore whether the features/covariates can be used to cluster the data according to their rock type. For that, the cluster assignments are compared to their real rock type. Subsequently, the *accuracy* of the cluster-based assignment is evaluated.

Used Parameters

Five cases are compared to evaluate the performance of the k-means classification. Each case uses a different set of features. Case 1 uses only the features classified as "suited" by the selection algorithm as described in Chapter 6.1.2. Case 2 adds *YXQ95* and *YXIQR*. The reason is that these are the only features that are classified as partially suited and at the same time, consider F_y. With Case 3, a sensor assembly that only measures F_x and F_z and no y-component is simulated. Hence, only features derived from these two force components and received an S-rating are utilised.

Case 4 investigates a feature set consisting of the moving-window-mean of the raw force components F_x, F_y, F_z and F_{res}. Case 5 uses only the *mean* of F_x and F_z. These last cases represent a "traditional" approach to cutting force measurement. The cases are summarised in Table 19.

Table 19: Cases investigated with k-means algorithm for Experiment CO

Case	Features used
1	XZGM, ZXQ95, ZXIQR, XRMEA, XRMED, XRGM, RXGM, RXQ95, RXIQR
2	*as above* + YXQ95, YXIQR
3	XZGM, ZXQ95, ZXIQR
4	XMEA, ZMEA, YMEA, RMEA
5	XMEA, ZMEA

Figure 61 shows the results for Cases 1 and 4. A complete list of all classification results can be seen in Annex 0. The IDs of the clusters were manually assigned to their respective zones. This is necessary due to the nature of the k-means clustering algorithm. The initial starting points of the clusters were set up randomly; the optimisation algorithm then changed the cluster positions iteratively. Because of that, the naming of the clusters was inconsistent and was assigned manually after the clustering process. The vertical lines indicate the border between the different concrete zones. Generally, Cases 1, 2, and 3 performed very similarly—as did 4 and 5. Hence, Case 1 serves as an example for the FCR-based clustering and Case 4 for the raw-force-based clustering.

The clustering results in Figure 61 are shown separately for all combinations of cutting parameters. It is seen that the FCR-based classification performed better. Also, the classification based on FCR shows relatively consistent results compared to the raw forces cases. Within Case 1, the classification shows less precise results for d =12 mm and s/d = 3 and 4. Generally, small misclassification patches appear in CO1. This can be attributed to two points:

a) The rock hardness for the same zones varied between CO1 and CO2.
b) The clustering was done for the whole dataset, consisting of the data of CO1 and CO2 conjoined.

Here, parts of Zone 2 were classified as Zone 1. In CO2, wrong patches did not occur; however, higher deviations of the classified rock type boundaries to the actual boundaries occurred. The black rectangles indicate those experiments conducted with the same absolute *spacing*—simulating the passthrough during a crescent cut (see p. 16). Results in this sub-group are very consistent.

For Case 4, the classification is skewed towards Zone 1 at small cutting parameters (Marking a). For d = 6 mm and s/d = 2, the whole block is classified as Material 1. For medium cutting parameters, the classification shows Zones 1 and 2. However, CO1 does not consist of Material 1 at all. An accurate classification could only be obtained with the highest cutting parameters in CO1. During the cutting of CO2, Material 3 is not detected for smaller cutting parameters. For the crescent cut scenario, the results are also far less consistent than the results of Case 1.
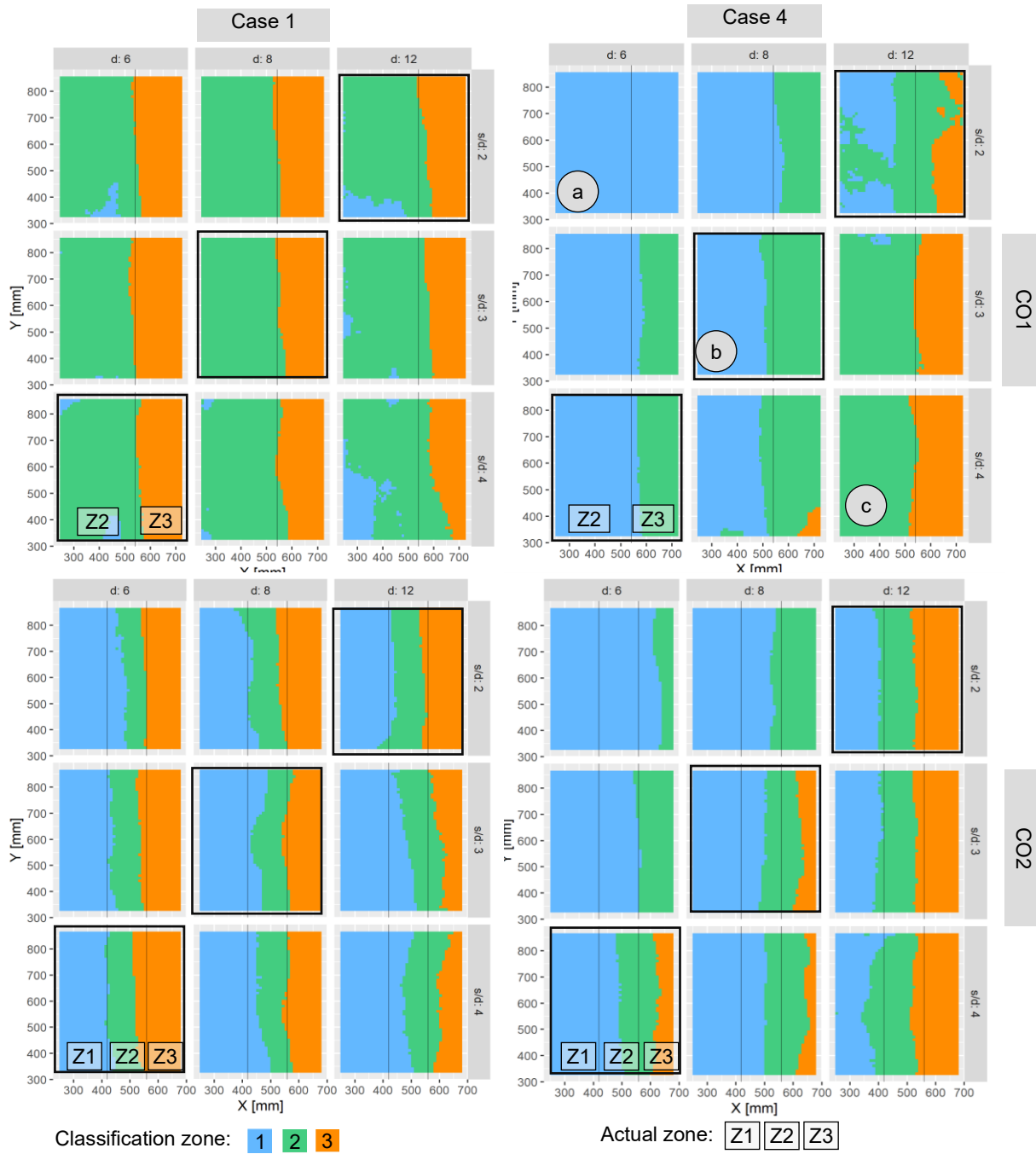
Figure 61: Mapping of k-means based classification for Cases 1 and 4, black rectangles indicate cuts with d = 24 mm

Figure 62 shows the summary of the performance of the k-means clustering. Detailed results for each case are located in Annex 0.

On the left side, the overall *accuracy* is shown as calculated after Equation (19). The global *accuracy* (anthracite) shows the *accuracy* for all experiments merged together. Here, the highest *accuracy* is achieved by Case 1 with 89%. Case 2, where *YXQ95* and *YXIQR* were added as predictors, achieved slightly less *accuracy* with 88.2%. Case 3 achieved 86.7%—the worst performance of the FCR-based clustering cases. This coincides with the empirical evaluation, which indicated that FCR involving F_{res} might yield better results. Cases 4 and 5 show the clustering based on the raw force features. Here, the performance lies much lower with 41.7% respective 43.0%.

The grey bars summarise the individual sets' *median*, *minimum*, and *maximum* performance. Similar to the global results, Cases 1 to 3 perform similarly well, whereas the raw-force-based classifications show low accuracies.

The figures marked with a yellow asterisk show the experiments with fixed *spacing*. For this situation, the overall *accuracy* of Cases 1–3 lies in a tight range of 90–93%. The lowest performance occurs at $d = 12$ mm and $s/d = 4$. The worst performance in Cases 1–3 occurs at Case 2 for the same cutting parameters.

Case 1

	d [mm]				
6	8	12			
90.4%	93.9%	*90.4%	2		
93.3%	*92.7%	83.7%	3		s/d
*93.3%	91.7%	73.2%	4		

Mean	89.2%	Median	92%
Min	73.2%	Q1	90%
Max	93.9%	Q3	93%
		IQR	3%

Case 4

	d [mm]				
6	8	12			
18.9%	26.6%	*87.0%	2		
22.7%	*41.2%	91.6%	3		s/d
*28.5%	30.5%	96.0%	4		

Mean	49.2%	Median	30%
Min	18.9%	Q1	27%
Max	96.0%	Q3	87%
		IQR	60%

Accuracy

100.0%	
80.0%	
60.0%	
40.0%	
20.0%	
0.0%	

	1	2	3	4	5
Global	89.0%	88.2%	86.7%	41.7%	43.0%
Median	91.7%	91.2%	90.6%	30.5%	36.2%
Maximum	93.9%	93.6%	93.0%	96.0%	93.0%
Minimum	73.2%	69.2%	73.1%	18.9%	18.9%
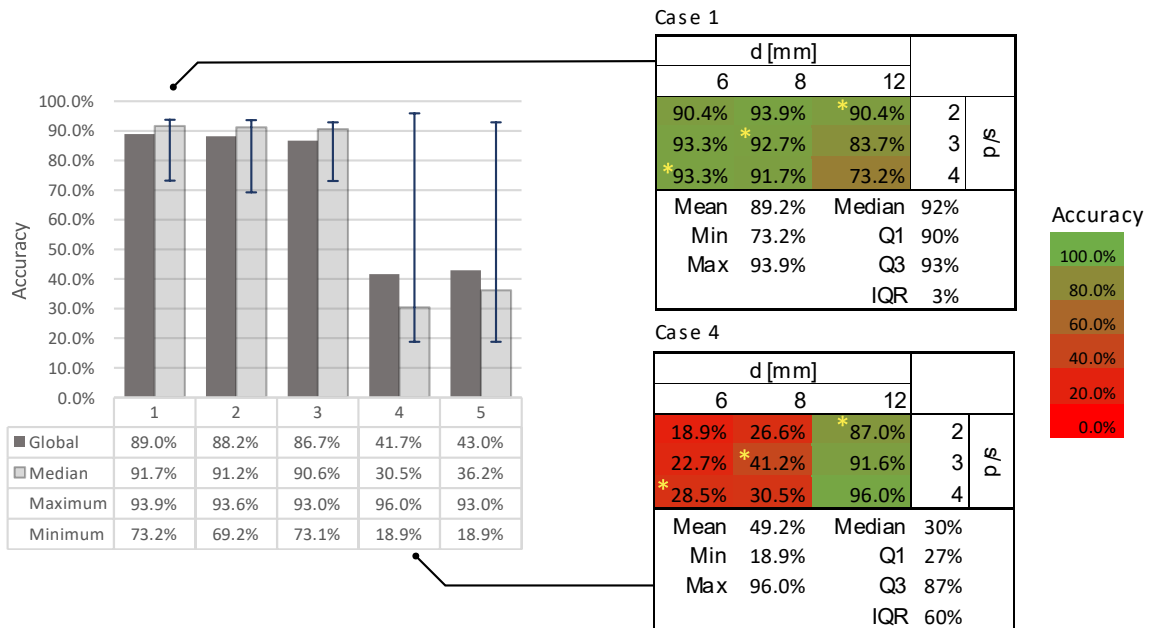
Figure 62: Accuracy values for k-means clustering (left), detailed accuracy for Cases 1 and 4 (right)

Cases 4 and 5 show peak accuracies comparable to those of Cases 1–3. They are even higher with 96.0%. However, an *accuracy* above 85% only occurs at the highest *cutting depth*. At the two lower levels for the *cutting depth*, *accuracy* shows its highest value at 41%. Also, the *accuracy* values for the crescent-cut-subset does not show consistent results with ranges from 28–87%.

Precision of Boundary Detection

From the gridded results, the *precision* of the boundary detection was calculated. Figure 63 shows the estimation results. The mean values of the *precision* ranges between 24.5 and 37 mm. Generally, the *precision* is smaller for the transition of Zones 2–3. Hereby, Case 1 shows the smallest (best) *precision* estimates. The *precision* values for the transition of Zones 1–2 are slightly worse. This is plausible with regard to the small difference in rock hardness between Zones 1–2. However, the *standard deviation* for Cases 2 and 3 in Zone 2–3 is higher than the other values.

Comparing Cases 1–3 with each other, it appears that Case 1 generally shows the best results; Cases 2 and 3 show slightly worse precision values. Especially for the transition of Zones 2–3, this becomes apparent.
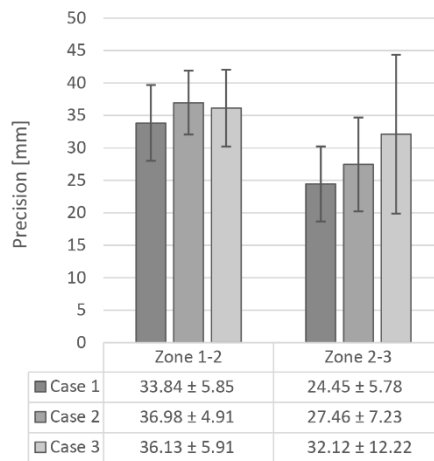
Figure 63: Boundary detection precision for Cases 1–3, values in the form: mean ± standard deviation

Further Considerations to Internals of K-Means

To understand the clustering process, the two features, ZXIQR and XZGM; as well as ZMEA and XMEA, are plotted against each other in Figure 64.
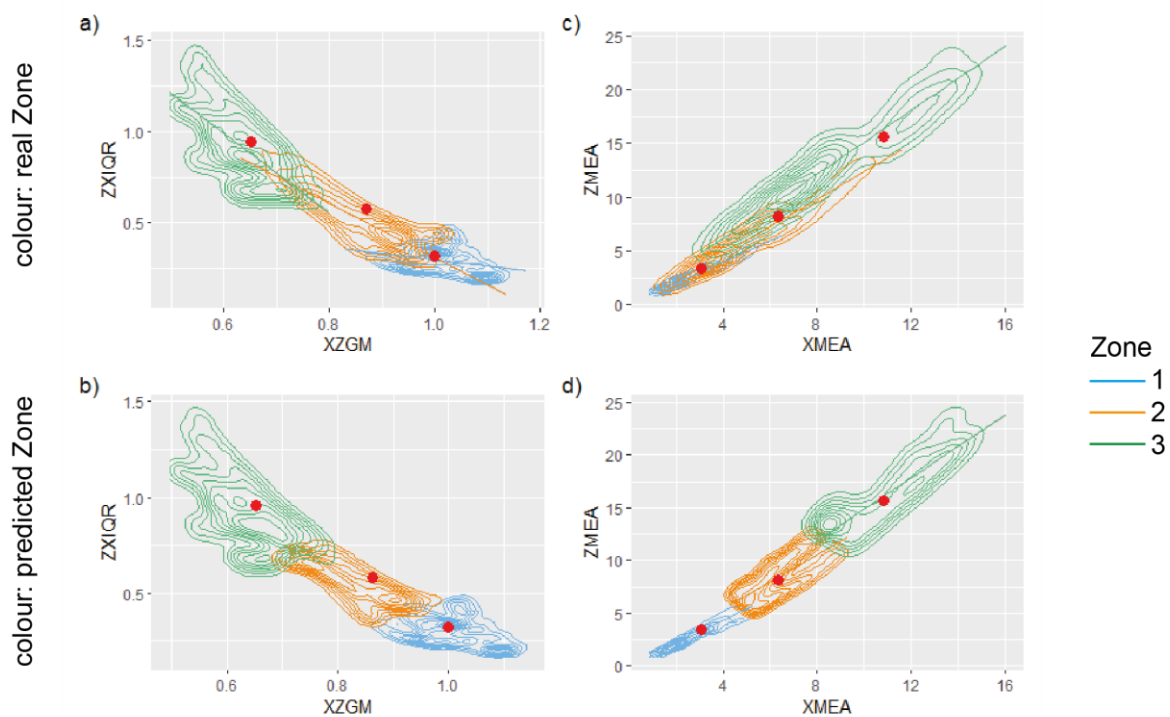
Figure 64: a) & b) Density of ZXIQR to XZGM; c) & d) density of ZMEA to XMEA for sample CO2; colour shows the real zone in the top row, and predicted zone in the bottom row

In the plots, the relative density of the grid data points is drawn with a kernel estimator. The red dots show the position of the clusters on the planes formed by the features. In Panels a) and c), the colours indicate the true rock zone. In Panels b) and d), the colours indicate the cluster assignments from k-means. Reality and prediction and are very close for the FCR-based features on the left side. However, reality and prediction deviate strongly for the clustering with raw force-based features on the right side.

This is because k-means works with minimising Euclidean distances. As such, the clusters tend to drift towards the shape of a (multidimensional) spherical object. The real zone assignments for the FCR-based features already support this behaviour. There is minor overlap between the data for the three

zones as seen in Panel a). The data for the raw force features overlap each other strongly, as seen in Panel c). The algorithm can not deal well with this overlap but has to split the data into three clusters. This results in a cluster assignment that is different from the real rock zones. Here, small forces are generally attributed to the weakest zone, and high forces are generally attributed to the highest zone. However, low forces occur in the weakest rock, but also result from low cutting parameters. This explains, why k-means over-assigns the weakest zone for low cutting parameters—even if the weakest zone is not even present.

Feature Importance with Distributed Random Forest

During clustering, the pre-selected feature Case 1, showed the best performance. However, evaluating the feature importance is not directly possible for k-means. Therefore, a DRF classification is used to train on the dataset and the *feature importance* is evaluated on the trained DRF. The maximum tree depth was set to 5 to prevent overfitting. All data were used to train the DRFs, so no training-validation split was applied. Further details on DRF can be found in Chapter 5.11.4.

First, the overall *accuracy* for the five learners was calculated. The results can be seen in Table 20. Generally, the accuracy is higher for DRF than for k-means. This can be attributed to the fact that DRF is a supervised algorithm that minimises *classification error.* Similar to k-means clustering, FCR-based cases show better results. The *accuracy* is almost equally high for Cases 1–3, with slightly lower results in Case 3. The *accuracy* for Cases 4 and 5 is substantially better than with the unsupervised k-means. Detailed classification results and zone mapping can be found in Annex J.5.

Table 20: Accuracy for DRF classification of Campaign CO

Case	Accuracy
1	94.4%
2	94.6%
3	93.8%
4	85.1%
5	83.3%

Figure 65 shows the results of the feature importance analysis. For the base Case 1, *RXIQR* received the highest weighting, followed by *XRGM* and its reciprocal, *RXGM*. Expectedly, the two features show a strong *correlation coefficient* of -0.993 in the correlation analysis. As described in Chapter 5.5, the correlation is not perfect due to data processing. However, redundancy can be assumed for these two covariates. It stands out that *XRMEA* received a very low importance rating. This speaks for the assumption that the *geometric mean* is a better measure of centrality for force component ratios. The features derived from F_x and F_z received medium values.

For Case 2, the situation is very similar to Case 1. Additionally, the features that involve F_y receive the lowest ratings, as expected from the procedural selection algorithm.

The importance values are relatively equal for Case 3, which only used three features. Therefore, it can be assumed that there is little redundancy in these covariates. Comparing this with the results of the correlation analysis shows that the correlation of *XZGM* and *XZQ95* with *ZXIQR* lies at -0.844 and -0.838, respectively. This is comparatively low for correlations between FCR-features, meaning that the redundancy for this pair is comparatively low.

For Cases 4 and 5 that only used the raw forces, *ZMEA* is the most important predictor. It stands out that for Case 4, *XMEA* received the smallest importance.
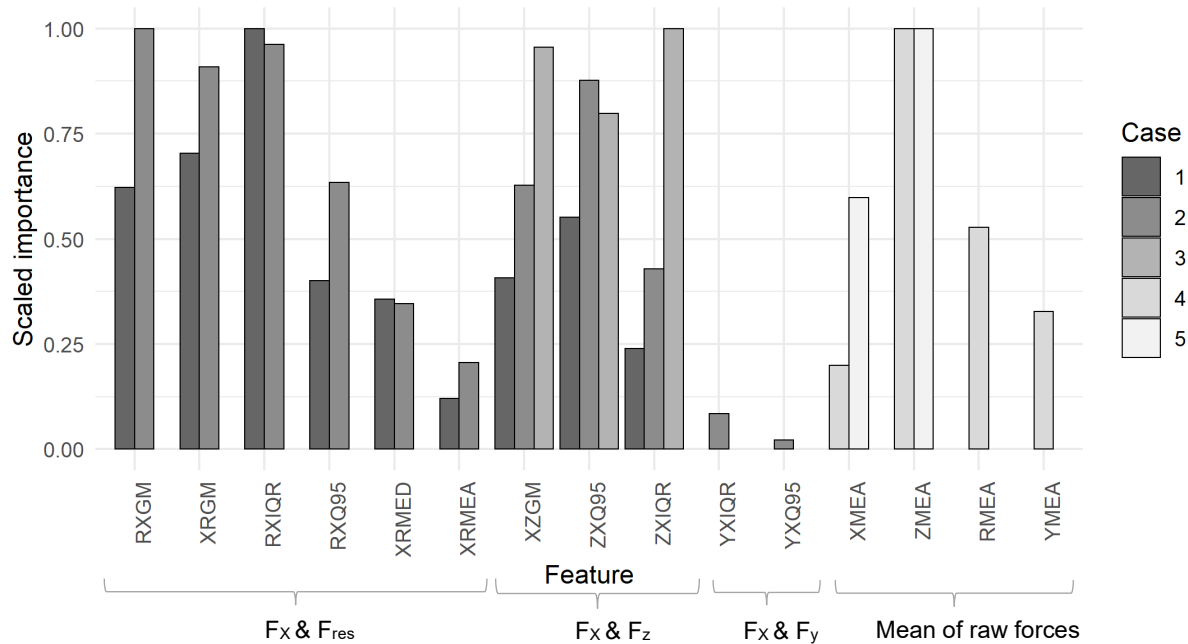
Figure 65: Scaled importance of the features for DRF classification for Cases 1–5 of Experiment CO

Summary

Unsupervised k-means clustering with FCR-based features provides consistent and relatively good classification results. The *accuracy* lies at slightly below 90%. The precision with respect to the material boundaries lies on average below 3.7 cm in cutting direction for the three cases.

Within the group of FCR-based features, all three variants performed well. Case 1, which takes all S-rated covariates into account, performs best. Case 3, only taking *XZGM*, *ZXQ95* and *ZXIQR* into account, follows second. Case 2, which takes into account two covariates derived from F_y, shows a slightly lower performance. This is in line with the results from the correlation analysis, which showed a correlation of these features with the *spacing*. A correlation with the *spacing* is undesirable.

In contrast, the using of mean values of raw cutting force components is highly disturbed by varying cutting parameters. Hence, it is only accurate for a small range of cutting parameters. This suggests that features utilising mean values of raw cutting forces should be avoided for MWC applications.

FCR-based k-means clustering does not require already classified data. Therefore, it could be used to identify changes in rock toughness, when no training dataset is available, or to verify results of other classification methods.

6.2 GN – Foliated Gneiss

The following chapter investigates the possible effects of foliation on an FCR-based rock classification. This can usher in understanding how foliation influences a near-tool MWC rock characterisation system. First, an understanding of the responses of the raw force component is established with respect to the different layering situations. It turns out that the influence of *spacing* and *cutting depth* is altered to some extent depending on the foliation orientation. This effect is further investigated. Subsequently, the behaviour of the most FCR-features is analysed. Annex K contains additional details on the results presented in this chapter.

6.2.1 Cutting Forces

Figure 66 shows an overview of the raw force responses of the experiments. Here, all experiments are shown together. A detailed analysis follows below. The forces for Side A are the lowest, followed by B and C. This is true for all four force components. The effect of foliation on all cutting force components is relatively high. The *mean* for F_x ranges from 3.5 kN for Side A to 9.8 kN for Side C, an increase of 2.8. The $Q_{0.95}(F_x)$ ranges from 9.7 kN for Side A to 20.1 kN for Side C. This equals a factor of 2.1. For F_z, *mean* values are in the range 6.8–19.6 kN, for $Q_{0.95}$ they are in the range of 11.9–29.3 kN. Accordingly, the F_y and F_{res} values follow this pattern of increasing forces between Sides A to C. Also, it can be seen that all force distributions are not symmetrical but slightly skewed to the right. This means that very high maximum values can occur. Detailed boxplots where results are split by cutting parameters can be accessed in Annex K, Figure K-1.
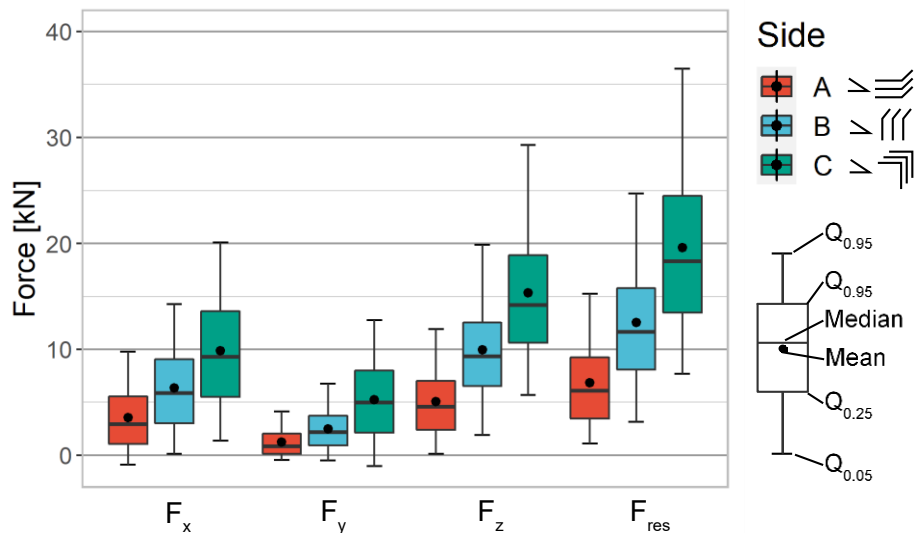
Figure 66: Raw force response ranges for Experiment GN

Figure 67 shows more detailed results of the experiments concerning F_x in relation to *s* and *d*. It shows the *mean*, $Q_{0.95}$, and the ratio of $Q_{0.95}$ to *mean(F_x)*. Semi-relieved and unrelieved conditions are shown. The mean forces for Side A are in the range 2.26–6.65 kN, for Side B they are in the range 4.22–11.94 kN, and for Side C, they range from 7.22 to 11.94 kN. The $Q_{0.95}(F_x)$ exhibits similar behaviour; however, at a higher level. Here, the total range of values is 6.81–20.37 kN. The $Q_{0.95}(F_x)$ for Side A is similar as the *mean(F_x)* of Side C.

The ratio of $Q_{0.95}$ to *mean* shows a diametric picture to the previous graphs. The highest peaks compared to the *mean* are recorded for Side A, ranging from 2.10 to 3.13. Medium ratios are recorded for Side B, ranging from 2.00 to 2.31. The lowest ratio appears for Side C, ranging from 1.72 to 1.94. Generally, this points towards different outbreak patterns of the chips. When the ratio is small, smaller chips break out, and the breakage process is repeated more often. When the ratio is higher, larger chips break out, creating comparably high peak forces. This hypothesis is supported by the works of Mohammadi et al. (2020) [190] and Keller (2020) [41].

It stands out that the influence of the cutting parameters *d* and *s* on F_x is different for the three foliation orientations. While an increase in *d* coincides with an increase in F_x, this is only partially the case with *s*. General knowledge from the literature indicates that increasing the *spacing* increases F_x—although the effect of *s* is smaller than the effect of *d*. This cannot be confirmed for all foliation directions. Only for Side B, an increase of *s* increases the *mean* and $Q_{0.95}$ of F_x. An increase of *s* does not increase F_x for

Sides A and C. For the *cutting depth* 6 mm, both the *mean* and $Q_{0.95}$ even decrease between a *spacing* of 12 to 16 mm.
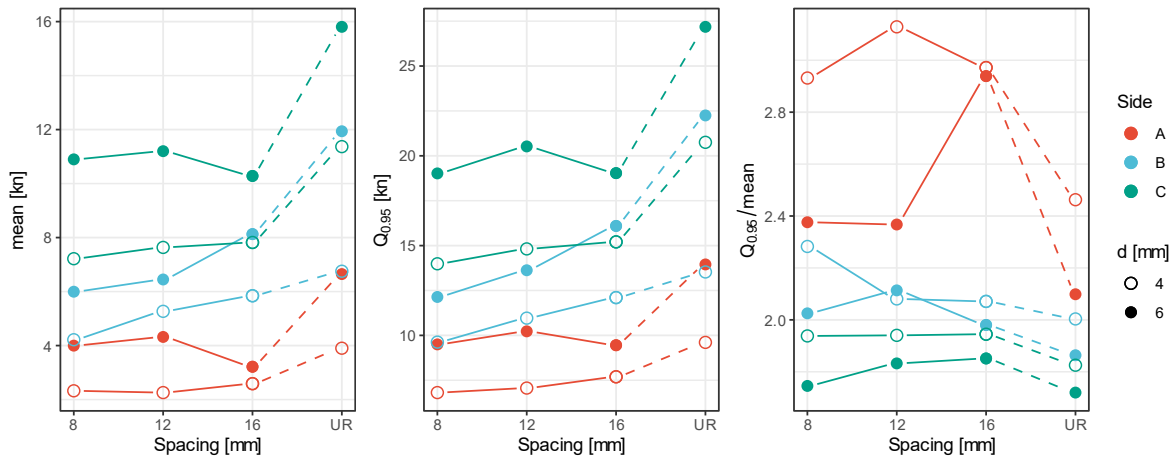
Figure 67: Mean values, $Q_{0.95}$ and ratio of $Q_{0.95}$/mean for F_x for Experiment GN

Figure 68 shows the force for F_z in the same fashion as above. Very similar behaviour to the figure shown above can be observed. However, for Side C, *mean(F_z)* decreases with increasing *spacing* for $d = 6$ mm. Also differing from the behaviour of F_x, the ratio $Q_{0.95}(F_z)$/mean (F_z) increases to up to 2.6 for Side A, $d = 6$ mm, and s = 16 mm. At the same time, $Q_{0.95}(F_z)$/mean(F_z) does not show such an increase for $d = 4$ mm.
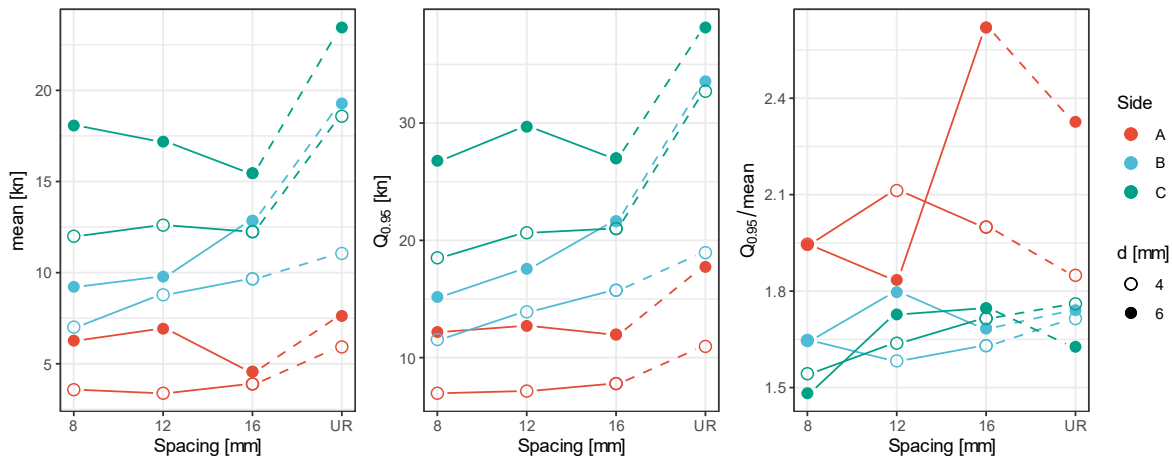
Figure 68: Mean values, $Q_{0.95}$ and ratio of $Q_{0.95}$/mean for F_z for Experiment GN

Figure 69 shows the results for F_y. Generally, a higher *cutting depth* is in line with a higher *side force*. Also, for most situations, the F_y decreases with increasing *s*. An exception to this is Side B, $d = 6$ mm. Here, an increase in F_y can be monitored, both for the *mean* and for $Q_{0.95}$.

Decreasing F_y with increasing *s* finds its culmination for the unrelieved cuts. There, the symmetrical confinement of the pick—in theory—results in *side forces* of 0 kN. Curiously, a slight deviation from this can be observed. The values of *mean(F_y)* for the unrelieved cuts are lowest for Side A (-0.14 and 0.12 kN), slightly higher for Side B (0.34 and -0.31 kN), and highest for Side C (0.87 resp. 1.03 kN). The $Q_{0.95}$ for Side C, unrelieved cut, shows relatively high values (5.18 and 7.27 kN). To confirm the reliability of these results, the *standard error* was calculated for these experiments. It ranges from 0.0035 to 0.0123 for Side A, $d = 4$ mm, and Side C, $d = 6$ mm, respectively. This is almost two magnitudes smaller than the values. As such, it is suspected that these observations are not random, and the

orientation of the foliation seems to have an effect on the *side force*. Imperfections in the foliation orientation towards the cutting direction might contribute to these results.
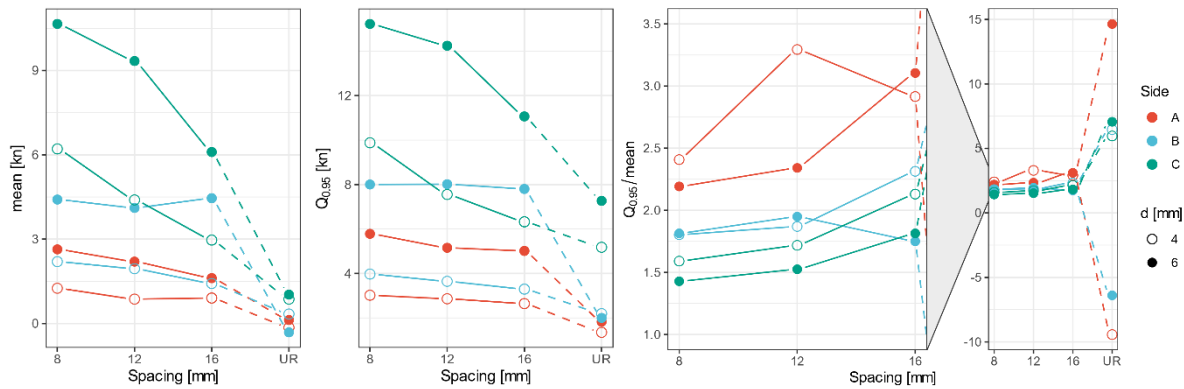
Figure 69: Mean values, $Q_{0.95}$ and ratio of $Q_{0.95}$/mean for F_y for Experiment GN

For most combinations of cutting parameters, an increase in the *spacing* correlates with an increase in the ratio $Q_{0.95}(F_y)/mean(F_y)$. Here, the values for the unrelieved cuts reach very high values both on the positive and on the negative axis. They range from -9.43 to 14.65 for the unrelieved cuts. At the same time, the values for the semi-relieved cuts range from 1.43 to 3.11. This is not surprising since the *mean(F_y)* values are close to 0 but still peak values occur creating very high $Q_{0.95}$/mean ratios.

6.2.2 Regression Analysis of Effect

To estimate the effect of the influence of the parameters *s* and *d* on the force levels, linear regression is used to estimate their relative contribution (for method, see Chapter 5.10). Only mean forces are considered for this analysis.

Regression for *mean(F_x)*

Table 21 shows the linear regression results for *mean(F_x)*. Generally, the linear model results in a relatively good fit for all three sides (R^2 between 0.83 and 0.96). The *relative contribution (c_{rel})* of *s* is generally lower than that of *d*. The *relative contribution* of *s* to *mean(F_x)* follows the decreasing order B>A>C. Hereby, the value for B lies at 22%, while the values for A and C lie at 3% and 0.4%, respectively. Also, for Sides A and C, the *p-value* for *s* is high (0.73 and 0.93, respectively), indicating no significant effect of *s* on *mean(F_x)*. In comparison, the *p-value* for *s* on Side B lies at 0.009. This indicates that the effect of *s* is significant. This corresponds to c_{rel} of *d* for Sides A (97%) and C (99.7%); and 78.4% for Side B. Also, the *p-values* here suggest significance ($p < 0.05$).

Table 21: Regression statistics for mean(F_x), with predictors in brackets for reference

Side	Coefficient			R^2	t-statistic			p-value			c_{rel}	
	b_0	b_1 (s)	b_2 (d)	R^2	b_0	b_1 (s)	b_2 (d)	b_0	b_1 (s)	b_2 (d)	s	d
A	-0.194	-0.022	0.710	0.827	-0.164	-0.383	3.770	0.880	0.727	0.033	3.02%	96.98%
B	-0.985	0.226	0.819	0.966	-1.309	6.165	6.837	0.282	0.009	0.006	21.64%	78.36%
C	0.855	0.006	1.602	0.964	0.758	0.102	8.921	0.504	0.926	0.003	0.35%	99.65%

This means that for Side A and C, the *spacing* has no significant influence on the *mean(F_x)* within the tested parameter space.

Regression for *mean(F_z)*

For the regression of F_z, similar effects as for F_x can be observed. The R^2 statistic ranges from 0.76 to 0.93. Generally, c_{rel} of s is lower than c_{rel} of d. For Sides A and C, the values are ~6%. For Side B it lies at 28%. The *p-value* indicates a nonsignificant contribution of s to *mean(F_z)* with values of 0.57 for Side A and 0.28 for Side C. For Side B, the *contribution* is significant (p<0.05). This compares to a *relative contribution* of 94% of the *cutting depth* for Sides A and C, and 72% for Side B.

Table 22: Regression statistics for mean(F_z), with predictors in brackets for reference

	Coefficient			R^2	t-statistic			p-value			c_{rel}	
Side	b_0	b_1 (s)	b_2 (d)	R^2	b_0	b_1 (s)	b_2 (d)	b_0	b_1 (s)	b_2 (d)	s	d
A	-0.051	-0.072	1.117	0.758	-0.022	-0.632	3.002	0.984	0.572	0.058	6.06%	93.94%
B	0.078	0.366	0.927	0.925	0.050	4.822	3.737	0.963	0.017	0.033	28.32%	71.68%
C	4.574	-0.138	2.223	0.935	2.109	-1.306	6.442	0.126	0.283	0.008	5.85%	94.15%

Regression for *mean(F_y)*

Table 23 shows the regression statistics for *mean(F_y)*. The R^2 statistic is higher than for *mean(F_x)* and *mean(F_z)*, ranging from 0.94 to 0.98. The relative contribution of s to *mean(F_y)* is generally lower than c_{rel} of d. The contribution follows the order C>A>B, ranging from 4–19%; with a significant contribution for Side C (*p<0.05*). However, the *p-value* for c_{ref} of s for Side A is significant with *p<0.1*. For d, the *relative contribution* lies between 81% and 95%. All *contributions* there are significant with *p<0.01*.

Table 23: Regression statistics for mean(F_y), with predictors in brackets for reference

	Coefficient			R^2	t-statistic			p-value			c_{rel}	
Side	b_0	b_1 (s)	b_2 (d)	R^2	b_0	b_1 (s)	b_2 (d)	b_0	b_1 (s)	b_2 (d)	s	d
A	-0.291	-0.079	0.559	0.944	-0.535	-2.980	6.461	0.630	0.059	0.008	12.37%	87.63%
B	-2.241	-0.050	1.159	0.974	-3.234	-1.479	10.515	0.048	0.236	0.002	4.13%	95.87%
C	1.777	-0.469	2.045	0.976	1.223	-6.633	8.847	0.309	0.007	0.003	18.67%	81.33%

Comparison and Summary of the Regression Results

In summary, it can be observed that:

- For Sides A and C, s has no effect on the *means* of F_x and F_z. An effect was only measurable for Side B. The effect of s on F_x and F_z for Side B is considerably lower than the effect of d.

- In contrast, the effect of s on F_y behaves differently. For Sides A and B, a measurable influence of s on F_y is recognised. For Side B, the effect is insignificant.

This behaviour deviates from the cutting theory, especially for F_x and F_z. Hence further investigations are presented in the following chapter.

6.2.3 Details Irregular Behaviour

In the two previous chapters, the results partially contradict the classical understanding of the cutting force behaviour concerning the cutting parameters d and s. It was shown that, for Sides A and C, both F_x and F_z are not significantly affected by the *spacing*. This chapter explores the reasons behind this behaviour by taking an in-depth view of the raw data and the distribution characteristics of the cutting forces.

Figure 70 shows the *force-time* diagrams of F_z for three subsequent cuts of the experiment with $d = 6$ mm, $s = 16$ mm, Side A. Here the foliation is coplanar to the x-y-plane and the rock surface. It can be seen that large "valleys" appear in the F-t diagrams. These can be attributed to very large chips breaking off, resulting in a free movement of the pick through the cavity where the chip was located.
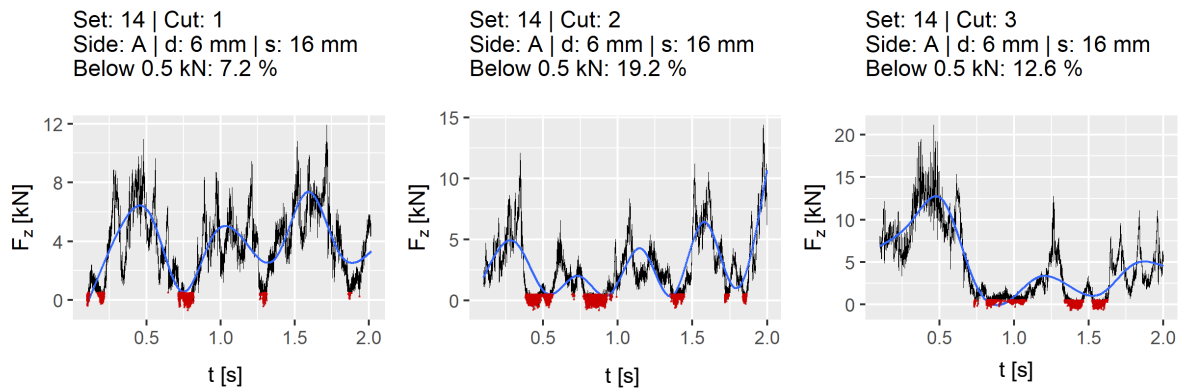
Figure 70: Force-time diagrams for Side A, F_z; red marks F_z below 0.5 kN, blue line shows trend line

To quantify this effect further, the proportion of data points below the threshold of 0 kN for F_x and 0.5 kN for F_z, named PP_{x0} resp. PP_{z05}, as well as the *variation coefficient* (v) of F_z, are computed. The results are shown in Figure 71. It shows that for Side A higher proportions of data points occur below these thresholds. Also, $v(F_z)$ shows this behaviour.
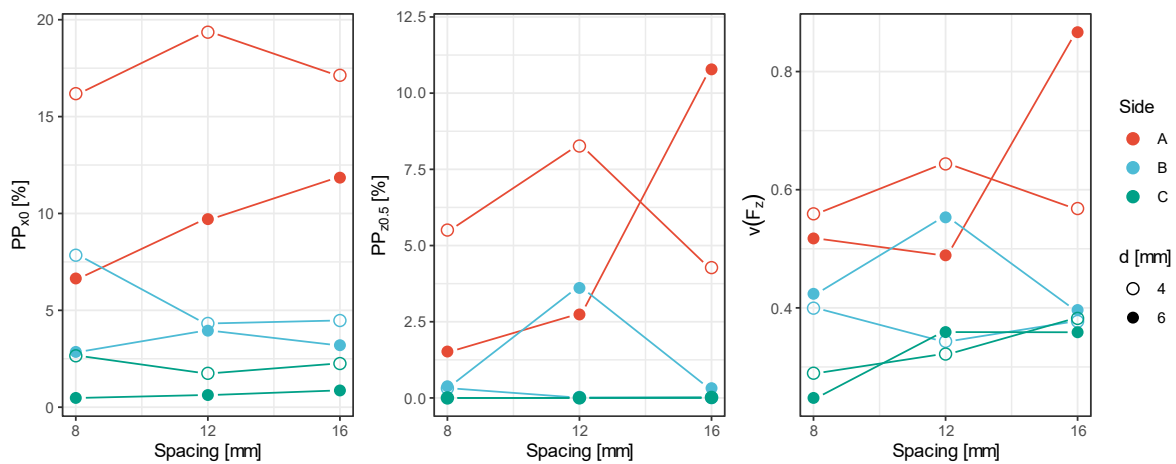
Figure 71: Proportion of data points below threshold PP_{x0} and $PP_{z0.5}$, and variation coefficient of F_z for Experiment GN

Additionally, it is visible that for the *cutting depth* of 6 mm, with increasing *spacing*, PP_{x0} and especially $PP_{z0.5}$ rise significantly. Remarkable is the increase from 3.3 to 17.6% for $PP_{z0.5}$ from $d = 12$ mm to $d = 16$ mm, respectively. The figure also indicates that similarly strong effects cannot be discovered for Side C—although Side C shows a similar behaviour of lower forces for the highest *spacing*.

Figure 72 shows a violin plot for the distributions of F_z. A violin plot is similar to a distribution density diagram—but vertical. The x-axis depicts the *spacing*, and the y-axis depicts the force level of F_z. The thickness of the elements (= "violins") depicts the relative distribution density. The horizontal lines within the violins show $Q_{0.25}$, *median* and $Q_{0.75}$. Additionally, the dot shows the *mean* value. The *cutting depth* is coded as saturation of the colour.
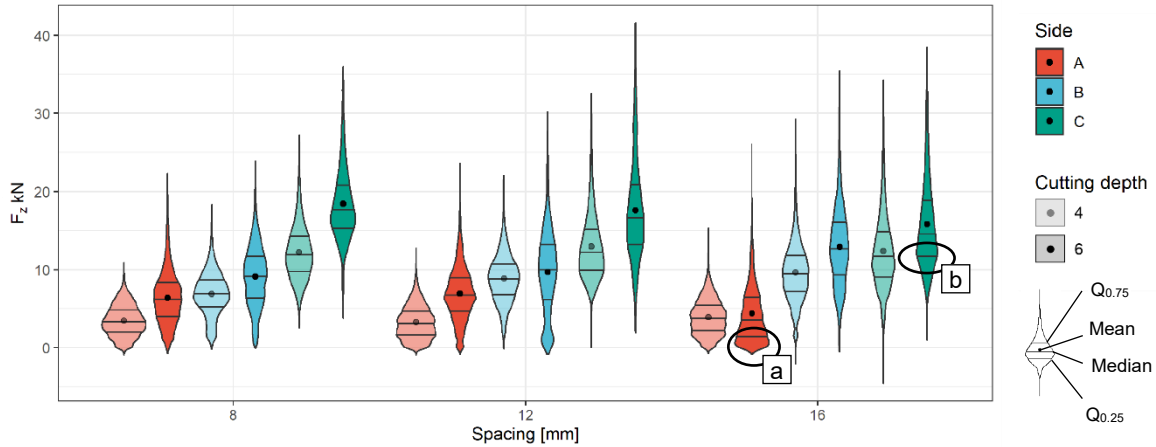
Figure 72: Violin plot for distribution of F_z for Experiment GN

The two Markings a and b show points of interest. Marking (a) shows the distribution of experiment $d = 6$ mm, $s = 16$ mm, Side A. While peak values for F_z go up to 26 kN, the *mode* of the distribution lies at 2 kN. This is the lowest reading for the *mode* throughout the whole diagram. This large proportion of low forces leads to a low *mean*, *median*, and $Q_{0.25}$. This can be attributed to the aforementioned effect of overbreak. When overbreak occurs, the pick loses contact with the rock. This causes small F_z values to occur. As such, it confirms the theory of overbreak affecting the mean forces while peak forces are within the normal expected range. Marking (b) shows the situation for Side C, $d = 6$ mm, $s = 16$ mm. Here, a lower *mode* also appears. However, the *mode* appears close to $Q_{0.25}$ and at a significantly higher force level (14 kN). The distributions for all three *spacings* show a similar shape for Side C, $d = 6$ mm. Resulting from these observations, it is assumed that a minor overbreak might occur, which does not leave large traces in the overall distribution.

Figure 73 shows detailed F-t diagrams for F_z for Sides B and C. It shows that there are no force valleys with very low forces; the force valleys reach lows between 5 and 15 kN. This supports the observation that no major overbreak occurs where the pick looses contact with the rock.
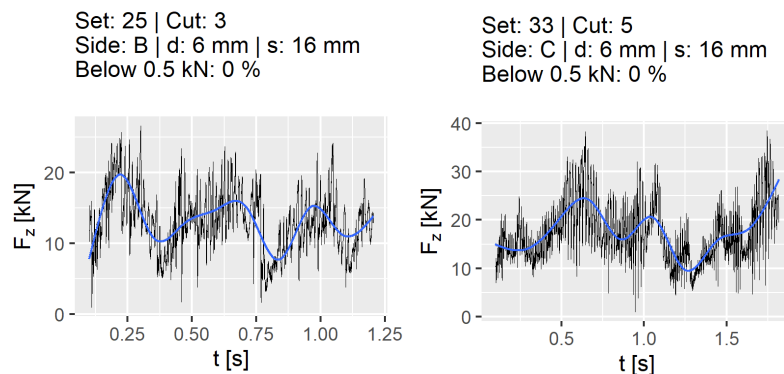
Figure 73: Exemplary force-time diagrams for F_z, sides B and C; blue line shows trend line

6.2.4 Interpretation of Anisotropic Behaviour

To put the previous observations into perspective, Figure 74 shows laser scans of the cut surfaces for $d = 6$ mm, $s = 16$ mm. For Side A, overbreak in a floe-like shape can be observed. For Side B, a relatively normal surface shape after cutting remains. Partial ribs occur, which is consistent with observations on homogeneous rocks and the general knowledge of the cutting process (s. Figure 12, p. 15). For Side C, the situation is less clear. It appears as a mixture of the observations on Sides A and B. While some small parts with partial ribs occur, parts with overbreak occur as well. This overbreak is relatively small and oriented along the foliation. It shows sizes of maximally 2×0.5 cm. In comparison, the large, flat overbreak on Side A shows diameters of ~4 cm.
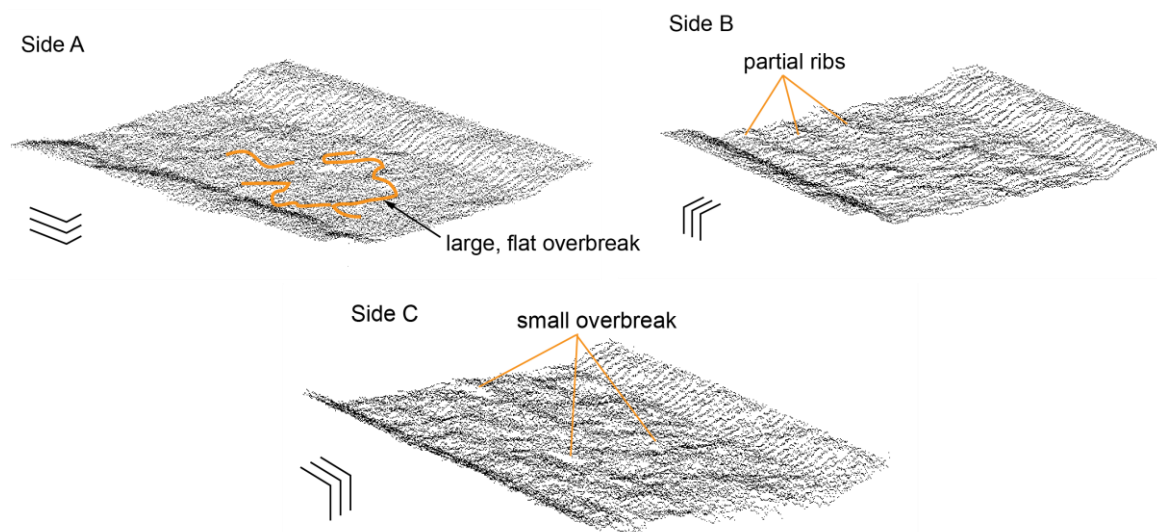
Figure 74: Surface scans for Sides A, B, and C for d = 6 mm and s = 16 mm

In conclusion of these observations, for Side A, the foliation direction supports the crack propagation between cuts to such an extent that large *spacings* create very large outbreaks—with the result that the mean forces are actually lower for the highest *spacing*. For Side C, where the foliation plane is in x-z-direction, a similar effect was observed—however, less significant. For Side A, these results show the effects of a preferred crack propagation along the foliation planes, allowing for wider spacing between picks than in a more homogeneous rock—if the foliation direction can be exploited. While a similar effect could be observed for Side C, the forces are generally on the highest level of all three sides. An excavation in this direction to the foliation should be avoided if possible.

6.2.5 Force Component Ratios

Figure 75 shows the features that were selected from the previous Experiment CO. The features extracted from F_{res} and F_x show similar trends. The features *RXGM*, *RXIQR,* and *RXQ95* decrease with increasing spacing. For *RXGM*, the values range from 1.93 to 2.45, for *RXIQR* from 0.66 to 1.23 and for *RXQ95* from 4.38 to 9.18.

The features extracted from F_z and F_x show a stronger dependency on the foliation direction than those extracted from F_x and F_{res}. Especially, the feature *ZXMEA* shows the strongest dependency on the foliation direction. Hereby, the *ZXMEA* for Side A forms a value corridor from 0.96 to 1.62. The distinction between Sides B and C is less clear. The value corridor ranges from 1.63 to 1.97 for Side B and from 1.73 to 2.11 for Side C.
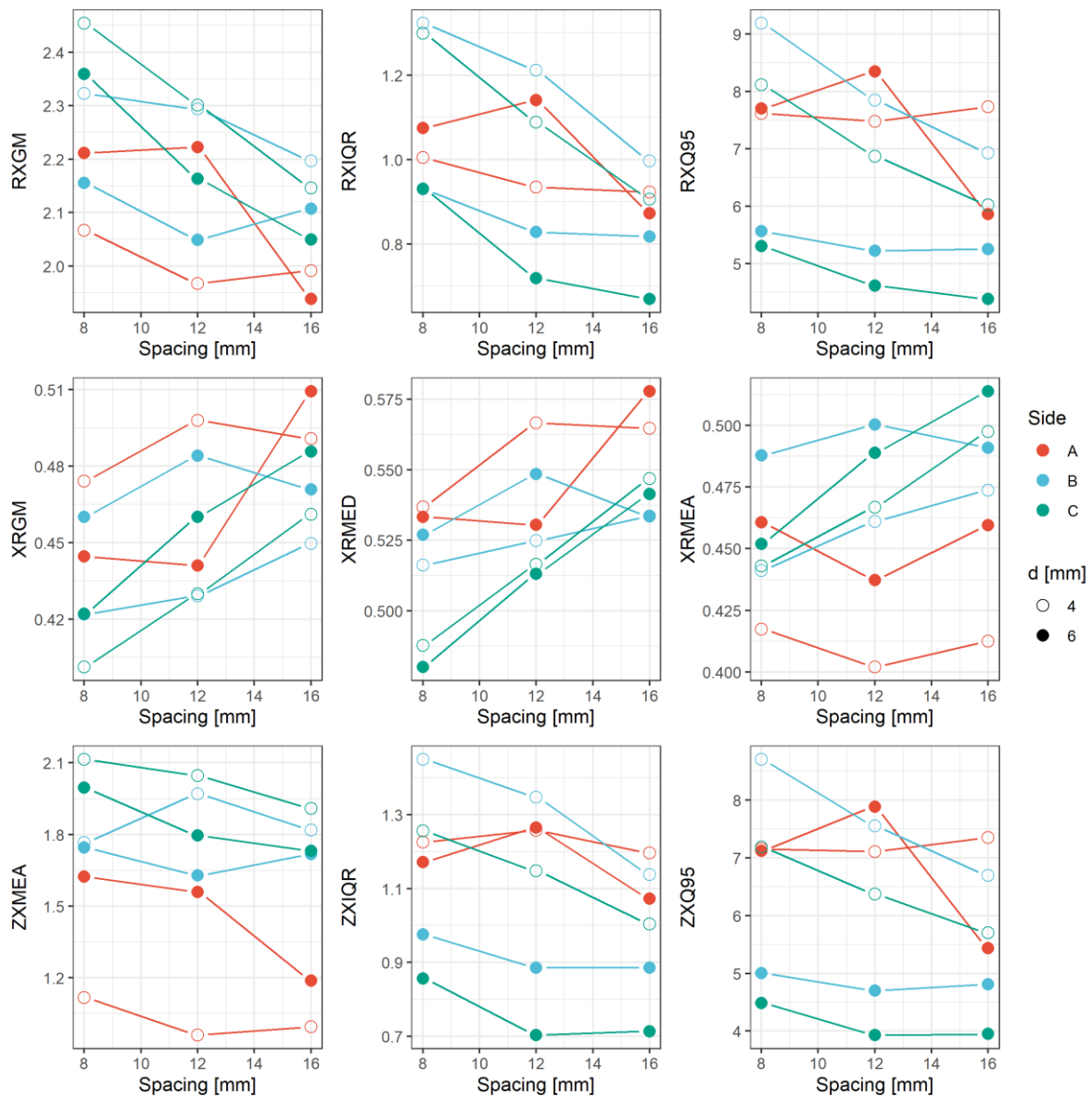
Figure 75: Response values for the features selected for material classification

6.2.6 Summary and Interpretations of Results

From the viewpoint of rock characterisation, directional anisotropy could potentially complicate the FCR-based rock classification process, as it alters the general behaviour of the force component ratios. However, this effect could be used to monitor the foliation direction with regard to the excavation direction. It showed that features incorporating $FCR(F_x/F_z)$ could provide more reliable results for such a monitoring.

In terms of excavation efficiency, the low effect of the *spacing* on F_x and F_z for foliation Sides A and C could be utilised to improve the efficiency of the process by choosing a higher *spacing*.

Due to restrictions of maximum forces and the very high dynamic behaviour induced on the test stand during cutting of Sides B and C, the maximum d was limited to 6 mm, the lower value for d was set to 4 mm. As was shown in Experiment CO, a very low *cutting depth* changes the behaviour of the force

components. As such, limited statements can be made about the suitability of the features. Further considerations on this can be found in the discussion in Chapter 7.1.2.

6.3 CR – Cracked Granite

In this chapter, the results of Experiment GR are presented concerning the force components and their ratios. This analysis extends the already published results that can be found in [38, 105–107, 163]. There, the effect of microwave radiation on cutting forces was presented. A spatial analysis is conducted regarding the cracking state of the samples. The behaviour of the features is shown, and the additional feature *contact ratio* is introduced as a result of the Experiments GN and GR.

During this experiment, the *cutting depth* could not be varied; only the *spacing* was varied in two steps. Because of this, the influence of changing *cutting depth* on the behaviour of features cannot be assessed. However, general assumptions can be made by combining the results with the learnings from Experiment CO.

Figure 76 shows photos of Samples B30 and B45. The samples were treated with a crack marking spray. While cracks can be seen in both samples, for B45 it shows clearly that due to the cracks, overbreak occurs. This overbreak effect cannot be seen in B30, and this observation affects all the following results.
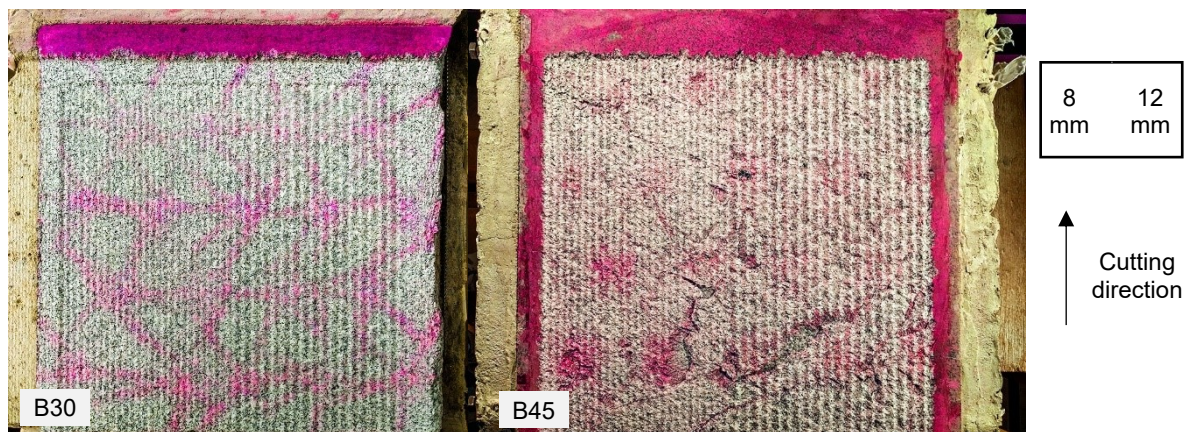
Figure 76: Photos of B30 and B45 during cutting experiments, with crack marking spray applied; magenta saturation enhanced with Adobe Photoshop

6.3.1 Force Component Results

The statistical summary of the results for the force components is shown in Figure 77. Table K-1 with the respective values can be found in Annex K.

Generally, F_z is the highest component, with a *mean* ranging from 7.0 kN for $s = 8$ mm and 45 s radiation time to 17.1 kN for $s = 12$ mm and 30 s radiation time; *mean(F_x)* ranges from 4.2 to 7.0 kN for the respective parameter combinations. This means that the average ratio of F_x/F_z ranges from 1.7 for B45 to 2.4 for B30. The *mean* of F_y shows considerably lower values with 2.1–3.5 kN. The *resulting force* shows *mean* values ranging from 9 to 19.5 kN. The values for $Q_{0.95}$ show a similar behaviour. They range from 10.6 to 15.3 for F_x, from 14.3 to 27.6 kN for Fz, and from 5.1 to 7.9 kN for F_y. This also means that the ratio $Q_{0.95}(F_z)/Q_{0.95}(F_x)$ is lower for than for the mean forces (1.3–1.8). At the same time, $Q_{0.95}$ for F_{res} ranges from 17.7 to 31.1 kN.
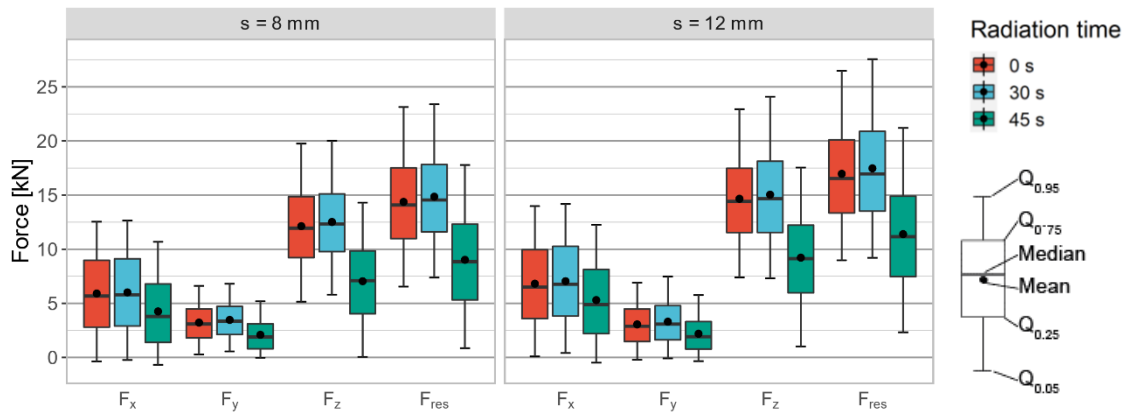
Figure 77: Cutting force components for different radiation time and spacing, layers 2–4 of Experiment GR

To summarise, most force component statistics are the highest for 30 s radiation time and the lowest for 45 s radiation time. In B45, F_z showed the largest decline. The reduction in the *mean* of F_z is 49%. At the same time, F_y shows a reduction of 42% and F_x a reduction of 34%. This can be related to the areas where overbreak occurred, resulting in no force in z-direction while the tool was in the area of the cavities.

Figure 78 presents the proportion of data points below 0 kN for F_x (PP_{x0}) and the proportion of data points below 0.5 kN for F_z ($PP_{z0.5}$). It shows that, for both force components, the values show little difference between 0 and 30 s radiation time. For PP_{x0} they lie between 3.3% and 5.9%, for $PP_{z0.5}$ they range from 0.1% to 0.8%.

For B45 that showed visible overbreak during cutting, the results for PP_{x0} between 9% and 7,4%. This represents a relative increase of 52% to 62%, respectively, compared to B0. For $PP_{z0.5}$, the values increase to 8.4% and 3.6%. Compared to B0, this represents an 18- and 14-fold increase, respectively.
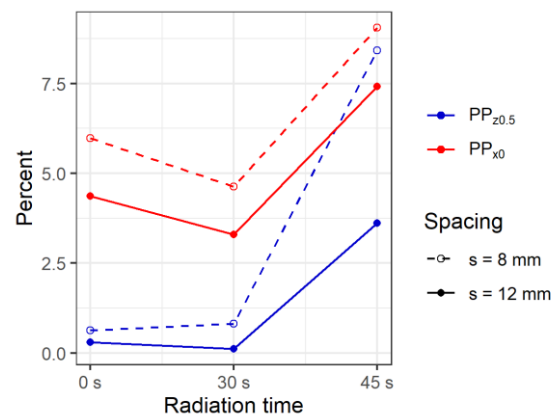
Figure 78: Proportion of data points below 0 kN for F_x and below 0.5 kN for F_z for Experiment GR

Figure 79 shows the behaviour of the features that were selected in Experiment CO. Additionally, *YXQ95*, *YXIQR*, and *CR* are shown. The features are calculated from the real-time data. For the three radiation times, all features indicate little or no change from 0 to 30 s for both *spacings*. However, a sharp change occurs from 30 to 45 s. Here, *XZGM*, *XRMEA*, *XRME*, *XRGM*, and *CR* show an increase and the features *RXGM*, *ZXQ95*, *ZXIQR*, *RXQ95*, and *RXIQR* all decrease. All these features show a higher difference between uncracked and cracked rock states, while the values for the different *spacings* do not differ to that extent. *YXIQR* and *YXQ95* show another behaviour. Here, the difference in the values is majorly defined by the *spacing*. For *YXQ95*, $s = 12$ mm, the values range in a band of 2 to 2.2, whereas the values for $s = 8$ mm range from 2.3 to 2.6. A similar picture is presented for *YXQ95*. There, the values for $s = 12$ mm are in a narrow corridor between 0.53 and 0,54 while the values for $s = 8$ mm form a wider corridor from 0.49 to 0.58.
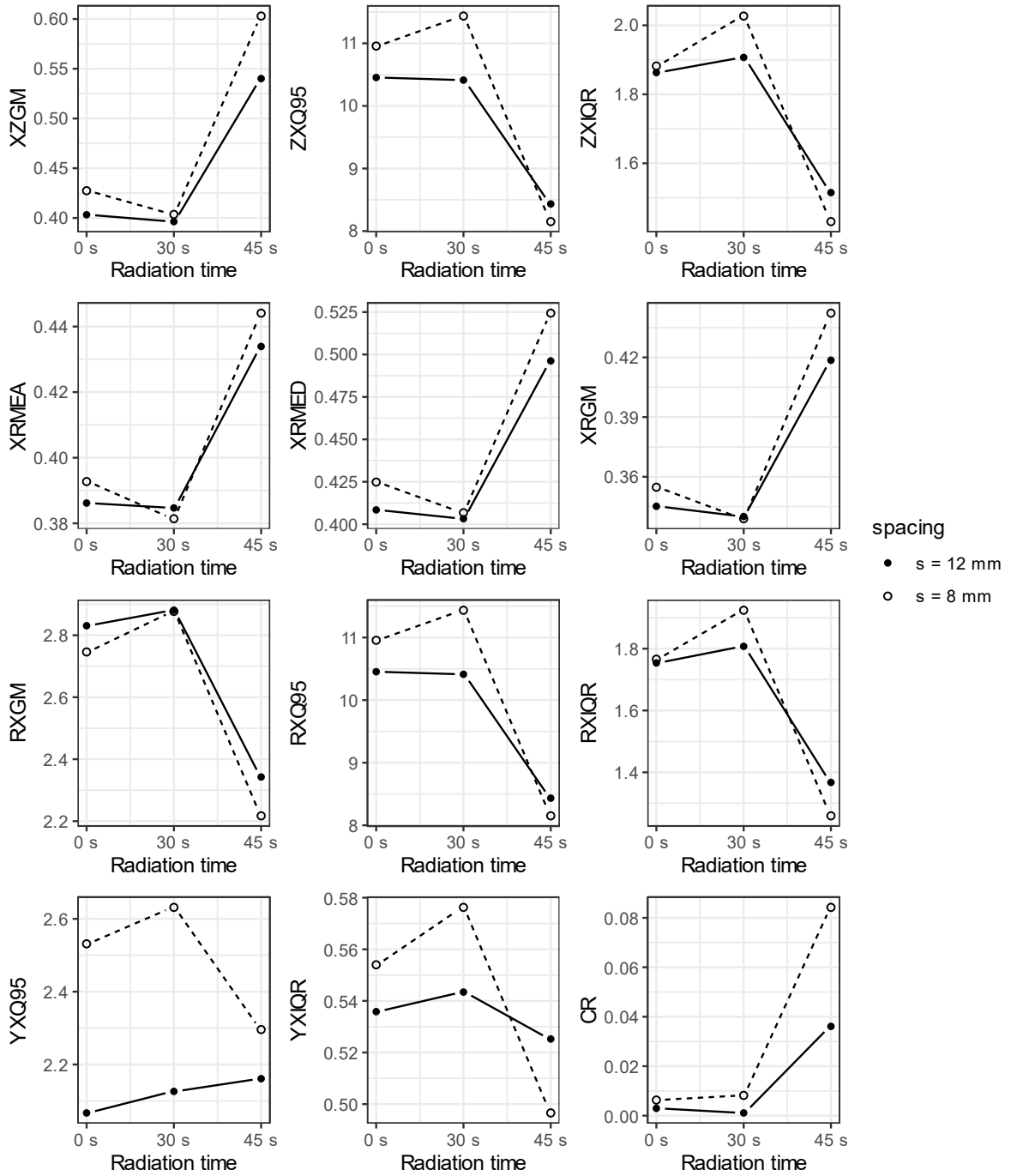
Figure 79: Behaviour of features for Experiment GR

6.3.2 Spatial Analysis

The previous chapter showed significant differences in both raw forces and in extractable features between B45 and the other two samples. To evaluate the effects of these discoveries, the results are analysed in spatial relation to the occurrence of cavities. This analysis is done exemplarily on the data of the 4th layer of blocks B45 and B30. Figure 80 shows the laser scans of this layer for the two blocks. The overbreak for B45 is clearly visible.
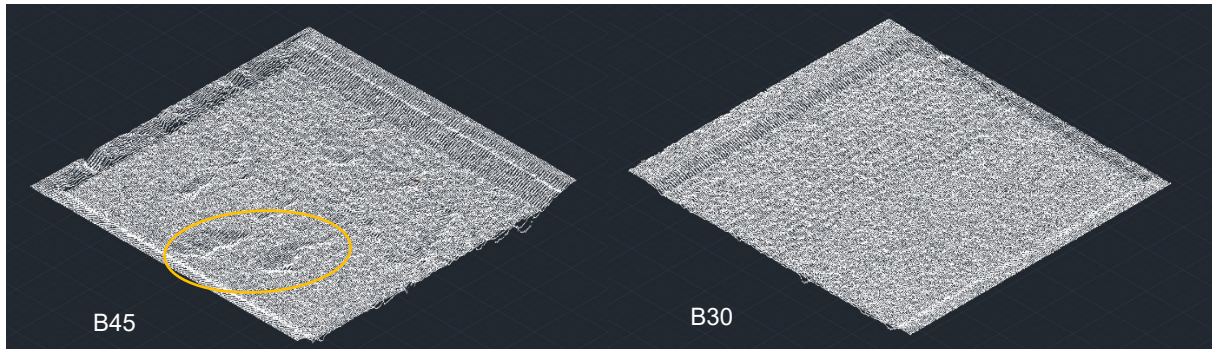
Figure 80: Overbreak in B45 and B30, Layer 4

Figure 81 shows the force F_z in relation to the cavities. A sample of 1% of the raw data points is plotted. The black isolines show the cavities that were extracted from the laser scan. For this, the 10% of all grid points with the lowest z-values were selected. It can be seen that very low forces are recorded over the cavities and in their vicinity. It can also be seen that forces of over 30 kN occur in areas without cavities.
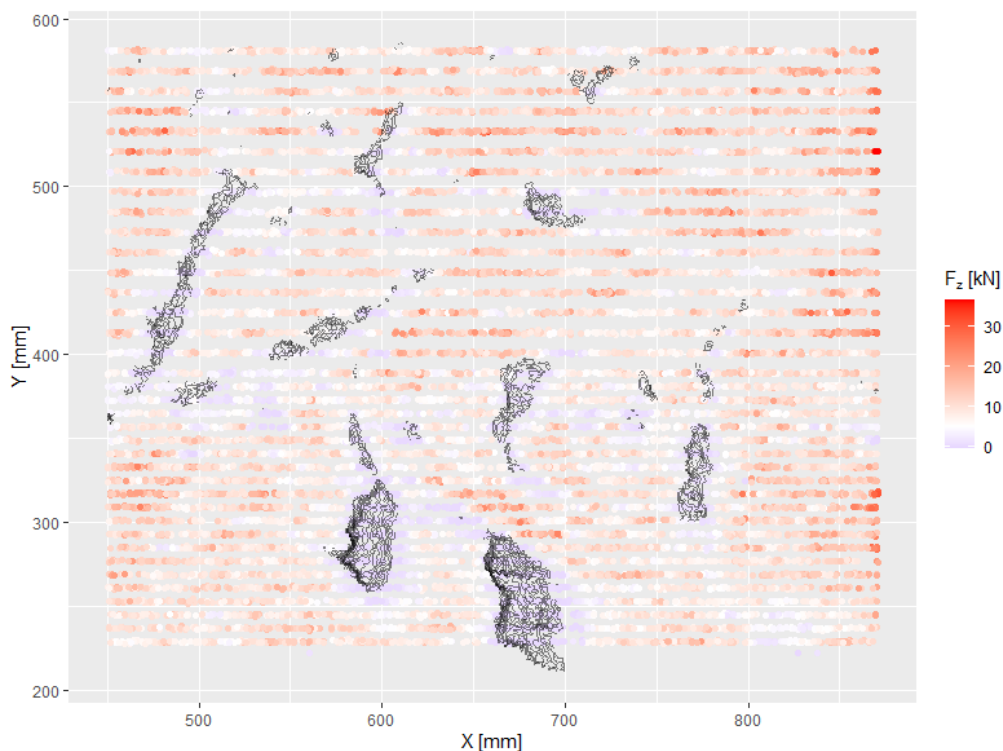
Figure 81: F_z in relation to overbreak; black isolines: overbreak

Resulting from this, the *contact ratio (CR)* was calculated in a grid model (grid node spacing = 1 mm) with different *search radii (SR)* after the method described in Chapter 5.8. Figure 82 shows the results of this calculation. *Search radii* from 10 to 150 mm are plotted for B45. The cavities are again shown as black isolines. The same layer is plotted for B30 with an *SR* of 50 mm as a control example. The

97

variation of the *SR* shows that smaller *radii* emphasise smaller structures, while larger *SR* present a blurrier, more general picture. The *SR* of 10 mm shows the beginning effects of a recurring tooth-shaped structure on the edges of the cavities that resembles a Moiré effect. For the control sample B30, a uniform mapping result can be seen. In addition, *CR* values are very low, with a local maximum of approximately 0.001. This means that the pick was in contact with the rock all the time while cutting B30. The local values for B45, *SR* = 50 mm, reach 0.55 for the main cavities. For *SR* higher than 50 mm, a superposition effect can be observed. Grid points between two cavities receive large *CR* values, although no cavity is located on this spot. This is related to the fact that these grid points receive many low F_z values from multiple adjacent cracks—which causes *CR* to rise.
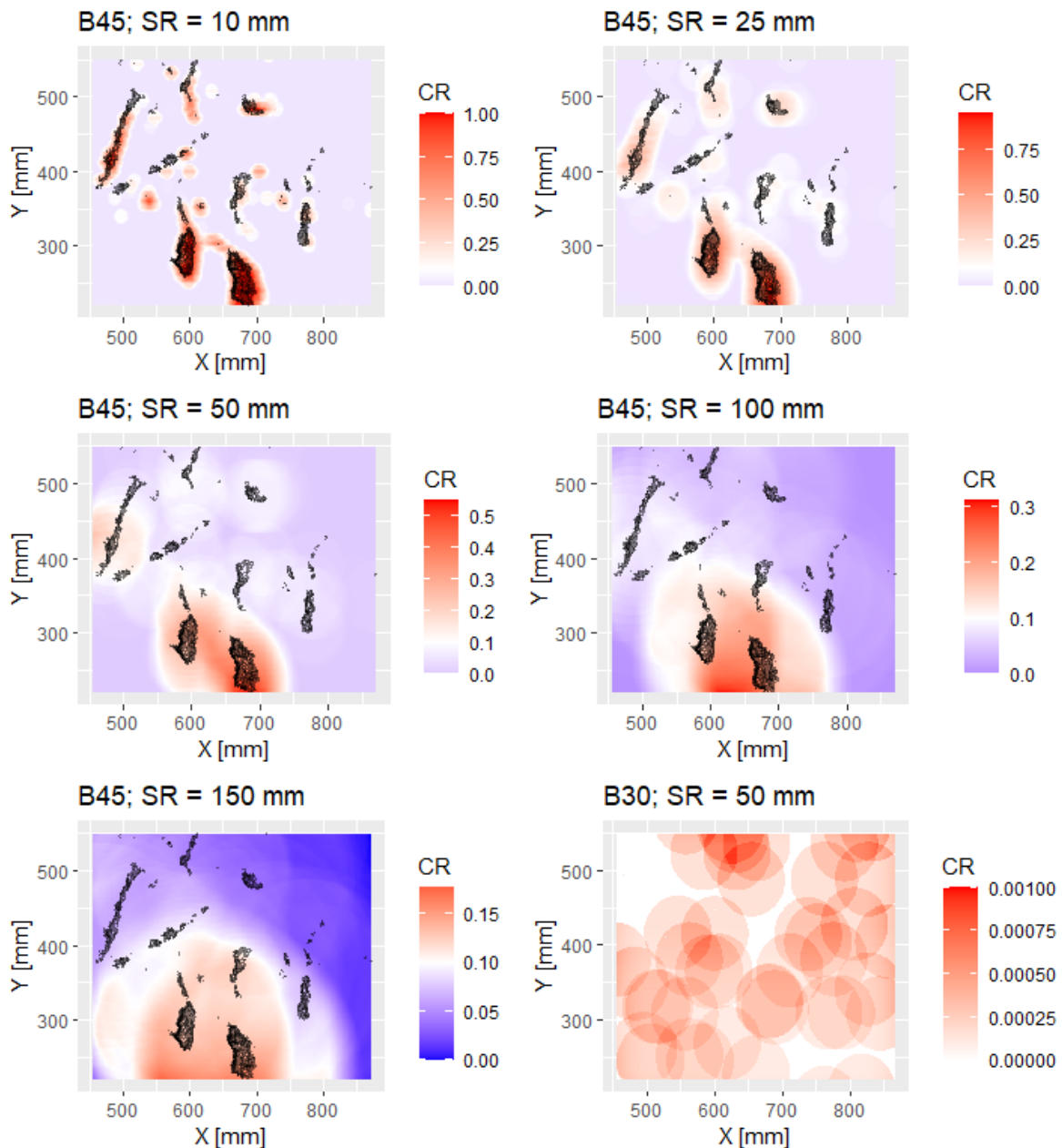
Figure 82: Contact ratio (CR) for different search radii (SR) for B45; B30 as reference

Both size and density of the cracks influence the result, as well as the cutting parameters. If the distance between individual cuts is higher than the *SR*, Moiré effects can be expected. Resulting from this, a *search radius* of 25 or 50 mm appears as a reasonable trade-off between *accuracy* and robustness for the identifying cavities with *CR*.

6.3.3 Error Analysis

Between B0 and B30, little difference in force responses was measured compared to B45. B30 shows no measurable weakening effect due to the microwave radiation. B30 even shows slightly increased cutting force responses compared to B0.

Reasons for this could be:

a) Block B30 was generally tougher than the other two blocks.
b) The induced cracks in B30 are present, but the grains are still interlocked – resulting in no measurable weakening of the rock.
c) Due to thermal processes, an internal stress-relieving effect occurs. Some researchers made similar findings when investigating the effects of microwave radiation on rock integrity [191, 192]. Also, already present microcracks could be closed due to the heating [107].

One, two, or all three reasons could play a role. To investigate possible Causes a) and b), the backside of B30 was cut in the same fashion as B0. No cracks were visible on the backside of B30, and no cracks from the frontside could be observed throughout this additional experiment. The results are shown in Figure 83. The values for the figure are located in Annex L

The *mean* force responses for F_x, F_y, and F_z with the respective *standard deviation* are shown. It is obvious that the values for the unirradiated side of B30 and B0 are similar. For F_z, $d = 16$ mm, they are 14.3 and 15.2 kN, respectively. The values for all forces of the radiated side of B30 are higher than those of and B0 and the unirradiated side of B30. For example, the *mean* of F_z, $s = 16$ mm for the radiated side of B30 is 14% higher than for the unirradiated side.
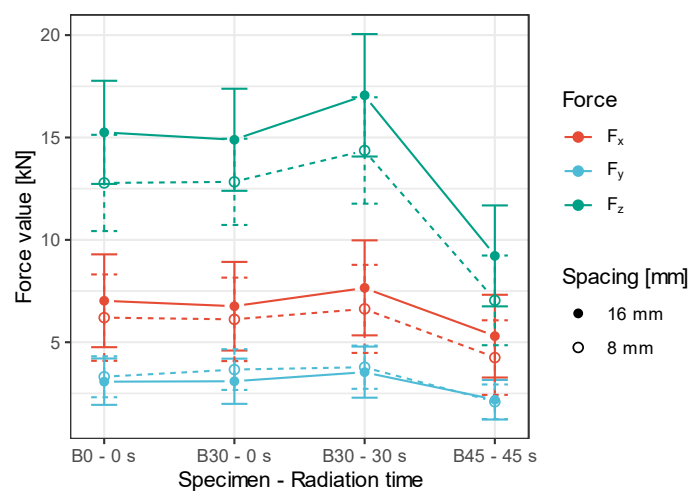
Figure 83: Mean values of forces F_x, F_y, and F_z with standard deviation (error bars), including repetition of untreated block

Since the forces of the radiated side are higher than the forces of the unirradiated side. Causes a) and b) appear to be unlikely reasons for the higher forces. This speaks for the hypothesis that the radiation of B30 seems to have an effect that increases the cutting resistance of that rock, although cracks are at least

visually present in the rock. The damaging effect was not sufficient to override the strengthening effect of the microwave radiation in this sample.

6.3.4 Summary

In summary, the occurrence of cracks influences the force components and the FCR on the scale of the whole experiment. However, to show a weakening effect on the cutting resistance, it appears that the cracks must have a minimum opening to override strengthening effects of the microwave radiation. When the weakening effect of the crack network is high enough, overbreak occurs. This overbreak results in cavities where the pick does not have contact with the rock. This substantially alters the measurable forces and the extractable features.

The sensitivity of $PP_{z0.5}$ is much higher than that of PP_{x0}. As such, $PP_{z0.5}$ is chosen to serve as an indicator for cavities. As a feature, it is called *contact ratio* (*CR*). For further use, the *search radius* is important as it influences the noise and *accuracy* of *CR*. For the case study in Chapter 6.4, a *search radius* of 50 mm will be used for the computation of *CR*.

6.4 Case Study

In this case study, the machine learning algorithms as described in Chapter 5.11 are utilised to estimate their suitability for rock classification from cutting force data. Prior to conducting this study, a preliminary assessment on the applicability of the workflow proposed in this work was conducted on a limited dataset (Annex M). For this final case study, a set of features is derived from the results of Experiment CO (Chapter 6.1) and extended by the feature *CR* after Experiments GR and GN (Chapters 6.2 and 6.3, respectively). The final set of features was chosen based on a limited, iterative, hyperparameter variation as explained in Annex N.1.

The final feature set was: *XZGM*, *ZXQ95*, *ZXIQR*, *XRMED*, *RXGM*, *RXQ95*, *RXIQR*, and *CR.* The cutoff for *CR* was set to 0.55. Blocks from the block model that received a *CR* of more than 0.55 were considered "air". These blocks were exempted from the machine learning process.

The workflow for this case study is outlined in Chapter 5.12. The code for the calculations can be accessed in Annex O (on CD). The calculated 3d-models can be explored online under:

Link to Results of Case Study

https://brunanza.shinyapps.io/RockModelVieweR/

Figure 84: QR-code to access detailed visualisation of results of the case study

Eight different training cases were used for this study (Table 24). Five training cases consisted of only one sample (FBA1 to FBA3, PB1, and PB2). In the other three training cases, multiple samples were used for training. Case All uses all samples for training, representing a large and diverse dataset with three rock types (concrete, F-Ba ore, and Pb-Zn ore). The Case Only_FBA represents all three FBA samples together. Accordingly, Only_Pb represents the two PB samples together. As such, these two training cases represent smaller and more homogeneous subcases of Case All. Each machine learning algorithm was trained with the eight training cases and its general performance during training was evaluated.

Furthermore, all trained learners were applied to all other cases to predict rock zones. As such, they are cross-compared to each other (e.g., a classifier trained with FBA1 is used to predict not only itself, but also the Cases FBA2, FBA3, All, etc.). This results in a matrix of 64 predictions per ML-algorithm. Since the classifiers are also used to classify the training case they are trained with, n-fold training and cross-validation (see Chapter 5.11) are used to prevent overfitting.

Table 24: Training cases for case study

Training case	Samples used
All	FBA1, FBA2, FBA3, PB1, PB2
FBA1	FBA1
FBA2	FBA2
FBA3	FBA3
Only_FBA	FBA1, FBA2, FBA3
PB1	PB1
PB2	PB2
Only_PB	PB1, PB2

Before the actual machine learning, the features were coded into the block models. The computation times are shown in Table 25. The FCR-features and feature *CR* were computed separately because they utilise different *search radii*.

Table 25: Times for moving-window feature computation

Sample	Time for all FCR-features [min]	Time for CR [min]	Total time [min]
FBA1	4.0	1.7	5.7
FBA2	13.3	6.1	19.4
FBA3	15.1	8.3	23.4
PB1	7.3	2.0	9.3
PB2	3.5	1.1	4.6

Also, a variation of the training data was performed for the two supervised algorithms (DRF and ANN). Hereby, the training-test split was varied from 2% to 99% training data. By that, additional information on the required amount of training data was achieved.

6.4.1 Feature Distribution in Block Models

The distributions of selected features are investigated to understand how the machine learning classifiers operate and to draw conclusions between the machine learning side and the practical engineering side. The feature calculation is based on a moving-window algorithm, as explained in Chapter 5.8. The plots show the distribution of features for the different material types within a sample. The results are presented as violin plots. The distribution density is shown as thickness of the violins; the mean dot inside the violins. The distribution of the three features that incorporate the ratio F_{res}/F_x, namely *RXGM*, *RXIQR* and *RXQ95*, are shown in Figure 85.

A bimodal distribution can be observed for some combinations of samples and features. This is clearly visible for PB1, features *RXIQR* and *RXQ95,* to some extent for PB2 (*RXGM*, *RXIQR, RXQ95)*, and FBA1 (*RXIQR, RXQ95).*

For *RXGM* and *RXIQR*, the mean values increase from FBA1 to FBA3. For *RXQ95*, this increase from FBA2 to FBA3 is not very pronounced. The values between rock types are relatively similar for PB1 and PB2. Especially, the distribution of *RXIQR* for PB1 is remarkably similar between concrete and ore. Furthermore, it can be seen that some distributions show comparatively wide distributions (FBA3, *RXQ95*), while others appear in a narrower window (FBA1, *RXGM*). Lastly, some distributions show a

pronounced one-sided tail behaviour, for example, *RXGM* for PB1 (concrete) or RXIQR for FBA3 (both materials).
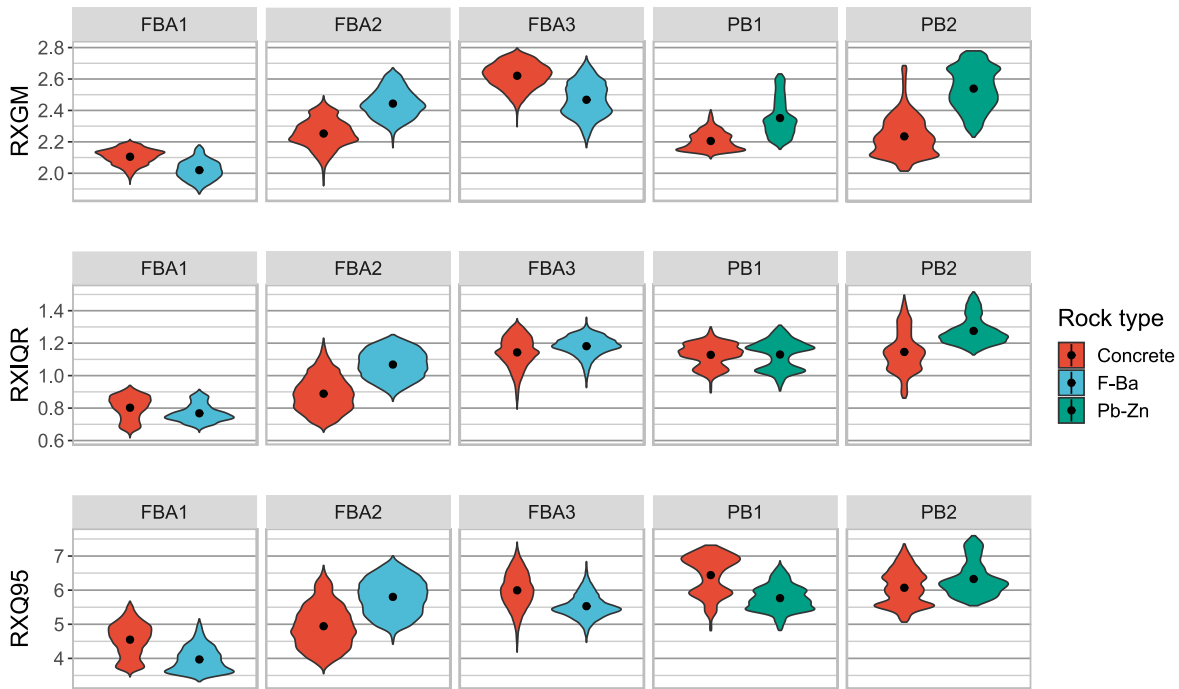
Figure 85: Distribution density of features RXGM, RXIQR and RXQ95 for the five experiments of the case study as violin plot; • – mean value

Figure 86 shows the violin plots for the feature *contact ratio*. The results deviate strongly from the previous plots. The samples PB1 and PB2 show very low values, indicating little overbreak for both concrete and ore—the material was solid. This is different for the FBA samples. Here, higher values are typically observed for the F-Ba ore, except for FBA2. This indicates that the ore samples in FBA1 and FBA3 are of relatively low integrity. It stands out that the concrete shows comparably high values for *CR*—although it should show a solid composition. This can be explained by a spillover effect. Since the features are calculated with a moving window algorithm, blocks that belong to the concrete, partially receive values that are located in the adjacent F-Ba areas. Additionally, most distributions show a long tail towards high *CR* values.
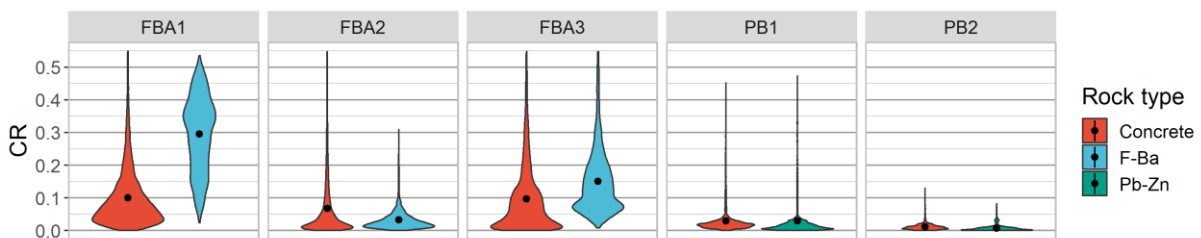
Figure 86: Distribution of contact ratio for the five samples of the case study as violin plot; • – mean value

Figure 87 a) exemplarily shows the spatial distribution of *RXGM* for all samples of this case study. The range of *RXGM* is approximately 1.8–2.8. In four of the five concrete samples, the values of the concrete range between 1.9 and 2.3. Only for FBA3 do the values reach up to 2.8.

Due to the moving-average feature calculation, soft transitions in the feature levels between the rock zones can be observed.

In addition, it can be seen that the *RXGM* distribution is more homogeneous for the PB samples, with the exception that the right part of the PB1 sample appears to behave differently from the other parts and shows values more similar to the concrete. In fact, this leads to classification problems. This can be seen in the online results of the case study (QR-Code, Figure 84) or in Panel b) of Figure 87. It can be seen that the DRF that was trained on sample PB2 could not identify this part of the Pb-Zn ore—because its features were too similar to the concrete.

In addition, a cavity is located in the ore part of FBA3. This cavity is identified as a cavity because the values for *CR* are above 0.55. Also, it can be seen that parts of the sides of the edges of the blocks are filtered out. These sides also triggered the *CR* filtering.

In summary, the differences between the material types are visible both in the grouped violin plots and in the spatial distribution of the values. However, especially the FBA-samples present very inconsistent feature distributions, both for the F-Ba and the concrete zones. This leads to performance problems, which will be discussed in detail in the following chapters.

a)
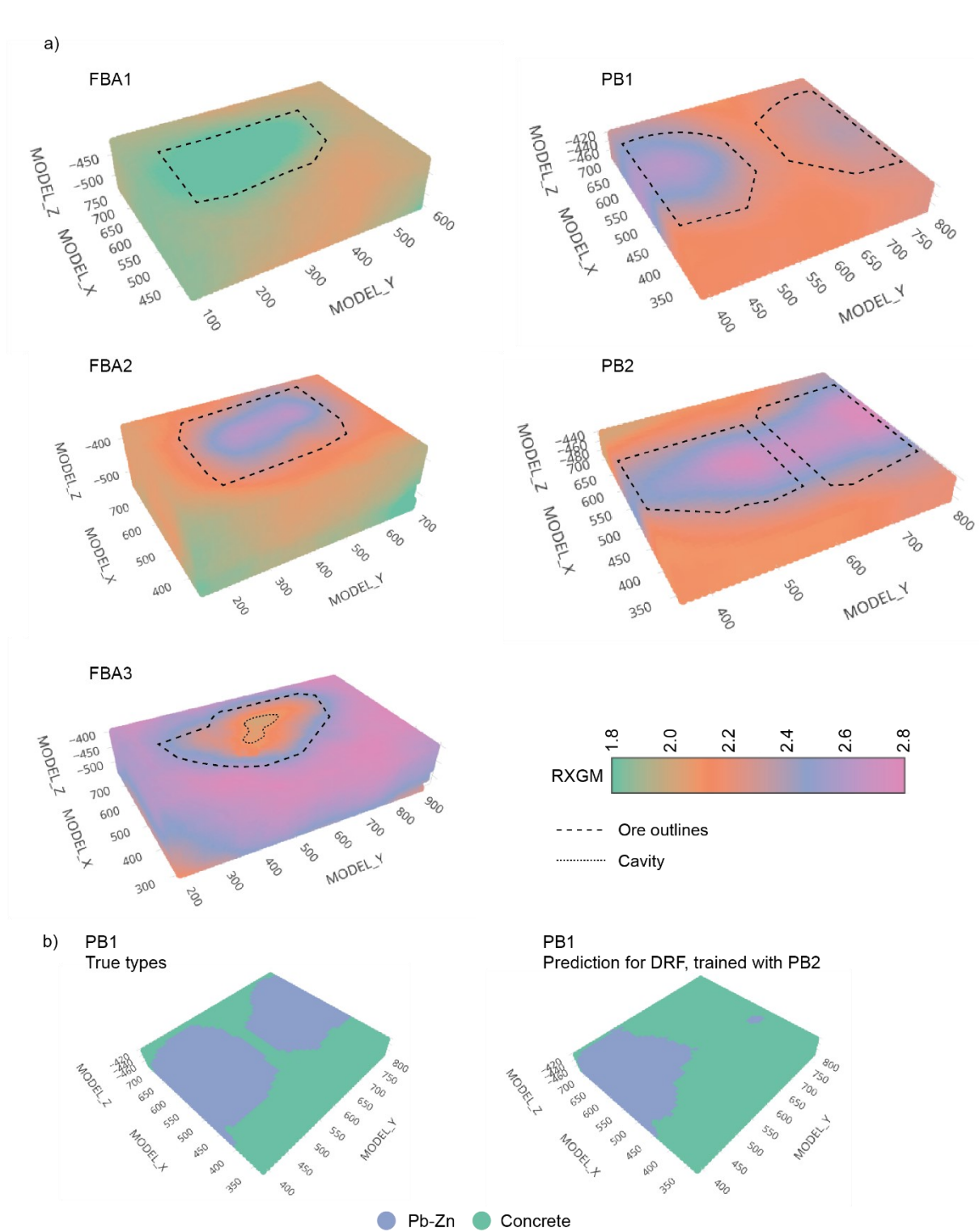
Figure 87: a) Distribution of feature RXGM for all samples of case study, the dashed line indicates the approximate location of the samples' ore part; b) wrong prediction of ore for DRF trained on PB2 and applied on PB1

6.4.2 Distributed Random Forest

The basic data for the DRF training process are shown in Table 26. The mean training time was 5.2 to 99.8 s per model. The training statistics refer to a full training cycle of the n-fold training. The training time depends largely on the size and the number of classes present in the dataset. Case All had the longest training time, whereas the training time of Case Only_FBA was one-third of the latter—although Only_FBA has 86% of the number of cells of Case All. Case All had to consider all three rock classes during training, whereas the other cases only had to take into account two cases. The cross-validation results are consistent for all cases. The mean *cross-validation accuracy* was 91–96%. The standard deviation was sufficiently low to suggest consistent training (maximum 0.7%). For Only_FBA, the mean number of leaves was 709.7, which is higher than for the more complex Case All. Additionally, the number of leaves for FBA1 and FBA2 is comparably high. This indicates that these samples are relatively complex.

Table 26: Calculation times and general properties for the DRF model

Name	Training time [s]		CV-accuracy		Mean nr. of leaves	Nr. of cells	Mean cells / s
	mean	± σ	mean	± σ			
FBA1	25.3	± 0.7	0.946	0.004	328.6	21,927	866.6
FBA2	26.1	± 1.0	0.924	0.004	446.5	44,860	1718.8
FBA3	26.5	± 1.0	0.961	0.002	455.0	50,720	1914.0
PB1	5.6	± 0.5	0.957	0.003	139.3	10,080	1800.0
PB2	5.2	± 0.4	0.962	0.007	114.2	8,970	1725.0
All	99.8	± 3.5	0.915	0.001	546.0	136,557	1368.3
Only_FBA	33.9	± 1.2	0.922	0.002	709.7	117,507	3466.2
Only_PB	23.8	± 0.7	0.954	0.003	241.9	19,050	800.4

General Properties of DRF

Features: XZGM, ZXQ95, ZXIQR, XRMED, RXGM, RXQ95, RXIQR, CR

Max tree depth: 11	Training/validation: 0.2/0.8
Number of trees: 100	Column sample rate: 3/8
Balancing of classes: on	Row sample rate: 0.632
nfolds: 5	

In this work, the key parameter to define classification success is *accuracy*. Figure 88 shows the *accuracy* heatmap for the DRF model. The columns indicate the cases with which the model was trained; the rows indicate the cases the learner was applied to. The diagonal shows the *self accuracy* when the learner predicts the full dataset from which it received its training data. Related to the markings in the figure, it can be seen that:

a) The DRF that has been trained with all the data shows an overall *accuracy* of 0.91–0.95. Furthermore, if the algorithm learned on a training sample of all rock samples, it can classify the remaining data with comparably high *accuracy*. It means that the DRF is capable of capturing the variation of all rock type behaviours relatively well.

b) The *cross-accuracy* between the samples FBA1 and FBA2 lies at 0.62 and 0.73, respectively. This is substantially lower than the *accuracy* of the DRF trained with all samples. However, parts of the block are identified correctly. The DRF trained with sample FBA3 shows an *accuracy* below 50% for samples FBA1 and FBA2. This means that the algorithm classifies systematically wrong in this situation. In cases where one sample from the FBA group was used to classify Cases Only_FBA or other individual FBA samples, the performance was not sufficient due to a partial systematic false classification. This is related to the systematically wrong classification between FBA3 and the other two FBA samples.

c) Expectedly, the classification of the DRFs trained with the PB samples is systematically wrong in the group of FBA samples. The same is true for FBA to PB. This is expected as the FBA samples do not "know" the Class of Pb-Zn ore and vice versa. The only material that both samples share is the concrete matrix. Accuracies above 30% show that major parts of the concrete were identified correctly.

d) In the group of the PB training cases, the *cross-accuracy* is much higher than in the group of the FBA training cases. The DRF trained with PB1 shows a *accuracy* of 0.83 for PB2, whereas the DRF trained with PB2 shows an *accuracy* of 0.62 for PB1.

The results confirm that the learning algorithm does not recognise rock types it has not been trained on. This goes in line with the findings from a), that if a model has been trained with a sample of all specimens, it is well capable of classifying the rest of the data—because they are sufficiently similar. The *cross-accuracy* between the FBA samples is comparably low. The *cross-accuracy* between the PB samples is partially higher. This illustrates that the variation of the rock properties between different samples of the same group can be relatively high—to the extent that it is no longer possible for the learner to perform accurately on other samples of the same group.
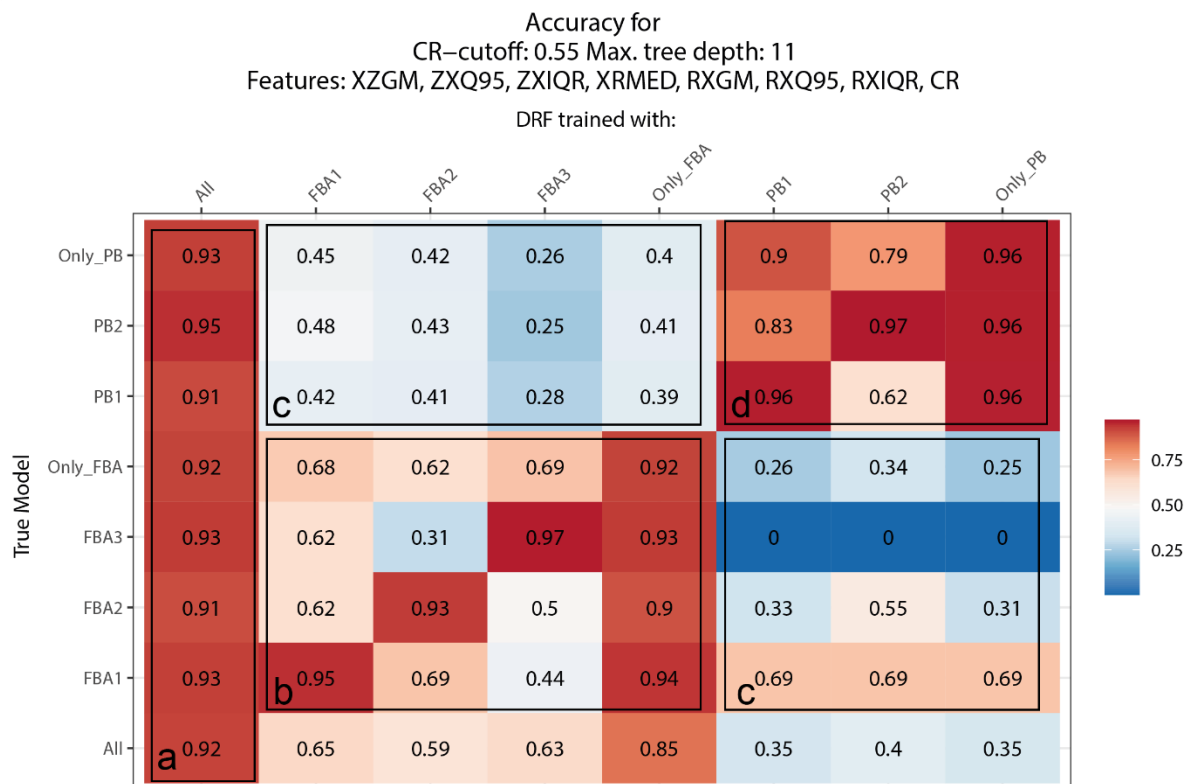
Figure 88: Accuracy heatmap for distributed random forest classification

Feature Importance

Figure 89 shows the *standardised feature importance* for the eight different training cases. Most training situations show one dominant parameter and a maximum of four parameters that receive an importance rating of more than 0.65. Balanced feature importance ratings speak for the necessity of all features for classification. The dominant parameter is *XZGM*, which has the highest importance rating in four of the eight training cases. It is followed by *CR*, *XRMED,* and *RXGM*. Compared to the results from Figure 65, p. 85, where the scaled importance of the DRF for Experiment CO was shown, the *feature importance* is slightly different here. For Experiment CO, *RXIQR*, *RXGM* and *ZXQ95* received a rating

above 0.70. Here, *RXIQR* received higher ratings for Cases All, FBA2, and Only_FBA. *RXGM* received a high rating for FBA2, FBA3, and Only_FBA. *ZXQ95* did not receive higher ratings at all.

However, few features receive a rating below 0.2. These features contribute relatively little to the final result. If feature reduction is the aim, these would be removed first. It is noteworthy that the features are more balanced for training situations that incorporate a diverse set of samples. This is especially true for Case Only_FBA, which incorporates all FBA samples.

Additionally, it is noteworthy that the contact ratio received the highest rating for two training situations (All and FBA1). At the same time, the *contact ratio* received low to medium ratings for the other training situations.

Figure 89: Feature importance heatmap for distributed random forest classification

6.4.3 Artificial Neural Network

The basic data for the ANN training process are shown in Table 27. Three hidden layers with 25 neurons each were chosen as architecture. The same set of features as for the DRF model was used. Further details on the architecture can be found in Chapter 5.11 and Annex N.1.

It can be seen that the training of the ANN takes significantly more time than the training of the DRF. During the training of the largest dataset, Case All, the *training time* of the ANN was higher than that of the DRF by a factor of 4.6. The trainings of FBA2 and Only_FBA stand out, since they show the longest training times—although the datasets are not the largest. The longer training time means that it is more "complicated" for the ANN to adjust to the data. Furthermore, the *CV-accuracy* is slightly lower for the ANN than for the DRF. The *standard deviation* of the *CV-accuracy* is also slightly higher. This indicates less consistent results.

Table 27: Calculation times and general properties for the ANN model

Name	Training time [s] mean	± σ	CV-accuracy mean	± σ	Epochs mean	Nr. of cells	Mean cells / s
FBA1	76.1	± 50.9	0.952	± 0.006	54	21927	288.0
FBA2	365.7	± 92.4	0.915	± 0.022	322	44860	122.7
FBA3	94.4	± 53.1	0.952	± 0.006	39	50720	537.3
PB1	72.5	± 40.9	0.955	± 0.003	200	10080	139.0
PB2	25.1	± 21.9	0.950	± 0.012	63	8970	356.9
All	466.5	± 110.9	0.900	± 0.004	77	136557	292.7
Only_FBA	455.1	± 106.2	0.916	± 0.006	152	117507	258.2
Only_PB	243.5	± 98.9	0.923	± 0.029	242	19050	78.2
General Properties of ANN							

Features: XZGM, ZXQ95, ZXIQR, XRMED, RXGM, RXQ95, RXIQR, CR

Activation function: rectifier   nfolds: 5

Architecture: 8-25-25-25-(2/3)   Training/validation: 0.2/0.8

Balancing of classes: on

Figure 90 shows the *accuracy* heatmap for the ANN model. It follows the same procedure as in the previous Chapter 6.4.2. The columns indicate the cases the model has been trained with; the rows indicate the case on which the model has been tested. The diagonal shows the *self-accuracy*, and the other cells show the *cross-accuracy*. The results are generally similar to the results from the DRF training.
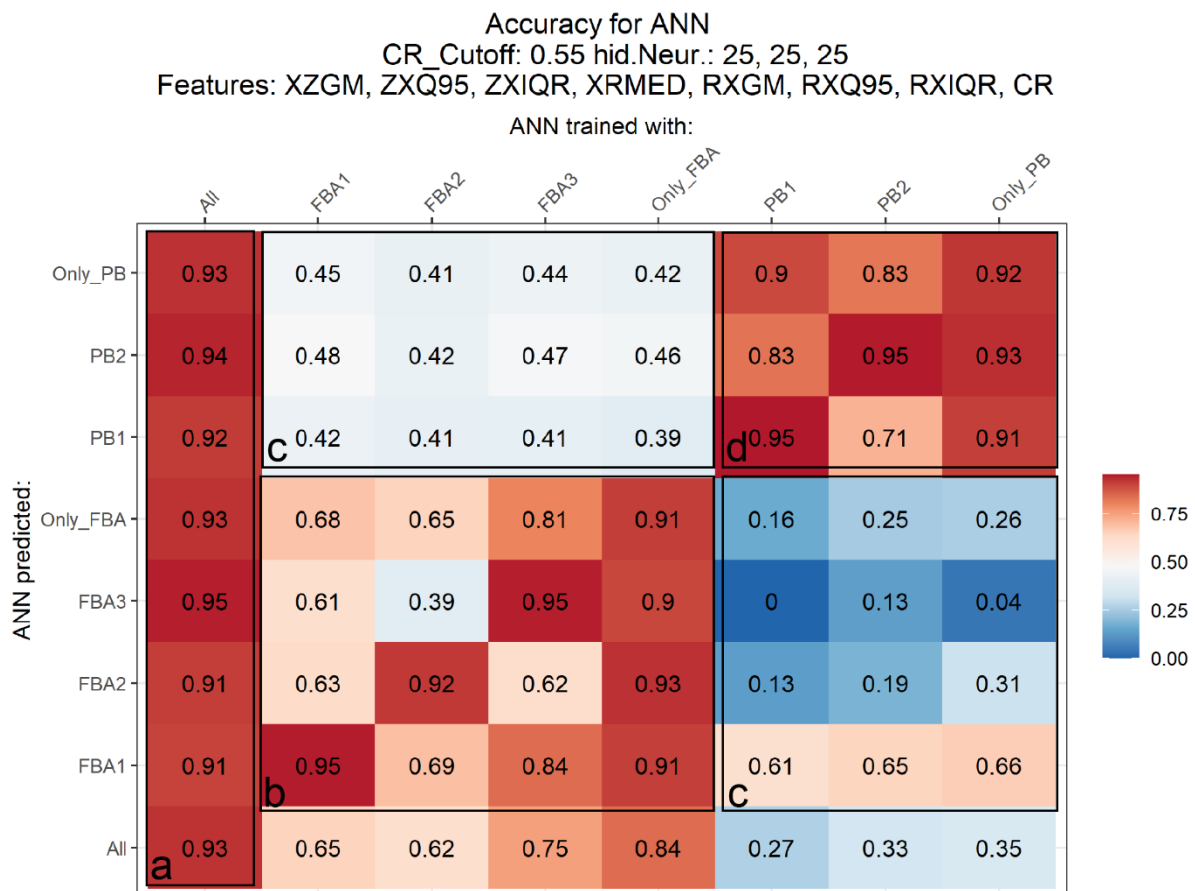
Figure 90: Accuracy heatmap for ANN classification

a) The network trained with all the data shows an *accuracy* of 0.91–0.95 for the individual data scenarios.

b) Between the samples FBA1 and FBA2, the *cross-accuracy* lies at 0.62, respectively 0.69. The ANN trained with sample FBA3 shows an *accuracy* below 50% for samples FBA1 and FBA2. This means that the algorithm classifies systematically wrong in this situation. If the ANN was trained only with one sample from the group of FBA-samples, it is not well able to classify the FBA samples. This is similar to the DRF behaviour.

c) The classification of the ANN trained with the PB samples is systematically wrong in the group of FBA samples and vice versa. Again, this is expected.

d) The classification results of the ANN trained with the PB samples show good *cross-accuracy* results. Here, the *accuracy* is slightly better than for the DRF. Especially for the training Case PB2 applied to PB1. There, 71% *accuracy* compares to 62% for the DRF.

These results are similar to the DRF results, whereas the ANN shows partially better performance for the *cross-accuracy* between cases. This suggests a better generalization behaviour.

Feature importance

Figure 91 shows the heatmap for the *standardised feature importance* for the ANN. Feature *XZGM* is among the most important features. It receives a high rating (>0.8) six times, followed by *RXGM (*five times). Also, *ZXIQR* generally shows higher ratings above 0.7 (seven times). The features *XRMED*, *RXIQR* receive medium ratings, *RXQ95*, *ZXQ95*, and the *contact ratio* receive lower ratings for most training cases. It stands out that *CR* receives high ratings for FBA3, PB1, and Only_PB. That *CR* receives high ratings for PB1 and Only_PB is surprising, because little difference in *CR* is observed between ore and concrete for this sample. However, a zone of altered gneiss is found in PB1 which causes high *CR* values.
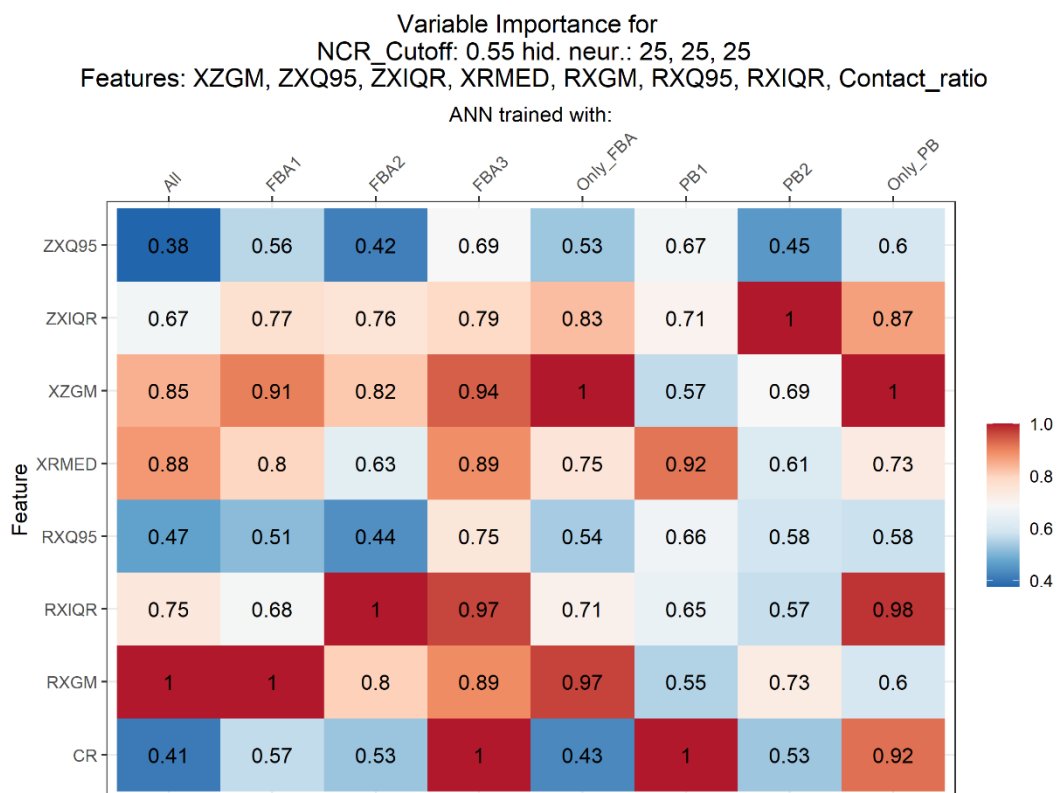
Figure 91: Feature importance heatmap for ANN classification

Summary

The ANN performed similarly to the DRF in terms of *accuracy*. The ANN provided a slightly higher *cross-accuracy* than the DRF. However, the training times for the ANN were longer than for the DRF. Additionally, the ANN shows a more balanced weighing of the features.

6.4.4 K-Means

For the k-means clustering, the same set of features was chosen as for the two supervised classifications. Table 28 shows the general properties of the algorithm used. It can be seen that the calculation times, in general, are very short. The biggest training Case, All, required a mean of 2.27 s for clustering. This compares to 99.8 and 466.5 s for DRF and ANN, respectively. The number of iterations shows how often the algorithms had to be repeated to find the optimal solution. Here, the largest training Case All stands out with 53 to 57 iterations. The other cases show a maximum of 20 iterations. This suggests that the number of clusters has a smaller effect than the size of the data set.

Table 28: Calculation times and general properties for the k-means clustering

Case	Training time [s]		Iterations	Nr. of cells	Mean cells / s
	mean	± σ	min-max		
FBA1	0.72	± 0.06	10-13	21,927	30,454
FBA2	0.30	± 0.01	12-13	44,860	149,533
FBA3	0.35	± 0.01	14-20	50,720	144,914
PB1	0.11	± 0.01	11-13	10,080	91,636
PB2	0.07	± 0.01	10-19	8,970	128,143
All	2.27	± 0.13	53-57	13,6557	60,157
Only_FBA	0.42	± 0.01	10-11	11,7507	279,779
Only_PB	0.21	± 0.01	12-16	19,050	90,714

General Properties of k-means

Features: XZGM, ZXQ95, ZXIQR, XRMED, RXGM, RXQ95, RXIQR, CR

k-clusters: 2/3/4	nfolds: 5
Balancing of classes: on	Training/validation: 0.2/0.8

Figure 92 shows the *accuracy* heatmap for the k-means clustering. It follows the same procedure as for the two supervised algorithms. The columns indicate the cases the algorithm has been trained with; the rows indicate the case on which the model was tested. The diagonal shows the *accuracy* when the learner is applied to the full dataset and not just the training data. Generally, the performance deviates strongly from the other two algorithms. With respect to the markings in the figure, it can be seen that:

a) Training Case All yielded highly varying results for each Case it classified. The *accuracy* is in the range of 0.02 to 0.64 for the classification of FBA3 and FBA1, respectively. This result differs significantly from the results of the two supervised algorithms (Chapters 6.4.2 and 6.4.3). There, the *accuracy* was consistently above 0.8. However, in this case, only the predictions of FBA1 and PB2 show results equal to and above 0.6. The predictions for Only_PB, PB1, and FBA2 are around 0.5. The predictions for Only_FBA, FBA3, and All are below 0.35, which suggests systematic misclassification.

b) For the cross-comparison in the group of FBA-training cases, a lower *accuracy* than for the supervised results is also observed. The *self-accuracy* is 0.61–0.82 for Cases Only_FBA and FBA2, respectively. With one exception, c*ross-accuracy* ranges between 0.33 and 0.61.

c) Between the PB and FBA samples, *accuracies* around 0.5 or below 0.4 occur. Both of which do not represent a successful classification. This again is expected and shows that unknown rock types cannot be predicted.

d) In the group of the PB training cases, the *accuracy* is much better than in the group of the FBA training cases. The *self-accuracy* ranges from 0.72 to 0.81 for Cases Only_PB and PB1, respectively. The *cross-accuracy* is lowest at PB2 predicting PB1 (0.5) whereas for PB1 predicting PB2, it is 0.76.
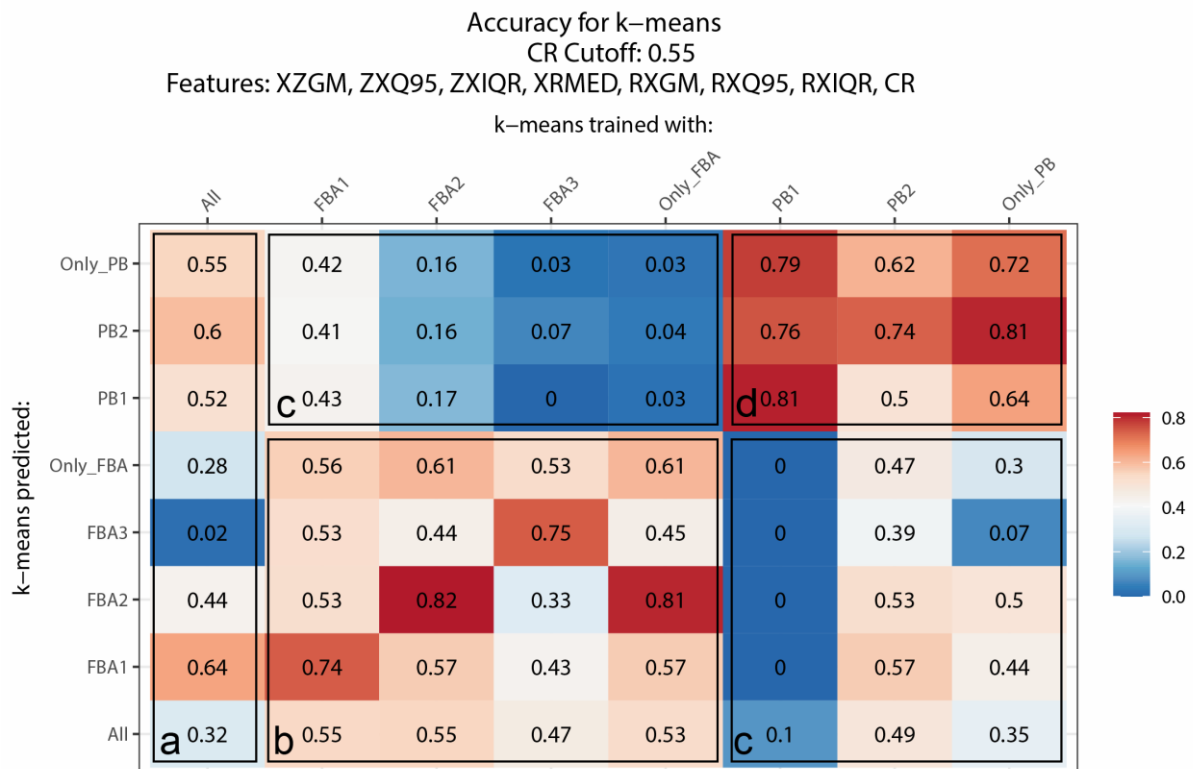
Figure 92: Accuracy heatmap for k-means classification

While these results show a lower *accuracy* than the supervised algorithms, acceptable results are shown for the *self-accuracy*. Especially since the algorithm is not supervised, the classification can be considered successful. Additionally, the limited *accuracy* of Case All implies that the number of clusters probably was not high enough for the variance that this dataset brings. As such, a high number of false predictions occurred.

6.4.5 Training Data Required

To gain further insight into the required amount of training data, the training of the learners was repeated varying the training-validation splits (2, 5, 10, 20, 40, 80, and 99% training data). For this analysis, n-fold training was not used. The training and evaluation process was repeated 15 times using resampling with replacement. The *mean* and *standard error* of the *training* and *validation accuracy* were calculated for the different training splits. The results are displayed in Figure 93 on the next page. The y-axis represents the *accuracy*, and the x-axis represents the percentages of training data.

At first sight, all results are relatively similar. The *training* and *validation accuracy* start converging at approximately 20–40% of training data. However, the *training* and *validation accuracy* of ANN converge generally at lower training splits than those of DRF.

Expectedly, for most situations, the best *accuracy* for the validation data is reached at 99% training data. The point of ideal convergence between training and validation accuracy is 80% for almost all Cases.

The *standard error* for the *validation accuracy* is lower for the DRF than for the ANN. Both show their maximum at 2% training data for sample PB1. For DRF, it is 0.006, and for ANN, it is 0.019. It stands out that the ANN also shows higher *standard errors* for the *training accuracy*. This means that the DRF training results are slightly more consistent.

Expectedly, the compound classification Cases All, Only_FBA and Only_PB show worse *validation accuracy* than the cases that only incorporate one sample. For Case All, the *validation accuracy* reaches a maximum at 0.9 for ANN and 0.92 for DRF. For Only_PB, a maximum of 0.96, and for Only_FBA, a maximum of 0.93 for both algorithms is recorded. Compared to this, the maximum for the individual samples was as high as 0.95 to 0.98.

In terms of approaching the maximum *validation accuracy*, the results are similar across all cases. The lowest *validation accuracies* appear at 2% training data, then rise steeply until 10–20% training data. The further increase from 20 to 40% is lower. Between 40% to 80% only a limited *accuracy* increase can be seen. The ANN even shows reducing *accuracy* for this step for Case Only_FBA. This means that 10–40% of the training data appear sufficient for the scenarios investigated. It should be noted that even training-validation splits of 2% show acceptable validation accuracy.

In summary, the ANN generally shows a better *validation accuracy* for low training splits. However, both algorithms show similar performance for medium training splits.
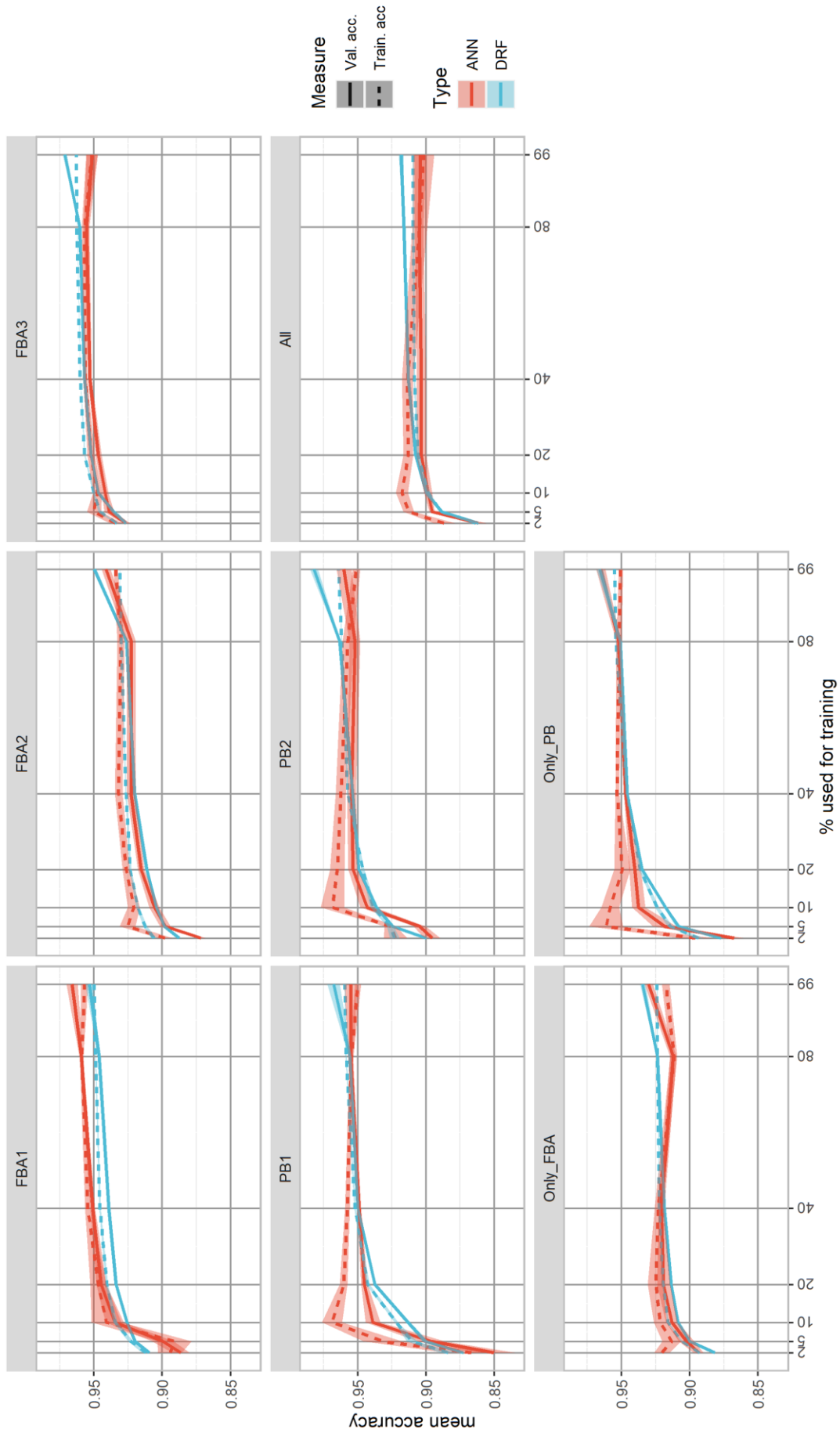
Figure 93: Proportion of training data used for training vs. mean accuracy for ANN and DRF; shaded regions show standard error

7 Discussion

This chapter puts the findings of the experiments into perspective with the literature review and the research goals of this work. First, the experiments conducted are critically reviewed and their outcomes are interpreted. From these considerations, a comparison of the three machine learning algorithms used in this study is presented. The chapter concludes with general considerations towards a near-tool MWC system.

7.1 Critical Discussion of Experimental Results

This chapter critically assesses the practical side of the cutting experiments, conditions of the experimental design, execution, and the experiments' results.

7.1.1 Experiment CO

Experiment CO showed very clear results. The features selected with the procedural algorithm performed well with the untrained k-means algorithm. It is obvious that the FCR-features show only minor correlation with the cutting parameters, whereas the regular cutting force components F_x, F_y, F_z, and F_{res} correlate stronger with the cutting parameters. This is also well visible for the spatial k-means analysis that shows precisions below 3.7 cm for the identification of a boundary layer between two concrete types. In contrast, k-means analysis using regular force components provided an insufficient *accuracy* for boundary layer detection.

Critically viewed, these experiments can be seen as a "best-case scenario" for the task of rock classification with a near-tool measure-while-cutting concept. The zone borders were clear and straight, and the rock zones were homogeneous. Even mixing the data from the two concrete samples posed no problem for the algorithm. In a real-world application, comparable rock conditions are unlikely.

An uncertainty during this experiment is that the definitions of the borders between neighbouring rock zones were considered perfectly straight. Although plastic sheets separated the concrete zones during casting, minor secondary deformations might have occurred after their removal. However, these secondary deformations appear to have played an insignificant role in the results. This is supported by the fact that k-means is unsupervised and still showed a good *precision* to the boundaries.

Another possible weakness of the experiment is the repeating consistency during casting of the two concrete blocks. The comparison between CO1 and CO2 shows that there was a certain variation in the toughness of the concrete. However, this variation does not seem to impair the quality of the results significantly.

The dataset is relatively extensive and could be used for further research. To extend the results of this experiment, a 3d-modelling based on the spatial data, similar to the case study, could be conducted. In addition, different training-classification scenarios could be investigated. For example, it could be examined whether training an algorithm with one combination of cutting parameters would yield acceptable classification results for other combinations of cutting parameters. This would give answers to whether a classification algorithm would have to be trained with the entire range of cutting parameters or whether limited training can be extended to other cutting parameters. In addition, different machine learning techniques could be tested.

7.1.2 Experiment GN

For this experiment, only two relatively small samples were available. As such, the parameter space that could be evaluated was relatively limited. Another aspect was the high cutting resistance of the gneiss for certain foliation orientations. During the cutting of Sides B and C, high forces and a strong dynamic oscillation of the rock cutting rig occurred. As a result, the *cutting depth* could only be varied in two relatively shallow levels, 4 and 6 mm. Experiment CO suggests that a very low *cutting depth* changes the behaviour of the force components.

In addition, only the three main foliation directions were investigated. These three foliation directions are coplanar to the x-y-, x-z- and y-z-planes. However, from the literature, it is known that a foliation direction between these directions yields results that lie between these terminal orientations [100, 103, 193].

The effects of certain boundary layer angles and foliation directions are already well researched, mainly on application scale [43, 99, 100, 103, 193, 194]. Experiment GN showed that similar effects could also be expected on the scale of the single tool. Insights into the cutting process during the cutting of anisotropic rocks could be obtained. The main results were that foliation could potentially alter certain features to a significant extent. This may lead to additional complexities during machine learning.

However, putting these results in relation to the case study, a supervised machine learner could be able to learn the highly varying behaviour of one rock class and still identify it correctly—given that the training data already provide enough information about the variability of the pick-rock-interaction. To give a clearer answer to this question, additional experiments are required. Mainly, the range of the cutting parameters *spacing* and *cutting depth* should be extended; but also the range of foliation angles in relation to the cutting trajectory. Eventually, fully scaled experiments with rotary tools are advised to deeper understand the influence of foliation towards rock classification.

Because a cutting direction parallel to the foliation allows the outbreak of large chips, situations in which the pick has only limited contact with the rock face occur more often than for the other two sides. There, the number of data points below a threshold; in this case, 0.5 kN for F_z is significantly higher. This discovery led to the decision to add another feature, the *contact ratio*, to the set of features—which proved important during the case study.

An unexpected additional finding was revealed by the regression-based analysis of the effect of *spacing* and *cutting depth* on the force components F_x, F_y, and F_z. It shows that the *spacing* has no significant effect on F_x and F_z for the layering conditions A and C. Within the boundaries of the cutting parameter variation, the limit of this effect could not be found. However, it could be shown that there is a clear difference between unrelieved and semi-relieved cuts. As such, there must be a limit to this effect. This discovery should be investigated with an extended parameter range, as it poses significant optimisation potential for the excavation efficiency of a cutting machine. The work regimen or even the cutter drum design, especially with regard to the pick lacing, could be optimised. The picks could be spaced further apart. This could, in turn, reduce the *specific energy consumption* of the cutter head and, as such, increase the advance rate of the excavation machine, given the same cutter head power [41].

In a real-world application of a force sensor system, an exact identification of the foliation direction would only be of economic interest with regard to finding and exploiting it. In the case researched here, this would be Side A. However, the optimum foliation direction can only be utilised to a limited extent due to the rotary nature of most cutter heads. Nevertheless, these preliminary results indicate that the preferred foliation direction could be identified during an upscaled MCW-sensor implementation.

7.1.3 Experiment GR

During this experiment, it was shown that the cutting forces react mainly to cavities and less to the pure existence of cracks. This is coherent with the previously published results this analysis builds upon. It showed that it is necessary to distinguish between detecting cavities and cracks. Only cavities or sufficiently opened cracks would be detectable with a near-tool MWC-system.

With this analysis, it could be shown that the use of the *contact ratio* for the detection of cavities performs well. Single cavities could be traced spatially. However, it also was shown that most features except those incorporating F_y show good distinctions between damaged and undamaged rock.

Only a minor variation of the cutting parameters was performed. This is because the main aim of this experiment was related to the previously published articles: to understand the level and depth of damage induced by high-power microwave radiation. On the other hand, these results are viewed in the context to Experiment CO where a sufficiently large parameter variation was done.

To extend this analysis further, a 3d-modelling of cavities based on cutting force data could be conducted. There, the question could be answered how cavities extend between different cuts as this was not the focus of this work. Additionally, a *CR*-based analysis method could be used to investigate further how deep into the rock a measurable effect of a crack network extends.

7.1.4 Case Study

The purpose of the case study was not only to estimate the capabilities of machine learning-based rock classification in 3d, but also to estimate and visualise the limits of such a classification. The three different rock types served different "roles". Generally, the concrete served as a specimen for a relatively homogeneous, isotropic rock without structural defects. The lead-zinc ore served as a representative of a medium homogeneous rock without major structural defects. The fluorite-barite ore served as a worst-case scenario in terms of homogeneity and structural integrity. The ore comprised layers and clusters of fluorite and barite—both are relatively soft minerals. Quartz bands formed very hard fractions. Larger parts of strongly weathered gneiss occurred as well. These parts appeared very soft and could be damaged with a knife. FBA3 additionally contained a larger cavity, which further added to structural heterogeneity. Figure 94 shows a detail of this. Additionally, the ore showed a layered structure, which could additionally have added to classification complexity.

Legend:
aGn - Altered gneiss
Qu - Quarz bands
FBa - Fluorite-barite ore
Co - Concrete
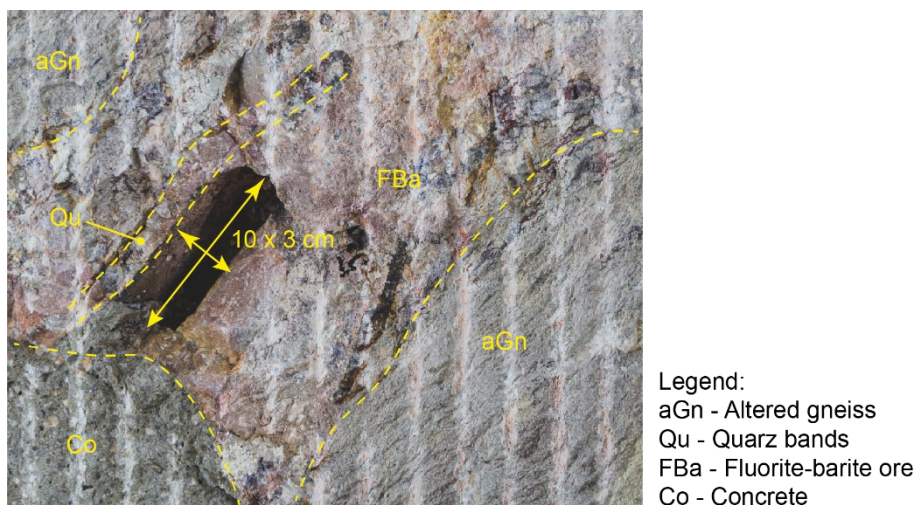
Figure 94: Detail of sample FBA3

Furthermore, the concrete of the FBA samples showed an unexplainably varying behaviour. The FCR-answers of the concrete in the samples FBA1, -2 and -3 varied considerably to the extent that it complicated the classification task substantially. This part of the experiment was not expected and the reason for this is not entirely clear. One possibility might be errors in the preparation process of the concrete, as it was mixed by hand. Another possible reason could be a varying time from casting the blocks to execution of the experiments. At first sight, seems improbable. The blocks were cut after a drying time of 30 days—and cut within a timeframe of two weeks. According to the datasheet, the concrete reaches 95% of its final strength after 30 days. However, the blocks had different sizes. This might have affected the hardening rate of the blocks. Block FBA3, which was the hardest—as indicated by the highest $FCR(F_z/F_x)$— was cut last in this two-week period.

The FBA-samples were expected to show the boundaries of the machine learning possibilities, and these expectations were clearly met. The cross-comparisons in between the group of FBA-samples yielded partially unsatisfying results. Remarkable, however, is that the supervised learners were able to provide acceptable results for the compound Cases All, Only_FBA, and Only_PB. It shows that machine learners could provide acceptable results even for complex multiclass problems.

The current method of feature extraction does not incorporate time as an input dimension. This has advantages and disadvantages. The advantage is that this method is robust because additional error sources that come with measuring time are eliminated. Also, variations in *cutting speed* play no role with the current method.

The disadvantage is that analysis methods that use the time domain in some way are not usable. For example, frequency analyses cannot be incorporated directly. Such methods would include discrete or fast Fourier-transformations [22], or empirical mode decomposition [114].

Apart from these considerations, the case study experiments were designed to simulate a real-world application with the linear rock cutting rig as closely as possible. A further extension of these experiments could only be achieved by upscaling the experimental environment to rotary cutter heads.

7.1.5 Additional Outcomes

An aspect is quality control of measurement data. During regular, state-of-the-art cutting experiments, only a limited number of repeating cuts are conducted, e.g., five repetitions per parameter combination—like in Experiment GN. In most of the experiments conducted for this work, a far greater number of single cuts was performed. For Experiments PB1 and PB2, 463 and 264 cuts were executed, respectively. For the largest experiment, FBA3, 512 cuts were performed on 16 layers.

In total, approximately 2000 cuts were executed and measured for the case study only. These amounts require a fast and efficient quality control programme. Until now, individual cuts would be manually inspected from the measurement files, manually exported, and results would be computed in Excel. Such a method is time-consuming for such a large number of cuts. To manage this, an updated workflow was introduced. The updated programme was implemented in Flexpro and R-Studio. In the new programme, all cuts were exported first. Summary statistics were computed and outlier cuts were directly eliminated. For more detailed quality control, a Shiny app allowed quickly browsing through the cuts; for each cut, the user can decide whether the cut is rejected or—if necessary, the cut can be truncated. The latter might be necessary when defects in the triggers that start the experiments occur. This was particularly the case during Experiment PB. The code to the app can be found in Annex O. Additional information on the updated quality control during cutting experiments is located in Annex G.

7.2 Comparison of Machine Learning Algorithms

This chapter summarises the observations regarding the machine learners and concludes with final recommendations for their potential use in further development of near-tool MWC-systems.

7.2.1 K-Means

While k-means performed very well during Experiment CO, the limits were shown during the case study. The performance for complex situations was very limited. Especially the *cross-performance* was dissatisfactory. Because k-means optimises based on Euclidean distances, the features are all weighed equal by definition. Also, the cluster shapes in the multidimensional space drift towards a spherical object (within the range of available data points) and can not be modified as with supervised methods. Especially, when multiple subtypes of rock are summarised in one rock class, the performance drops significantly. However, a workaround to this is possible, as illustrated in Figure 95.
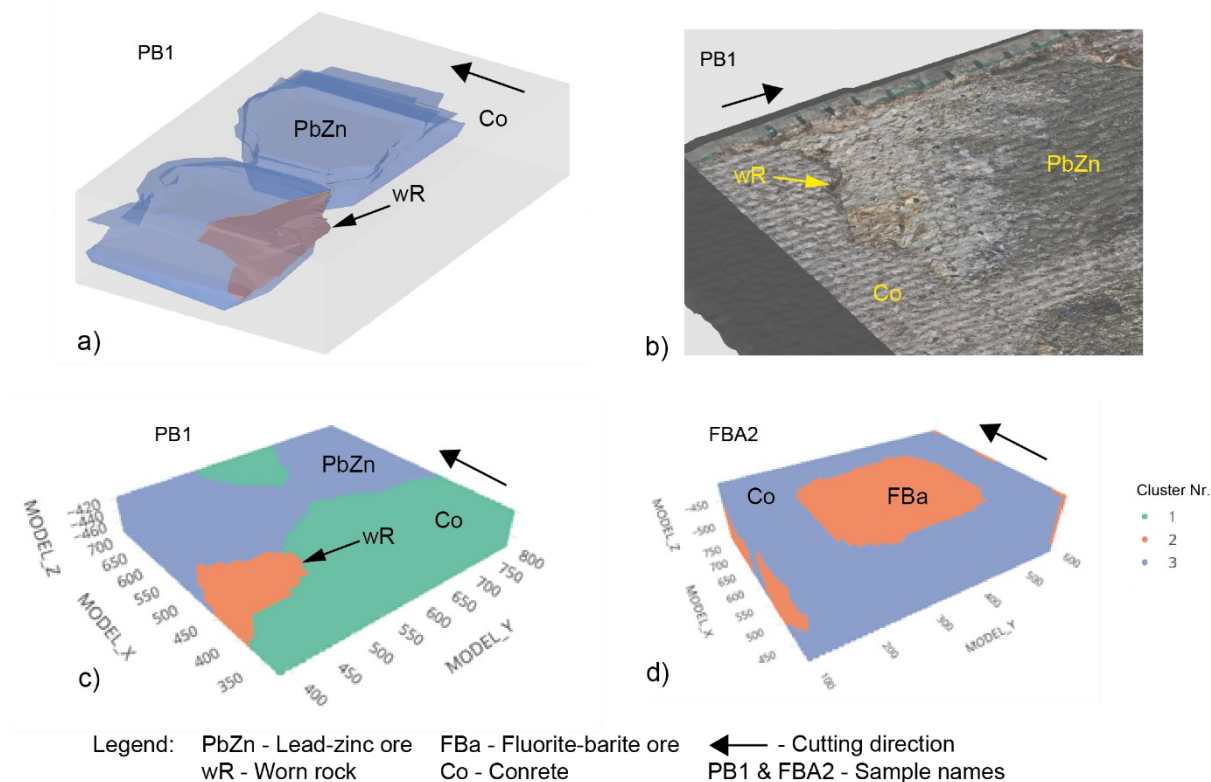
Figure 95: a) Model of rock types for sample PB1; b) photo draped on 3d-scan of surface shows overbreak in the worn zone; c) k-means classification results; d) prediction of FBA2 for k-means trained with PB1

Sample PB1 consisted of concrete and lead-zinc ore. However, the lead-zinc ore showed an anomaly: a piece of worn, altered gneiss. As seen in Panel a), the anomaly (wR) had the shape of a floe on the corner of one ore lump. Panel b) shows a photo of the situation draped on a 3d-scan of the block during cutting. The worn zone showed significant overbreak—leading to very low forces. Such a cutting behaviour is very different from the rest of the Pb-Zn parts but formally, the piece belongs to these Pb-Zn parts.

The workaround consists in defining more clusters than formal rock classes. This results in sub-classes. Two or more sub-classes then can be summarised to form their respective parent class. Panel c) shows the result of the clustering with $k = 3$. The cluster identification coincides with the Pb-Zn ore, the worn

rock, and the concrete, respectively. For the main analysis in the case study, the cluster identifying the worn zone was added to the Pb-Zn zone to achieve comparability to the other results.

Panel d) shows further considerations to this. The prediction result of the k-means clustering trained with Sample PB1 (with $k = 3$) was applied to Sample FBA2. The cluster that associates to the worn zone of PB1 now identifies the fluorite-barite ore, and the concrete is identified as Pb-Zn ore. This means that the F-Ba ore acts similarly to the worn zone, and the Pb-Zn ore of PB1 acts similarly to the concrete of FBA2. This information would be lost by only using $k = 2$. This illustrates how k-means can be used for an exploratory analysis to find zones in the rock that act similarly. That way, with a higher number of clusters, finer differences in rock types can be made visible. This can accompany a supervised algorithm.

Another modification of k-means was used for the *accuracy* analysis of the case study. Manual assignment of the clusters to the rock types after classification was not possible due to the high number of different cases. Therefore, the starting clusters were not randomly chosen, but the centre of gravity of each zone in the feature space was used as starting cluster positions. This defined which cluster corresponds to which rock zone before clustering. In the broader sense, this method enables a "semi-supervised" mode for k-means. Here, the user can provide the clustering algorithm with limited information about known rock zones, and then let the algorithm find the boundaries of the rock zones on its own. Such a function is similar to a colour picker/pipette function in many graphics softwares.

In summary, k-means clustering can be a valuable explorative or auxiliary tool to identify subtypes in known rock zones or when only limited labelled training data are present. For direct classification, the performance is minor to the two supervised algorithms.

7.2.2 Artificial Neural Networks and Distributed Random Forest

Both supervised algorithms performed very similarly in terms of *accuracy* and generalisation performance. Thus, their differences are more on the side of deployment complexity and computation time. The ANN showed considerably longer computation times than the DRF.

In addition, ANNs have a relatively large number of parameters for the user to consider (91 for ANN and 50 for DRF in the H2O package [187, 189]). This makes the process of reaching the final training for ANN comparatively time-consuming and subject to many unknowns. Furthermore, understanding the exact internal functionality is a complex task for ANN.

Hastie et al. (2017) state that *"[ANN] are especially effective in problems with a high signal-to-noise ratio and settings where prediction without interpretation is the goal"* [177]. The signal-to-noise ratio can be considered partially problematic due to the varying cutting process. However, the noise from the cutting process itself is reduced by the employed data pre-processing methods. As such, the signal-to-noise ratio is considered a medium problem for this application. Another aspect is repeating accuracy, which varies stronger for ANN than for DRF.

DRFs, on the other hand, are comparatively simple to set up. The most important parameter is the tree depth, which has a big influence on the over- or under-fitting behaviour of the algorithm. Other parameters such as column and row sampling rates, or the number of trees, have less influence on the output. Also, the computation of the feature importance is well understood. Furthermore, the DRF showed little variation in the *accuracy* for repeated training, making it slightly more reliable.

Furthermore, ANN provided a slightly better *cross-accuracy* between cases and better *validation accuracy* with little training data, indicating that it shows a slightly better generalisation behaviour.

7.2.3 Summary

Table 29 summarises the performance properties of the algorithms in this study. A direct comparison between the three types of machine learning algorithms showed that while all the algorithms could distinguish between the different rock zones,

- k-means shows the lowest *accuracy* but fast calculation times and does not require training,
- ANN and DRF showed similar *accuracy*; however, the ANN showed longer training times,
- ANN needs slightly less training data and shows a slightly better generalisation behaviour.
- Both supervised algorithms yielded good results with relatively little training data. However, the training data must capture the expected geologic variability.

Table 29: Summary of machine learning algorithm performance during this study

	Artificial neural network	Distributed random forest	K-means
Computation time	-	+	+
Accuracy	+	+	-
Amount of training data	+	0	/
Generalisation behaviour	+	(+)	-
Training complexity	-	0	+
Understanding of internals	0	+	+
Use case	Prediction of rock classes	Prediction of rock classes	Auxiliary use / when supervised training is not possible

In summary, both ANN and DRF could be used for application when training data is available. K-means should be used as a supporting tool or when no labelling of data is possible.

7.3 Considerations Towards Sensor System

In terms of the technology readiness classification as defined by the European Commission (s. Table 30), a classification of near-tool measure-while-cutting systems in relation to this work can be assessed. Depending on how the boundaries of the classification are defined, the outcomes differ. Regarding rock cutting, the basic principles of FCRs have been known since 1981, and the basic technology concepts of cutting force measurement have been formulated since the 1970s. Sensors have also been tested in an industrial environment (fully scaled cutting machine), but have not been in regular operation yet. The behaviour of real-time-calculated FCR and the spatial interpretation of FCR have not yet been documented. As such, the pure sensor side of this technology would range at TRL 5–6 while the data interpretation and evaluation side can be lifted to TRL 3–4 with this work.

In the present study, the analysis of FCR is performed posteriorly to the actual cutting. As a next improvement, an online or inline system would have to be demonstrated that combines an MWC-sensor concept with the rock classification methods that are presented in this study. Depending on the scale, this could be done on the scale of TRL 5 (single tool linear cutting system) or TRL 6 (on a rotating, fully scaled cutter head).

Table 30: Technology readiness levels, originally defined by NASA and refined by the European Commission [195]

TRL	Description
1	Basic principles observed
2	Technology concept formulated
3	Experimental proof of concept
4	Technology validated in lab
5	Technology validated in relevant environment (industrially relevant environment in the case of key enabling technologies)
6	Technology demonstrated in relevant environment (industrially relevant environment in the case of key enabling technologies)
7	System prototype demonstration in an operational environment
8	System complete and qualified
9	Actual system is proven in operational environment (competitive manufacturing in the case of key enabling technologies; or in space)

(This work — TRL 3 & 4)

7.3.1 Force Vectors and Data Acquisition Rate

In this work, one of the research questions is to define the basic requirements that a near-tool sensor system must meet for a precise operation in order to usher in the development of this technology. It was shown that the use of FCR could significantly improve the classification result over the use of "standard" force components. In fact, the use of FCR unlocks a robust classification that performs well under a variation of the cutting parameters. As such, it can be summarised:

1. FCR utilising features derived from F_x, F_y, and F_z yield best results.
2. FCR utilising features derived from only F_x and F_z still yield good results.
3. The use of "classic" force components did not yield suitable results.

This means that the sensor assembly should be able to at least measure the force acting in cutting direction (F_x) and the *normal force*. Since most excavation machines utilise rotating drums, the force acting in cutting direction would then be called *tangential cutting force*. This is defined as a <u>minimum requirement</u>.

Although FCR incorporating F_y directly decreased the classification success, FCR incorporating F_{res} yielded the best results. For the computation of F_{res}, the measurement of F_y is required. As such, the additional measurement of the *side force* is defined as the <u>optimum requirement</u>.

Generalised, the key element of this near-tool MWC concept is the use of two to three orthogonal forces that are measured at a high frequency. During the experiments, the data acquisition rate was 1000 Hz at a *cutting speed* of 0.1 m/s. This results in a DAQ rate of 10,000 data points per meter *cutting length*. Industrial cutter heads operate at cutting speeds around 1.5–3.5 m/s [196–198]. If the same DAQ rate per meter is desired, this will translate into 15,000–35,000 Hz per channel per pick equipped with sensors. Table 31 summarises these requirements.

Table 31: General requirements for an FCR-based MWC sensor system

	Minimum Requirements	**Optimal Requirements**
Measured force directions	F_x and F_z	F_x, F_y and F_s
DAQ rate	Depending on cutting speed: ca. 15,000–35,000 Hz per channel per pick	

However, also lower DAQ rates could capture the rock characteristics sufficiently well. Additional investigations would be required to identify a minimum DAQ rate that should be met. These additional investigations could also be done with the datasets from this study.

7.3.2 Sensor Types

The forces could be measured by several sensor types as shown in Figure 96. The use of piezo sensors, b) and c) would be one possibility. They could be installed as bolts in special drill holes or attached to a surface—similar to regular resistive strain gauges. However, their use is restricted by the natural frequency of the sensor. Depending on the exact design of the sensor, the frequency can range from 2 to 200 kHz [199]. For resistive strain gauges, a) and d), higher frequencies are possible without degradation of the signal [200]. However, the main restriction of the maximum measurement frequency lies in the design of the entire assembly: tool–holder–sensor [199, 201].

One alternative to piezoelectric and resistive gauges are fibre-Bragg gauges, shown in Figure 96 e). These tools are offered primarily for purposes of geotechnical and construction deformation measurement. However, they are also available on the market as versions similar to strain gauges. The advantages of these sensors in the mining context are their resistance to electromagnetic influences since they work optically (except for the DAQ device). However, the required fibre optic cables can inhibit a use on moving parts [202].

Given the fact that an application of a near-tool MWC system takes place in the rock cutting and mining context, the environmental conditions that apply there must be considered: very high peak forces, very high accelerations and vibrations, dust, and/or water. The dust might contain aggressive or abrasive minerals (salts, pyrite, quartz). Natural occurring water might be highly mineralised and acidic. The tip of the pick can reach very high temperatures of up to 1100 °C [60]. Although this is the temperature of the tip, still high temperatures above 100° C should be expected around the tool in some cases. Lastly,

ferromagnetic ores can occur and electric cutter head drives of up to 400 kW power (for roadheaders) [203] might incur strong electromagnetic fields—adding electronic disturbances.
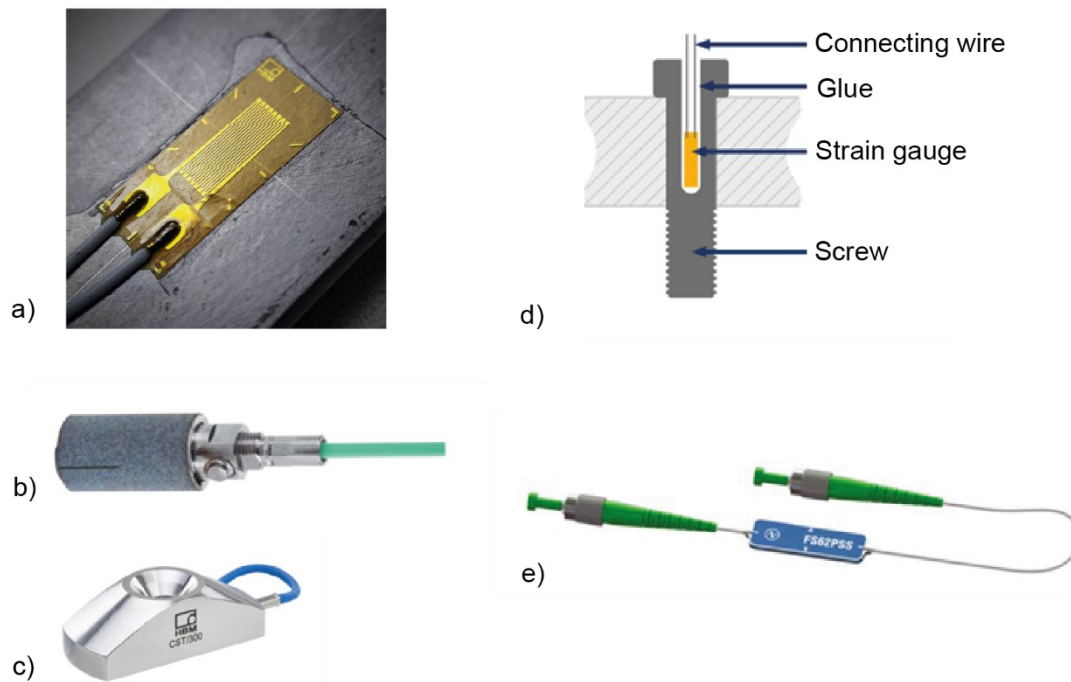
Figure 96: Different deformation sensors: a) resistive strain gauge, b) piezo-bolt, c) piezo strain gauge, d) resistive strain gauge for use in bolts or drill holes, e) fibre-Bragg-strain gauge [204–208][17]

7.3.3 Computation Speed

The calculations carried out in this work are in the form of a posterior or offline analysis. However, this analysis could be performed automatically in batches from the measured data as an online analysis. Vraetz (2018) classifies an online analysis as "*an automated [...] analysis that can be conducted in under 10 min, and the information can be fed back into the process*" [157]. With the data structure and volumes processed in this work, this would be possible.

The greater goal is an inline analysis. Here, the information is analysed and fed back into the process in under 1 min. The slewing speed of a cutter head can reach up to 20 m/min. The precision of boundary layer detection under optimal laboratory conditions was below 3.7 cm. Assuming a desired precision of 5 cm, this would mean that the distance of 5 cm is traversed in up to 0.15 s. As such, the reaction speed of the system should ideally meet this threshold. This is only a rough estimate to illustrate the magnitude of the required reaction speed. An exact calculation requires additional parameters. The swivel speed of the boom is subject to the rock properties, cutter head type, rotation speed of the cutter head, general machine parameters, and working regimen. During 0.15 s, one pick could have travelled a theoretical cutting length between 0.22 and 0.53 m based on the cutting speeds stated above. This is equivalent to one to two single cuts on the cutting test stand of TU BAF.

Generally, the computation and classification method presented in this work is the first published method that allows for spatial feature computation and subsequent classification with reasonable computation times. Irrespective of being an online or inline analysis, the computational speed can be a potential bottleneck. Figure 97 summarises the computation workflow with the range of calculation

---

[17] Images: a) Haehne Elektronische Messgeräte GmbH, b) Kistler Holding AG, c), d) & e) HBM Messtechnik GmbH

times for the individual cases from the case study. It can be seen that the largest portion of the total calculation time is consumed by the moving-average feature calculation, followed by the training time for a neural network.

The s*earch radius* is a major parameter that influences the computation speed. However, reducing the *search radius* preserves more noise, negatively influencing the classification results. A method of improving computation speed while preserving noise reduction could be a stepwise calculation of the features with increasing *search radii*. For example: first calculate the feature block model with $SR = 25$, then summarise the block model with $SR = 50$, followed by a final summary with $SR = 100$. This would greatly reduce the computation requirements for the first step. The refinement of the block models is neglectable in comparison to the first computation (raw data for FBA3 contain 2.5 million data points, the block model contains 51,000 data points). Such an approach is similar to Gaussian filtering in image processing. However, it should be investigated whether this changes the *accuracy* of the results. Such an approach should be combined with the spatial divide-and-conquer approach, which already reduced computation times substantially.

The training times for the distributed random forest and k-means clustering are neglectable, as well as the time for the computation of the actual prediction of the rock types. Only the training of the ANN took longer than 2 min. However, training of whole datasets does not have to be done consistently—only during (re-)calibration of such a system.
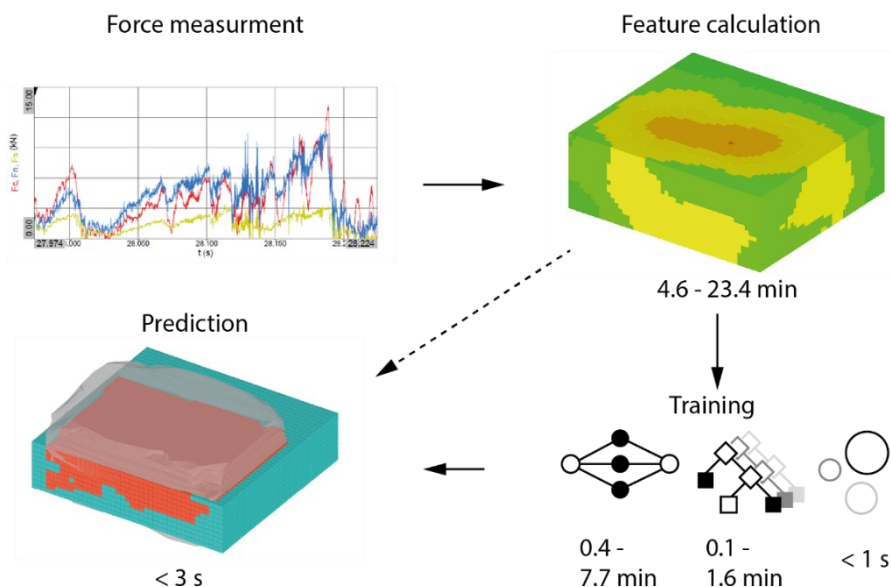
Figure 97: Summary of classification workflow with approximate computation times from case study; symbols indicate (f.l.t.r): neural network, distributed random forest, k-means

Algorithm optimisation was not the focus of this work. However, a limited computation time optimisation was implemented for the moving-average feature calculation. This was done by implementing a parallel divide-and-conquer algorithm, which results in a substantial increase in computation speed. Without divide-and-conquer, computation times of up to 6 h were recorded; after the improvement, they could be reduced to under 30 min. Further improvements to computation speed can possibly be achieved by using lower-level programming languages, such as C++, which is known for its speed. Here, a further improvement of speed by one magnitude could be expected [209, 210].

8 Summary and Outlook

The overarching goal of this work is to evaluate the possibility of using machine learning for the classification of rock types based on cutting force measurements with conical picks. This was mainly achieved by utilising features extracted from real-time force component ratios with the help of a moving-window algorithm. Such a methodology can potentially be used in a near-tool-sensor (NTS) arrangement to serve in measure-while-cutting (MWC) technologies.

With these technologies, it is possible to integrate an excavation machine into a Mining 4.0 environment. The machine would be able to work highly automated or even autonomously; furthermore, it would be possible to integrate the obtained data into the deposit model. Data from the deposit model can help navigate the excavation machine, and the data won by the excavation machine can be fed back into the deposit model to update and concretise it.

Although this technology has been under research since the 1970s, it did not yet leave the prototype stage while a similar technology, the measure-while-drilling technology (MWD), reached market readiness. For MWC, however, the development is less sophisticated. Full-scale cutting force sensor assemblies with analysis methods are published almost only for disk cutters. Sensor concepts and prototypes are published for conical picks, but without a complete analysis system. This could be attributed to the fact that the cutting parameters *cutting depth* and *spacing* constantly vary during the use of these machines.

Therefore, an overview of the parameters that influence the rock cutting process was conducted. This overview concludes that the *normal* to *cutting force ratio* holds a usable information value about the rock type being cut—and is possibly robust against changing cutting parameters. Following, an overview of the state of the art of cutting force measurement, research and its reporting conventions showed that there is a knowledge gap in detailed statistical analysis of the cutting forces in general, but especially of the behaviour of force component ratios. This information indicates that cutting force-based rock classification for conical picks is not yet fully understood. At the same time, machine learning for the identification of rock types and production optimisation is a field under broad research.

These literature findings led to the development of a new approach for rock characterisation based on cutting force component ratios. This was achieved by designing a procedural algorithm to preselect possible features from a group of 72 force component-based feature candidates. The algorithm was applied to the results of a rock cutting experiment with nine different cutting parameter levels and three different concrete hardness zones. The algorithm selected a set of nine suitable parameters. Based on these parameters, k-means clustering was used to identify the three different rock zones. There, the features from the preselection were tested against four other sets of features. Two of these were a variation of the immediate feature selection and two represented features based on "classic" cutting force measurements. The boundaries between rock types with differences as low as 7.7 MPa *UCS* could be identified from the extracted features with the unsupervised k-means clustering. The mean spatial *precision* to identify a boundary between two adjacent types of concrete ranged from 2.4 to 3.7 cm. A correlation analysis and a feature importance analysis were performed based on a distributed random forest algorithm to further determine the significance of the features. It showed that some features may be dropped to avoid redundancy.

Two more experiments were conducted to supplement these first results: a cutting experiment on an anisotropic rock, gneiss; and a cutting experiment that compares uncracked with cracked rock. For the latter, a granite was used where two out of three samples were treated with high-power microwave

radiation to induce a crack network. The gneiss experiments showed that anisotropic rock might be problematic for any machine learning classification algorithm. The results further revealed that the *spacing* between neighbouring cuts has no significant effect on the cutting forces in layering orientations along the x-y- and x-z-planes with respect to the cutting trajectory. This experiment also showed that certain layering orientations might be well identified by an additional feature that describes how often the pick loses contact with the rock. This occurs when very large chips break out and overbreak occurs. This feature is called *contact ratio* and was added to the set of features used in the subsequent experiments.

The second auxiliary experiment, cracked granite, showed that a crack network must show a certain opening state so that the cracks can act as an additional free face—resulting in overbreak. This overbreak can be precisely described with the *contact ratio* defined before.

All these findings were incorporated into a final case study. Five samples, composed of two different materials, were each cut with two different cutting parameter combinations. Two samples consisted of lead-zinc ore in the centre and concrete on the outside; three consisted of fluorite-barite ore and concrete. The concrete for all five samples was the same.

The data from these samples were used to test the classification behaviour of three different machine learning algorithms: k-means clustering, feedforward artificial neural network, and distributed random forest. The first is an unsupervised algorithm, and the latter two are supervised.

The three machine learning algorithms were trained with eight different training cases, and their performance was evaluated. Five training cases consisted of the five individual samples; the remaining three were composite cases combining data from multiple samples. It showed that generally, if learners were presented data from samples that they were trained with, they could classify the rest of the sample with high *accuracy*. However, a prediction of samples on which no training was performed, achieved limited success. Here, only the Pb-Zn samples yielded acceptable *cross-accuracy*. The F-Ba samples proved to be too diverse in their material properties. However, if a learner was presented with training data from multiple samples, the accuracy increased substantially.

Additionally, it was investigated, how much data the supervised algorithms require for reliable results. It showed that 20–40% of the total data amount is sufficient, acceptable results can be obtained even with as little as 2–5% of the total data.

Expectedly, the key lesson is that any learner must be presented with the geologic variability that a rock class might exhibit before it can identify it. An analogy are human kids as highly sophisticated learners. If a child has so far only seen cats, it will also identify the picture of a dog as a cat, because it has never learned the difference between a cat and a dog.

Generally, the distributed random forest and the neural network showed similar performances with the practical implication that the ANN requires slightly less training data and shows a slightly better generalisation behaviour, but needs longer training times; also hyperparameter tuning is more complex. The unsupervised k-means algorithm did not show the same *accuracy* as the two supervised algorithms. It performed worst when the rock types present were very diverse. The problem is that k-means creates clusters that resemble a spherical shape in the multidimensional feature space. It cannot capture more complex shapes. However, the computation times are very short. This suggests that k-means may be used for exploratory analysis of features when the true rock classes are not entirely known or to identify sub-classes of rock types.

The essential results are that features derived from force component ratios in conjunction with the additional feature *contact ratio* characterise the cutting process sufficiently well—and prove a good tool for material characterisation on conical picks. Regarding ushering in the unlocking of a cutting force measurement-based MWC technology, it is crucial to measure at least the F_x and F_z components of the cutting force; optimal results can only be expected when F_y is additionally measured. All three force components are required to compute the necessary force component ratios that, in turn, are required to extract the features that provide maximum *accuracy*. Apart from measuring these forces, a rock classification system must also be able to analyse the incoming data stream of up to three channels. Based on the experiences in this work, a sampling rate as high as 15,000–36,000 Hz per channel is suggested. From the raw data stream, a spatial block model containing the features must be computed sufficiently fast. Designing such a system was not part of this work, but it could be shown that there is room for optimising and substantially speeding up the algorithms for feature generation. Once the feature model is constructed, the actual training and prediction are computationally less problematic.

In summary, the perspective for the potential capabilities of a near-tool MWC system could be outlined and positive prospects of identifying even relatively small rock toughness differences (7.7 Mpa *UCS*) as well as changing rock mass states were shown.

<u>Outlook</u>

The focus of the methods derived in this work lies in a potentially robust system—as robustness is one of the key desirables in the mining and construction industry. However, as the development of MWC systems is far from over, many potential extensions and additions to foster such systems remain to be developed.

Regarding the analyses conducted, the major future foci of work should investigate the influence of the wear of a pick, as well as the influence of a varying cutting speed towards the classification behaviour of FCR-based rock classification. These two parameters of the cutting process could not be investigated in the scope of this work, but knowledge of their influence is the next crucial element in the advancement of FCR-based rock classification. Another aspect is increasing the knowledge of classification capabilities in anisotropic or cracked rocks. Here, only foundations could be created, and more in-depth research is required. While the approach to compute the features with a moving-window algorithm was chosen with the goal in mind to create a method as robust as possible, more research into the refinement of the method appears promising. This starts with an extension of descriptive statistics like kurtosis or skewness and can be extended to the use of histogram bins, as well as directional statistics. Furthermore, investigating frequency analysis methods, or peak extraction algorithms—the list of methods to characterise data is sheer endless and finding the perfect solution is an extensive process.

The ultimate step to continue research in the field of MWC is an upscaling of the method, as it provides a more realistic picture of its capabilities. Such an upscaling would have to go in line with a working sensor assembly, and in the wake of this—provide a demonstrator. Questions like *"How many sensor-equipped tools does one need for a performant rock classification?"*, *"How do machine dynamics influence the measurement? Can it even be a feature?"*, and *"What is the lifetime of the sensors?"* can only be answered there. Such a demonstrator could be equipped with additional sensors, allowing multi-sensor-fusion concepts, where machine vibrations, cutter drive current, hydraulic pressure, and more could be utilised—further ushering in a "feeling" excavation machine of the future.

So that the old miners saying: *"All is dark in front of the pick"* one day becomes
"The pick lights the way".

———————————— ⚒ ————————————

References

[1]   J. Jeswiet and A. Szekeres, "Energy Consumption in Mining Comminution", *Procedia CIRP*, vol. 48, pp. 140–145, 2016, doi: 10.1016/j.procir.2016.03.250.

[2]   A.-Z. M. Abouzeid and D. W. Fuerstenau, "Grinding of mineral mixtures in high-pressure grinding rolls", *International Journal of Mineral Processing*, vol. 93, no. 1, pp. 59–65, 2009, doi: 10.1016/j.minpro.2009.05.008.

[3]   A. Soofastaei, E. Karimpour, P. Knights, and M. Kizil, "Energy-Efficient Loading and Hauling Operations", in *Green Energy and Technology, Energy Efficiency in the Minerals Industry: Best Practices and Research Directions*, K. Awuah-Offei, Ed., Cham: Springer, 2018, pp. 121–146. Accessed: Jan. 29 2020.

[4]   European Commission, *Critical Raw Materials.* [Online]. Available: http://ec.europa.eu/growth/sectors/raw-materials/specific-interest/critical_de (accessed: Aug. 9 2018).

[5]   European Commission, "Report on Critical Raw Materials and the Circular Economy" 2018. [Online]. Available: https://op.europa.eu/s/witl

[6]   F. Marscheider-Weidemann *et al., Rohstoffe für Zukunftstechnologien 2016: Auftragsstudie,* 2016th ed. Berlin: Deutsche Rohstoffagentur (DERA) in der Bundesanstalt für Geowissenschaften und Rohstoffe (BGR), 2016.

[7]   B. Reuter, A. Hendrich, J. Hengstler, S. Kupferschmid, M. Schwenk, and thinkstep AG, "Rohstoffe für innovative Fahrzeugtechnolgoien: Herausforderungen und Lösungsansätze" 2019. Accessed: Aug. 20 2019.

[8]   S. Walter, "Akzeptanzkommunikation in der Energie- und Rohstoffwirtschaft – Chancen und Grenzen für kleine und mittlere Unternehmen zur Verbesserung des Akzeptanzniveaus am Beispiel des Freistaats Sachsen" Dissertation, Institut für Bergbau und Spezialtiefbau, Freiberg, 2021.

[9]   PricewaterhouseCoopers International Limited, "Mine Report 2019", 2019. [Online]. Available: www.pwc.com/mine

[10]   N. A. Sifferlinger, P. Hartlieb, and P. Moser, "The Importance of Research on Alternative and Hybrid Rock Extraction Methods" *BHM Berg- und Hüttenmännische Monatshefte*, vol. 162, no. 2, pp. 58–66, 2017.

[11]   Wirtgen Group, "PCD Milling Tools", Windhagen, 2018. Accessed: Jan. 26 2020. [Online]. Available: https://www.wirtgen-group.com/en-lv/products/wirtgen/technologies/cutting-technology/cutting-tools/cold-milling-machines/

[12]   D. Belnap and L. Hillberg, "PCD inserts for improved hard rock mining efficiency", *International Technical Conference on Diamond, Cubic Boron Nitride and Their Applications, INTERTECH*, 2006.

[13]   D. Johansson, A. Hrechuk, V. Bushlya, M. Mårtensson, A. Can, and J.-E. Ståhl, "Small scale testing of PCD and WC-Co tooling in rock cutting using longitudinal turning", *Wear*, 426-427, pp. 1515–1522, 2019, doi: 10.1016/j.wear.2018.11.036.

[14]   P. K. Singh, M. P. Roy, R. K. Paswan, R. K. Dubey, and C. Drebenstedt, "Blast vibration effects in an underground mine caused by open-pit mining", *International Journal of Rock Mechanics and Mining Sciences*, vol. 80, pp. 79–88, 2015, doi: 10.1016/j.ijrmms.2015.09.009.

[15]   R. J. Plinninger, *Roadheaders as an alternative excavation method in urban tunneling - chances and risks,* Veröffentlichungen zur 18. Tagung für Ingenieurgeologie und zum Forum für junge Ingenieurgeologen. Berlin, *Veröffentlichungen zur 18. Tagung für Ingenieurgeologie und zum Forum für junge Ingenieurgeologen.* [Online]. Available: http://www.plinninger.de/images/pdfs/2011_18taging_tsm.pdf

[16] B. Brino, M. Cardu, S. Gennaro, and Gianotti, *Technical- Economic Comparison between Excavation by D&B and by Roadheader in two Underground Gypsum Quarries*. Antalya: 23rd International Mining Congress of Turkey, UCTEA Chamber of Mining Engineers of Turkey, 2013.

[17] R. Ghosh, A. Gustafson, and H. Schunnesson, "Development of a geological model for chargeability assessment of borehole using drill monitoring technique", *International Journal of Rock Mechanics and Mining Sciences*, vol. 109, pp. 9–18, 2018, doi: 10.1016/j.ijrmms.2018.06.015.

[18] Jeroen van Eldert, "Analysis of Excavation Damage, Rock Mass Characterisation and Rock Support Design using Drilling Monitoring", Licentiate Thesis, Division of Mining and Geotechnical Engineering, Luleå Tekniska Universitet, 2018. Accessed: Jan. 26 2020.

[19] J. van Eldert, H. Ittner, H. Schunnesson, and D. Johansson, *Evaluation of alternative techniques for excavation damage characterization // ITA-AITES World Tunnel Congress 2016 (WTC 2016): San Francisco, California, USA, 22-28 April 2016*. Red Hook, NY: Society for Mining, Metallurgy and Exploration; Curran Associates Inc, 20169781510822627.

[20] J. Navarro *et al.,* "Blastability and Ore Grade Assessment from Drill Monitoring for Open Pit Applications", *International Journal of Rock Mechanics and Rock Engineering*, vol. 54, no. 6, pp. 3209–3228, 2021, doi: 10.1007/s00603-020-02354-2.

[21] C. Drebenstedt and S. Paessler, "Analysis of cutting resistances for bucket wheel excavators in hard clays", *Proceedings of the 14th International Symposium on Mine Planning and Equipment Selection, MPES 2005 and the 5th International Conference on Computer Applications in the Minerals Industries, CAMI 2005*, 2005. [Online]. Available: https://www.scopus.com/inward/record.uri?eid=2-s2.0-84892650537&partnerID=40&md5=8153dc8a4562ba0ff2059df845846d52

[22] M. Entacher, G. Winter, T. Bumberger, K. Decker, I. Godor, and R. Galler, "Cutter force measurement on tunnel boring machines – System design", *Tunnelling and Underground Space Technology*, vol. 31, pp. 97–106, 2012, doi: 10.1016/j.tust.2012.04.011.

[23] R. Gerer, "Anordnung Zum Erfassen Der Belastung Eines Meissels Von Schrämmaschinen", WO2011116405A2, Sep 29, 2011.

[24] W. R. George, "Messvorrichtung, insbesondere zur Verwendung am Schneidkopf einer Gewinnungsmaschine für den Bergbau", DE2349827, also: US4181360A, FR7335974, GB4657072, Großbrittanien, Apr 18, 1974.

[25] J. Rieckhoff, "Verfahren zur Regelung des Schnitthorizontes von Walzenschrämmaschinen", DE2919499C2.

[26] D. Alford, R. Lukaszewicz, and B. Record, "Pick Assembly", GB2036127A, Jun 25, 1980.

[27] M. Vorona, C. Drebenstedt, G. Kholodnyakov, and G. Kunze, "Optimierung des Schneidprozesses und Prognose der relevanten Arbeitsgrößen bei der Gesteinszerstörung unter Berücksichtigung des Meißelverschleißes", Dissertation, TU Bergakademie Freiberg, Freiberg, 2012. Accessed: Apr. 28 2017.

[28] Wirtgen GmbH, *Wirtgen Surface Mining Manual: Applications and Planning Guide,* 2nd ed. Windhagen, 2017.

[29] Element Six UK Ltd., "Infografiken Bergbau & Bauindustrie", [Online]. Available: https://e6-prd-cdn-01.azureedge.net/mediacontainer/medialibraries/element6/documents/e6-website18-mining-infographic-layout_v10-(002)_final-approved-05-12-18.pdf?ext=.pdf

[30] bd baumaschinendienst, *Surface Miner für Rohstoffgewinnung.* [Online]. Available: https://www.baumaschinendienst.de/artikel/surface-miner-fuer-rohstoffgewinnung-und-trassierungsarbeiten-10368/ (accessed: Jan. 21 2020).

[31] N. Bilgin, H. Copur, and C. Balci, *Mechanical Excavation in Mining and Civil Industries,* 1st ed. Boca Ranton, FL: Crc Press; Taylor & Francis Group, 2014978-1-4665-8474-7.

[32]   N. Bilgin, M. A. Demircin, H. Copur, C. Balci, H. Tuncdemir, and N. Akcin, "Dominant rock properties affecting the performance of conical picks and the comparison of some experimental and theoretical results", *International Journal of Rock Mechanics and Mining Sciences*, vol. 43, no. 1, pp. 139–156, 2006, doi: 10.1016/j.ijrmms.2005.04.009.

[33]   B. Grafe, C. Drebenstedt, and T. Shepel, "Ways towards highly selective mechanical production chains", *Proceedings 5th International Colloquium of Non-Blasting Rock Destruction 19th - 22th November 2017*, 2018.

[34]   X. Wang, Q.-F. Wang, Y.-P. Liang, O. Su, and L. Yang, "Dominant Cutting Parameters Affecting the Specific Energy of Selected Sandstones when Using Conical Picks and the Development of Empirical Prediction Models", *International Journal of Rock Mechanics and Rock Engineering*, vol. 51, no. 10, pp. 3111–3128, 2018, doi: 10.1007/s00603-018-1522-1.

[35]   O. Z. Hekimoglu, "Investigations into tilt angles and order of cutting sequences for cutting head design of roadheaders", *Tunnelling and Underground Space Technology*, vol. 76, pp. 160–171, 2018, doi: 10.1016/j.tust.2018.03.017.

[36]   O. Z. Hekimoglu, "A pick force calculation method suggested for tool lacing of mechanical excavators employing drag tools", *International Journal of Mining, Reclamation and Environment*, vol. 32, no. 8, pp. 564–585, 2018, doi: 10.1080/17480930.2017.1317946.

[37]   B. Grafe and C. Drebenstedt, "Laboratory Research on Alternative Cutting Concepts on the Example of Undercutting", *BHM Berg- und Hüttenmännische Monatshefte*, vol. 162, no. 2, pp. 72–76, 2017, doi: 10.1007/s00501-016-0572-5.

[38]   B. Grafe, C. Drebenstedt, P. Hartlieb, and T. Shepel, "Studies on the effect of high power microwave irradiation as a means of inducing damage to very hard rock to reduce the cutting resistance during mechanical excavation", in *Mine Planning and Equipment Selection // Proceeding of the 26th International Symposium on Mine Planning and Equipment Selection: MPES 2017*, 2017. Accessed: May 27 2018.

[39]   P. Hartlieb and B. Grafe, *Untersuchungen zur Erhöhung der Schneidbarkeit von Gesteinen durch den Einsatz alternativer Methoden: in Tagungsband Bergbau, Energie und Rohstoffe 2015*. Freiberg: TU Bergakademie Freiberg, 2015978-3-938390-40-5.

[40]   E. Hoek, *Rock Mass Classification.* [Online]. Available: https://www.rocscience.com/assets/resources/learning/hoek/Practical-Rock-Engineering-Chapter-3-Rock-Mass-Classification.pdf (accessed: Mar. 2 2020).

[41]   A. Keller, "Prognose von Aktivierungsparametern für die maschinelle Gewinnung hochfester Gesteine", Dissertation, Institut für Bergbau und Spezialtiefbau, TU Bergakademie Freiberg, Freiberg, 2020. Accessed: Oct. 4 2021. [Online]. Available: https://nbn-resolving.org/urn:nbn:de:bsz:105-qucosa2-752564

[42]   I. Rostamsowlat, T. Richard, and B. Evans, "An experimental study of the effect of back rake angle in rock cutting", *International Journal of Rock Mechanics and Mining Sciences*, vol. 107, pp. 224–232, 2018, doi: 10.1016/j.ijrmms.2018.04.046.

[43]   K. Thuro, "Geologisch-felsmechanische Grundlagen der Gebirgslösung im Tunnelbau", Habilitation, Ingenieurgeologie, Technische Universität München, Munich, 2002.

[44]   C. Drebenstedt and M. Vorona, "Optimierung von Gewinnungsmaschinen im Tagebau – Vom Schneidprozess zur Virtuellen Realität", in *5. Fachtagung Baumaschinentechnik 2012*, Freiberg: TU Bergakademie Freiberg, 2012, pp. 72–86.

[45]   P. V. Quang, "Beitrag zur Staubentstehung und -verhütung bei spanender Gesteinszerstörung", Dissertation, TU Bergakademie Freiberg, Freiberg, 2007.

[46]   P. V. Quang, "The determination of coal dust emission and percentage of quartz in coal dust emission during the cutting anthracite coal by shearing and bottom blade of the plow", *Procedia Earth and Planetary Science 1*, pp. 250–256, 2009.

[47] B. Grafe, "Potential des Hinterschneidens mit Rundschaftmeißeln zur Steigerung der Schneideffizienz", Diploma thesis, Institut für Bergbau und Spezialtiefbau, TU Bergakademie Freiberg, Freiberg, 2014.

[48] Y. Sun and X. Li, "Slant Angle and Its Influence on Rock Cutting Performance", *Advances in Civil Engineering*, vol. 2018, pp. 1–11, 2018, doi: 10.1155/2018/6519029.

[49] W. Zhou, H. Wang, D. Wang, K. Zhang, Y. Du, and H. Yang, "The effect of geometries and cutting parameters of conical pick on the characteristics of dust generation: Experimental investigation and theoretical exploration", *Fuel Processing Technology*, vol. 198, p. 106243, 2020, doi: 10.1016/j.fuproc.2019.106243.

[50] H. Jendersie, *Kali- und Steinsalzbergbau*. Leipzig: VEB Deutscher Verlag für Grundstoffindustrie, 1969.

[51] P. Sobek, "Ermitteln Sie anhand der internationalen Fachliteratur sowie aus Schnittversuchen mit Rundschaftmeißeln verschiedenen Typs die für die Einsätze von Ausleger-Teilschnittmaschinen innerhalb des Erzbergbaues der DDR günstigste Meißelgeometrie!", Dissertation, TU Bergakademie Freiberg, 1987.

[52] O. Su, "Numerical Modeling of Cuttability and Shear Behavior of Chisel Picks", *International Journal of Rock Mechanics and Rock Engineering*, vol. 52, no. 6, pp. 1803–1817, 2019, doi: 10.1007/s00603-018-1644-5.

[53] P. Hartlieb and S. Bock, "Theoretical Investigations on the Influence of Artificially Altered Rock Mass Properties on Mechanical Excavation", *International Journal of Rock Mechanics and Rock Engineering*, vol. 51, no. 3, pp. 801–809, 2018, doi: 10.1007/s00603-017-1355-3.

[54] S. Yadav, C. Saldana, and T. G. Murthy, "Experimental investigations on deformation of soft rock during cutting", *International Journal of Rock Mechanics and Mining Sciences*, vol. 105, pp. 123–132, 2018, doi: 10.1016/j.ijrmms.2018.03.003.

[55] P. L. Menezes, M. R. Lovell, I. V. Avdeev, and C. F. Higgs, "Studies on the formation of discontinuous rock fragments during cutting operation", *International Journal of Rock Mechanics and Mining Sciences*, vol. 71, pp. 131–142, 2014, doi: 10.1016/j.ijrmms.2014.03.019.

[56] P. N. W. Verhoef, *Wear of Rock Cutting Tools: Implications for the site investigation of rock dredging projects*. Rotterdam: A.A. Balkema, 19979054104341.

[57] M. Entacher, K. Lassnig, and R. Galler, *Analysis of Force Path Diagrams of Linear Cutting Machine - Tests regarding Geotechnical Parameters // GeoCongress 2012 (Geotechnical Special Publication (GSP) 225): State of the Art and Practice in Geotechnical Engineering*. Oakland, CL: GeoCongress 2012; American Society of Civil Engineers, 20129780784412121.

[58] A. Keller and B. Grafe, *Alternative cutting concepts - learnings from laboratory tests*. Presentation, International symposium on mechanical hard rock excavation. Leoben: Montanuniversität Leoben, 2016.

[59] A. Keller and C. Drebenstedt, "Hard Rock Cutting and Activated Cutting - Lessons Learned from the Laboratory", *BHM Berg- und Hüttenmännische Monatshefte*, vol. 162, no. 2, pp. 67–71, 2017, doi: 10.1007/s00501-016-0573-4.

[60] W. Shao, X. Li, Y. Sun, H. Huang, and J. Tang, "An experimental study of temperature at the tip of point-attack pick during rock cutting process", *International Journal of Rock Mechanics and Mining Sciences*, vol. 107, pp. 39–47, 2018, doi: 10.1016/j.ijrmms.2018.04.044.

[61] J. P. Loui and U. R. Karanam, "Heat transfer simulation in drag–pick cutting of rocks", *Tunnelling and Underground Space Technology*, vol. 20, no. 3, pp. 263–270, 2005, doi: 10.1016/j.tust.2004.08.010.

[62] U. Restner and R. J. Plinninger, "Rock Mechanical Aspects of Roadheader Excavation: International Society for Rock Mechanics and Rock Engineering.", *64th Geomechanics*

Colloquium, 2015. [Online]. Available: https://www.onepetro.org/download/conference-paper/ISRM-EUROCK-2015-041?id=conference-paper%2FISRM-EUROCK-2015-041

[63] D. Neil, J. Rostami, L. Özdemir, and R. Gertsch, "Construction and estimation techniques for underground development and production by road headers.", 1994. [Online]. Available: https://www.researchgate.net/publication/237795297_Production_estimating_techniques_for_underground_mining_using_roadheaders

[64] F. F. Roxborough, P. King, and E. J. Pedroncelli, "Tests on the cutting performance of a continuous miner", *The Journal of The South African Institute of Mining and Metallurgy*, January, 1981.

[65] J. Pajer, F. Kurth, and M. Pfeifer, *Tagebaugrossgeraete und Universalbagger*. Berlin: Verl. Technik, 1971. [Online]. Available: https://katalog.ub.tu-freiberg.de//Record/0-1114702129

[66] N. Bilgin, D. Tumac, C. Feridunoglu, and A.R. Karakas and M. Akgul, "The performance of a roadheader in high strength rock formations in Küçüksu tunnel",

[67] X. Wang, O. Su, Q.-F. Wang, and Y.-P. Liang, "Effect of cutting depth and line spacing on the cuttability behavior of sandstones by conical picks", *Arabian Journal of Geosciences*, vol. 10, no. 23, p. 633, 2017, doi: 10.1007/s12517-017-3307-3.

[68] Eric Drüppel, "Entwicklung eines Konzeptes für die schneidende Gewinnung im Steinsalz", Dissertation, Fakultät für Georessourcen und Materialtechnik, RWTH Aachen, Aachen, 2010.

[69] E. Sarwary and P. C. Hagan, "The effect of changes in tool tip angle on the cutting performance of a pointed pick", *Mining Technology*, vol. 125, no. 3, pp. 184–190, 2016, doi: 10.1080/14749009.2016.1159056.

[70] O. Popov, "Beitrag zur mathematisch-petrographischen Gefügecharakterisierung für die Beurteilung der Festgesteine hinsichtlich ihrer Aufbereitung und ihrer Produkteigenschaften", Dissertation, Fakultät für Maschinenbau, Verfahrens- und Energietechnik, Technischen Universität Bergakademie Freiberg, Freiberg, 2007. Accessed: Jan. 17 2017.

[71] A. Naeimipour, J. Rostami, I. S. Buyuksagis, and O. Frough, "Estimation of rock strength using scratch test by a miniature disc cutter on rock cores or inside boreholes", *International Journal of Rock Mechanics and Mining Sciences*, vol. 107, pp. 9–18, 2018, doi: 10.1016/j.ijrmms.2018.03.020.

[72] J. Haavisto, A. Husso, and A. Laaksonen, "Compressive strength of core specimens drilled from concrete test cylinders", *Structural Concrete*, vol. 22, S1, 2021, doi: 10.1002/suco.202000428.

[73] J. Rusnak and C. Mark, "Using The Point Load Test To Determine The Uniaxial Compressive Strength Of Coal Measure Rock: Proceedings of the 19th International Conference on Ground Control in Mining, August 8-10", *Morgantown, West Virginia*, 2000.

[74] Normenausschuss Materialprüfung (NMP) im DIN Normenausschuss Bauwesen (NABau) im DIN, "Prüfverfahren für Naturstein – Bestimmung der einachsigen Druckfestigkeit; Deutsche Fassung EN 1926:2006: Prüfverfahren für Naturstein – Bestimmung der einachsigen Druckfestigkeit; Deutsche Fassung EN 1926:2006 Natural stone test methods – Determination of uniaxial compressive strength; German version EN 1926:2006", 2007.

[75] E. Hoek, "Rock mechanics laboratory testing in the context of a consulting engineering organization", *International Journal of Rock Mechanics and Mining Sciences & Geomechanics Abstracts*, vol. 14, no. 2, pp. 93–101, 1977, doi: 10.1016/0148-9062(77)90201-7.

[76] K. Thuro, "Empfehlung Nr. 5 "Punktlastversuche an Gesteinsproben" des Arbeitskreises 3.3 "Versuchstechnik Fels" der Deutschen Gesellschaft für Geotechnik", *Bautechnik*, vol. 87, no. 6, pp. 322–330, 2010, doi: 10.1002/bate.201010025.

[77] B. Tiryaki and A. C. Dikmen, "Effects of Rock Properties on Specific Cutting Energy in Linear Cutting of Sandstones by Picks", *International Journal of Rock Mechanics and Rock Engineering*, vol. 39, no. 2, pp. 89–120, 2006, doi: 10.1007/s00603-005-0062-7.

[78] C. Ai, J. Zhang, Y. Li, J. Zeng, X. Yang, and J. Wang, "Estimation Criteria for Rock Brittleness Based on Energy Analysis During the Rupturing Process", *International Journal of Rock Mechanics and Rock Engineering*, vol. 49, no. 12, pp. 4681–4698, 2016, doi: 10.1007/s00603-016-1078-x.

[79] A. E. Dursun and M. K. Gokay, "Cuttability Assessment of Selected Rocks Through Different Brittleness Values", *International Journal of Rock Mechanics and Rock Engineering*, vol. 49, no. 4, pp. 1173–1190, 2016, doi: 10.1007/s00603-015-0810-2.

[80] R. Altindag and A. Guney, "Predicting the relationships between brittleness and mechanical properties (UCS, TS and SH) of rocks", *Scientific Research and Essays*, vol. 16, no. 5, pp. 2107–2118, 2010. [Online]. Available: https://link.springer.com/content/pdf/10.1007/s00603-015-0810-2.pdf

[81] S. Yasar, "A General Semi-Theoretical Model for Conical Picks", *International Journal of Rock Mechanics and Rock Engineering*, 44 / 53, no. 6, pp. 2557–2579, 2020, doi: 10.1007/s00603-020-02078-3.

[82] R. M. Goktan and N. Gunes, "A comparative study of Schmidt hammer testing procedures with reference to rock cutting machine performance prediction", *International Journal of Rock Mechanics and Mining Sciences*, vol. 42, no. 3, pp. 466–472, 2005, doi: 10.1016/j.ijrmms.2004.12.002.

[83] U. Restner and K. Gehring, "Quantification of rock mass influence on cuttability with roadheaders", in *Proceedings TUR 2002*, Krakow - Krynica, 2002, pp. 53–68.

[84] A. Walther and M. Wilcke, "Zerstörungsfreie Ermittlung der Betondruckfestigkeit im Bestand mit kombinierten Prüfverfahren", TA Esslingen, 4. Colloquium Erhaltung von Bauwerken, Jan. 2015. Accessed: Apr. 14 2020.

[85] M. Kazemi, R. Madandoust, and J. d. Brito, "Compressive strength assessment of recycled aggregate concrete using Schmidt rebound hammer and core testing", *Construction and Building Materials*, vol. 224, pp. 630–638, 2019, doi: 10.1016/j.conbuildmat.2019.07.110.

[86] T. Rinder and H.-W. Reinhardt, "Bestimmung der Druckfestigkeit von hochfestem Beton mittels Rückprallhammer", *Beton- und Stahlbetonbau*, vol. 95, no. 6, pp. 330–335, 2000.

[87] A. Aydin and A. Basu, "The Schmidt hammer in rock material characterization", *Engineering Geology*, vol. 81, no. 1, pp. 1–14, 2005, doi: 10.1016/j.enggeo.2005.06.006.

[88] A. Bolla and P. Paronuzzi, "UCS field estimation of intact rock using the Schmidt hammer: A new empirical approach", *IOP Conference Series: Earth and Environmental Science*, vol. 833, no. 1, 2021, doi: 10.1088/1755-1315/833/1/012014.

[89] R. Barzegar, M. Sattarpour, R. Deo, E. Fijani, and J. Adamowski, "An ensemble tree-based machine learning model for predicting the uniaxial compressive strength of travertine rocks", *Neural Computing and Applications*, vol. 32, no. 13, pp. 9065–9080, 2020, doi: 10.1007/s00521-019-04418-z.

[90] E. Özdemir, "A New Predictive Model for Uniaxial Compressive Strength of Rock Using Machine Learning Method: Artificial Intelligence-Based Age-Layered Population Structure Genetic Programming (ALPS-GP)", *Arabian Journal for Science and Engineering*, 2021, doi: 10.1007/s13369-021-05761-x.

[91] A. Mahmoodzadeh *et al.,* "Artificial intelligence forecasting models of uniaxial compressive strength", *Transportation Geotechnics*, vol. 27, p. 100499, 2021, doi: 10.1016/j.trgeo.2020.100499.

[92] Q. Fang, B. Yazdani Bejarbaneh, M. Vatandoust, D. Jahed Armaghani, B. Ramesh Murlidhar, and E. Tonnizam Mohamad, "Strength evaluation of granite block samples with different predictive models", *Engineering with Computers*, vol. 37, no. 2, pp. 891–908, 2021, doi: 10.1007/s00366-019-00872-4.

[93]   Z. Tang, S. Li, S. Huang, F. Huang, and F. Wan, "Indirect Estimation of Rock Uniaxial Compressive Strength from Simple Index Tests: Review and Improved Least Squares Regression Tree Predictive Model", *Geotechnical and Geological Engineering*, vol. 39, no. 5, pp. 3843–3862, 2021, doi: 10.1007/s10706-021-01731-0.

[94]   S. Yasar, M. ÇapIk, and A. O. Yilmaz, "Investigation of relationships between cuttability parameters and schmidt hardness [Schmidt sertligi ile kesilebilirlik parametreleri arasindaki iliskilerin incelenmesi]", *Madencilik*, vol. 53, 1-2, pp. 31–38, 2014. [Online]. Available: https://www.scopus.com/inward/record.uri?eid=2-s2.0-85018184162&partnerID=40&md5=f55efe4ea9aadc745c237ff3df02c803

[95]   Y. L. Zheng, Q. B. Zhang, and J. Zhao, "Effect of microwave treatment on thermal and ultrasonic properties of gabbro", *Applied Thermal Engineering*, vol. 127, pp. 359–369, 2017, doi: 10.1016/j.applthermaleng.2017.08.060.

[96]   C. Doğruöz and N. Bölükbaşi, "Effect of Cone Indenter Hardness on Specific Energy of Rock Cutting", *SDÜ Fen Bil Enst Der*, vol. 21, no. 3, p. 743, 2017, doi: 10.19113/sdufbed.44433.

[97]   R. Altindag and A. Güney, "ISRM Suggested Method for determining the Shore Hardness value for rock", *International Journal of Rock Mechanics and Mining Sciences*, vol. 43, no. 1, pp. 19–22, 2006, doi: 10.1016/j.ijrmms.2005.04.004.

[98]   A. Basu, D. A. Mishra, and K. Roychowdhury, "Rock failure modes under uniaxial compression, Brazilian, and point load tests", *Bulletin of Engineering Geology and the Environment*, vol. 72, 3-4, pp. 457–475, 2013, doi: 10.1007/s10064-013-0505-4.

[99]   M. Entacher and K. Lassnig, "Findings from disc cutting tests on alpine lithologies / Erkenntnisse aus Diskenschneidversuchen an alpinen Lithologien", *Geomechanik Tunnelbau*, vol. 5, no. 5, pp. 547–556, 2012, doi: 10.1002/geot.201200041.

[100]   M. Entacher and E. Schuller, "Angular dependence of rock cutting forces due to foliation", *Tunnelling and Underground Space Technology*, vol. 71, pp. 215–222, 2018, doi: 10.1016/j.tust.2017.08.009.

[101]   P. Kirschner and A. Moser, "Anwendung von Gebirgsklassifikationssystemen im untertägigen Bergbau", *BHM Berg- und Hüttenmännische Monatshefte*, vol. 162, no. 6, pp. 216–222, 2017, doi: 10.1007/s00501-017-0606-7.

[102]   E. Hoek, "Practical Rock Engineering", 2006. [Online]. Available: https://www.rocscience.com/assets/resources/learning/hoek/Practical-Rock-Engineering-Full-Text.pdf

[103]   M. Entacher and J. Rostami, "TBM performance prediction model with a linear base function and adjustment factors obtained from rock cutting and indentation tests", *Tunnelling and Underground Space Technology*, vol. 93, p. 103085, 2019, doi: 10.1016/j.tust.2019.103085.

[104]   U. Restner and R. J. Plinninger, "Rock Mechanical Aspects of Roadheader Excavation", Salzburg, 2015.

[105]   P. Hartlieb and B. Grafe, "Experimental Study on Microwave Assisted Hard Rock Cutting of Granite", *BHM Berg- und Hüttenmännische Monatshefte*, vol. 162, no. 2, pp. 77–81, 2017, doi: 10.1007/s00501-016-0569-0.

[106]   P. Hartlieb, B. Grafe, T. Shepel, A. Malovyk, and B. Akbari, "Experimental study on artificially induced crack patterns and their consequences on mechanical excavation processes", *International Journal of Rock Mechanics and Mining Sciences*, vol. 100, pp. 160–169, 2017, doi: 10.1016/j.ijrmms.2017.10.024.

[107]   T. Shepel, B. Grafe, P. Hartlieb, C. Drebenstedt, and A. Malovyk, "Evaluation of cutting forces in granite treated with microwaves on the basis of multiple linear regression analysis", *International Journal of Rock Mechanics and Mining Sciences*, vol. 107, pp. 69–74, 2018, doi: 10.1016/j.ijrmms.2018.04.043.

[108]   X. Wang, Y. Liang, Q. Wang, and Z. Zhang, "Empirical models for tool forces prediction of drag-typed picks based on principal component regression and ridge regression methods",

Tunnelling and Underground Space Technology, vol. 62, pp. 75–95, 2017, doi: 10.1016/j.tust.2016.11.006.

[109] H. Copur, N. Bilgin, H. Tuncdemir, and C. Balci, "A set of indices based on indentation tests for assessment of rock cutting performance and rock properties", *The Journal of The South African Institute of Mining and Metallurgy*, vol. 103, 2003.

[110] R. Taylor, "Interpretation of the Correlation Coefficient: A Basic Review", *Journal of Diagnostic Medical Sonography*, no. 1, pp. 35–39, 1990.

[111] S. G. Demou, R. C. Olson, and C. F. Wingquist, *Determination of bit forces encountered in hard rock cutting for application to continuous miner design.: Report of Investigations 8748;*: United States Department of the Interior, 1983.

[112] P. Frenyo and W. Lange, "Die Auslegung von Schneidköpfen für optimale Löseleistungen", *Glückauf*, vol. 129, pp. 524–532, 1993.

[113] P. Frenyo and J. Henneke, "Gegenwärtiger Stand und mögliche Entwicklung der Teilschnitt-Vortriebstechnik.", *Glückauf*, 79-84.

[114] X. Li, S. Wang, S. Ge, R. Malekian, Z. Li, and Y. Li, "A study on drum cutting properties with full-scale experiments and numerical simulations", *Measurement*, vol. 114, pp. 25–36, 2018, doi: 10.1016/j.measurement.2017.09.006.

[115] J. Rieckhof and L. Heck, "Verfahren zur automatischen Regelung des Schnitthorizontes von Walzenschrämladern nach dem Flözverlauf", DE2349827C2, Oct 20, 1983.

[116] J. Rieckhof and L. Heck, "Verfahren zur automatischen Regelung des Schnitthorizontes von Walzenschrämladern nach dem Flözverlauf", DE2349827A1.

[117] M. He, Y. Liu, and Q. Zhang, "Cutting head used for on-line identification of coal rock hardness grade and using method", CN000107575226A, Jan 12, 2018.

[118] P. Cheluszka, M. Dolipski, R. Mann, P. Sobota, and M. Golabek, "Device for method for measuring dynamic loads of the working unit cutting picks, preferably of mechanical coal miners", PL228215B1; PL415965A1, Poland.

[119] P. Cheluszka, "Experimental Identification Of The Dynamic Load Of Conical Picks During The Cutting Process Of Transverse Cutting Heads Of Boom–Type Roadheader", in *GEOLINKS Conference Proceedings*, 2019. [Online]. Available: https://www.geolinks.info/library/experimental-identification-of-the-dynamic-load-of-conical-picks-during-the-cutting-process-of-transverse-cutting-heads-of-boom%E2%80%93type-roadheader

[120] M. Entacher and R. Galler, "Development of a disc cutter force and face monitoring system for mechanized tunnelling / Ortsbrustmonitoring und Leistungsprognose bei TBM-Vortrieben", *Geomechanik Tunnelbau*, vol. 6, no. 6, pp. 725–731, 2013, doi: 10.1002/geot.201310013.

[121] M. Entacher, G. Winter, and R. Galler, "Cutter force measurement on tunnel boring machines – Implementation at Koralm tunnel", *Tunnelling and Underground Space Technology*, vol. 38, pp. 487–496, 2013, doi: 10.1016/j.tust.2013.08.010.

[122] M. Entacher, E. Schuller, and R. Galler, "Rock Failure and Crack Propagation Beneath Disc Cutters", *International Journal of Rock Mechanics and Rock Engineering*, vol. 48, no. 4, pp. 1559–1572, 2015, doi: 10.1007/s00603-014-0661-2.

[123] J. van Eldert, H. Schunnesson, and D. Johansson, "The History and Future of Rock Mass Characterisation by Drilling in Drifting: From sledgehammer to PC-tablet", in *Mine Planning and Equipment Selection // Proceeding of the 26th International Symposium on Mine Planning and Equipment Selection: MPES 2017*, 2017, pp. 99–105.

[124] V. Jouni, "Investigation Ahead of the Tunnel Face by Use of a Measurement-While-Drilling System at Olkiluoto, Finland: Working Report", Accessed: Feb. 11 2020.

[125] H. Schunnesson, "Drill Process Monitoring in Percussive Drilling: a multivariate approach to data analysis", Licenciate Thesis, Division of Mining Equipment Engineering, Luleå University Of Technology, LULEÅ, 1990.

[126]   J. Navarro, H. Schunnesson, R. Ghosh, P. Segarra, D. Johansson, and J. Á. Sanchidrián, "Application of drill-monitoring for chargeability assessment in sublevel caving", *International Journal of Rock Mechanics and Mining Sciences*, vol. 119, pp. 180–192, 2019, doi: 10.1016/j.ijrmms.2019.03.026.

[127]   M. Danielsson, R. Ghosh, M. Navarro, D. Johansson, and H. Schunnesson, "Utilizing production data to predict operational disturbances in sublevel caving: A data driven approach", in *Mine Planning and Equipment Selection // Proceeding of the 26th International Symposium on Mine Planning and Equipment Selection: MPES 2017*, 2017.

[128]   W. Liu, J. Rostami, A. Ray, and D. Elsworth, "Statistical Analysis of the Capabilities of Various Pattern Recognition Algorithms for Fracture Detection Based on Monitoring Drilling Parameters", *International Journal of Rock Mechanics and Rock Engineering*, vol. 25, no. 5, p. 905, 2019, doi: 10.1007/s00603-019-01965-8.

[129]   E. Clausen *et al.,* "Geotechnical parameter definition from machine performance measures for sonic drilling", *2nd International Raw Materials Extraction Innovation Conference*, no. 2, pp. 128–148, 2019. [Online]. Available: https://tu-freiberg.de/sites/default/files/media/institut-fuer-markscheidewesen-und-geodaesie-12465/institut/publikationen/schriftenreihe/tagungsbandrtm2019.pdf

[130]   V. S. Vezhapparambu and S. L. Ellefmo, "Estimating the blast sill thickness using changepoint analysis of MWD data", *International Journal of Rock Mechanics and Mining Sciences*, vol. 134, p. 104443, 2020, doi: 10.1016/j.ijrmms.2020.104443.

[131]   B. Duppong, P. Kornev, F. Kuhnemund, C. Moberg, M. Teiner, and T. Temmann, "Machine Control System For Milling Arched Roof Structures", WO002018112337A1, Jun 21, 2018.

[132]   G. Chevrette, P. H. Hennecke, Henderson Everett James, Piefenbrink Wilfried, J. N. Repski, and J. A. Saint-Pierre, "Automatic Control Of A Machine Used For Excavating Drifts, Tunnels,Stopes, Caverns Or The Like", WO 001996019639 A1, Jun 27, 1996.

[133]   J. R. Hayes and H. A. Smith, "Continuous Control System For A Mining Or Tunnelling Machine", EP0807203B1, Dec 16, 1998.

[134]   H. Kargl, A. T. Gaal, H. Haubmann, and A. T. Knittelfeld, "Verfahren zum Regeln des Antriebs einer Vortriebs- oder Gewinnungsmaschine", DE 11 2007 000 152 B4, Oct 29, 2015.

[135]   Z. A. Jokonya Persistence and Joy Mm Delaware Inc, Us, "Automated Operations Of A Mining Machine", WO 2013/020056A1, Feb 7, 2013.

[136]   C. S. Tasman and N. K. Ray, "All-In-One Integrated Sensing Device For Machine Control", WO002016032685A1, Mar 3, 2016.

[137]   Sandvik Mining & Construction Oy, "Understanding Underground", 2015. [Online]. Available: https://www.rocktechnology.sandvik/en/products/mechanical-cutting-equipment/roadheaders-for-tunneling/mt520-roadheader-for-tunneling/

[138]   H. Andreasson, S. Joyce, R. Lundh, M. Mansouri, and F. Pecora, "Method And System For Assigning Tasks To Drill Rigs", WO002017058089A1, Apr 6, 2017.

[139]   Caterpillar Global, *Dozer D11 | Bulldozer | Kettendozer | Cat | Caterpillar.* [Online]. Available: https://www.cat.com/de_DE/products/new/equipment/dozers/large-dozers/15969853.html (accessed: May 27 2022).

[140]   U. Restner, "Hard Rock Continuous Mining: Rapid Mine Development System", International symposium on mechanical hard rock excavation. Leoben, Oct. 13 2016.

[141]   G. Schaffner, J. Stirnimann, A. Kirchheim, and Veselovac, Drazen, Schmitz, René, "Tool Condition Monitoring System", WO 2007/025404A1, Mar 8, 2007.

[142]   F. Gutberlet, S. Hebgen, and C. Wirtz, "Device for measuring wear in disc cutters, especially on tunnel drilling machines, has amagnet in the wearing layer at the circumference of the disc and a sensor for measuring the magnetic field strength", DE102005016346B3, Jan 4, 2007.

[143] C. Stewart, "System And Method For Determining Efficiency Of An Industrial Machine", EP 3 495 608 A1, Jun 12, 2019.

[144] "Bedienerfreundliche Sensorik zum Ermitteln einer mechanischen Belastung eines Abbauwerkzeugs einer Tunnelbohrmaschine", DE202012103593U1, DE 202012103593, Jan 10, 2013.

[145] S. Barwart and R. Galler, "Hochpräzise Sensorik zum Ermitteln einer mechanischen Belastung eines Abbauwerkzeugs einer Tunnelbohrmaschine", DE102014105014, DE, Oct 8, 2015.

[146] C. Barimani, G. Hähn, and S. Wagner, "Verfahren zur Bestimmung des Verschleißzustandes", DE 102008045470 A1, Mar 4, 2001.

[147] K. Heemann, B. Holl, G. Hähn, and A. Mahlberg, "DE000010203732A1", DE 000010203732 A1, Aug 21, 2003.

[148] D. Hall, "Sensored pick assembly", US000009234422B2, Jan 12, 2016.

[149] E. Lill and D. Freymann, "Anordnung einer Beschädigungs-Warnsensorik an den Meißelhalterungen einer Teilschnittmaschine", DE4415824C1, 23.11.95.

[150] B. Tiryaki, "Predicting intact rock strength for mechanical excavation using multivariate statistics, artificial neural networks, and regression trees", *Engineering Geology*, vol. 99, 1-2, pp. 51–60, 2008, doi: 10.1016/j.enggeo.2008.02.003.

[151] R. B. Kaunda and B. Asbury, "Prediction of rock brittleness using nondestructive methods for hard rock tunneling", *Journal of Rock Mechanics and Geotechnical Engineering*, vol. 8, no. 4, pp. 533–540, 2016, doi: 10.1016/j.jrmge.2016.03.002.

[152] O. Saeidi, S. R. Torabi, and M. Ataei, "Prediction of the Rock Mass Diggability Index by Using Fuzzy Clustering-Based, ANN and Multiple Regression Methods", *International Journal of Rock Mechanics and Rock Engineering*, vol. 47, no. 2, pp. 717–732, 2014, doi: 10.1007/s00603-013-0426-3.

[153] A. Aras, H. Özşen, and A. E. Dursun, "Using Artificial Neural Networks for the Prediction of Bond Work Index from Rock Mechanics Properties", *Mineral Processing and Extractive Metallurgy Review*, vol. 41, no. 3, pp. 145–152, 2020, doi: 10.1080/08827508.2019.1575216.

[154] A. Salimi, J. Rostami, and C. Moormann, "Application of rock mass classification systems for performance estimation of rock TBMs using regression tree and artificial intelligence algorithms", *Tunnelling and Underground Space Technology*, vol. 92, p. 103046, 2019, doi: 10.1016/j.tust.2019.103046.

[155] T. Liu, C. Lu, Q. Liu, and Y. Zha, "Coal and Rock Hardness Identification Based on EEMD and Multi-Scale Permutation Entropy", *Entropy*, vol. 23, no. 9, 2021, doi: 10.3390/e23091113.

[156] H. Wang, S. Lu, M. Huang, and X. Zhao, "Bulletin of the Polish Academy of Sciences: Technical Sciences", 2020. Accessed: Jan. 17 2022.

[157] T. Vraetz, *Entwicklung und Anwendung eines innovativen Konzepts zur Inline-Charakterisierung von Stoffgemischen in kontinuierlichen Massenströmen mittels der Acoustic Emission Technologie; 1. Auflage*: RWTH Aachen University, 2018.

[158] B. Grafe *et al.,* "InnoCrush: New Solutions for Highly Selective Process Chains", in *Innovation-Based Development of the Mineral Resources Sector: Proceedings of the 11th Russian-German Raw Materials Conference, November 7-8, 2018, Potsdam, Germany*, V. Litvinenko, Ed., Milton: Chapman and Hall/CRC, 2018.

[159] K. Lassnig, M. Entacher, F. Biermeier, R. Galler, and F. Ebner, "Decrease of Schmidt hammer hardness controlled by schistosity orientation of metamorphic rocks after loading with TBM cutters", *International Journal of Rock Mechanics and Mining Sciences*, vol. 56, 27-33, 2012. [Online]. Available: https://www.sciencedirect.com/science/article/pii/S1365160912001542

[160] P.-F. Yin and S.-Q. Yang, "Experimental investigation of the strength and failure behavior of layered sandstone under uniaxial compression and Brazilian testing", *Acta Geophys.*, vol. 66, no. 4, pp. 585–605, 2018, doi: 10.1007/s11600-018-0152-z.

References

[161] M. Hakala, H. Kuula, and J. A. Hudson, "Estimating the transversely isotropic elastic intact rock properties for in situ stress measurement data reduction: A case study of the Olkiluoto mica gneiss, Finland", *International Journal of Rock Mechanics and Mining Sciences*, vol. 44, no. 1, pp. 14–46, 2007, doi: 10.1016/j.ijrmms.2006.04.003.

[162] J.-W. Cho, H. Kim, S. Jeon, and K.-B. Min, "Deformation and strength anisotropy of Asan gneiss, Boryeong shale, and Yeoncheon schist", *International Journal of Rock Mechanics and Mining Sciences*, vol. 50, pp. 158–169, 2012, doi: 10.1016/j.ijrmms.2011.12.004.

[163] B. Grafe, "High power microwave irradiation as a means of inducing damage to very hard rock to reduce the cutting resistance during mechanical excavation", ISCSM 2016 – 13th International Symposium Continuous Surface Mining. Belgrade, Sep. 12 2016.

[164] U. Sebastian, *Die Geologie des Erzgebirges,* 1st ed. Heidelberg: Springer Berlin / Heidelberg, 2013978-3-8274-2977-3.

[165] P. Rimos, "Possibilities of Utilizing Cutting Force Analysis for Sensing Different Lithologies during Mechanical Excavation", Master thesis, Institute of Mining and Special Civil Construction, TU Bergakademie Freiberg, Freiberg, 2017.

[166] D. Cook, *Practical machine learning with H2O: Powerful, scalable techniques for deep learning and AI*. Sebastopol, CA: O'Reilly Media, 2017978-1-491-96460-6.

[167] K. Byrne, G. Lesage, W. A. Morris, R. J. Enkin, S. A. Gleeson, and R. Lee, "Variability of outcrop magnetic susceptibility and its relationship to the porphyry Cu centers in the Highland Valley Copper district", *Ore Geology Reviews*, vol. 107, pp. 201–217, 2019, doi: 10.1016/j.oregeorev.2019.02.015.

[168] R. J. Hyndman and Y. Fan, "Sample Quantiles in Statistical Packages", *The American Statistician*, vol. 50, no. 4, pp. 361–365, 1996, doi: 10.2307/2684934.

[169] J. A. Pérez, G. R. Gonçalves, J. M. G. Rangel, and P. F. Ortega, "Accuracy and effectiveness of orthophotos obtained from low cost UASs video imagery for traffic accident scenes documentation", *Advances in Engineering Software*, vol. 132, pp. 47–54, 2019, doi: 10.1016/j.advengsoft.2019.03.010.

[170] G. S. Smith, *Digital Orthophotography and GIS.* [Online]. Available: https://proceedings.esri.com/library/userconf/proc95/to150/p124.html (accessed: Dec. 26 2020).

[171] A. Malovyk, "Investigating the reduction of cutting resistance of granite specimen induced by microwave irradiation with varying irradiation times", Master thesis, Institue of Mining and Special Civil Engineering, TU Bergakademie Freiberg, Freiberg, 2017.

[172] Ş. Gül, "Estimation of Accuracy of Force-Component-Ratio Based Material Differentiation on 3D Scale on Fluorite-Barite Concrete Samples", Master thesis, Institute for Mining and Special Civil Engineering, TU Bergakademie Freiberg, Freiberg, 2020.

[173] S. Ranganathan, M. Gribskov, K. Nakai, and C. Schönbach, Eds., *Encyclopedia of bioinformatics and computational biology*. Amsterdam, Boston, Heidelberg: Elsevier, 2019. [Online]. Available: https://www.sciencedirect.com/science/referenceworks/9780128114322

[174] N. Altman and M. Krzywinski, "Association, correlation and causation", *Nature methods*, vol. 12, no. 10, pp. 899–900, 2015, doi: 10.1038/nmeth.3587.

[175] W. Revelle, *psych: Procedures for Psychological, Psychometric, and Personality Research*. Evanston, Illinois: Northwestern University, 2020. [Online]. Available: https://cran.r-project.org/package=psych

[176] C. Molnar, *Interpretable machine learning: A guide for making black box models explainable*. Munich: Christoph Molnar, 2022. [Online]. Available: https://christophm.github.io/interpretable-ml-book/

[177] T. Hastie, R. Tibshirani, and J. H. Friedman, *The elements of statistical learning: Data mining, inference, and prediction,* 12th ed. New York, NY: Springer, 2017978-03-8784-857-0.

[178] H2O.ai, *K-Means Clustering — H2O 3.36.1.2 documentation.* [Online]. Available: https://docs.h2o.ai/h2o/latest-stable/h2o-docs/data-science/k-means.html (accessed: May 29 2022).

[179] F. Günther and S. Fritsch, "neuralnet: Training of Neural Networks", *The R Journal*, vol. 2010, 2:1, pp. 30–38, Jun. 2010, doi: 10.32614/RJ-2010-006.

[180] D. Becker, "Rectified Linear Units (ReLU) in Deep Learning", *Kaggle*, 07 May., 2018. https://www.kaggle.com/dansbecker/rectified-linear-units-relu-in-deep-learning/notebook (accessed: Oct. 18 2021).

[181] P. Ramachandran, B. Zoph, and Q. Le V, "Searching for Activation Functions", Oct. 2017. [Online]. Available: https://arxiv.org/pdf/1710.05941

[182] Mohammad Adil, Rahat Ullah, Salma Noor, and Neelam Gohar, "Effect of number of neurons and layers in an artificial neural network for generalized concrete mix design", *Neural Computing and Applications*, pp. 1–9, doi: 10.1007/s00521-020-05305-8.

[183] J. D. Olden, M. K. Joy, and R. G. Death, "An accurate comparison of methods for quantifying variable importance in artificial neural networks using simulated data", *Ecological Modelling*, vol. 178, 3-4, pp. 389–397, 2004, doi: 10.1016/J.ECOLMODEL.2004.03.013.

[184] S. Samarasinghe, D. Kulasiri, and T. Jamieson, "Neural networks for predicting fracture toughness of individual wood samples", *Silva Fenn.*, vol. 41, no. 1, 2007, doi: 10.14214/sf.309.

[185] R. Hecht-Nielsen, "Kolmogorov's Mapping Neural Network Existence Theorem", *Mathematics*, 1987. [Online]. Available: https://www.semanticscholar.org/paper/Kolmogorov"s-Mapping-Neural-Network-Existence-Hecht-Nielsen

[186] J. Heaton, *The Number of Hidden Layers*. Blog post. [Online]. Available: https://www.heatonresearch.com/2017/06/01/hidden-layers.html (accessed: Oct. 11 2020).

[187] *Deep Learning (Neural Networks) — H2O 3.36.1.2 documentation.* [Online]. Available: https://docs.h2o.ai/h2o/latest-stable/h2o-docs/data-science/deep-learning.html (accessed: Jun. 3 2022).

[188] T. D. Gedeon, "Data Mining of Inputs: Analysing Magnitude and Functional Measures", *International Journal of Neural Systems*, vol. 08, no. 02, pp. 209–218, 1997, doi: 10.1142/S0129065797000227.

[189] H2O.ai, *Distributed Random Forest (DRF) — H2O 3.34.0.7 documentation.* [Online]. Available: https://docs.h2o.ai/h2o/latest-stable/h2o-docs/data-science/drf.html (accessed: Dec. 27 2021).

[190] M. Mohammadi, J. Khademi Hamidi, J. Rostami, and K. Goshtasbi, "A Closer Look into Chip Shape/Size and Efficiency of Rock Cutting with a Simple Chisel Pick: A Laboratory Scale Investigation", *International Journal of Rock Mechanics and Rock Engineering*, vol. 53, no. 3, pp. 1375–1392, 2020, doi: 10.1007/s00603-019-01984-5.

[191] P. Hartlieb, M. Leindl, F. Kuchar, T. Antretter, and P. Moser, "Damage of basalt induced by microwave irradiation: Special Issue - Physical Separation", *Minerals Engineering*, vol. 31, pp. 82–89, 2012, doi: 10.1016/j.mineng.2012.01.011.

[192] T. Peinsitt *et al.,* "Microwave heating of dry and water saturated basalt, granite and sandstone", *International Journal of Mining and Mineral Engineering*, vol. 2, no. 1, p. 18, 2010, doi: 10.1504/IJMME.2010.031810.

[193] K. Thuro and R. J. Plinninger, "Hard rock tunnel boring, cutting, drilling and blasting: Rock parameters for excavatability: conference paper", *ISRM - –Technology roadmap for rock mechanics, South African Institute of Mining and Metallurgy*, 2003. [Online]. Available: https://www.researchgate.net/publication/285379710

[194] M. Sheng, Z. Cheng, S. Gao, H. Shi, and Y. Zhang, "Shale bedding planes control rock removal behaviors of PDC cutter: Single cutter experiment", *Journal of Petroleum Science and Engineering*, vol. 185, p. 106640, 2020, doi: 10.1016/j.petrol.2019.106640.

[195]   European Comission, *HORIZON 2020 – Work Programme 2014-2015: Commission Decision C(2014)4995.* [Online]. Available: https://ec.europa.eu/transparency/documents-register/detail?ref=C(2014)4995&lang=de (accessed: Jan. 16 2022).

[196]   BBM GmbH, *Datenblatt Teilschnittmaschine BRH 130.* [Online]. Available: https://www.operta-bbm.de/maschinenbau/fertigung/ (accessed: Jan. 15 2022).

[197]   BBM GmbH, *Datenblatt Teilschnittmaschine BRH 300/400.* [Online]. Available: https://www.operta-bbm.de/maschinenbau/fertigung/ (accessed: Jan. 15 2022).

[198]   Sandvik Mining, "Sandvik MT520 Roadheader Product Leaflet", 2017. [Online]. Available: https://www.rocktechnology.sandvik/en/products/mechanical-cutting-equipment/roadheaders-for-tunneling/mt520-roadheader-for-tunneling/

[199]   Kistler Holding AG, "Kraftsensoren: Product range document", 2021. [Online]. Available: https://www.kistler.com/de/produkt/type-9076c4/

[200]   K. Ueda and A. Umeda, "Dynamic response of strain gages up to 300 kHz", *Experimental Mechanics*, vol. 38, pp. 93–98, 1998.

[201]   Kistler Holding AG, "Instruction Manual Piezoelectric triaxial force sensor Type 90x7C, 90x8C,090x6C4", 2021.

[202]   Hbm, *newLight FS62 | Optischer Dehnungssensor.* [Online]. Available: https://www.hbm.com/de/8120/newlight-fs62-optischer-dehnungssensor/ (accessed: Jan. 16 2022).

[203]   *TDR 140 - Products | ADVANTEC Tunnel & Mining.* [Online]. Available: https://tunnel-mining.advantec.company/en/products/tdr-140 (accessed: Jan. 15 2022).

[204]   Hbm, "FS62PSS; Patch-Dehnungssensor; Datenblatt; B05141",

[205]   *Dehnmessstreifen - HAEHNE Elektronische Messgeräte GmbH.* [Online]. Available: https://haehne.de/service/glossar-kraftaufnehmer/dehnmessstreifen (accessed: Jan. 16 2022).

[206]   Kistler Holding AG, "Quarz-Quermessdübel Typ 9240AA3, 9240AB3, 09240AC3: Pruduct sheet", 2019.

[207]   HBM Messtechnik GmbH, "CST/300 Piezoelectric Strain Transducer: Product Datasheet", 2019.

[208]   HBM Messtechnik GmbH, "Dehnungsmessstreifen: Product Palette", 2021.

[209]   S. Prabhakaran, *Strategies to Speedup R Code.* [Online]. Available: https://www.r-bloggers.com/strategies-to-speedup-r-code/ (accessed: Nov. 5 2019).

[210]   H. Wickham, *Advanced R,* 2nd ed.: Chapman and Hall/CRC, 2019978-0815384571. [Online]. Available: https://adv-r.hadley.nz/index.html

[211]   *T1655III Terrain Leveler SEM | Equipment | Vermeer.* [Online]. Available: https://www.vermeer.com/LA/en/N/equipment/terrain_leveler_sem/t1655iii_terrain_leveler_sem (accessed: Feb. 12 2020).

[212]   *Über uns | Wirtgen Group.* [Online]. Available: https://www.wirtgen-group.com/de-de/unternehmen/wirtgen-group/ (accessed: Feb. 12 2020).

[213]   Bauer, "Einsatz von Surface MInern in der Mineralstoffgewinnung: BVÖ Herbstveranstaltung 2016", Leoben, 2016.

[214]   Tesmec, *Surface Miners | Tesmec.* [Online]. Available: https://www.tesmec.com/trenchers/products/surface-miners (accessed: Jun. 6 2022).

[215]   *Surface Miner | Mining Equipment | Mining Equipments in India.* [Online]. Available: https://www.puzzolana.net/mining/surface-miner (accessed: Feb. 13 2020).

[216]   C. Niemann-Delius, C. Drebenstedt, K. Müllensiefen, and R. D. Stoll, *Der Braunkohlentagebau: Bedeutung, Planung, Betrieb, Technik, Umwelt.* Berlin: Springer-Verlag, 2008978-35-4078-400-5.

[217]   K. Dey and J. Bhattacharya, "Operation of Surface Miner: Retrospect of a Decade Journey in India", *Procedia Engineering*, vol. 46, pp. 97–104, 2012, doi: 10.1016/j.proeng.2012.09.451.

[218] *L&T Surface Miner KSM 304 in Operation.* [Online]. Available: https://www.youtube.com/ watch?v=R2-EQyBKrJk (accessed: Feb. 13 2020).

[219] *NACoal | Surface Miner Operation & Maintenance.* [Online]. Available: https:// www.nacoal.com/contract-mining/maintenance (accessed: Feb. 13 2020).

[220] *TAKRAF - Mining Technology | Mining News and Views Updated Daily.* [Online]. Available: https://www.mining-technology.com/contractors/highwall/takraf/ (accessed: Feb. 13 2020).

[221] "KSM 403 Surface Miner - lntecc", [Online]. Available: https://www.google.com/url?sa=t&rct= j&q=&esrc=s&source=web&cd=1&ved= 2ahUKEwjMiNiv187nAhXEy6QKHeRUAEEQFjAAegQIAxAB&url= https%3A%2F%2Fwww.lntecc.com%2Fhomepage%2Fmultislug%2Fdemos%2Fimages%2Fm mh%2FKSM403_surface_miner.pdf&usg=AOvVaw2TdGAyX9s0u-a1m84f-kAA

[222] H. Copur, Ozdemir, Levent, and J. Rostami, "Roadheader applications in mining and tunneling industries", *Mining Engineering*, no. 12, 1998.

[223] Wikimedia Commons, *Axial Roadheader.* [Online]. Available: https://commons.wikimedia.org /wiki/File:Maszyny_urzadzenia_gornicze_targiMTPGIH_0025.JPG (accessed: Jun. 3 2022).

[224] J. Townsend, "Innovation in Coal-mining Machinery: the Case of the Anderton Shearer Loader", in *Science Policy Research Unit book, Technical innovation and British economic performance*, K. Pavitt, Ed., London: Macmillan, 1982, pp. 142–158.

[225] Peabody Energy, Inc., *Longwall shearer and armored face conveyor operating at the Twentymile underground coal mine.* [Online]. Available: https://commons.wikimedia.org/wiki/ File:Twentymile_Underground_Coal_Mine.png (accessed: Jun. 3 2022).

[226] *Eickhoff SL900 shearer helps set world production record at SUEK's Yalevsky mine - International Mining.* [Online]. Available: https://im-mining.com/2018/09/11/eickhoff-sl900- shearer-helps-set-world-production-record-sueks-yalevsky-mine/ (accessed: Mar. 9 2020).

[227] *Australia's Grasstree mine does it again: another record with Eickhoff | MINING REPORT.* [Online]. Available: https://mining-report.de/english/blog/australias-grasstree-mine-does-it- again-another-record-with-eickhoff/ (accessed: Mar. 9 2020).

[228] H. Jeong, S. Choi, S. Lee, and S. Jeon, *Relationship between brittleness of rock, CAI and cutting performance of a TBM disc cutter*: Jeju Island, Korea, 2019.

[229] R. Galler, T. Stoxreiter, and R. Wenighofer, "Disc cutter load monitoring and face monitoring in TBM-tunnelling - developments for detailed analysis of the cutting process", Leoben, Sep. 14 2016.

[230] C. Niedrighaus, T. Vraetz, C. Bernet, and K. Nienhaus, "Intelligent Telescopic Boom for Underground Scaling", *Mining Report Glückauf*, no. 154, pp. 105–113, 2018.

[231] S. Yasar and A. O. Yilmaz, "Drag pick cutting tests: A comparison between experimental and theoretical results", *Journal of Rock Mechanics and Geotechnical Engineering*, 2018, doi: 10.1016/j.jrmge.2018.02.007.

[232] Y. Sun and X. S. Li, "A probabilistic approach for assessing failure risk of cutting tools in underground excavation", *Tunnelling and Underground Space Technology*, vol. 70, pp. 299– 308, 2017, doi: 10.1016/j.tust.2017.08.029.

[233] J.-Y. Park *et al.,* "A study on rock cutting efficiency and structural stability of a point attack pick cutter by lab-scale linear cutting machine testing and finite element analysis", *International Journal of Rock Mechanics and Mining Sciences*, vol. 103, pp. 215–229, 2018, doi: 10.1016/j.ijrmms.2018.01.034.

[234] H. Kang *et al.,* "A new linear cutting machine for assessing the rock-cutting performance of a pick cutter", *International Journal of Rock Mechanics and Mining Sciences*, vol. 88, pp. 129– 136, 2016, doi: 10.1016/j.ijrmms.2016.07.021.

[235] C. Dogruoz, N. Bolukbasi, J. Rostami, and C. Acar, "An Experimental Study of Cutting Performances of Worn Picks", *International Journal of Rock Mechanics and Rock Engineering*, vol. 49, no. 1, pp. 213–224, 2016, doi: 10.1007/s00603-015-0734-x.

[236] R. Gertsch, L. Gertsch, and J. Rostami, "Disc cutting tests in Colorado Red Granite: Implications for TBM performance prediction", *International Journal of Rock Mechanics and Mining Sciences*, vol. 44, no. 2, pp. 238–246, 2007, doi: 10.1016/j.ijrmms.2006.07.007.

[237] B. He, W. Shao, J. Y. Tang, X. M. Zong, and K. X. Kang, "The Effect of Pick Profile on the Cutting Performance of Point Attack Picks", *Key Engineering Materials*, vol. 789, pp. 31–36, 2018, doi: 10.4028/www.scientific.net/KEM.789.31.

[238] B. Tiryaki, I. D. Gipps, and X. S. Li, "Laboratory Comparison of Mini-Discs with Point-Attack Picks", *Advanced Materials Research*, 126-128, pp. 189–194, 2010, doi: 10.4028/www.scientific.net/AMR.126-128.189.

[239] Y. Pan, Q. Liu, X. Peng, X. Kong, J. Liu, and X. Zhang, "Full-Scale Rotary Cutting Test to Study the Influence of Disc Cutter Installment Radius on Rock Cutting Forces", *International Journal of Rock Mechanics and Rock Engineering*, vol. 51, no. 7, pp. 2223–2236, 2018, doi: 10.1007/s00603-018-1460-y.

[240] X. Zhang, J. Li, Y. Xia, L. Lin, M. Li, and L. Chen, "Cutting Characteristics and Layout of Pre-cutting Machine Cutter", *Period. Polytech. Civil Eng.*, 2015, doi: 10.3311/PPci.15339.

[241] S. Liu, H. Ji, and X. Liu, "Effect of pick working angle on the cutting performance of a cutting head", *Journal of the Brazilian Society of Mechanical Sciences and Engineering*, vol. 39, no. 10, pp. 4147–4159, 2017, doi: 10.1007/s40430-017-0806-9.

[242] B. Tiryaki, J. N. Boland, and X. S. Li, "Empirical models to predict mean cutting forces on point-attack pick cutters", *International Journal of Rock Mechanics and Mining Sciences*, vol. 47, no. 5, pp. 858–864, 2010, doi: 10.1016/j.ijrmms.2010.04.012.

[243] S. Yasar and A. O. Yilmaz, "Drag pick cutting tests: A comparison between experimental and theoretical results", *Journal of Rock Mechanics and Geotechnical Engineering*, vol. 10, no. 5, pp. 893–906, 2018, doi: 10.1016/j.jrmge.2018.02.007.

[244] S. Yasar, "Predictive plots for conical pick performance using mechanical and elastoplastic properties of rocks", 2020, doi: 10.1016/J.JRMGE.2019.12.020.

[245] S. Yasar and A. O. Yilmaz, "Vertical rock cutting rig (VRCR) suggested for performance prediction of roadheaders", *International Journal of Mining, Reclamation and Environment*, vol. 33, no. 3, pp. 149–168, 2017, doi: 10.1080/17480930.2017.1363482.

[246] C. Balci, M. A. Demircin, H. Copur, and H. Tuncdemir, "Estimation of optimum specific energy based on rock properties for assessment of roadheader performance", *The Journal of The South African Institute of Mining and Metallurgy*, no. 11, pp. 633–641, 2004. [Online]. Available: https://www.saimm.co.za/publications/journal-papers/

[247] R. Comakli, S. Kahraman, C. Balci, and D. Tumac, "Estimating specific energy from the brittleness indexes in cutting metallic ores", *The Journal of The South African Institute of Mining and Metallurgy*, vol. 116, no. 8, pp. 763–768, 2016, doi: 10.17159/2411-9717/2016/v116n8a8.

[248] H. Jeong and S. Jeon, "Characteristic of size distribution of rock chip produced by rock cutting with a pick cutter", *Geomechanics and Engineering*, vol. 15, no. 3, pp. 811–822, 2018.

[249] X. Wang, O. Su, and K. Gao, "Evaluation of normal forces at varying cutting angles of conical picks on sandstones", *Arabian Journal of Geosciences*, vol. 14, no. 7, 2021, doi: 10.1007/s12517-021-06924-8.

[250] K. Fukui and S. Okubo, "Some Attempts for Estimating Rock Strength and Rock Mass Classification from Cutting Force and Investigation of Optimum Operation of Tunnel Boring Machines", *International Journal of Rock Mechanics and Rock Engineering*, vol. 39, no. 1, pp. 25–44, 2006, doi: 10.1007/s00603-005-0071-6.

[251] X. Wang, Q.-F. Wang, and O. Su, "Tool Forces And Specific Energy Prediction Models In The Process Of Sandstones Cutting By Using Conical Picks // KALEM UÇLU KESKİLERLE KUMTAŞI KAZISINDA KESKİ KUVVETLERİ VE SPESİFİK ENERJİ TAHMİN MODELLERİ", *Bilimsel Madencilik Dergisi*, pp. 5–14, 2018, doi: 10.30797/madencilik.422814.

[252] H. Jeong, S. Choi, and S. Jeon, "Effect of skew angle on the cutting performance and cutting stability of point-attack type picks", *Tunnelling and Underground Space Technology*, vol. 103, p. 103507, 2020, doi: 10.1016/j.tust.2020.103507.

[253] M. Cardu, A. Rispoli, G. Iabichino, P. Oreste, and F. Vagnon, "Theoretical and Experimental Results from Laboratory Tests by ILCM", *Geotechnical and Geological Engineering*, vol. 39, no. 5, pp. 3573–3597, 2021, doi: 10.1007/s10706-021-01712-3.

[254] Jeong Hoyoung and Jeon Seokwon, "Characteristic of size distribution of rock chip produced by rock cutting with a pick cutter", *Geomechanics and Engineering*, vol. 15, no. 3, pp. 811–822, 2018, doi: 10.12989/GAE.2018.15.3.811.

[255] H. Copur, "Linear stone cutting tests with chisel tools for identification of cutting principles and predicting performance of chain saw machines", *International Journal of Rock Mechanics and Mining Sciences*, vol. 47, no. 1, pp. 104–120, 2010, doi: 10.1016/j.ijrmms.2009.09.006.

[256] H. Copur, N. Bilgin, C. Balci, D. Tumac, and E. Avunduk, "Effects of Different Cutting Patterns and Experimental Conditions on the Performance of a Conical Drag Tool", *International Journal of Rock Mechanics and Rock Engineering*, vol. 50, no. 6, pp. 1585–1609, 2017, doi: 10.1007/s00603-017-1172-8.

[257] D. Tumac, H. Copur, C. Balci, S. Er, and E. Avunduk, "Investigation into the Effects of Textural Properties on Cuttability Performance of a Chisel Tool", *International Journal of Rock Mechanics and Rock Engineering*, vol. 51, no. 4, pp. 1227–1248, 2018, doi: 10.1007/s00603-017-1376-y.

[258] W. Shao, X. S. Li, Y. Sun, and H. Huang, "Linear Rock Cutting with SMART*CUT Picks", *Applied Mechanics and Materials*, 477-478, pp. 1378–1384, 2013, doi: 10.4028/www.scientific.net/AMM.477-478.1378.

[259] W. R. George, "Messvorrichtung, Insbesondere Zur Verwendung Am Schneidkopf Einer Gewinnungsmaschine Fuer Den Bergbau", DE2349827, Apr 18, 1973.

[260] K.-H. Weber, "Verfahren zum Betreiben von im Untertagebergbau eingesetzten Gewinnungsmaschinen oder Teilschnittmaschinen", DE3631087A1, DE, Mar 24, 1988.

[261] M. Entacher, R. Galler, and R. Wenighofer, "System For Determining A Working-Face Image", WO 2015/014655 A2, EP, Feb 5, 2015.

[262] M. Entacher and R. Galler, "Device and method for model cutting trials", EP2796851B1, Oct 29, 2014.

[263] M. Beresford and A. Crowther, "Akustischer Messfühler", DE 000069517166 T2 27.03.199, Oct 5, 2000.

[264] H. Wotruba *et al.,* "Method and Arrangement for Analysis of a Material Flow", WO 2016/124165A1, Aug 11, 2016.

[265] S. Dobilas, "How to Benefit from the Semi-Supervised Learning with Label Spreading Algorithm", *Towards Data Science*, 28 Nov., 2021. https://towardsdatascience.com/how-to-benefit-from-the-semi-supervised-learning-with-label-spreading-algorithm-2f373ae5de96 (accessed: Dec. 5 2021).

[266] Stefan Fritsch, Frauke Guenther, and Marvin N. Wright, *neuralnet: Training of Neural Networks: R package version 1.44.2.* [Online]. Available: https://cran.r-project.org/package=neuralnet

[267] M. W. Beck, "NeuralNetTools: Visualization and Analysis Tools for Neural Networks", *Journal of statistical software*, vol. 85, no. 11, pp. 1–20, 2018, doi: 10.18637/jss.v085.i11.

[268] Martin A. Riedmiller and H. Braun, "A direct adaptive method for faster backpropagation learning: the RPROP algorithm", *IEEE International Conference on Neural Networks*, 586-591 vol.1, 1993.

[269] J. D. Olden and D. A. Jackson, "Illuminating the "black box": a randomization approach for understanding variable contributions in artificial neural networks", 2002, doi: 10.1016/S0304-3800(02)00064-9.

Annex A   Fields of Application of Conical Tools

Conical picks are widely used tools for rock excavation throughout the industry. The main machine types that use them are: continuous surface miner, continuous miner, roadheader, and shearer loader. This chapter provides additional information on the machines introduced in Chapter 2.

A.1   Continuous Surface Miner

The Continuous Surface Miner (CSM) is used not only in open-pit mining but also in construction excavation—or as a so-called cold planer in road milling and construction.

Surface miners can be divided into three groups according to the position of their cutting drum: front, central, and rear cutting drum. Front and back cutting drums offer advantages in cutting corners and border areas; they are also more mobile. Central cutting drums allow for a more efficient use of the machine's weight to ensure a sufficient penetration of the drum into the rock face [27].

Furthermore, they can be divided into top-down and bottom-up cutting, depending on the rotational direction of the drum in relation to the movement direction of the machine. Top-down cutting offers a more homogeneous particle size distribution of the material [211]. Bottom-up cutting, however, is reported to be more energy efficient because it allows for an unrelieved outbreak of bigger slabs as the pick moves towards the surface [28].

The biggest supplier for surface miners is Wirtgen (part of John Deere Group), offering surface miners with central bottom-up rotating drums. Wirtgen reports 514 Surface Miners worldwide in operation (2014) and ca. 3 bill. € Revenue in 2019 [212, 213]. Another supplier is Vermeer (ca. 1 bill. € revenue), which offers top-down rotating drums that are attached to the backside of the machine. Additionally, there are smaller suppliers such as Tesmec, which offer back-side drums that also cut bottom-up [214], and Puzzalona from India offering a system comparable to Wirtgen [215].

Other suppliers described in the literature, such as Tenova TAKRAF, Thyssen Mining Solutions, and L&T, Huron or FLSmith's Rahco do not offer their machines publicly as of 2020 [27, 216–218], although these machines are still in operation or at least were shipped in the last 10 years [219–221].

A.2   Continuous Miner

The underground counterpart of the continuous surface miner is the continuous miner. Here, the cutting drum is attached to a boom that moves the cutting drum from top to bottom so that the entire working face can be worked. The main producers are Joy (part of Komatsu), Sandvik, and Eickhoff.

The boom is supported by hydraulic cylinders connected to the chassis and is non-telescopic. Because the boom has only one degree of freedom, rectangle-shaped profiles are created as shown in Figure A-1 a) and b). Continuous miners are counted to the group of partial face machines. This means they work one area of the face at a time. During excavation, the rotating drum is vertically moved over the face by the boom. Figure A-1, c) shows the working cycle:

1. The continuous miner advances with a raised boom so that the rotating drum starts penetrating the rock until the drum is sunk in the rock at roughly its radius.
2. The boom is lowered while cutting. When the drum reaches floor level, a small gusset is still left on the floor. The machine drives backward to remove the gusset and level the floor.
3. Depending on the type of machine and geologic conditions, the cycle is repeated by either raising the boom and restarting from step one; or continued by an insertion cut of the drum at floor level.

4. If the machine continues from the bottom, the drum now cuts upwards by raising the boom. There, the drum's penetration depth is lower because the cutting performance of the drum is reduced. In this case, also a small gusset has to be removed at the roof [68].
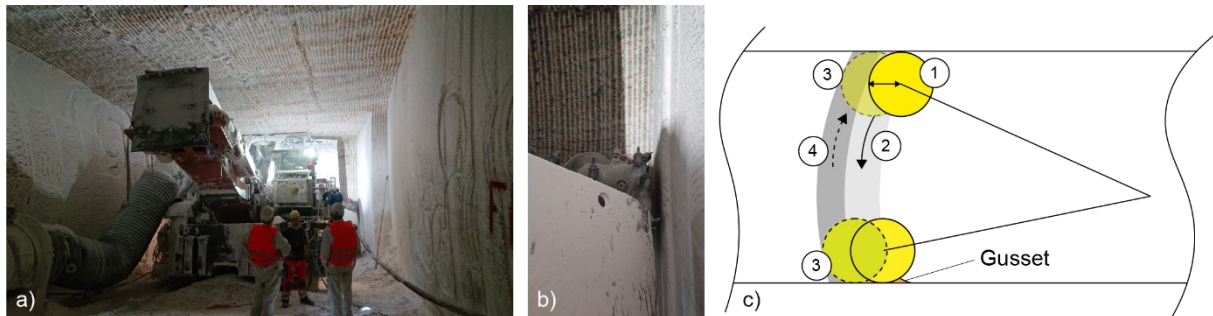
Figure A-1: a) & b) profile excavated by continuous miner, c) working scheme continuous miner [68][18]

Continuous miners are mainly applied in softer rock like coal, salt, potash, trona, gypsum, and phosphate. This is based on the fact that with a wide drum, many picks are cutting at the same time. This requires a higher total penetration force to keep the drum and the picks at the designated *cutting depth* [222].

A.3 Roadheaders

The cutter head of the roadheaders is, similar to the continuous miner, attached to a boom (s. Figure A-2). However, the boom can move with two degrees of freedom, and the cutter head does not have the width of the entire face but only a portion of it. This results in the ability to excavate varying profiles. Due to their smaller cutter head, fewer picks attack the face simultaneously, resulting in a higher cutting power concentration than most other mechanical excavators. The working principle is similar to that of the continuous miner. The machine starts the cutting sequence by advancing so that the cutter head sinks into the rock until the desired *cutting depth* is reached. The cutting boom then moves in a zig-zag movement over the entire face profile until the whole slice is won. Some machines also come with a telescopic boom which further increases their versatility.
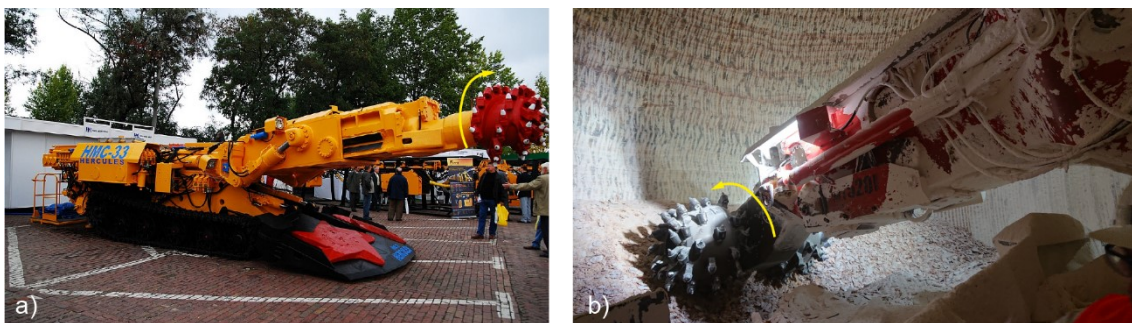
Figure A-2: a) Roadheader with axial cutting head [223], b) transverse cutter[19]

---

[18] Photos: Author, with kind permission of K+S Agriculture and Minerals GmbH
[19] Photos: a) License CC BY-SA 3.0, via Wikimedia commons; b) Author, with kind permission of K+S Agriculture and Minerals GmbH

The initial task of the roadheader was the preparation of drifts and roads in hard coal. However, they soon found applications in other tasks and environments. Today they are used for scaling, rehabilitating underground structures, in tunnelling, as a vertical version in shaft sinking, and even in production mining. They are preferably used in softer to medium-hard rocks.

There are two types of cutter heads that are applied by road headers. These are axial and transverse cutter heads as shown in Figure A-2 a) and b), respectively. They differ in the rotation direction relative to the boom axis. Axial cutter heads can create a more uniform profile due to their geometry. However, the material flies sideways, which can cause loading problems. Furthermore, the reaction forces act sideways to the advancement direction. This can cause slippage of the entire machine body under certain (muddy, wet) floor conditions. Their range of application goes up to 60–80 MPa *UCS*. Transverse heads show a better loading performance of the cut material because it flies in the direction of the loading table. In addition, the reaction forces are centrally transferred towards the machine body. These machines can be applied in harder rocks up to 120 MPa UCS [31, 68].

Roadheaders combine flexibility, mobility, a highly selective mining capacity, and relatively low investment cost compared to other machines with the ability to cut harder rock. Copur (1998) mentions that an application can be feasible with rocks as hard as 160 MPa if the jointing is favourable at a low RQD. A feasible cutting range of up to 120 MPa *UCS* for lower abrasivity indices is also stated [222].

A.4 Shearer Loaders

Shearer loaders originate from coal mining in the 1950s when the Anderton Shearer Loader revolutionised coal mining underground. By 1972, 75% of the underground coal produced was excavated mechanically [224].

The machine is shown in Figure A-3. Shearer Loaders can only be used in longwall mining, where they work together with a set of shield support (1) to keep the face open and safe; and an armoured face conveyor (2) to transport the excavated material off the face to the main conveying drives. The excavation direction (3) is perpendicular to the mining direction (4).

Figure A-3: Longwall shearer and armoured face conveyor operating at the Twentymile mine [225][20]

The shearer excavates the full face height in one passthrough, but only one slice at a time. One slice has the thickness of the cutting drum. Longwall mining is usually applied in softer tabular deposits like coal and potash. It can achieve very high production rates and a high recovery rate. However, because it is

---

[20]Photo: Peabody Energy, Inc., CC BY-SA 4.0 , via Wikimedia Commons

usually applied without backfill, it induces considerable levels of ground subsidence. This can cause damage to surface structures and alter the groundwater situation up to the point that the after-mining surface would lie below the original groundwater level. This can create high eternal post-mining costs.

Production rates can reach 900 t/h [226]. The production record per machine as of 2018 was 9 Mt for the entire year [227]. Since the excavation drums are located on arms, the total cutting height can be adjusted to the available seam height.

Shearer loaders have been the target of long-lasting automation approaches. The whole excavation process has been automated, and concepts for sensing boundaries between the seam and the host rock have also been presented over the years. Some of the approaches are discussed further in Chapter 3.2.1.

Annex B   Supplements Cutting and Rock Parameters

B.1   Specific Energy – Measurement of Outbroken Volume

In Chapter 2.1, Subsection Specific Energy, the calculation of the *specific energy E_{sp}* is described. One element for the calculation of E_{sp} is the measurement of the outbroken volume. In experimental setups, there are three possibilities for this:

a)   The weighing of outbroken material if the density has been measured before.
b)   Measuring the outbroken volume by filling the outbreaks with modelling clay and then measuring the volume of the clay by a water displacement measure.
c)   Measuring of the outbroken cavity with a laser scanner.

The last variant is the most convenient and exact. Since there are multiple methods to measure the volume, results from different experimental setups and routines must be compared with caution. If the exact volume of the outbroken material cannot be measured, the *specific energy* consumption can be derived from the cutting parameters.
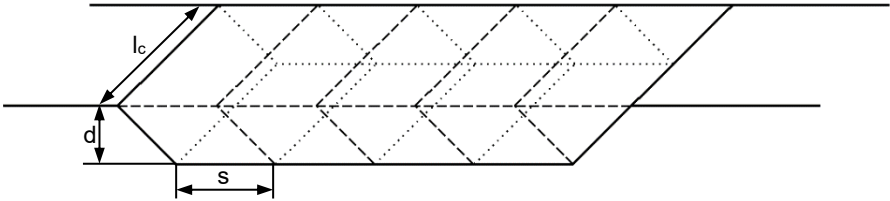
Figure B-1: Simplified cutting volume [47]

As shown in Figure B-1, the *spacing* (*s*), the *cutting depth* (*d*), and the *length of the cut* (l_c) are used as well as the number of cuts. If the number of cuts is sufficiently large, the difference between the calculated and the real outbroken volume becomes smaller. In a previous study conducted by the author, the difference between measured and estimated E_{sp} ca. 7% (6.97 kWh/m³ measured vs. 6.5 kWh/m³; after Annex V of [47]).

B.2 Brittleness

Table 2, p. 19 summarizes an array of methods to calculate the brittleness of a rock. Supplementary information is listed here. Note: The variables used here are not stated in the list of variables of the main part of this work, since they are only used here.

Table B-1: Different methods of calculating brittleness

Number	Formula	Description	Source
1	$b_1 = \dfrac{V_{\text{Quartz}}}{V_{\text{Quartz}} + V_{\text{Carbonate}} + V_{\text{Clay}}}$	V_{Quartz} – volume Quartz $V_{\text{Carbonate}}$ – volume Carbonate V_{Clay} – volume Clay	[78]
2	$b_2 = \dfrac{\sum_{i=1}^{m} a_i M_i}{\sum_{j=1}^{m} a_j M_j}$	a – weight coefficient of each mineral i – type of brittle mineral j – all minerals M – mineral content (volume fraction)	[78]
3	$b_3 = \dfrac{\sigma_c}{\sigma_t}$	σ_c – uniaxial compressive strength σ_t – tensile strength	[78]
4	$b_4 = \dfrac{\sigma_c \sigma_t}{2}$		[78]
5	$b_5 = \sqrt{\dfrac{\sigma_c \sigma_t}{2}}$		[78]
6	$b_6 = \dfrac{8\sigma_c}{\sigma_{ci}}$	σ_{ci} – Initiation stress of rock material	[78]
7	$b_7 = \dfrac{\sigma_c \sigma_{ci}}{16}$		[78]
8	$b_8 = \sqrt{\dfrac{\sigma_c \sigma_{ci}}{16}}$		[78]
9	$b_9 = \dfrac{1}{2}\left(\dfrac{E - E_{\min}}{E_{\max} - E_{\min}} + \dfrac{v - v_{\max}}{E_{\min} - E_{\max}}\right)$	E – elastic modulus v – Poisson's ratio based on seismic data $E_{\max}$, $E_{\min}$ – maximum and minimum values of the Elastic modulus	[78]
10	$b_{10} = \dfrac{\varepsilon_{el}}{\varepsilon_{tot}}$	ε_{el} – elastic strain the pre-peak stage of stress–strain curves ε_{tot} – total strain of pre-peak stage	[78]
11	$b_{11} = \dfrac{\sigma_p - \sigma_r}{\sigma_p}$	σ_p, σ_r – peak strength and residual strength of the whole stress–strain curve	[78]
12	$b_{12} = \dfrac{\varepsilon_p - \varepsilon_r}{\varepsilon_p}$	ε_p, ε_r – peak strain and residual strain of the whole stress–strain curve	[78]
13	$B_1 = \dfrac{dW_f + dW_d}{dW_{ue} + dW_d}$	dW_f – fracture energy dW_{ue} – unloading elastic energy dW_d – dissipation energy of pre peak stage	[78]
14	$B_2 = \dfrac{dW_x}{dW_{ue} + dW_d}$	dW_x – extra energy required (type I behavior) or the excess energy released (type II behavior) dW_e – total elastic energy accumulated in the rock specimen when reaching the peak strength dW_t – energy which unconsumed or converts into other forms	[78]
15	$b_{15} = q\sigma_c$	"q is the percentage of fines formed in the Protodyakonov impact test"	[79]

Continuation Table B-1

Number	Formula	Description	Source
16	$b_{16} = S_{20}$	S_{20} is the percentage of fines (<11.2 mm) formed in an impact test for TBM performance prediction in the NTNU (1998) model	[79]
17	$b_{17} = \dfrac{F_{max}}{p}$	During a pin penetration test: F_{max} – maximum force applied on a rock sample (kN) p – corresponding penetration at maximum force	[79]
18	$b_{18} = \dfrac{p_{inc}}{p_{dec}}$	P_{inc} and P_{dec} refer to the force increment and decrement, respectively, in the test	[79]
19	$b_{19} = 0.002\,\sigma_c - 0.490\,\sigma_{bt} - 4.939\,ls_{50} + 91.179$		[79]

Table B-2: Data compiled from Yasar (2020) with additional normalized force and brittleness calculations, after [81]

Rock sample	d [mm]	α_w [°]	α_a [°]	UCS [MPa]	TS [MPa]	F_x [N]	F_x' [N]	F_x'/F_x [1]	b_1 [1]	F_{x-n} [N/(mm*MPa)]	Type
Limestone	3	80	55	121.0	7.8	3874	11611	3.00	15.51	10.67	sedimentary
Claystone	3	80	55	58.0	5.6	1167	3746	3.21	10.36	6.71	sedimentary
Sandstone 1	3	80	55	114.0	6.6	3834	8953	2.34	17.27	11.21	sedimentary
Sandstone 2	3	80	55	174.0	11.6	4021	9022	2.24	15.00	7.70	sedimentary
Siltstone	3	80	55	58.0	5.3	3069	7335	2.39	10.94	17.64	sedimentary
Claystone	5	80	55	58.0	5.6	2952	8797	2.98	10.36	10.18	sedimentary
Claystone	7	80	55	58.0	5.6	3168	10778	3.40	10.36	7.80	sedimentary
Claystone	9	80	55	58.0	5.6	5247	16593	3.16	10.36	10.05	sedimentary
Trona	5	80	55	30.0	2.2	1363	3805	2.79	13.64	9.09	sedimentary
Anhydrite	5	80	55	82.0	5.5	3315	12278	3.70	14.91	8.09	sedimentary
Selestite	5	80	55	29.0	4.0	1471	4648	3.16	7.25	10.14	sedimentary
Jips	5	80	55	33.0	3.0	3932	8551	2.17	11.00	23.83	sedimentary
Sandstone-1	5	80	55	114.0	6.6	7433	19309	2.60	17.27	13.04	sedimentary
Sandstone-2	5	80	55	174.0	11.6	8041	22800	2.84	15.00	9.24	sedimentary
Sandstone-3	5	80	55	87.0	8.3	3717	8914	2.40	10.48	8.54	sedimentary
Siltstone	5	80	55	58.0	5.3	7267	22595	3.11	10.94	25.06	sedimentary
Limestone	5	80	55	121.0	7.8	7316	21094	2.88	15.51	12.09	sedimentary
Serpantinite	9	80	55	38.0	5.7	6963	19760	2.84	6.67	20.36	sedimentary
Trona	9	80	55	30.0	2.2	4119	12023	2.92	13.64	15.26	sedimentary
Anhydrite	9	80	55	82.0	5.5	5090	15985	3.14	14.91	6.90	sedimentary
Selestite	9	80	55	29.0	4.0	3364	8895	2.64	7.25	12.89	sedimentary
Jips	9	80	55	33.0	3.0	3315	6404	1.93	11.00	11.16	sedimentary
Sandstone-1	9	80	55	114.0	6.6	9728	28949	2.98	17.27	9.48	sedimentary
Sandstone-2	9	80	55	174.0	11.6	16534	47170	2.85	15.00	10.56	sedimentary
Sandstone-3	9	80	55	87.0	8.3	6423	15612	2.43	10.48	8.20	sedimentary
Siltstone	9	80	55	58.0	5.3	8267	31381	3.80	10.94	15.84	sedimentary
Limestone	9	80	55	121.0	7.8	11935	32215	2.70	15.51	10.96	sedimentary

Continuation Table B-2

Rock sample	d [mm]	α_w [°]	α_a [°]	UCS [MPa]	TS [MPa]	F_x [N]	F_x' [N]	F_x'/F_x [1]	b_1 [1]	$F_{x\text{-}n}$ [N/(mm*MPa)]	Type
Sandstone 1	3	80	55	17.9	1.6	551	886	1.61	10.92	10.25	sedimentary
Sandstone 1	6	80	55	17.9	1.6	1256	2009	1.60	10.92	11.69	sedimentary
Sandstone 1	9	80	55	17.9	1.6	2034	3397	1.67	10.92	12.62	sedimentary
Sandstone 1	12	80	55	17.9	1.6	2740	4774	1.74	10.92	12.75	sedimentary
Sandstone 1	15	80	55	17.9	1.6	3421	6767	1.98	10.92	12.73	sedimentary
Sandstone 1	18	80	55	17.9	1.6	4329	8602	1.99	10.92	13.43	sedimentary
Sandstone 2	3	80	55	79.2	5.0	1410	2708	1.92	15.94	5.93	sedimentary
Sandstone 2	6	80	55	79.2	5.0	2661	5660	2.13	15.94	5.60	sedimentary
Sandstone 2	9	80	55	79.2	5.0	4108	8862	2.16	15.94	5.76	sedimentary
Sandstone 2	12	80	55	79.2	5.0	6601	13545	2.05	15.94	6.95	sedimentary
Sandstone 2	15	80	55	79.2	5.0	8252	17986	2.18	15.94	6.95	sedimentary
Sandstone 3	3	80	55	53.0	3.7	928	1520	1.64	14.44	5.84	sedimentary
Sandstone 3	6	80	55	53.0	3.7	1613	3260	2.02	14.44	5.07	sedimentary
Sandstone 3	9	80	55	53.0	3.7	2991	5464	1.83	14.44	6.27	sedimentary
Sandstone 3	12	80	55	53.0	3.7	4601	8815	1.92	14.44	7.24	sedimentary
Sandstone 3	15	80	55	53.0	3.7	6224	11656	1.87	14.44	7.83	sedimentary
Sandstone 4	3	80	55	59.8	3.9	932	1836	1.97	15.22	5.20	sedimentary
Sandstone 4	6	80	55	59.8	3.9	2369	4670	1.97	15.22	6.60	sedimentary
Sandstone 4	9	80	55	59.8	3.9	3709	8849	2.39	15.22	6.89	sedimentary
Sandstone 4	12	80	55	59.8	3.9	5713	12944	2.27	15.22	7.96	sedimentary
Sandstone 4	15	80	55	59.8	3.9	8178	18180	2.22	15.22	9.12	sedimentary
Sandstone 5	3	80	55	86.0	3.7	1348	2676	1.99	23.30	5.23	sedimentary
Sandstone 5	6	80	55	86.0	3.7	2223	4895	2.20	23.30	4.31	sedimentary
Sandstone 5	9	80	55	86.0	3.7	3275	8401	2.57	23.30	4.23	sedimentary
Sandstone 5	12	80	55	86.0	3.7	5577	13849	2.48	23.30	5.41	sedimentary
High-grade chromite	5	80	55	32.0	3.7	2736	7022	2.57	8.65	17.10	igneous

Continuation Table B-2

Rock sample	d [mm]	α_w [°]	α_a [°]	UCS [MPa]	TS [MPa]	F_x [N]	F_x' [N]	F_x'/F_x [1]	b_1 [1]	F_{x-n} [N/(mm*MPa)]	Type
Medium-grade chromite	5	80	55	47.0	4.5	3668	10013	2.73	10.44	15.61	igneous
Low-grade chromite	5	80	55	46.0	3.7	3128	8542	2.73	12.43	13.60	igneous
Harsburgite	5	80	55	58.0	5.5	5207	14681	2.82	10.55	17.96	igneous
Serpantinite	5	80	55	38.0	5.7	2893	7698	2.66	6.67	15.23	igneous
Tuff 1	5	80	55	10.0	0.9	726	2010	2.77	11.11	14.52	igneous
Tuff 2	5	80	55	11.0	1.2	1922	6943	3.61	9.17	34.95	igneous
Tuff 3	5	80	55	27.0	2.6	1226	3697	3.02	10.38	9.08	igneous
Tuff 4	5	80	55	14.0	1.5	912	2775	3.04	9.33	13.03	igneous
Tuff 5	5	80	55	19.0	2.3	1344	3373	2.51	8.26	14.15	igneous
High-grade chromite	9	80	55	32.0	3.7	5198	14543	2.80	8.65	18.05	igneous
Medium-grade chromite	9	80	55	47.0	4.5	9130	25977	2.85	10.44	21.58	igneous
Low-grade chromite	9	80	55	46.0	3.7	6502	15925	2.45	12.43	15.71	igneous
Harsburgite	9	80	55	58.0	5.5	9042	26390	2.92	10.55	17.32	igneous
Tuff 1	9	80	55	10.0	0.9	1579	3942	2.50	11.11	17.54	igneous
Tuff 2	9	80	55	11.0	1.2	3795	11611	3.06	9.17	38.33	igneous
Tuff 3	9	80	55	27.0	2.6	2687	7080	2.64	10.38	11.06	igneous
Tuff 4	9	80	55	14.0	1.5	2432	7159	2.94	9.33	19.30	igneous
Tuff 5	9	80	55	19.0	2.3	2932	7208	2.46	8.26	17.15	igneous
Copper ore (yellow)	5	80	55	33.0	3.4	1667	4315	2.59	9.71	10.10	unknown
Copper ore (black)	5	80	55	41.0	5.7	2648	7188	2.71	7.19	12.92	unknown
Copper ore (yellow)	9	80	55	33.0	3.4	4992	14779	2.96	9.71	16.81	unknown
Copper ore (black)	9	80	55	41.0	5.7	8904	25321	2.84	7.19	24.13	unknown

Annex C   Details Topic-Analysis Rock Cutting Publications

Table C-1: Details for all classified articles

Source	Year	F/t or F/l	Frequency analysis	States mean	Peak forces	Other measure of distribution	Specific energy	Grain size / shape analysis	Spatial relation of forces mentioned	Type	More than one FC shown	FCR mentioned	Comment
[22]	2012	y	y	n	y	n	n	n	n	d	y	n	
[121]	2013	y	n	y	y	n	n	n	y	d	y	n	
[57]	2012	y	n	y	y	y	n	n	n	d	y	n	F/way
[99]	2012	y	n	y	y	n	n	y	y	d	n	n	Grain Size & Shape Analysis
[122]	2015	y	n	y	y	n	n	n	y	d	y	n	
[100]	2018	y	n	y	n	n	n	n	n	d	y	n	Foliation
[229]	2016	y	n	n	n	n	n	n	y	d	n	n	presentation for [99] & [57]
[71]	2018	y	n	y	n	n	n	n	n	d/o	y	n	Regression analysis f. Minidisc cutter
[230]	2018	y	n	n	n	n	n	n	n	o	n	n	Stress on Scaler arm
[64]	1981	y	n	y	n	n	y	y	n	p	y	y	Mainly in-Situ tests w. CM
[60]	2018	y	n	y	n	n	y	n	n	p	y	n	Focus on Temperature at Tool
[231]	2018	y	n	y	y	n	n	n	n	p	n	n	F_{max} determination unclear
[43]	2002	n	n	n	n	y	y	n	n	p	n	n	No direct Force measurement, but performance data
[31]	2014	y	n	n	y	n	y	y	n	p/d	y	n	Teaching book
[232]	2017	n	n	n	n	y	n	n	n	p	y	y	Probabilistic Risk Failure Assessment
[27]	2012	y	n	y	n	n	y	y	n	p	y	y	Also dust, cutting behaviour of worn picks
[233]	2018	n	n	y	y	n	y	n	n	p	y	y	
[234]	2016	y	n	y	n	n	n	n	n	p	y	n	
[103]	2019	y	n	n	n	y	n	n	n	d	y	n	Calculates derivatives of F vs. t
[235]	2016	n	n	y	n	n	y	n	n	o	n	n	
[236]	2007	n	n	y	n	n	y	n	n	d	y	n	
[32]	2006	n	n	y	y	n	y	n	n	p	y	n	Mentions peak to mean ratio
[237]	2018	n	n	y	y	n	n	n	n	p	y	n	
[36]	2018	n	n	y	y	n	n	n	n	p	y	n	
[238]	2010	n	n	y	n	n	y	n	n	p/d	y	n	
[239]	2020	y	n	y	n	n	n	n	n	d	y	n	
[52]	2019	y	n	y	y	n	n	n	n	p	y	n	
[108]	2017	n	n	y	y	n	n	n	y	p	y	y	Mentions F_x to F_z
[69]	2016	n	n	y	n	y	n	n	y	p	y	n	
[81]	2020	n	n	y	y	n	n	n	n	p	n	n	Meta study
[51]	1987	n	n	y	n	n	n	n	n	p	y	y	Mentions F_x to F_z
[48]	2018	y	n	y	n	n	n	n	n	p	y	n	
[240]	2015	y	n	n	n	n	y	n	n	p	y	n	
[241]	2017	y	n	y	n	n	n	n	n	p	y	n	

Continuation Table C-1

Source	Year	F/t or F/l	Fre-quency analysis	States mean	Peak forces	Other measure of distribution	Specific energy	Grain size / shape analysis	Spatial relation of forces mentioned	Type	More than one FC shown	FCR mentioned	Comment
[35]	2018	n	n	y	n	n	y	n	n	p	y	n	
[242]	2010	n	n	y	n	y	n	n	n	p	n	n	
[243]	2018	y	n	y	y	n	n	n	n	p	y	n	
[244]	2020	n	n	y	y	n	y	n	n	p	n	n	
[245]	2017	y	n	y	y	n	y	n	n	p	n	n	Mentions peak to mean ratio
[246]	2004	n	n	n	n	n	y	n	n	p	n	n	
[247]	2016	y	n	n	n	n	y	n	n	p	y	n	
[248]	2018	n	n	y	n	n	y	y	n	p	y	n	
[190]	2020	n	n	y	n	n	n	y	n	p	n	n	
[249]	2021	n	n	y	y	n	n	n	n	p	y	y	Considers cone angle of picks, considers F_x/F_z
[250]	2006	y	n	y	n	n	y	n	y	d	y	y	For discs
[41]	2020	y	n	y	y	y	y	n	n	p	y	y	
[59]	2017	y	n	y	n	n	y	n	n	p	y	y	
[42]	2018	n	n	y	n	n	y	n	n	o	y	n	
[114]	2017	y	y	y	y	y	n	n	y	p	y	n	
[251]	2018	y	n	y	n	n	y	n	n	p	y	n	
[252]	2020	n	n	y	y	n	y	n	n	p	y	n	
[253]	2021	y	n	y	y	n	y	y	n	d	y	y	
[34]	2018	n	n	y	n	n	y	y	n	p	n	n	
[254]	2018	-	-	y	y	-	y	y	-	p	-	-	Only abstract available
[255]	2010	n	n	y	n	n	y	n	n	o	n	n	For rock chain saw
[256]	2017	n	n	y	y	n	y	n	n	p	y	y	
[257]	2018	n	n	y	y	n	y	n	n	p	y	n	
[258]	2013	n	n	y	n	n	n	n	n	p	y	n	

Legend: y – topic mentioned; n – topic not mentioned; p – pick; d – disc; o – other

Annex D   Details Patent Analysis

This chapter presents the results of a patent analysis that was conducted by the author in the timeframe October 2019 to March 2020. The review focuses mainly on patents with respect to rock cutting force measurement. However, the search was extended to cover patents that could be relevant to the topic but were not strictly issued in the context of rock cutting force measurement. In addition, inventions that were not directly patented are added. The following Table D-1 shows the patents along a brief summary of the respective patent.

Table D-1: Patents and articles describing tool related sensor technologies

Nr.	Details	Summary
1	1980/1983 DE2831933 A1/C2 Bergwerksverband GmbH, Essen	Detection of boundary layers between coal and host rock with a "two pick method". The two picks are arranged in a way that one pick is at the most outward position and the other one is at an inner position with respect to the drums' centre. By such, the layer is "detected" if the outer pick receives higher peak forces than the inner pick. It was issued with respect to following a coal seam Limitations: - The exact method of acquisition of the Force values is not specified, just "strain gauges" as a means. - The tools only measure a one force peak per cutting event. - The decision whether a pick is in coal or host rock is made upon a fixed trigger value. - The values are taken on the basis of a fixed time window, with a fixed reset time, this requires a constant revolution speed and cutting direction. [115, 116]
2	1983 DE2919499C2 Bergwerksverband GmbH, Essen	One sensor pick that cuts fully blocked is used as a measuring pick. Only peak forces are measured. If peak forces are above a threshold, a control mechanism adjusts the drum height. Properties: - Only peak forces - No spatial relation, - Robust and simple system [25]
3	1974 DE2349827 Coal Industry (Patents) Ltd., London	System to measure peak forces during excavation and sending the information on a cordless basis to a receiving and steering unit. Claims are related to the transmission of the signal using a radio signal. Limitations: - The peak values are related to the zones they are supposed to appear in. For each zone a bandwidth of allowable peak forces is defined. - Only the component in cutting direction is measured (F_x) - Only usable with radial type picks - Exact method of utilising the data and steering the machine is not defined [259]
4	1995 DE4415824C1 Daimler-Benz Aerospace AG München	Suggests a sensor array that detects deformations and damage on the tool holder that are caused by worn picks and allows identification of the respective holder for replacement of the tool. Does not measure forces at all and not in relation to the position of the machine within the rock mass [149].

Continuation Table D-1

Nr.	Details	Summary
5	1980 GB2036127A Coal Industry (Patents) Ltd., London	Pick assembly for a rotary head machine with focus on coal / shearer loaders where two subsequently cutting picks are used. Nr. 1 cuts normally without a sensor, Nr. 2 is set up so that it cuts a bit deeper than Nr. 1, and follows Nr. 1 in the same groove. As such the *cutting depth* changes only minimally during cutting. The signal changes upon material change. Properties: • F_x is measured. • Limited impact of cutting parameters to measurement. Limitations: • Complicated design. • No respect to real cutting parameters. • Susceptible to flattening of the tip. • Not for round shank chisels, only for radial picks. [26]
6	2011 WO 2011116405 A2 Sandvik Mining and Construction GmbH	Claims on a measuring arrangement for conical picks where the measurement devices located in a slit between an intermediate holder-shell, the tool holder, and also behind the shank. • Measurement with strain gauges on the outside of the shell for axial and bending forces. • Additionally, measurement of axial forces possible with pressure sensor in the shell behind the chisels shank. • Saving of data with SD-Card; sender in the back of the holder-shell-assembly and an intermediate "repeater" for transmission of data to main processing unit. • Most advanced concept so far. Limitations: • Sender requires space. • No relation of the data to the position of the pick. • No mentioning of the exact use of the data. [23]
7	2015 DE 11 2007 000 152 B4 Sandvik Mining and Construction GmbH	System for controlling the slewing speed of a partial face machine in relation to general machine parameters, like position of the cutter head, tools, slewing speed, hydraulic pressures, power consumption of the drive. No spatial analysis of cutter forces. [134]
8	1988 DE3631087A1 Gebr. Eickhoff Maschinenfabrik u. Eisengießerei mbH	Proposes a possibility for a diagnosis system based on available machine data. The data are analysed by a computer and occurring errors are either mitigated or the machine drive parameters are reduced. Additionally, the errors are displayed until they are solved. No dedicated measures of how data are obtained or computations are made are given. [260]
9	1998 EP0807203B1 Advanced Technology for Rock Excavation Inc. Ontario	Steering System for following a pre-programmed profile. • No boundary layer detection. • No (spatial) force analysis. [133]
10	2015 WO2015014655A2 Montanuniversität Leoben	System for continuous photography of the working face for analysis purposes. However, no coupling with cutting force sensors is claimed. [261]

Continuation Table D-1

Nr.	Details	Summary
11	2014 EP2796851B1 Montanuniversität Leoben	The patent proposes a scaled down cutting experiment machine and a basic workflow to predict the advance rate of a corresponding TBM. However, no exact specifics upon how the cutting forces are measured is presented and no exact model for the correlation of the cutting forces to the full-scale forces is given. [262]
12	2015 DE102014105014A1 Montanuniversität Leoben	A cutting force measuring System for TBMs is proposed that can measure 3 components of the cutting forces, however for disk cutters. It is an evolution of DE202012103593U1. ▪ No spatial force analysis is claimed ▪ Only for disk cutters [22, 121, 144, 145] However, a spatial use of the forces is discussed in associated nonpatent sources [121, 229].
13	2019 EP 3 495 608 A1 Joy Global Underground Mining LLC	An assembly to measure cutting efficiency and to check whether a tool of a cutting machine is worn. Uses stress wave energy (SWE), ultrasonic, rotation speed of drum, temperature, acceleration, or vibration on gear or cutting drum. • Mentions sensing net cutting forces on the pick. • Should be measured via SWE or via various measures like hydraulic pressure the holds the cutter drum. The internal model translates this into cutting loads. • Comparison of SWE to cutting efficiency on basis of an empirical database or normal conditions. • Output is cutting efficiency and determining if cutter is worn based on the efficiency data. [143]
14	2013 Joy Global & Jokonya WO 2013/020056A1	Shows a method of operating an oscillating disc cutter mining machine automatically to find the face with a program. It utilises indirect force measurements over, e.g. hydraulic pressure of voltage/current indicators. [135]
15	2007 Hochtief AG DE102005016346B3	Wear sensing system that utilises a small magnetic layer in the disc to detect wear for disc cutters. [142]
16	2000 Thomson Marconi Sonar Ltd., GB DE69517166T2	A system that emits acoustic signals and also receives the reflected signals to identify changing rock properties. [263]
17	2007 Kistler Holding AG (CH) WO2007/025404A1	Assembly for measuring cutting forces on a per-tool-basis. No exact (spatial) use of the forces is mentioned. [141]
18	1996 Wirth Co KG WO 001996019639 A1	Automation for profiling using position recognition systems and utilising other parameters such as RPM, forces on the arms, and position of the machine itself. [132]
19	2016 Trimble Ltd.. US WO002016032685A1	Laser based orientation system for excavator and shovel. Relevant for referencing of boom. [136]
20	2018 Caterpillar Ltd. US WO002018112337A1	Control mechanism for CAT rock-straight roadheader, to follow an arch. Also, the general working principle of the machine is disclosed, but not the use of forces for automation. [131]

Continuation Table D-1

Nr.	Details	Summary
21	2017 Atlas Copco Rock Drill AB WO002017058089A1	Describes the Atlas Copco drill fleet management system to fulfil automated drilling of whole drill fields for multiple machines. [138]
22	2010 Wirtgen GmbH DE102008045470A1	Discloses a system to measure the state of wear of conical picks by comparing the distance of the wearing part to the distance of a fix point using a laser scanner and as such identifying worn tools. [146]
23	2003 Wirtgen GmbH DE10203732A1	Disclosed is a technology to combine vibration sensors with position sensors to identify worn or broken tools by comparing unnormal vibration behaviour to the respective rotational position of the cutting drum on surface miners. [147]
24	2016 Schlumberger US000009234422B2	The invention shows an in-pick sensor assembly with a connection unit. The sensors sit in bores inside of the pick. Several sensors are mentioned, including strain gauges, but also thermoelements, accelerometers, and magnetometers. No exact way of utilising force data is described, and the focus lies on wear detection. [148]
25	2018 Liaoning Technical University CN000107575226A	The invention shows a concept for a piezo sensor-box that can be fitted inside a tool holder. It is used for a coal hardness classification. [117]
26	2018 Politechnika Śląska & Famur Poland PL228215B1; PL415965A1	Patent for conical pick. Allows 3d /XYZ measurement of dynamic forces. Also explains coordinate transformation to convert forces from XYZ into local, pick related coordinate system. [118]
Nonpatent concepts		
27	Drebenstedt 2005	Strain gauges were used to evaluate the force distribution on a bucket wheel during operation and identify optimisation potential. No spatial use of the forces and no boundary layer detection conducted. [21]
28	Vraetz 2017	Describes a method for classifying a material flow based on the signals that are created when the flow hits a sensor plate [264]. It has been tested in mining environments with different classes of overburden in open pit Hambach and a limestone quarry to identify flintstone bearing material. In the industrial environment, the quality of the classification depends to an extend on securing an continuous measuring environment and defining not too much sub-classes [157].
29	Entacher 2015	Spatial use analysis of cutting forces is conducted for visualisation purposes during disc cutter measurements. [122]
31	Niedringhaus 2018	Describes the use of strain gauges on the boom of a scaler for correlation of the forces to different working cycles. However, no rock type correlation is aimed for so far. [230]

Annex E   Details Rock Cutting Unit HSX-1000-50

Table E-1: Specifications of the rock cutting test rig HXS 1000-50

Technical data linear cutting test rig HXS-1000-50	
Date of construction	2008 / refurbishment 2019
Nominal power	60 kW
Maximum speed	
X-axis (cutting direction)	1,67 m/s
Y-axis (side)	24,7 mm/s
Z-axis (vertical)	11,9 mm/s
Acceleration	10 m/s²
Maximum Forces	
X-axis (cutting direction)	50 kN / 75 kN
Y-axis (side)	30 kN / 50 kN
Z-axis (vertical)	50 kN / 75 kN
Max. DAQ frequency	10 kHz
Maximum sample size	
X-axis (cutting direction)	600 mm
Y-axis (side)	1200 mm
Z-axis (vertical	500 mm
Maximum sample weight	1300 kg
Nominal accuracy laser scanner	$\leq 70\ \mu m$
Pressurised air availability	5 bar
High-speed camera	Max. 10000 frames/s

Annex F   Details Used Pick
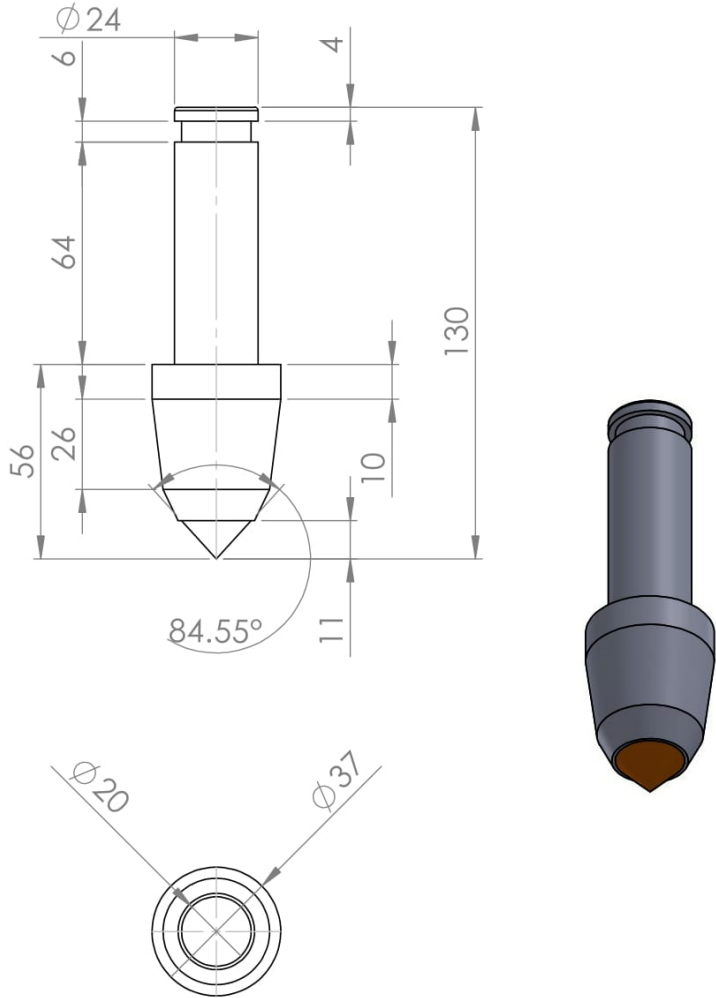
Figure F-1: Details of custom pick BETEK BSR112

Annex G Error Analysis Cutting Experiments

Due to the large amount of data required for this work, the general workflow for analysing cutting experiments was adopted, partially automated, and improved on an iterative basis. The following chapter deals with error sources that can occur during large-scale linear rock cutting tests, and how these sources can be mitigated during testing or corrected afterwards.

The updated workflow allows an analysis of larger datasets. It is conducted within Flexpro or with the help of a Shiny app that was written in R for this purpose. The outlines are explained in the following.

Analysis in Flexpro

In order to allow for the error analysis, the following queries are prepared:

- For each force (F_x, F_y, F_z, F_{res}), as well as for the y-position and z-position, return the mean value of the respective channel for each single cut.
- Return the file path within the database of each single cut.

This allows for different presentations of the summarised results of individual experiments. The main goal is to rule out obviously wrong cuts. Flexpro offers interactive diagram operations. Therefore, interactive worksheets can be created to identify certain kinds of errors. They can be inserted into any Flexpro Database storing cutting force experiments.

Here, the mean values of each cut for F_x, F_y, F_z, and F_{res} are plotted continuously. It allows an identification of failed experiments or other anomalies that need to be investigated in detail. Figure G-1 shows an example. The circle (1) indicates that the first experiments show negative values. The reason was an error in the calibration after the refurbishment of the sensors of the cutting machine. The spikes (2) are also abnormal. They show cutting data from the sides of a block. The sides of the block broke off easily, as such the forces are exceptionally low. The resulting data show rather high *side forces* while the other force components where minimal. The dashed line (3) shows a transition in the amplitudes of the diagram. This is because in this evaluation, two different cutting parameters are shown. The higher *cutting depth* behind marking (3) results in higher forces. The faulty cuts can then be quickly deleted from the database.
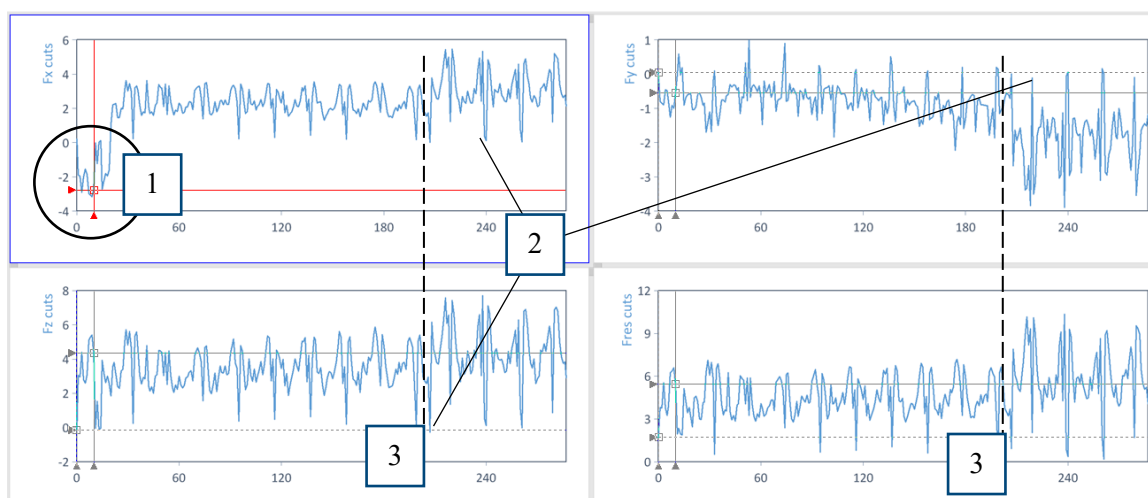
Figure G-1: Interactive worksheet within Flexpro showing F_x, F_y, F_z, F_{res}, for each single experiment

A second method to quickly analyse larger amounts of experiments is shown in Figure G-2. A faulty trigger setup can lead to a start of the measurement while the pick is still in mid-air. When this happens,

the total measurement time will be longer than in a normal measurement. The Figure shows such an example. Marking (1) shows unnormal high and low peaks. The high peaks are cuts where the measurement started too early. This can be corrected either in Flexpro or the files could be re-exported from Dewesoft with only the real cutting time being exported.
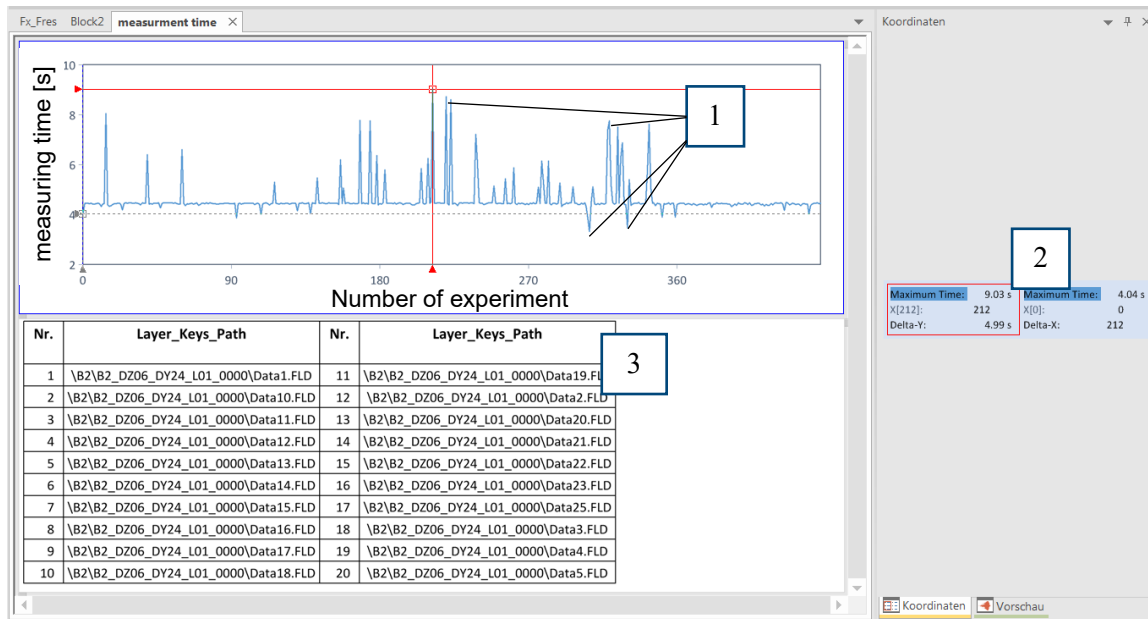
Figure G-2: Display of measurement time for all cuts of a cutting experiment

Additional to post processing with Flexpro, R-Studio was used. Two widgets were used that can be seen in Figure G-3. The first widget simply presents the results of all cuts of a certain experiment as a boxplot and by such allows a quick identification of outliers. These can be seen marked with circles in the figure. This functionality is similar to the Flexpro based analyses. Mouseover tooltips then can show the number of the cut for access of the raw data.

On the bottom of the figure, the Shiny app is shown that allows detailed access to the results of the single cuts. The functionalities of the app are: to quickly browse through cutting data, truncate them, and exempt single cuts from further calculations. With this app, detailed investigations of cutting data could be done in a short time. The main reason is that the time to switch between cuts and to export the cuts is reduced significantly compared to when the single cuts are investigated manually with the Dewesoft software.
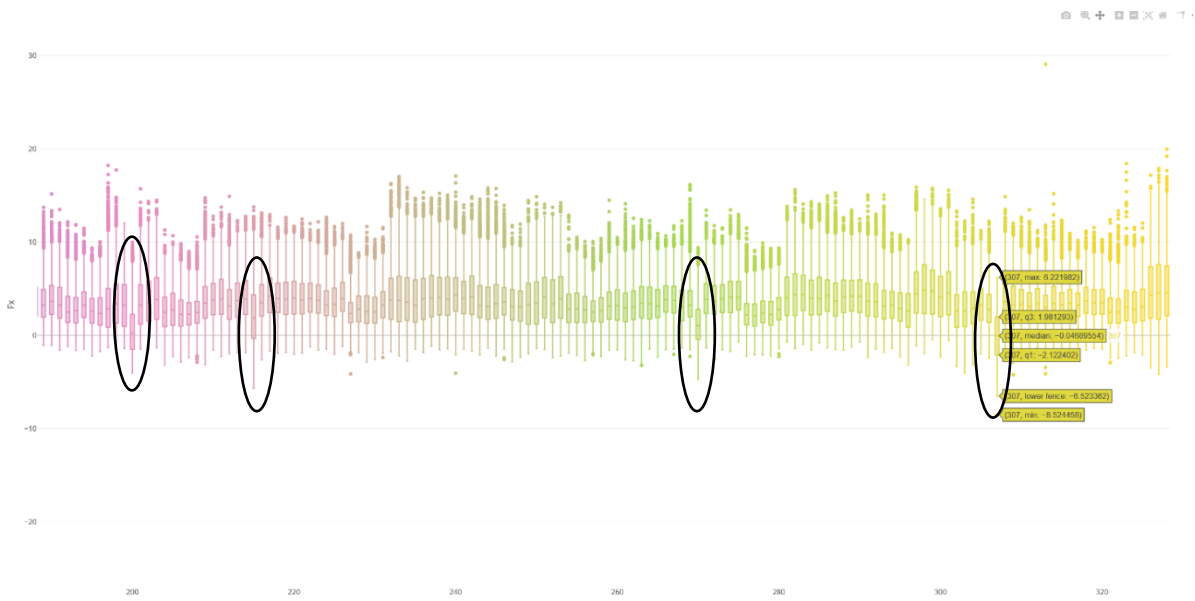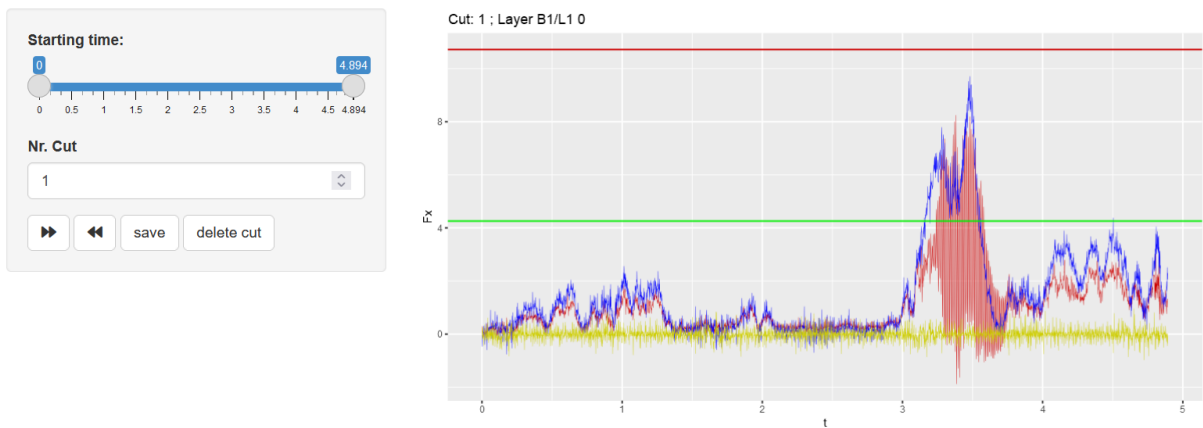
Figure G-3: Boxplot widget allows quick identification of erroneous measurements (top); Shiny app for truncation of cuts, it shows a faulty cut (bottom)

Annex H Details Photographic Modelling

Figure H-1 shows the screenshot of the referencing function of MinePlan. Four Edding-pen-points with known coordinates that were drawn on the sample are marked on the digital photo. The known coordinates of the points are then typed in. As a result, the photo now is spatially referenced to the coordinate system of the rock cutting machine.
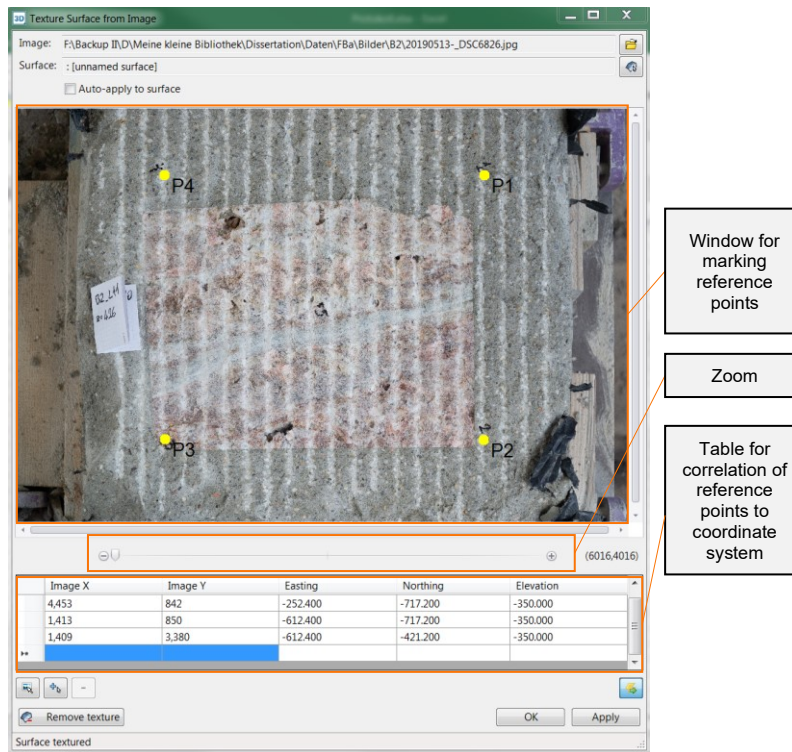
Figure H-1: Digitisation of reference points in MinePlan

Figure H-2 shows a detailed view of the digitisation process of the rock boundaries. The digitisation points were spaced roughly according to the *spacing*, so that in each cutting groove there is a digitisation point. Sometimes the exact boundary is not clearly visible. As such a certain inaccuracy must be accepted. It suspected in the range below 1 cm.
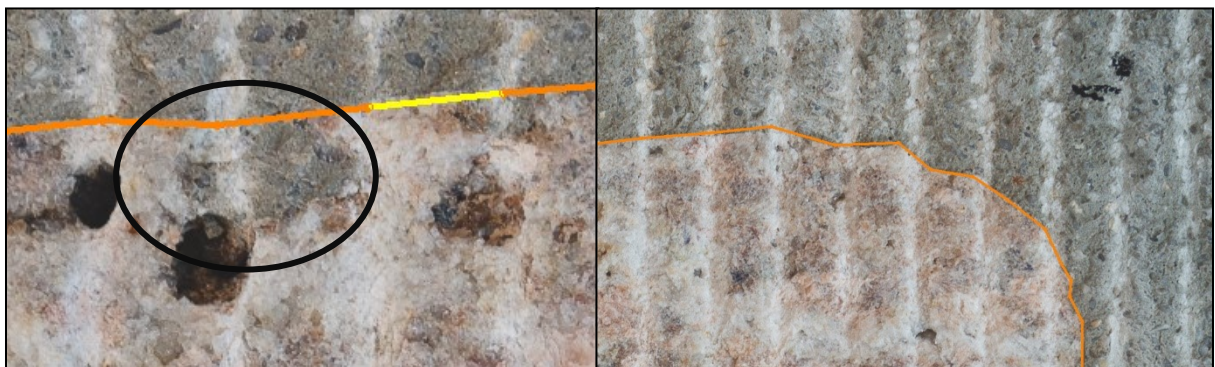
Figure H-2: Detail of digitisation of lithology outlines

Table H-1 shows the estimation of the maximum technical accuracy using a Pentax K-3 digital camera. The length of one pixel was measured on a referenced pictured, ca. 7.5 pixels make up for one mm, subsequently one pixel covers a length of ca. 0.1 mm.

Table H-1: estimation of photographic accuracy

	Sensor resolution	Used resolution	Block length	Pixel per mm	mm per pixel
y-axis	6015	4500	600	7.5	0.13
x-axis	4015	3800	500	7.6	0.13

Annex I   Laser Offset

For Experiment PB, a comparison of the picks location with the laser scans of the cut surfaces was necessary to ensure data integrity. Since the position of the picks tip is different from the measurement location of the laser scanner, the data from the laser scanner have to be recalculated to match the data from the cutting experiments. This is done using the offset defined in the following table.

Table I-1: Offset between tip of the pick and laser

	y-axis	x-axis	z-axis
Pick coordinates	257.6	342.2	415.1
Laser coordinates	260.8	509.4	239,1
Offset	3.2	167.2	176.0

Annex J Supplements Experiment CO

J.1 Raw force results

The following Table J-1 shows the results of the mean values of the Forces F_x, F_y, F_z and F_{res} for all experiments. The ranges of values from samples CO1 and CO2 are presented in Figure J-2 and Figure J-1.

Table J-1: Arithmetic mean of cutting forces F_x, F_y, F_z and F_{res} grouped by zones for CO1 and CO2, all values in kN

| Block 1 | | **Set** | | | | | | | | |
		1 s=6 mm; d=12 mm; s/d=2	**2** s=6 mm; d=24 mm; s/d=3	**3** s=6 mm; d=36 mm; s/d=4	**4** s=8 mm; d=12 mm; s/d=2	**5** s=8 mm; d=12 mm; s/d=3	**6** s=8 mm; d=12 mm; s/d=4	**7** s=12 mm; d=12 mm; s/d=2	**8** s=12 mm; d=12 mm; s/d=3	**9** s=12 mm; d=12 mm; s/d=4
Zone 2	F_x	1.62	2.53	2.74	3.07	4.04	4.18	4.97	6.17	6.60
Zone 3	F_x	3.81	5.06	5.51	5.71	7.09	7.38	8.90	10.99	12.25
Zone 2	F_y	0.66	0.66	0.64	1.29	1.24	0.58	2.09	1.60	1.00
Zone 3	F_y	2.02	1.53	1.46	3.10	2.65	1.13	5.05	4.28	1.94
Zone 2	F_z	1.67	2.89	2.91	3.30	4.37	4.50	5.02	6.50	6.85
Zone 3	F_z	5.32	7.70	7.76	7.97	9.87	10.39	11.79	15.33	17.05
Zone 2	F_{res}	2.56	4.05	4.22	4.89	6.33	6.43	7.62	9.39	9.86
Zone 3	F_{res}	7.41	9.79	10.08	10.72	12.90	13.28	16.07	19.91	21.63
Block 2										
Zone 1	F_x	1.03	1.50	2.19	1.62	2.30	2.22	3.51	3.98	4.91
Zone 2	F_x	2.14	3.23	4.62	3.72	4.40	4.45	7.21	7.31	7.77
Zone 3	F_x	4.71	6.05	8.51	6.91	9.02	8.42	13.03	13.74	13.45
Zone 1	F_y	0.48	0.56	0.56	0.66	0.73	0.28	1.19	1.02	0.17
Zone 2	F_y	1.00	1.27	1.34	1.56	1.64	0.63	2.62	2.52	0.97
Zone 3	F_y	2.63	3.16	3.39	3.73	4.54	1.50	7.31	6.58	0.50
Zone 1	F_z	1.00	1.51	2.32	1.55	2.25	2.07	3.61	3.63	4.45
Zone 2	F_z	2.29	3.61	5.58	4.11	4.92	4.91	8.51	7.96	8.67
Zone 3	F_z	7.41	9.77	14.54	10.75	13.84	12.88	21.69	19.98	19.94
Zone 1	F_{res}	1.62	2.27	3.32	2.49	3.38	3.14	5.26	5.56	6.73
Zone 2	F_{res}	3.41	5.18	7.59	6.00	7.00	6.89	11.70	11.36	12.02
Zone 3	F_{res}	9.63	12.35	17.61	13.79	17.58	15.97	26.85	25.68	24.79

Nr.	1	2	3	4	5	6	7	8	9
d [mm]	6	6	6	8	8	8	12	12	12
s [mm]	12	18	24	16	24	32	24	36	48
s/d	2	3	4	2	3	4	2	3	4
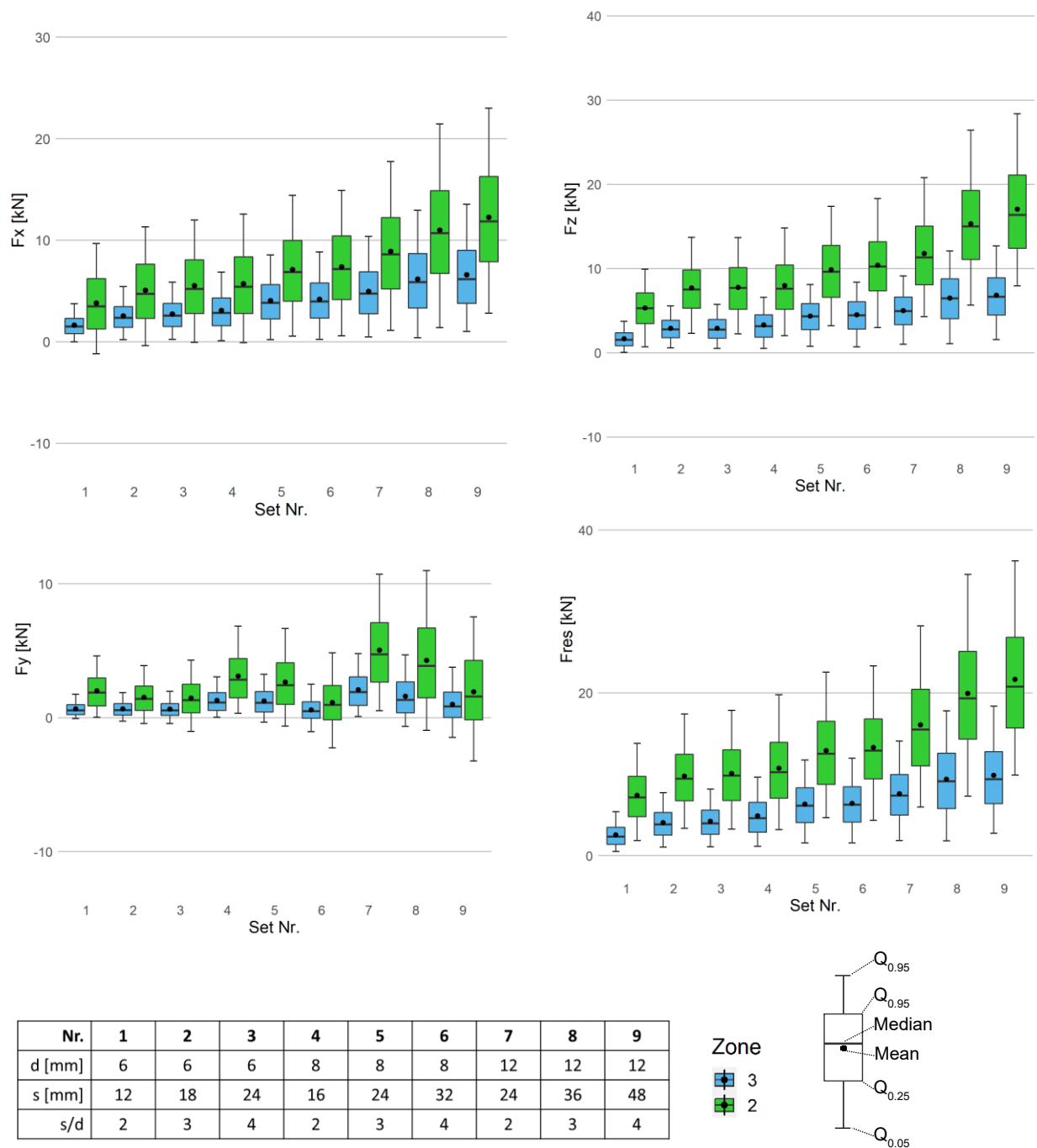
Figure J-1: Boxplots of cutting force components for Experiment CO1
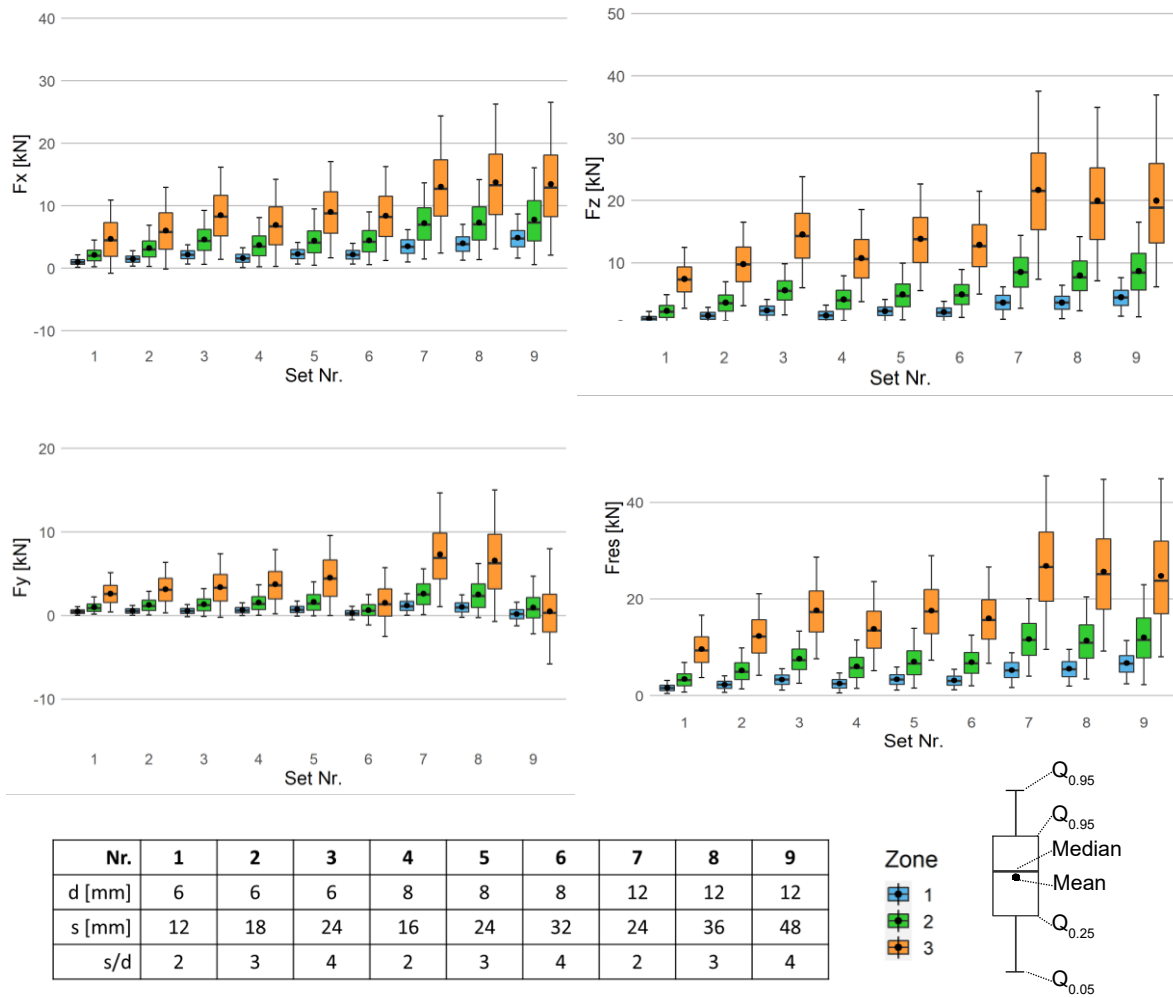
Figure J-2: Boxplots of cutting force components for Experiment CO2

J.2   Data Raw Results Procedural Selection Algorithm (CD)

The calculated data upon which the procedural selection algorithm chose the suitability of features are located on CD. Exemplary results for F_x/F_{res} are located in Table J-2 on the next page.

Table J-2: Results for force component ratio calculations and evaluation results of procedural selection algorithm for F_x/F_{res} CO1 and CO2

CO1	Zone	Set number 1	2	3	4	5	6	7	8	9	Calculation of differences max	min	mean	max.p	min.p	mean.p	res	res.p	class
$\bar{x}$	1	0.60	0.60	0.62	0.59	0.60	0.62	0.62	0.62	0.64	0.64	0.59	0.61	0.62	0.60	0.61	0.05	0.08	S
	2	0.45	0.48	0.51	0.50	0.53	0.53	0.53	0.53	0.55	0.55	0.45	0.51	0.53	0.51	0.52			
$\tilde{x}$	1	0.67	0.65	0.68	0.66	0.67	0.68	0.68	0.68	0.69	0.69	0.65	0.67	0.68	0.67	0.67	0.07	0.08	S
	2	0.58	0.56	0.59	0.57	0.58	0.59	0.57	0.57	0.58	0.59	0.56	0.58	0.59	0.57	0.58			
$\bar{x}_{geom}$	1	0.61	0.60	0.61	0.59	0.60	0.61	0.61	0.61	0.63	0.63	0.59	0.61	0.61	0.60	0.61	0.07	0.09	S
	2	0.48	0.46	0.49	0.48	0.50	0.51	0.51	0.51	0.52	0.52	0.46	0.49	0.51	0.49	0.50			
$Q_{0.95}$	1	0.89	0.86	0.88	0.87	0.87	0.87	0.85	0.85	0.85	0.89	0.85	0.87	0.88	0.85	0.87	-0.01	0.04	P
	2	0.85	0.80	0.81	0.81	0.79	0.80	0.77	0.75	0.74	0.85	0.74	0.79	0.81	0.77	0.79			
IQR	1	0.21	0.19	0.20	0.22	0.22	0.21	0.21	0.19	0.18	0.22	0.18	0.20	0.22	0.20	0.21	-0.04	0.01	P
	2	0.47	0.36	0.31	0.32	0.26	0.26	0.23	0.19	0.18	0.47	0.18	0.29	0.31	0.23	0.27			
v	1	0.50	0.43	0.40	0.47	0.43	0.41	0.39	0.40	0.35	0.50	0.35	0.42	0.43	0.39	0.41	-0.20	-0.03	U
	2	0.85	0.60	0.54	0.54	0.44	0.43	0.40	0.39	0.31	0.85	0.31	0.50	0.54	0.40	0.46			

CO2	Zone	Set number 1	2	3	4	5	6	7	8	9	Calculation of differences max	min	mean	max.p	min.p	mean.p	res	res.p	class
$\bar{x}$	1	0.63	0.66	0.66	0.63	0.68	0.71	0.66	0.71	0.72	0.72	0.63	0.67	0.68	0.66	0.67	0.01	0.05	S
	2	0.62	0.60	0.58	0.58	0.61	0.62	0.59	0.62	0.62	0.62	0.58	0.60	0.61	0.58	0.59	0.05	0.08	S
	3	0.44	0.46	0.47	0.47	0.50	0.51	0.48	0.52	0.53	0.53	0.44	0.49	0.50	0.47	0.48			
$\tilde{x}$	1	0.67	0.68	0.67	0.68	0.69	0.72	0.67	0.72	0.73	0.73	0.67	0.69	0.69	0.67	0.68	0.00	0.01	S
	2	0.66	0.65	0.64	0.65	0.66	0.67	0.63	0.66	0.67	0.67	0.63	0.65	0.66	0.63	0.64	0.06	0.10	S
	3	0.53	0.52	0.50	0.53	0.53	0.55	0.50	0.55	0.56	0.56	0.50	0.53	0.53	0.50	0.51			
$\bar{x}_{geom}$	1	0.64	0.65	0.66	0.65	0.67	0.70	0.66	0.71	0.72	0.72	0.64	0.67	0.67	0.66	0.66	0.03	0.06	S
	2	0.61	0.59	0.57	0.58	0.60	0.61	0.58	0.61	0.61	0.61	0.57	0.60	0.60	0.57	0.58	0.06	0.10	S
	3	0.43	0.44	0.43	0.45	0.47	0.48	0.46	0.50	0.51	0.51	0.43	0.46	0.47	0.43	0.45			
$Q_{0.95}$	1	0.86	0.85	0.82	0.85	0.85	0.87	0.80	0.85	0.85	0.87	0.80	0.84	0.85	0.80	0.82	-0.04	-0.02	U
	2	0.84	0.84	0.81	0.83	0.83	0.84	0.78	0.80	0.81	0.84	0.78	0.82	0.83	0.78	0.80	-0.01	0.04	P
	3	0.78	0.77	0.71	0.75	0.73	0.75	0.71	0.73	0.76	0.78	0.71	0.74	0.73	0.71	0.72			
IQR	1	0.13	0.11	0.09	0.11	0.10	0.09	0.08	0.08	0.07	0.13	0.07	0.10	0.10	0.08	0.09	0.02	0.08	S
	2	0.15	0.18	0.19	0.21	0.17	0.18	0.18	0.16	0.16	0.21	0.15	0.18	0.19	0.17	0.18	-0.03	0.00	U
	3	0.41	0.32	0.23	0.27	0.22	0.23	0.19	0.17	0.18	0.41	0.17	0.25	0.23	0.19	0.21			
v	1	0.35	0.22	0.19	0.41	0.21	0.19	0.23	0.13	0.13	0.41	0.13	0.23	0.23	0.19	0.21	-0.12	0.10	P
	2	0.34	0.39	0.37	0.44	0.37	0.37	0.33	0.30	0.31	0.44	0.30	0.36	0.37	0.33	0.36	-0.15	-0.01	U
	3	0.70	0.56	0.39	0.51	0.37	0.38	0.36	0.29	0.33	0.70	0.29	0.43	0.39	0.36	0.38			

Legend:
max, min and mean – maximum, minimum and mean values for the respective zone;
max.p, min.p and mean.p – maximum, minimum and mean values for the respective zone, but only for Set numbers 3, 5, and 7
res – smallest difference between two adjacent zones
res.p – smallest difference between two adjacent zones for set numbers 3, 5, and 7
class – classification rating resulting from res and res.p; S – suited, P partially suited, U – unsuited

J.3 Correlation Analysis

The individual results of the correlation analysis for the gridded results of the experiments CO1 and CO2 are shown. It can be seen that the results are very homogenous. As such, it is considered justified to summarise the individual correlation results in the main part of the work.
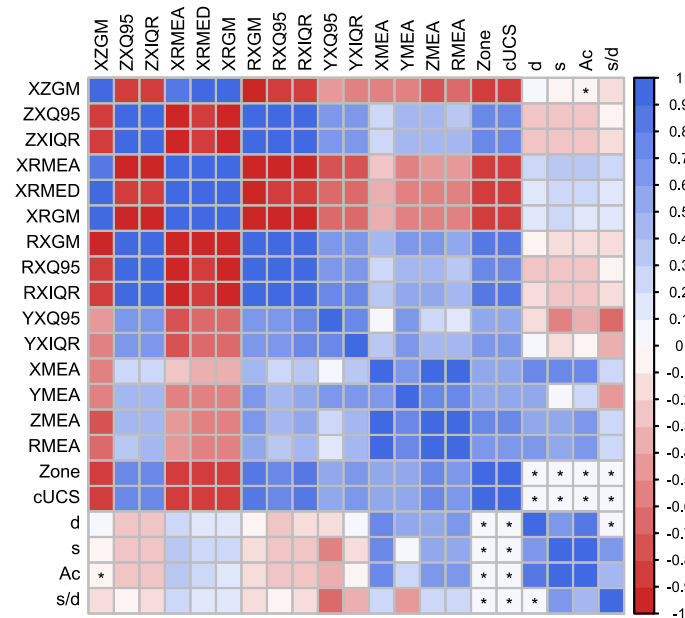
Figure J-3: Correlation analysis for features of experiment CO1; * marks statistically nonsignificant results at significance level = 0.01
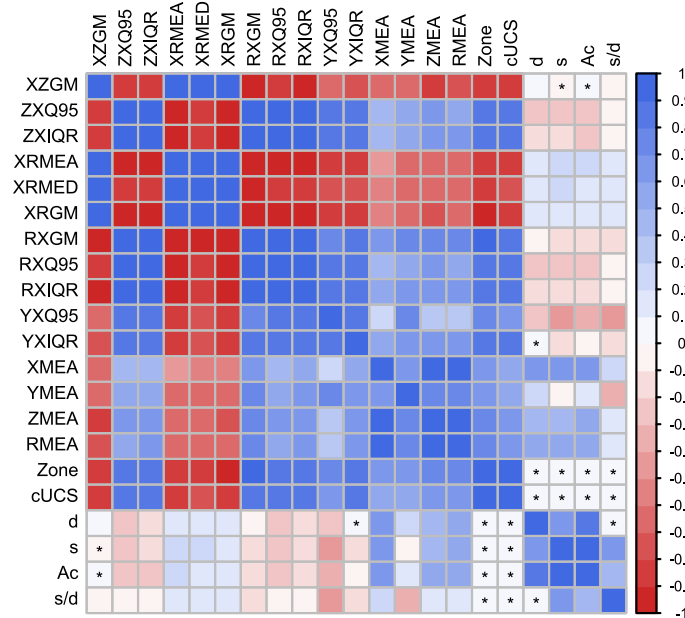
Figure J-4: Correlation analysis for features of experiment CO2; * marks statistically nonsignificant results at significance level = 0.01

Table J-3: Correlation matrix for all covariates for Experiment CO

	XZGM	ZXQ95	ZXIQR	XRMEA	XRMED	XRGM	RXGM	RXQ95	RXIQR	YXQ95	YXIQR	XMEA	YMEA	ZMEA	RMEA	Zone	cUCS	d	s	A_c	s/d
XZGM	1	-0.844	-0.838	0.831	0.903	0.924	-0.939	-0.844	-0.859	-0.451	-0.571	-0.536	-0.505	-0.714	-0.672	-0.831	-0.831	0.040	-0.059	-0.001	-0.133
ZXQ95	-0.844	1	0.961	-0.904	-0.821	-0.936	0.905	1.000	0.953	0.683	0.632	0.236	0.431	0.442	0.397	0.772	0.772	-0.273	-0.268	-0.296	-0.080
ZXIQR	-0.838	0.961	1	-0.933	-0.849	-0.936	0.909	0.961	0.988	0.698	0.684	0.270	0.449	0.476	0.434	0.790	0.790	-0.241	-0.260	-0.275	-0.110
XRMEA	0.831	-0.904	-0.933	1	0.926	0.949	-0.932	-0.904	-0.944	-0.736	-0.715	-0.268	-0.523	-0.476	-0.436	-0.813	-0.813	0.210	0.313	0.302	0.237
XRMED	0.903	-0.821	-0.849	0.926	1	0.947	-0.961	-0.821	-0.879	-0.626	-0.663	-0.374	-0.563	-0.574	-0.534	-0.833	-0.833	0.143	0.223	0.217	0.172
XRGM	0.924	-0.936	-0.936	0.949	0.947	1	-0.993	-0.936	-0.962	-0.698	-0.694	-0.378	-0.583	-0.581	-0.540	-0.832	-0.832	0.136	0.210	0.199	0.146
RXGM	-0.939	0.905	0.909	-0.932	-0.961	-0.993	1	0.905	0.942	0.668	0.683	0.431	0.607	0.624	0.585	0.835	0.835	-0.083	-0.161	-0.145	-0.131
RXQ95	-0.844	1	0.961	-0.904	-0.821	-0.936	0.905	1	0.953	0.683	0.632	0.236	0.431	0.442	0.397	0.772	0.772	-0.273	-0.268	-0.296	-0.080
RXIQR	-0.859	0.953	0.988	-0.944	-0.879	-0.962	0.942	0.953	1	0.737	0.719	0.336	0.547	0.536	0.497	0.811	0.811	-0.158	-0.236	-0.220	-0.159
YXQ95	-0.451	0.683	0.698	-0.736	-0.626	-0.698	0.668	0.683	0.737	1	0.756	0.061	0.667	0.214	0.200	0.543	0.543	-0.138	-0.552	-0.383	-0.649
YXIQR	-0.571	0.632	0.684	-0.715	-0.663	-0.694	0.683	0.632	0.719	0.756	1	0.358	0.670	0.482	0.472	0.679	0.679	0.053	-0.163	-0.062	-0.305
XMEA	-0.536	0.236	0.270	-0.268	-0.374	-0.378	0.431	0.236	0.336	0.061	0.358	1	0.658	0.967	0.980	0.538	0.538	0.752	0.717	0.789	0.264
YMEA	-0.505	0.431	0.449	-0.523	-0.563	-0.583	0.607	0.431	0.547	0.667	0.670	0.658	1	0.703	0.714	0.591	0.591	0.508	0.075	0.299	-0.417
ZMEA	-0.714	0.442	0.476	-0.476	-0.574	-0.581	0.624	0.442	0.536	0.214	0.482	0.967	0.703	1	0.997	0.702	0.702	0.591	0.576	0.625	0.227
RMEA	-0.672	0.397	0.434	-0.436	-0.534	-0.540	0.585	0.397	0.497	0.200	0.472	0.980	0.714	0.997	1	0.671	0.671	0.637	0.599	0.663	0.214
Zone	-0.831	0.772	0.790	-0.813	-0.833	-0.832	0.835	0.772	0.811	0.543	0.679	0.538	0.591	0.702	0.671	1	1	0	0	0	0
cUCS	-0.831	0.772	0.790	-0.813	-0.833	-0.832	0.835	0.772	0.811	0.543	0.679	0.538	0.591	0.702	0.671	1	1	0	0	0	0
d	0.040	-0.273	-0.241	0.210	0.143	0.136	-0.083	-0.273	-0.158	-0.138	0.053	0.752	0.508	0.591	0.637	0	0	1	0.697	0.896	0
s	-0.059	-0.268	-0.260	0.313	0.223	0.210	-0.161	-0.268	-0.236	-0.552	-0.163	0.717	0.075	0.576	0.599	0	0	0.697	1	0.932	0.697
A_c	-0.001	-0.296	-0.275	0.302	0.217	0.199	-0.145	-0.296	-0.220	-0.383	-0.062	0.789	0.299	0.625	0.663	0	0	0.896	0.932	1	0.422
s/d	-0.133	-0.080	-0.110	0.237	0.172	0.146	-0.131	-0.080	-0.159	-0.649	-0.305	0.264	-0.417	0.227	0.214	0	0	0	0.697	0.422	1

J.4   Graphs for k-means analysis

In the following, the details of the k-means cluster analysis for all five cases are presented. These sheets show case number, used covariates and the accuracy table according to the cutting parameters.

Case 1

Covariates: XZGM, ZXQ95, ZXIQR, XRMEA, XRMED, XRGM, RXGM, RXQ95, RXIQR

Plots
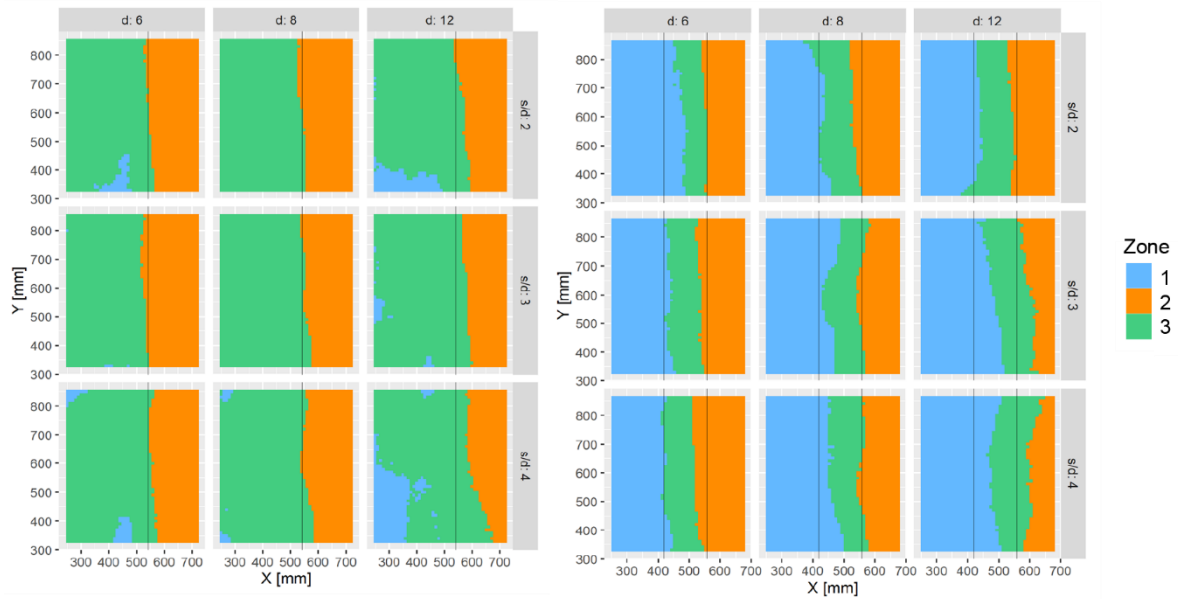
Accuracy

d [mm]					
6	**8**	**12**			
91.2%	93.6%	90.5%	**2**		
93.0%	91.7%	83.0%	**3**		**s/d**
93.0%	90.2%	69.2%	**4**		

Mean	88.4%	**Median**	91%
Min	69.2%	**Q$_{0.25}$**	90%
Max	93.6%	**Q$_{0.75}$**	93%
		IQR	3%

100.0%
80.0%
60.0%
40.0%
20.0%
0.0%
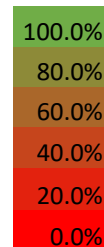
Case 2

<u>Covariates:</u> XZGM, ZXQ95, ZXIQR, XRMEA, XRMED, XRGM, RXGM, RXQ95, RXIQR, YXQ95, YXIQR

<u>Plots</u>

<u>Accuracy</u>

d [mm]					
6	**8**	**12**			
85.5%	92.7%	87.6%	**2**		
90.6%	92.1%	76.2%	**3**		**s/d**
91.5%	93.0%	73.1%	**4**		
Mean	86.9%	**Median**	91%		
Min	73.1%	**Q0.25**	85%		
Max	93.0%	**Q0.75**	92%		
		IQR	7%		

100.0%
80.0%
60.0%
40.0%
20.0%
0.0%
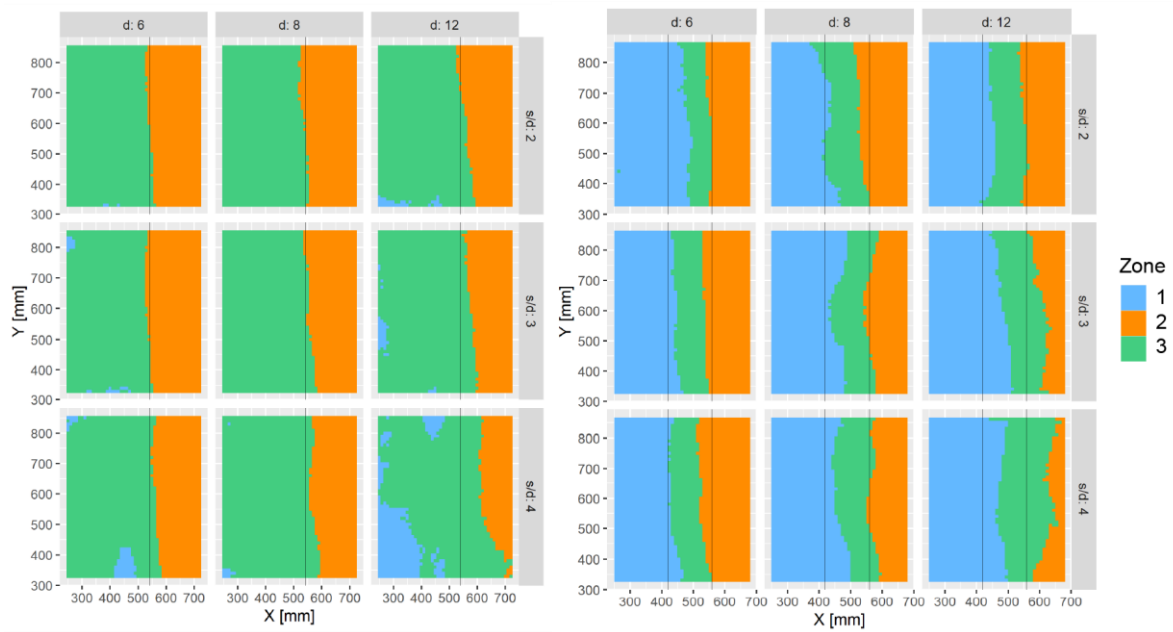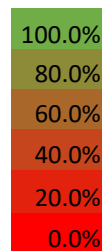
Case 3

Covariates: XZGM, ZXQ95, ZXIQR

Plots

Accuracy

d [mm]					
6	**8**	**12**			
85.5%	92.7%	87.6%	**2**		
90.6%	92.1%	76.2%	**3**	**s/d**	
91.5%	93.0%	73.1%	**4**		
Mean	86.9%	**Median**	91%		
Min	73.1%	**Q0.25**	85%		
Max	93.0%	**Q0.75**	92%		
		IQR	7%		

Case 4

Covariates: XMEA, ZMEA, YMEA, RMEA

Plots

Accuracy

d [mm]					Zone
6	**8**	**12**			
18.9%	26.6%	87.0%	**2**		100.0%
22.7%	41.2%	91.6%	**3**	p/s	80.0%
28.5%	30.5%	96.0%	**4**		60.0%

Mean	49.2%	**Median**	30%		40.0%
Min	18.9%	**Q0.25**	27%		20.0%
Max	96.0%	**Q0.75**	87%		0.0%
		IQR	60%		

Case 5

Covariates: XMEA, ZMEA

Plots

Accuracy

d [mm]				
6	**8**	**12**		
18.9%	22.4%	67.2%	**2**	
21.1%	36.2%	93.0%	**3**	**s/d**
26.3%	36.2%	89.4%	**4**	

Mean	45.6%	**Median**	36%
Min	18.9%	**Q$_{0.25}$**	22%
Max	93.0%	**Q$_{0.75}$**	67%
		IQR	45%

100.0%
80.0%
60.0%
40.0%
20.0%
0.0%
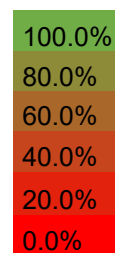
J.5 Distributed Random Forest classification results

In the following, the details of the DRF analysis are shown that was used for the feature importance calculation. The sheets show case number, used covariates, the plots of the classification and a confusion table of the results.

Case 1

Covariates: XZGM, ZXQ95, ZXIQR, XRMEA, XRMED, XRGM, RXGM, RXQ95, RXIQR
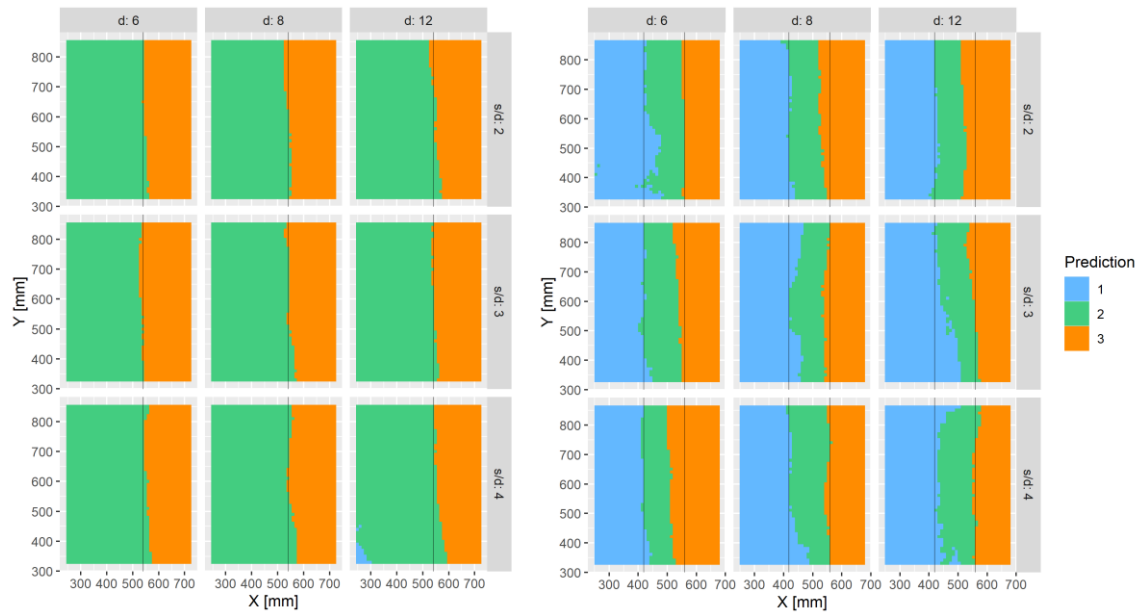
Plots

Confusion Matrix for all parameter combinations

		Real Class				
		1	**2**	**3**	**Error**	**Accuracy**
Prediction	**1**	8189	73	0	0.9%	99.1%
	2	836	19114	1164	9.5%	90.5%
	3	0	400	14018	2.8%	97.2%
	Totals	9025	19587	15182	**5.6%**	**94.4%**

Case 2

Covariates: XZGM, ZXQ95, ZXIQR, XRMEA, XRMED, XRGM, RXGM, RXQ95, RXIQR, YXQ95, YXIQR
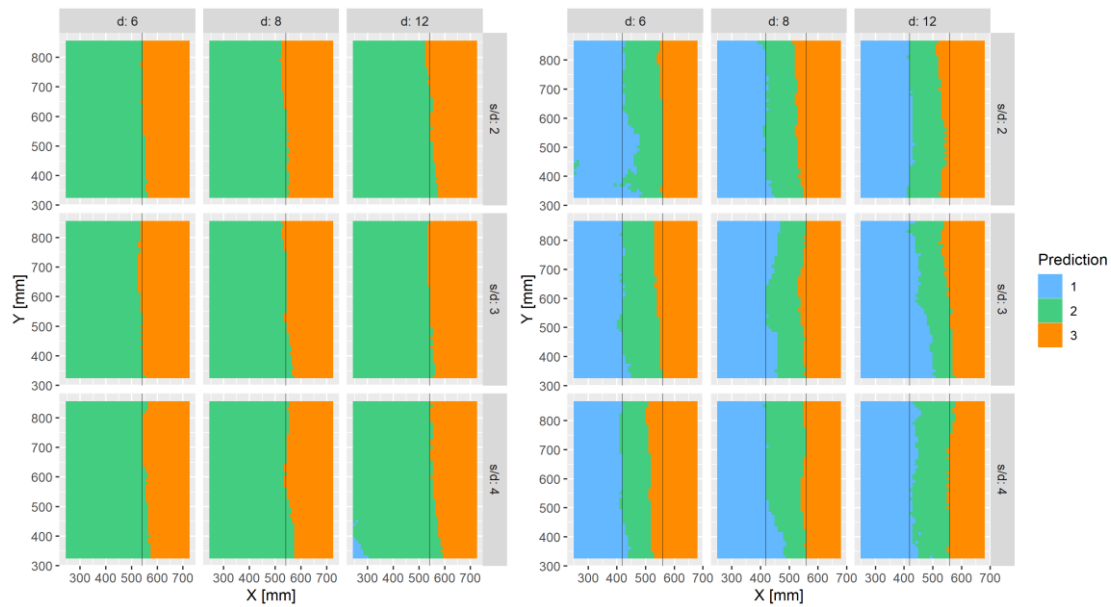
Plots

Confusion Matrix for all parameter combinations

		Real Class			Error	Accuracy
		1	**2**	**3**	**Error**	**Accuracy**
Prediction	**1**	8192	70	0	0.8%	99.2%
	2	831	19203	1080	9.1%	90.9%
	3	0	387	14031	2.7%	97.3%
	Totals	9023	19660	15111	**5.4%**	**94.6%**

Case 3

Covariates: XZGM, ZXQ95, ZXIQR
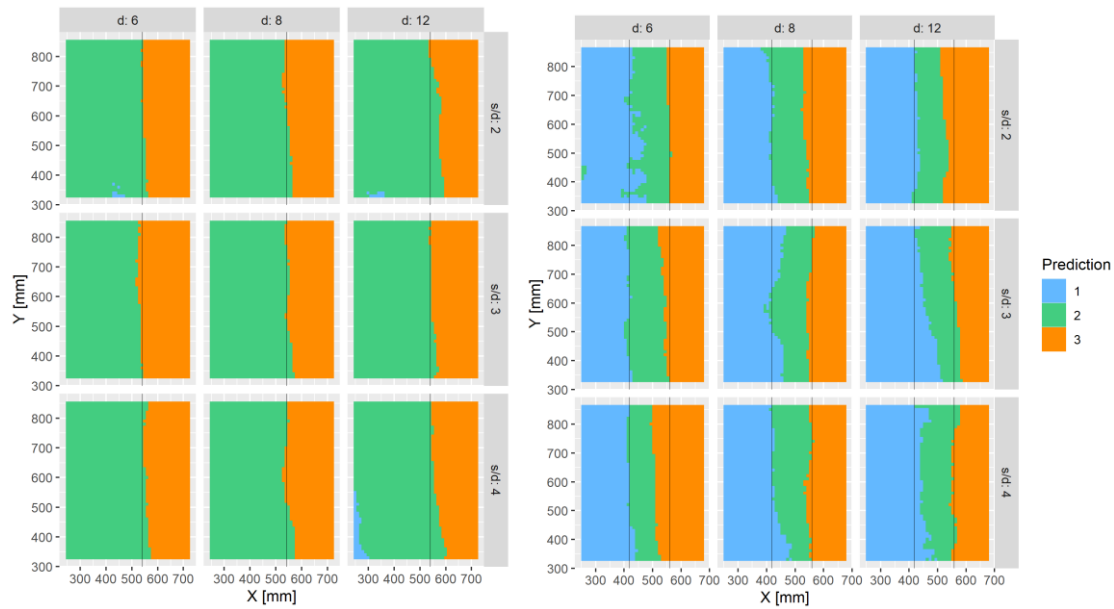
Plots

Confusion Matrix for all parameter combinations

		Real Class				Error	Accuracy
		1	**2**	**3**			
Prediction	**1**	8139	123	0		1.5%	98.5%
	2	925	19121	1068		9.4%	90.6%
	3	0	581	13837		4.0%	96.0%
	Totals	9064	19825	14905		**6.2%**	**93.8%**

Case 4

Covariates: XMEA, ZMEA, YMEA, RMEA
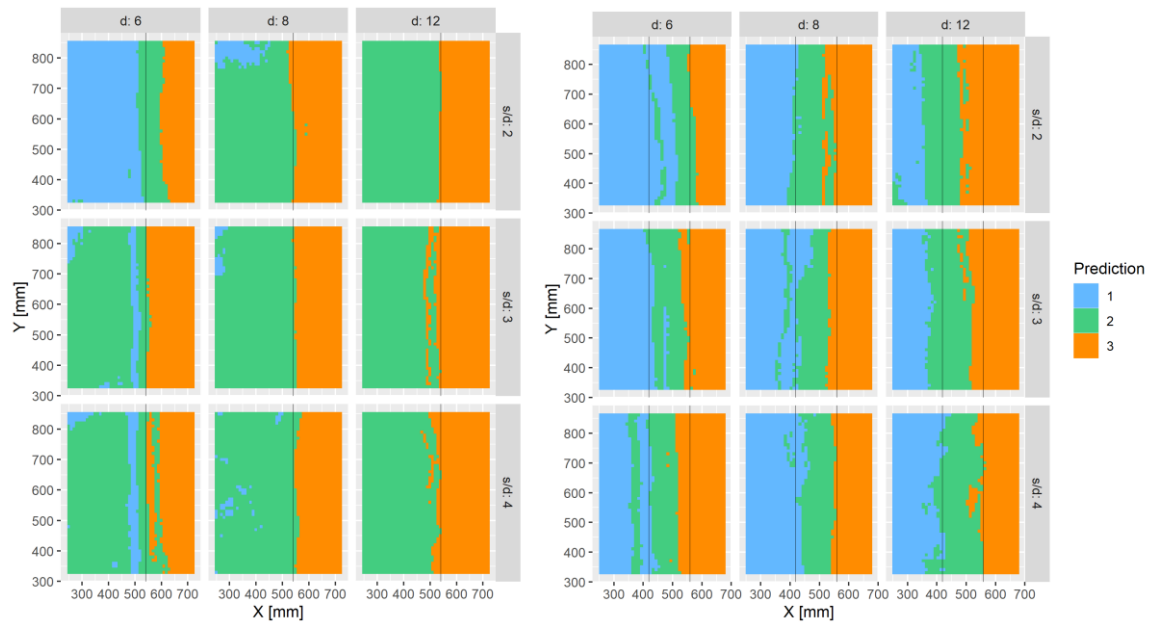
Plots

Confusion Matrix for all parameter combinations

		Real Class			Error	Accuracy
		1	**2**	**3**	**Error**	**Accuracy**
Prediction	**1**	7118	1144	0	13.8%	86.2%
	2	2767	16445	1902	22.1%	77.9%
	3	0	725	13693	5.0%	95.0%
	Totals	9885	18314	15595	**14.9%**	**85.1%**

Case 5

<u>Covariates: XMEA, ZMEA</u>
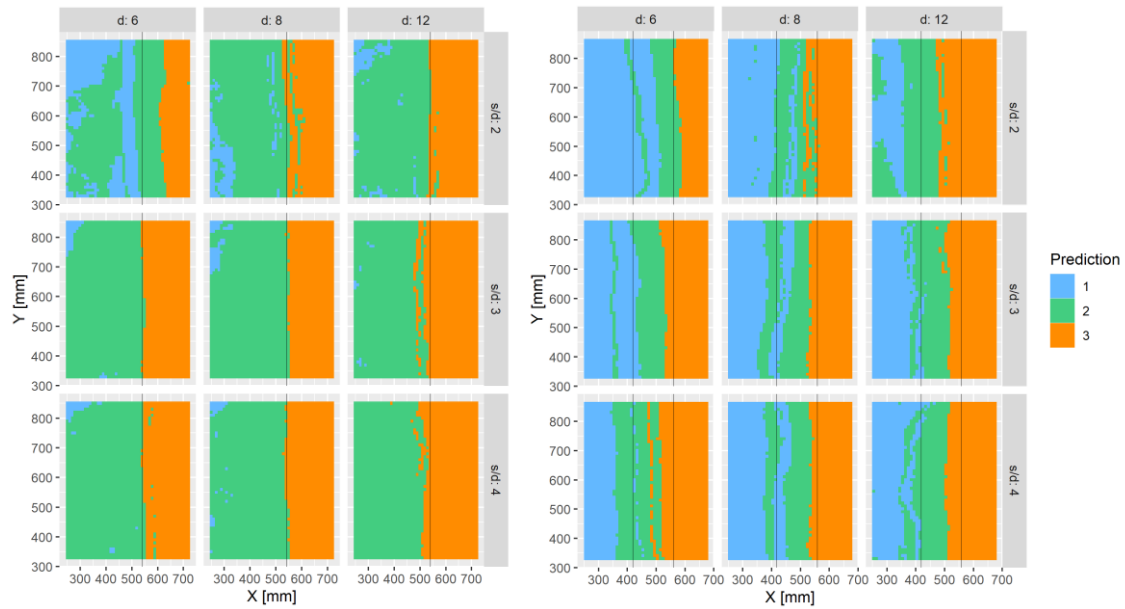
<u>Plots</u>

<u>Confusion Matrix for all parameter combinations</u>

		Real Class				Error	Accuracy
		1	**2**	**3**			
Prediction	**1**	6523	1738	1		21.0%	79.0%
	2	2547	16258	2309		23.0%	77.0%
	3	0	730	13688		5.1%	94.9%
	Totals	9070	18726	15998		**16.7%**	**83.3%**

J.6 Feature importance DRF classification

Table J-4: Feature importance for DRF classification for Experiment CO

case	variable	relative importance	scaled importance	percentage
1	RXIQR	297383.3	1	22.7%
1	XRGM	209342.4	0.703948	16.0%
1	RXGM	185092.9	0.622405	14.1%
1	ZXQ95	163978.3	0.551404	12.5%
1	XZGM	121071.3	0.407122	9.2%
1	RXQ95	119262.1	0.401039	9.1%
1	XRMED	106013.3	0.356487	8.1%
1	ZXIQR	70945.37	0.238565	5.4%
1	XRMEA	35916.55	0.120775	2.7%
2	RXGM	213753.1	1	16.4%
2	RXIQR	205804.4	0.962814	15.8%
2	XRGM	194282	0.908908	14.9%
2	ZXQ95	187434.1	0.876872	14.4%
2	RXQ95	135456.3	0.633705	10.4%
2	XZGM	134075.9	0.627246	10.3%
2	ZXIQR	91598.09	0.428523	7.0%
2	XRMED	73836.3	0.345428	5.7%
2	XRMEA	44108.86	0.206354	3.4%
2	YXIQR	18172.97	0.085018	1.4%
2	YXQ95	4629.026	0.021656	0.4%
3	ZXIQR	450017.7	1	36.3%
3	XZGM	430272.8	0.956124	34.7%
3	ZXQ95	358976.2	0.797694	29.0%
4	ZMEA	397752.5	1	48.7%
4	RMEA	209919.8	0.527765	25.7%
4	YMEA	130409.4	0.327866	16.0%
4	XMEA	79450.92	0.19975	9.7%
5	ZMEA	467677.2	1	62.6%
5	XMEA	279689.8	0.59804	37.4%

Annex K Supplements Experiment GN
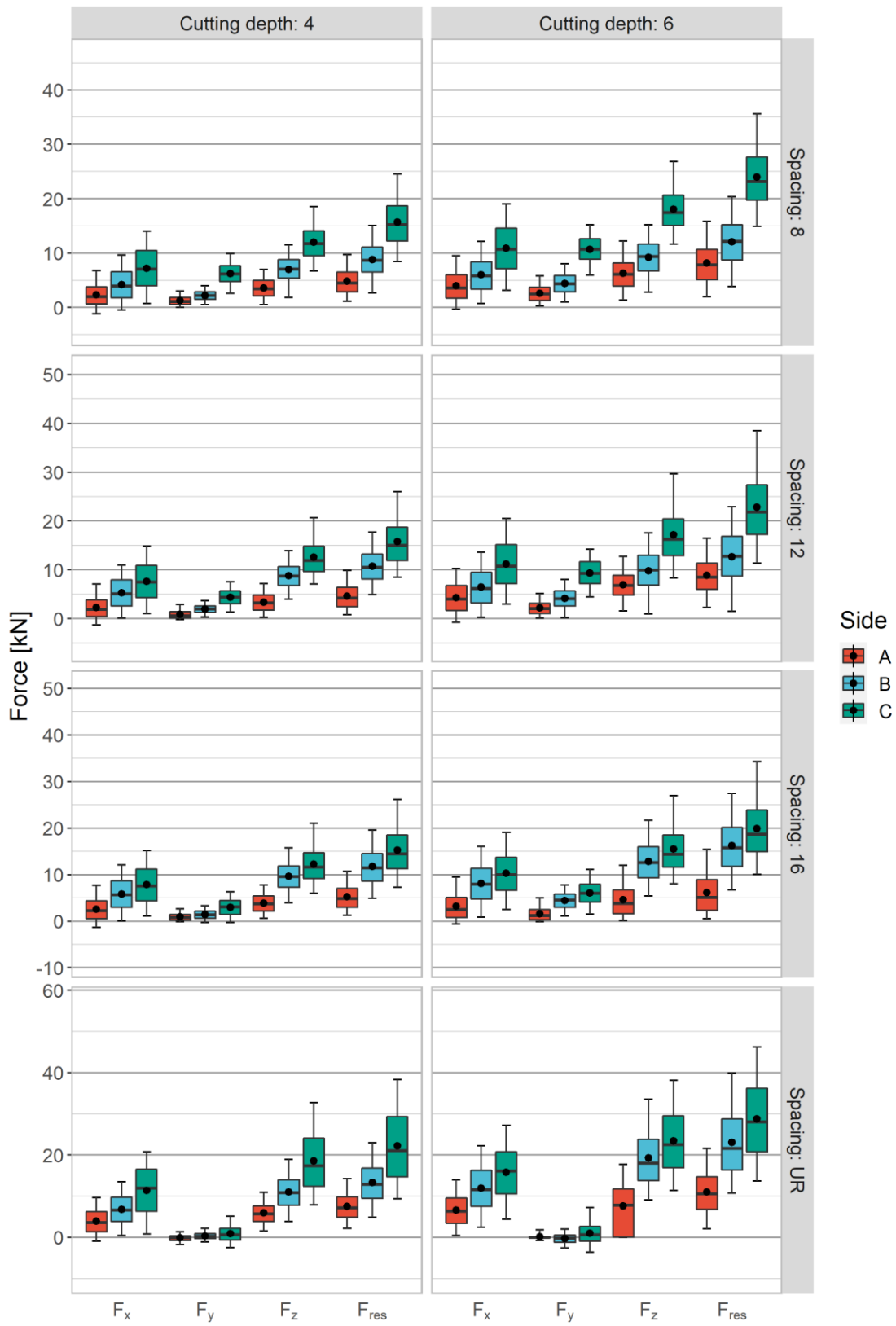
Figure K-1: Raw force responses for all Experiment GN; spacing and depth in mm,
UR – unrelieved cut

Table K-1: Force component results of Experiment GN

Side (Bedding)	Cutting depth [mm]	Spacing [mm]	Mean(Fx) [kN]	Q95(Fx) [kN]	mean(Fy) [kN]	Q95(Fy) [kN]	Mean(Fz) [kN]	Q95(Fz) [kN]	Mean(Fres) [kN]	Q95(Fres) [kN]	Q95(Fx)/mean(Fx)	Q95(Fy)/mean(Fy)	Q95(Fz)/mean(Fz)
A	4	8	2.32	6.81	1.25	3.02	3.58	6.97	4.83	9.67	2.93	1.95	2.41
A	4	12	2.26	7.07	0.87	2.86	3.39	7.15	4.63	9.84	3.13	2.11	3.29
A	4	16	2.59	7.69	0.91	2.64	3.89	7.79	5.23	10.69	2.97	2.00	2.92
A	4	UR	3.90	9.61	-0.14	1.35	5.93	10.96	7.52	14.27	2.46	1.85	-9.43
A	6	8	4.00	9.50	2.64	5.78	6.27	12.19	8.19	15.84	2.38	1.94	2.19
A	6	12	4.32	10.23	2.20	5.15	6.92	12.70	8.84	16.48	2.37	1.83	2.34
A	6	16	3.22	9.45	1.61	5.01	4.57	11.97	6.16	15.43	2.94	2.62	3.11
A	6	UR	6.65	13.95	0.12	1.83	7.62	17.74	11.04	21.60	2.10	2.33	14.65
B	4	8	4.22	9.62	2.20	3.97	7.01	11.55	8.80	15.07	2.28	1.65	1.80
B	4	12	5.27	10.96	1.95	3.64	8.78	13.90	10.75	17.67	2.08	1.58	1.87
B	4	16	5.84	12.10	1.42	3.29	9.66	15.75	11.72	19.59	2.07	1.63	2.31
B	4	UR	6.75	13.53	0.34	2.19	11.05	18.95	13.27	22.99	2.00	1.71	6.46
B	6	8	5.99	12.14	4.41	8.00	9.22	15.17	12.10	20.31	2.03	1.65	1.81
B	6	12	6.45	13.63	4.11	8.02	9.78	17.58	12.68	22.90	2.11	1.80	1.95
B	6	16	8.13	16.09	4.46	7.80	12.85	21.63	16.19	27.48	1.98	1.68	1.75
B	6	UR	11.94	22.25	-0.31	2.00	19.28	33.56	23.05	39.89	1.86	1.74	-6.39
C	4	8	7.22	13.99	6.21	9.88	12.00	18.51	15.67	24.54	1.94	1.54	1.59
C	4	12	7.64	14.82	4.39	7.55	12.61	20.65	15.74	25.98	1.94	1.64	1.72
C	4	16	7.82	15.21	2.97	6.32	12.25	21.00	15.25	26.16	1.94	1.71	2.13
C	4	UR	11.37	20.75	0.87	5.18	18.58	32.71	22.28	38.34	1.83	1.76	5.96
C	6	8	10.90	19.02	10.65	15.23	18.07	26.79	23.95	35.60	1.75	1.48	1.43
C	6	12	11.20	20.52	9.34	14.24	17.19	29.69	22.86	38.51	1.83	1.73	1.53
C	6	16	10.28	19.04	6.10	11.07	15.46	27.00	19.91	34.27	1.85	1.75	1.81
C	6	UR	15.81	27.18	1.03	7.27	23.45	38.15	28.77	46.27	1.72	1.63	7.06

Table K-2: Force component ratio results of Experiment GN

Side (Bedding)	Cutting depth [mm]	Spacing [mm]	RXGM	RXIQR	RXQ95	XRGM	XRMED	XRMEA	ZXMEA	ZXIQR	ZXQ95
A	4	8	2.09	1.03	7.80	0.47	0.53	0.41	1.14	1.24	7.34
A	4	12	1.99	0.96	7.64	0.49	0.56	0.39	0.96	1.27	7.26
A	4	16	2.02	0.95	7.92	0.48	0.56	0.41	1.00	1.22	7.52
A	4	UR	2.08	0.93	7.95	0.47	0.57	0.46	1.33	1.14	7.78
A	6	8	2.25	1.10	7.88	0.44	0.53	0.45	1.67	1.20	7.30
A	6	12	2.26	1.16	8.59	0.43	0.52	0.43	1.59	1.28	8.07
A	6	16	1.95	0.88	5.93	0.51	0.57	0.46	1.19	1.08	5.50
A	6	UR	1.75	0.91	4.75	0.57	0.62	0.60	1.35	1.73	4.57
B	4	8	2.36	1.36	9.36	0.41	0.51	0.44	1.84	1.48	8.86
B	4	12	2.34	1.25	7.97	0.42	0.52	0.46	2.03	1.38	7.68
B	4	16	2.25	1.02	7.08	0.44	0.53	0.46	1.89	1.15	6.82
B	4	UR	2.15	0.84	5.65	0.46	0.53	0.48	1.81	0.98	5.52
B	6	8	2.21	0.94	5.62	0.45	0.52	0.48	1.82	0.98	5.08
B	6	12	2.10	0.83	5.33	0.47	0.54	0.49	1.70	0.88	4.78
B	6	16	2.17	0.83	5.33	0.46	0.53	0.48	1.80	0.88	4.88
B	6	UR	2.05	0.55	4.17	0.48	0.54	0.50	1.81	0.65	4.03
C	4	8	2.50	1.33	8.20	0.39	0.48	0.43	2.17	1.27	7.26
C	4	12	2.34	1.12	6.98	0.42	0.51	0.46	2.13	1.17	6.47
C	4	16	2.18	0.93	6.12	0.45	0.54	0.49	1.96	1.01	5.79
C	4	UR	2.13	0.60	5.62	0.46	0.53	0.48	1.80	0.70	5.48
C	6	8	2.41	0.95	5.41	0.41	0.47	0.44	2.06	0.87	4.58
C	6	12	2.21	0.73	4.69	0.45	0.51	0.48	1.84	0.71	3.99
C	6	16	2.09	0.68	4.48	0.48	0.54	0.50	1.79	0.71	4.03
C	6	UR	1.93	0.46	3.66	0.52	0.57	0.54	1.71	0.54	3.48

Table K-3: Values for PP_{x0} for Experiment GN

Side	s [mm]	d [mm]	mean(PP_{x0}) [%]	SE(PP_{x0})
A	4	8	14.93	0.85
A	4	12	18.14	0.65
A	4	16	17.37	0.89
A	6	8	6.90	1.03
A	6	12	9.81	0.77
A	6	16	11.70	2.26
B	4	8	8.00	0.54
B	4	12	4.84	0.26
B	4	16	4.93	0.47
B	6	8	2.88	0.46
B	6	12	3.74	0.84
B	6	16	3.36	0.57
C	4	8	2.83	0.35
C	4	12	2.42	0.65
C	4	16	2.31	0.11
C	6	8	0.50	0.10
C	6	12	0.58	0.22
C	6	16	0.93	0.27

Table K-4: Values for PP_{z05} for Experiment GN

Side	s [mm]	d [mm]	mean(PP_{z1}) [%]	SE(PP_{z1})
A	4	8	11.15	2.73
A	4	12	15.25	1.80
A	4	16	8.70	2.90
A	6	8	4.27	1.49
A	6	12	3.94	1.06
A	6	16	17.53	3.26
B	4	8	2.32	0.53
B	4	12	1.46	0.39
B	4	16	1.12	0.33
B	6	8	2.45	0.88
B	6	12	6.17	1.97
B	6	16	2.67	0.60
C	4	8	1.14	0.38
C	4	12	1.93	1.08
C	4	16	0.64	0.21
C	6	8	0.92	0.24
C	6	12	0.38	0.14
C	6	16	0.51	0.13

Annex L   Supplements Experiment GR

Table L-1: Results of Experiment GR; values for F_x, F_y, F_z, and F_{res} in kN

Para-meter	Radiation time	Spacing [mm]	$Q_{0.05}$	$Q_{0.25}$	Median	Mean	Geom. mean	$Q_{0.75}$	$Q_{0.95}$	IQR
F_x	0 s	8	-0.235	2.995	5.959	6.202	5.071	9.308	13.017	6.313
F_x	0 s	12	0.150	3.697	6.694	7.026	5.780	10.195	14.350	6.498
F_x	30 s	8	0.089	3.365	6.373	6.629	5.427	9.830	13.643	6.466
F_x	30 s	12	0.584	4.193	7.332	7.658	6.338	10.998	15.307	6.805
F_x	45 s	8	-0.682	1.394	3.786	4.251	3.276	6.788	10.685	5.394
F_x	45 s	12	-0.481	2.197	4.883	5.298	4.247	8.131	12.254	5.935
F_y	0 s	8	0.276	1.875	3.179	3.314	2.758	4.615	6.810	2.740
F_y	0 s	12	-0.285	1.434	2.896	3.074	2.551	4.537	7.074	3.103
F_y	30 s	8	0.597	2.289	3.638	3.780	3.218	5.142	7.441	2.852
F_y	30 s	12	-0.105	1.748	3.307	3.538	2.924	5.104	7.948	3.356
F_y	45 s	8	-0.036	0.800	1.887	2.091	1.502	3.105	5.194	2.305
F_y	45 s	12	-0.343	0.771	1.918	2.191	1.681	3.314	5.774	2.543
F_z	0 s	8	5.462	9.722	12.574	12.780	11.684	15.627	20.857	5.905
F_z	0 s	12	7.604	12.008	14.995	15.247	14.224	18.231	23.860	6.224
F_z	30 s	8	6.559	11.086	14.128	14.367	13.362	17.458	23.198	6.372
F_z	30 s	12	8.213	13.007	16.564	17.055	15.897	20.595	27.627	7.588
F_z	45 s	8	0.050	4.037	7.096	7.044	5.415	9.844	14.304	5.807
F_z	45 s	12	1.011	5.974	9.130	9.218	7.578	12.227	17.545	6.253
F_r	0 s	8	7.015	11.551	14.767	15.101	13.879	18.344	24.351	6.794
F_r	0 s	12	9.252	13.838	17.150	17.591	16.474	20.902	27.461	7.064
F_r	30 s	8	8.325	13.071	16.436	16.814	15.662	20.218	26.628	7.147
F_r	30 s	12	10.238	15.077	18.937	19.581	18.444	23.407	31.157	8.330
F_r	45 s	8	0.852	5.313	8.846	9.017	6.907	12.320	17.781	7.006
F_r	45 s	12	2.323	7.467	11.156	11.394	9.498	14.899	21.200	7.432
XZ	0 s	8	-0.031	0.256	0.488	0.511	0.427	0.709	1.116	0.453
XZ	0 s	12	0.013	0.265	0.461	0.482	0.403	0.652	0.989	0.386
XZ	30 s	8	0.008	0.251	0.465	0.489	0.403	0.674	1.042	0.423
XZ	30 s	12	0.040	0.266	0.454	0.481	0.396	0.633	0.980	0.367
XZ	45 s	8	-0.411	0.286	0.632	0.609	0.593	0.946	1.898	0.660
XZ	45 s	12	-0.115	0.302	0.592	0.592	0.537	0.865	1.475	0.563
ZX	0 s	8	-4.079	1.297	1.829	2.021	2.076	3.179	5.000	1.882
ZX	0 s	12	0.478	1.451	2.014	2.227	2.218	3.314	5.000	1.863
ZX	30 s	8	0.313	1.393	1.980	2.232	2.188	3.420	5.000	2.027
ZX	30 s	12	0.687	1.516	2.088	2.349	2.263	3.423	5.000	1.907
ZX	45 s	8	-3.117	0.872	1.313	1.472	1.511	2.303	5.000	1.431
ZX	45 s	12	-2.421	1.018	1.477	1.672	1.691	2.533	5.000	1.515
XR	0 s	8	-0.024	0.241	0.425	0.393	0.355	0.562	0.727	0.321
XR	0 s	12	0.015	0.251	0.408	0.386	0.345	0.535	0.690	0.284
XR	30 s	8	0.008	0.235	0.407	0.381	0.339	0.542	0.699	0.307
XR	30 s	12	0.040	0.251	0.403	0.385	0.340	0.524	0.685	0.273
XR	45 s	8	-0.190	0.280	0.524	0.444	0.442	0.674	0.892	0.394
XR	45 s	12	-0.092	0.282	0.496	0.434	0.419	0.641	0.815	0.359

Continuation Table L-1

Para-meter	Radiation time	Spacing [mm]	Q0.05	Q0.25	Median	Mean	Geom. mean	Q0.75	Q0.95	IQR
RX	0 s	8	-4.286	1.686	2.155	2.304	2.488	3.452	5.000	1.766
RX	0 s	12	1.142	1.799	2.305	2.484	2.580	3.553	5.000	1.754
RX	30 s	8	1.092	1.768	2.297	2.504	2.591	3.693	5.000	1.924
RX	30 s	12	1.247	1.855	2.375	2.607	2.626	3.663	5.000	1.807
RX	45 s	8	-3.511	1.365	1.708	1.800	2.063	2.625	5.000	1.259
RX	45 s	12	-2.767	1.460	1.835	1.974	2.176	2.827	5.000	1.367
YX	0 s	8	-0.449	0.285	0.482	0.610	0.543	0.839	2.531	0.554
YX	0 s	12	-0.243	0.193	0.410	0.520	0.436	0.729	2.067	0.536
YX	30 s	8	-0.075	0.329	0.530	0.686	0.590	0.905	2.632	0.576
YX	30 s	12	-0.131	0.221	0.432	0.566	0.455	0.764	2.126	0.543
YX	45 s	8	-0.659	0.216	0.402	0.504	0.460	0.712	2.296	0.497
YX	45 s	12	-0.534	0.142	0.350	0.458	0.399	0.667	2.161	0.525

Table L-2: Results of Experiment GR with spacing summarised; values for F_x, F_y, F_z, and F_{res} in kN

Para-meter	Radiation time	Spacing [mm]	Q0.05	Q0.25	Median	Mean	geom. Mean	Q0.75	Q0.95
F_x	0 s	-0.079	3.271	6.257	6.536	5.350	9.652	13.614	6.380
F_x	30 s	0.249	3.684	6.756	7.045	5.781	10.294	14.382	6.611
F_x	45 s	-0.607	1.690	4.221	4.679	3.647	7.344	11.416	5.654
F_y	0 s	0.022	1.704	3.074	3.217	2.674	4.586	6.914	2.882
F_y	30 s	0.262	2.081	3.520	3.682	3.098	5.128	7.640	3.046
F_y	45 s	-0.149	0.788	1.900	2.132	1.571	3.184	5.436	2.397
F_z	0 s	6.081	10.526	13.539	13.780	12.655	16.788	22.325	6.262
F_z	30 s	7.143	11.750	15.029	15.454	14.338	18.756	25.397	7.007
F_z	45 s	0.207	4.767	7.866	7.932	6.225	10.872	15.923	6.105
F_{res}	0 s	7.674	12.371	15.734	16.111	14.878	19.455	25.818	7.083
F_{res}	30 s	8.994	13.781	17.374	17.933	16.732	21.534	28.808	7.753
F_{res}	45 s	1.315	6.088	9.761	9.989	7.867	13.406	19.455	7.318
XZ	0 s	-0.013	0.260	0.476	0.499	0.417	0.685	1.067	0.425
XZ	30 s	0.021	0.258	0.460	0.486	0.400	0.657	1.019	0.399
XZ	45 s	-0.246	0.293	0.614	0.602	0.569	0.912	1.692	0.619
ZX	0 s	-2.699	1.357	1.907	2.105	2.133	3.238	5.000	1.881
ZX	30 s	0.517	1.442	2.027	2.279	2.219	3.421	5.000	1.979
ZX	45 s	-2.879	0.930	1.381	1.554	1.583	2.402	5.000	1.472
XR	0 s	-0.008	0.245	0.417	0.390	0.351	0.551	0.713	0.306
XR	30 s	0.021	0.242	0.405	0.383	0.339	0.534	0.694	0.292
XR	45 s	-0.146	0.281	0.512	0.440	0.432	0.661	0.859	0.379
RX	0 s	-2.935	1.730	2.218	2.377	2.525	3.496	5.000	1.765
RX	30 s	1.169	1.803	2.330	2.546	2.605	3.679	5.000	1.876
RX	45 s	-3.239	1.402	1.761	1.871	2.109	2.711	5.000	1.308
YX	0 s	-0.329	0.248	0.454	0.574	0.497	0.794	2.347	0.547
YX	30 s	-0.111	0.285	0.492	0.638	0.532	0.849	2.434	0.564
YX	45 s	-0.603	0.185	0.383	0.485	0.435	0.694	2.242	0.510

Table L-3: Results Experiment GR with repetition measurement

Spacing	Radiation time	Variable	Mean	Standard deviation
[mm]	[s]		[kN]	[kN]
12	0	F_x	7.03	4.53
12	0	F_y	3.07	2.27
12	0	F_z	15.25	5.04
12	0 - rep.	F_x	6.76	4.33
12	0 - rep.	F_y	3.09	2.21
12	0 - rep.	F_z	14.89	4.99
12	30	F_x	7.66	4.64
12	30	F_y	3.54	2.50
12	30	F_z	17.06	5.98
12	45	F_x	5.30	4.04
12	45	F_y	2.19	1.93
12	45	F_z	9.22	4.93
8	0	F_x	6.20	4.22
8	0	F_y	3.31	2.00
8	0	F_z	12.78	4.70
8	0 - rep.	F_x	6.12	4.08
8	0 - rep.	F_y	3.67	1.99
8	0 - rep.	F_z	12.83	4.21
8	30	F_x	6.63	4.30
8	30	F_y	3.78	2.11
8	30	F_z	14.37	5.20
8	45	F_x	4.25	3.64
8	45	F_y	2.09	1.69
8	45	F_z	7.04	4.38

Table L-4: Values for proportions of datapoints below 0.5 kN for F_z, and below 0 kN for F_x for Experiment GR

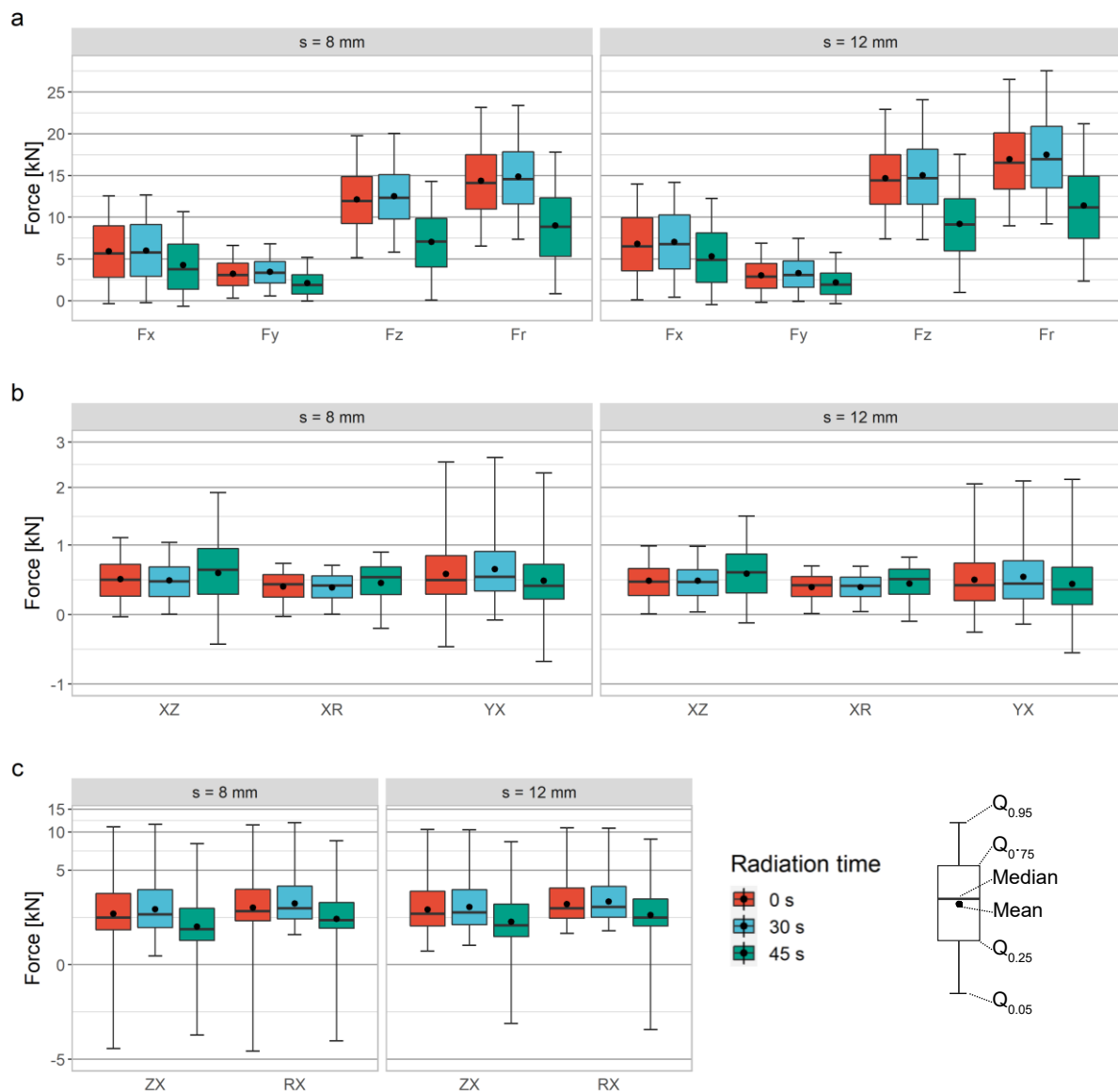| Spacing	Radiation time	$PP_{0.5}(F_z)$	$PP_0(F_x)$
s = 8 mm	0 s	0.63%	5.97%
s = 8 mm	30 s	0.82%	4.63%
s = 8 mm	45 s	8.42%	9.05%
s = 12 mm	0 s	0.30%	4.37%
s = 12 mm	30 s	0.11%	3.30%
s = 12 mm	45 s	3.61%	7.42%

Figure L-1: Results Experiment GR; a – Results of cutting forces for layer 2–4, b & c – results for FCR for layer 2–4; y-axis pseudo-logarithmically scaled

Annex M Preliminary Artificial Neural Network Training

This preparatory study was performed to analyse the potential implementation of a neural net-based classification of rock masses with force component ratios (FCR). This experiment is based on the learnings from Experiment CO (Chapter 5.3.2). There, different features were identified that could be used to differentiate between rock types. Here, five different feedforward architectures were tested. The training was conducted on the FBA2 dataset. In this preliminary study, the R package Neuralnet was used. This chapter describes the training of these neural networks for the classification between ore and concrete and shows its results. The general learning is that a feedforward neural network might be used for classification purposes. However, the calculation times are relatively long. Hence, for the final case study of this work, the H2O package was used, which shows significantly faster computation speeds.

The following coding is used for the FCR features. The features are statistical parameters describing the distribution of an FCR. For example, XZGM is the geometric mean ($\bar{x}_{geom}$) for F_x/F_z. Table M-1 shows all used encodings.

Table M-1: Coding of FCR and statistical descriptors for preliminary case study

Nr.	FCR-Code	Statistical descriptor code	FCR	Statistical parameter
1	XZ	GM	F_x/F_z	$\bar{x}_{geom}$
2	ZX	Q95	F_z/F_x	$Q_{0.95}$
3	ZX	IQR	F_z/F_x	IQR
4	XR	MEA	F_x/F_{res}	$\bar{x}$
5	XR	MED	F_x/F_{res}	$\tilde{x}$
6	XR	GM	F_x/F_{res}	$\bar{x}_{geom}$
7	RX	GM	F_{res}/F_x	$\bar{x}_{geom}$
8	RX	Q95	F_{res}/F_x	$Q_{0.95}$
9	RX	IQR	F_{res}/F_x	IQR
10	YX	Q95	F_y/F_x	$Q_{0.95}$
11	YX	IQR	F_y/F_x	IQR

Figure M-1 shows the boxplot of the raw force components as well as the used FCR for FBA2. On Panel a) the raw cutting forces components irrespectively of the *cutting depth* are shown. All cutting forces are generally higher in the vein material. Panel d) shows the raw force results split by the different levels of *cutting depth*. It shows that a classification based on the raw force components is subjected to noise from the *cutting depth*. An approach based on the raw cutting force components would likely produce a high error rate.

The Panels b) and c) of the figure show the FCR. Differences between the FCR can be seen for the two rock types. As such, a classification algorithm should be able to classify the different rock types based on the chosen features. As described in Chapter 5.11, the used features were standardised.
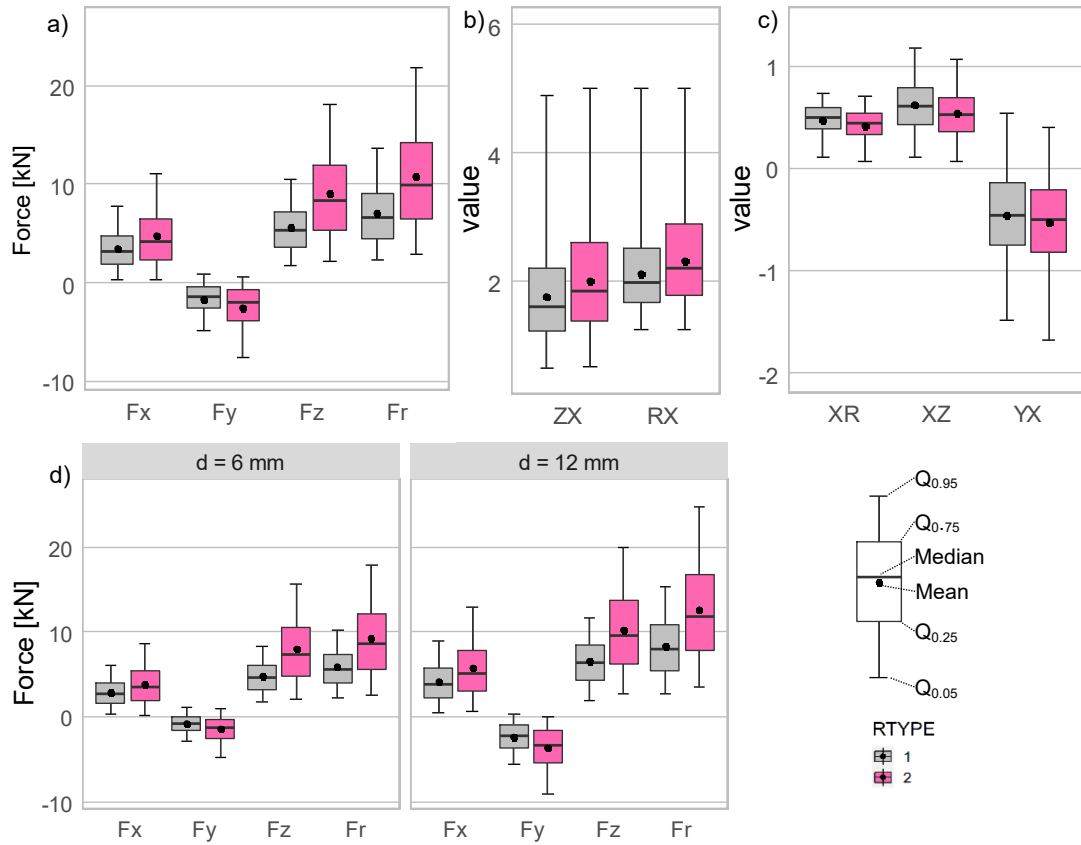
Figure M-1: Boxplots for distribution of F_x, F_y, F_z, F_{res} and FCR ZX, RX, XR, XZ and YX from raw measurement data for FBA2

In the experiment, several designs of neural nets were tested. The number of input and output neurons was kept constant. As convergence threshold of the partial derivative of the error function, 0.05 was chosen. The number of neurons was varied. Generally, the number of used neurons and layers is dependent on the complexity of the problem [179]. Core to the neural net classification is the R package Neuralnet which implements a variety of neural net functions [266] as well as the package NeuralNetTools to analyse the neural networks [267].

Different from the main part of this work, the activation function used for this preliminary study was the logistic function in the form of:

$$z(g) = \frac{1}{1 + e^{-g}} \qquad (34)$$

Here, $z(g)$ denotes the output to be given to the next synapse(s) and g is the input after integration of the input with Equation (28). As a learning algorithm, the rapid backpropagation algorithm with weight backtracking (rprop+) as proposed by Riedmiller (1993) was chosen. It provides a relatively faster learning process than traditional backpropagation algorithms [268]. The robust backpropagation algorithm stores the last state of the neural net. Weight backtracking allows undoing the last iteration and adding a smaller value to the weight in the next step. Without the usage of weight backtracking, the algorithm can jump over the minimum several times. Further explanations can be found in [179, 268].

In total, five networks (NN1 to NN5) have been trained and their results were evaluated. Table M-2 shows the networks. The first network uses an architecture of 11-5-2-1, meaning that 2 hidden layers were used—the first containing 5 neurons and the second containing 2 neurons. The other four neural networks consisted of a single layer. The number of neurons were 3, 5, 7 and 9 neurons, respectively.

During pre-tests, ANNs using 11 hidden neurons did not converge within 2.5 million iterations. This value was taken as a threshold to limit processing time.

Both NN1 and NN5 needed the highest number of iterations to complete the training. In the case of NN1, this might be related to the additional hidden layer. In the case of NN5, it might be related to the fact that 3 neurons are not enough to properly represent the problem. A high number of iterations usually goes along with a longer training time. However, the more nodes a neural net has, the longer the time per iteration step as shown in the last column. NN2–NN3 in this regard are considered to be more optimal in terms of training time. The *sum of squared errors* after Equation (30) for all NNs is in a similar range, with NN1 and NN3 performing the best here.

Table M-2: Results of the neural net calculations

Name	network design	training time [min]	SSE-Error	Nr. of iterations (in thousand)	Iterations per minute (thousand / minute)
NN1	11-5-2-1	94.8	67.4	1,419	15.0
NN2	11-9-1	12.7	71.3	239	18.8
NN3	11-7-1	34.0	64.6	821	24.2
NN4	11-5-1	16.7	75.8	526	31.5
NN5	11-3-1	54.3	78.3	2,440	44.9

Figure M-2, left side, shows the layout of the best performing network, NN3. The thickness of the connection line indicates the relative weight of the neuron connection. Black lines indicate positive weights and grey lines negative weights, the line thickness indicates the weight of the connection. No single input-hidden connection is outstanding on its own. The only weight outstanding is H2-O1 being a large negative weight.
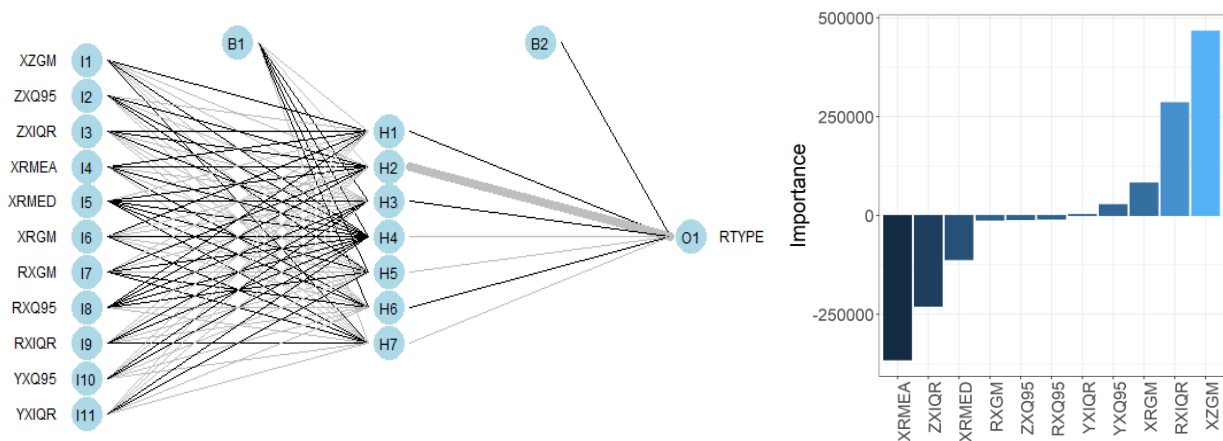
Figure M-2: Neural net layout for the best performing network in FBA2 (left); Olden feature importance (right)

For the computation of the feature importance, Olden's method of connection weights was used. This method is similar to Garson's algorithm. It was measured to be the most accurate algorithm in a comparative study that examined the accuracy of nine different methods to estimate the importance of covariates for neural networks. This study compared the algorithms with a simulated dataset in which the true weights to the output were known [183]. The calculation follows the equation;

$$II_i = \sum_{h=1}^{n} w_{ih} * w_{ho} \qquad (35)$$

197

The formula shows the calculation of the feature importance for the case of one hidden layer. The importance of the input feature II_i is calculated using the weights w_{ih} connecting each of the input neurons I_i to each of the hidden neurons H_h multiplied by the weights for the connections between the respective hidden neurons the output neuron O_o. As such. the formula calculates importance as the summed product of the raw input-hidden and hidden-output connection weights between each input and output node.

An advantage is that the relative contribution of each connection weight is maintained in both magnitude and sign [267, 269]. This separates this algorithm from Garson's algorithm, which uses absolute values and as such loses accuracy. Further information can be found in [269]. It must be mentioned that, since the importance ratings are basically sums of products, they are subject to the number of neurons in a network. As such, they can not be used when comparing the weights across different models [267].

To allow a quantitative evaluation of the influence of covariates across multiple neural networks, an extension of Oldens feature importance is used. The output should be a relative value and at the same time the positive or negative mathematical sign shall be retained. To allow this, the following extension of the output of the Olden formula is used:

$$RI_i = \frac{II_i}{\sum_{i=1}^{n}|II_i|} \tag{36}$$

Where RI_i is the relative importance of a covariate within the given neural net algorithm. II_i is the importance after Olden of a given covariate.

Figure M-3 left side, shows the RI results. It can be seen that NN1, NN3 and NN5 exhibit some similarities in weighing the features. For these, *XZGM* has the highest weight. Generally, *ZXQ95*, *RXQ95* and to some extent *YXQ95* and *YXIQR* have smaller weights. *ZXIQR*, *XRMEA*, and *XRMED* have medium weights. Curious is the fact that NN2 and NN4 show a somewhat inverted pattern to the other three neural networks. For these two neural networks, *XZGM* has a negative weight while *ZXIQR* and *XRMED* are mainly positive.

Since NN1, NN3, and NN5 on the one hand, and NN2 and NN4 on the other hand, show somewhat similar behaviour with their peers, a similar behaviour in the classification of these networks could be expected. Figure M-3, right side, shows which proportion the of data has been classified similarly by two compared ANNs. As such, it shows how similar the networks classify regardless of their accuracy towards the real rock type. Generally, all networks classify very similar, which is related by their overall good performance. Also, it shows that NN1 and NN3 classify very similar. Also NN2 and NN4 show high similarities. NN5 classifies similar to NN2 and NN4.

Summarising, certain similarities in low weights for *ZXQ95* and *RXQ95* speak for a small influence of these features while *XZGM* seems to play a dominant role together with *ZXIQR*, *XRMEA*, *XRMED* and *RXIQR*. However, the different weighing patterns imply that several weighing possibilities exist.

	XZGM	ZXQ95	ZXIQR	XRMEA	XRMED	XRGM	RXGM	RXQ95	RXIQR	YXQ95	YXIQR
NN1	0.28	0.01	-0.14	-0.17	-0.13	0.06	0.02	-0.01	0.16	0.03	0
NN2	-0.35	0	0.04	0.13	0.3	-0.01	0.01	0.02	0.02	-0.08	-0.03
NN3	0.29	-0.01	-0.14	-0.23	-0.07	0.05	-0.01	-0.01	0.18	0.02	0
NN4	-0.09	0	-0.04	0.29	0.06	-0.18	0.14	0	-0.01	0	-0.18
NN5	0.18	0	-0.14	-0.19	0.17	-0.05	0.04	0.01	0.17	0.02	-0.04

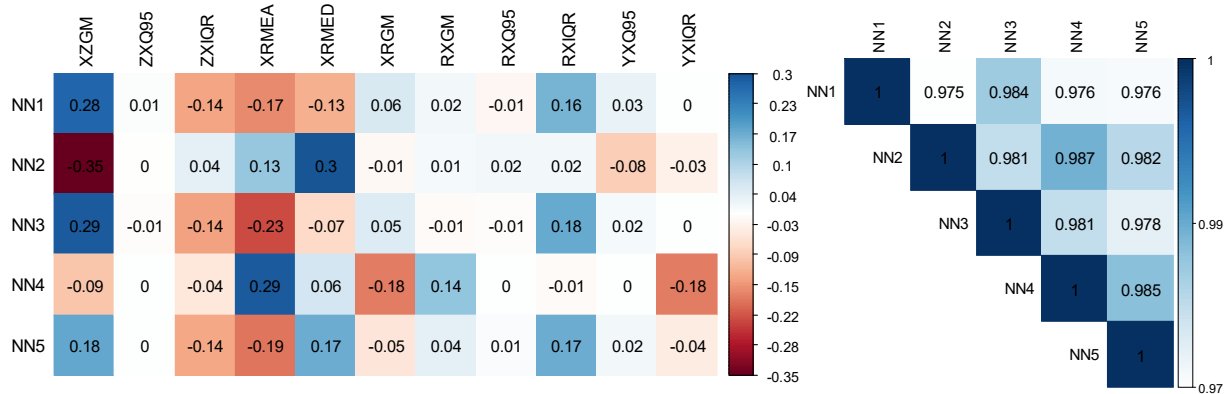|	NN1	NN2	NN3	NN4	NN5
NN1	1	0.975	0.984	0.976	0.976
NN2		1	0.981	0.987	0.982
NN3			1	0.981	0.978
NN4				1	0.985
NN5					1

Figure M-3: Heatmap for relative Olden scores for the features (left); similarity of classification for neural networks (right)

Figure M-4 visualises the classification results of NN1 for Block FBA2. Visible are: blocks classified as ore, the boundaries of the ore part, false positives and false negatives. Panel a) shows all blocks that have been classified as ore. The grey blocks are those that were falsely identified as ore, but are actually concrete (false positives). Panel b) only shows the false positives. Most false positives occur at the bottom of the sample. Panel c) of the figure only shows the false negatives. These are the blocks that where calculated to be concrete, although they where ore. They occur mainly at the boundary between the two rock types.

False positives and false negatives both occur at the boundary between the two rock types. Due to imprecisions in the digitisation of the rock type boundaries, it is expected that most errors occur there. The main body of the ore and concrete is classified correctly.
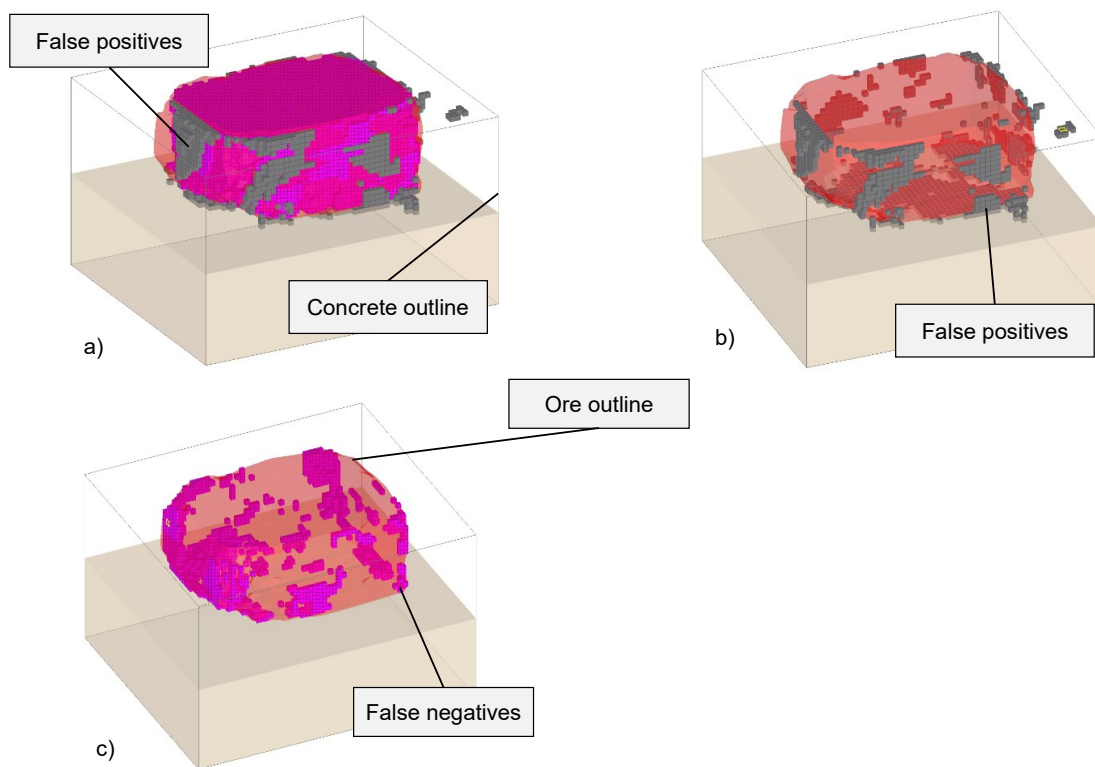

Figure M-4: Visualisation of classification results of NN1 for Sample FBA2

Table M-3 shows the general key performance values of the five neural networks tested. From the visual impression in Figure M-4, good results are already expected. Generally, there was very little difference

between the performance of the different networks. The sensitivity for all neural networks lies above 0.95, the specivity lies above 0.93. That means that at least 95% of all ore blocks are identified as ore, and at least 93% of all blocks that were identified as ore actually are ore. The overall misclassification error is. More importantly, the errors are almost completely located at the contact zone between the two rock types.

Table M-3: Summary for key performance values for neural networks for FBA-2

	NN1	NN2	NN3	NN4	NN5
Sensitivity	0.962	0.963	0.962	0.959	0.957
Specifity	0.944	0.946	0.950	0.938	0.942
Misclassification error	0.044	0.042	0.042	0.047	0.047

Annex N   Supplements Case Study (CD)

N.1   Pre-Analysis Feature-Set

In order to identify the final set of features as well as suitable hyperparameters for the DRF and ANN, a limited hyperparameter search was conducted on the data of the case study.

The parameters were varied as shown in Table N-1. The cutoff for the *CR* was varied in three steps. This parameter sets a filtering criterion. If the *CR*, that is assigned to a certain block of the block model, is higher than the *CR* cutoff, the respective block is counted as "air" and not included in the machine learning process. For the DRF, the maximum tree depth had to be defined. It was varied in three levels. A higher tree depth increases training accuracy but increases overfitting behaviour. The features were also varied at three levels. However, with a special procedure. First, a starting set consisting of nine features was chosen (*XZGM*, *ZXQ95*, *ZXIQR*, *XRMED*, *RXGM*, *XRGM*, *RXQ95*, *RXIQR*, *CR*). This represented the first level. The level with eight features was repeated nine times. In each repetition, one parameter from the features of the previous level was left out. This results in nine sublevels. The same procedure was repeated for the level with seven features (resulting in eight sublevels). The process was iterative; first, the *CR* cutoff was defined, then the tree depth, and den the optimal feature sets.

*Table N-1: Hyperparameter variation for DRF; * – winner*

Hyperparameter	Levels
CR cutoff	0.4 / 0.55* / 0.7
Maximum tree depth	5 / 8 / 11*
Feature sets:	9 / 8* (9 sublevels) / 7 (8 sublevels)

For the ANN, the hyperparameter variation was based on the results of the DRF hyperparameter variation. The main aspect was the variation of the architecture of the hidden neurons on 7 levels, as shown in Table N-2. For the variation of the features, two levels were chosen: one set with nine and one set with eight features. The set with eight features was the winner from the DRF feature selection, and the set with nine features was the original feature set.

*Table N-2: Hyperparameter variation for ANN; * – winner*

Hyperparameter	Levels
Architecture (hidden neurons)	5 / 7 / 9 / 11 / 5–2 / 25–25 / 25–25–25*
Feature Sets:	9 / 8*

The results were then assessed by comparing the accuracy heatmaps. A trade-off between *validation accuracy* and *cross-sample accuracy* was desired. The two winners of the hyperparameter variation are shown in Figure N-1. The full set of all plots created can be found on the accompanying CD.

For DRF, the final feature set was: *XZGM*, *ZXQ95*, *ZXIQR*, *XRMED*, *RXGM*, *RXQ95*, *RXIQR*, *CR*. The cutoff for CR was set to 0.55. The tree depth was set to 11. For the ANN, the same set of features was chosen. The final architecture was 25 neurons in 3 hidden layers each.
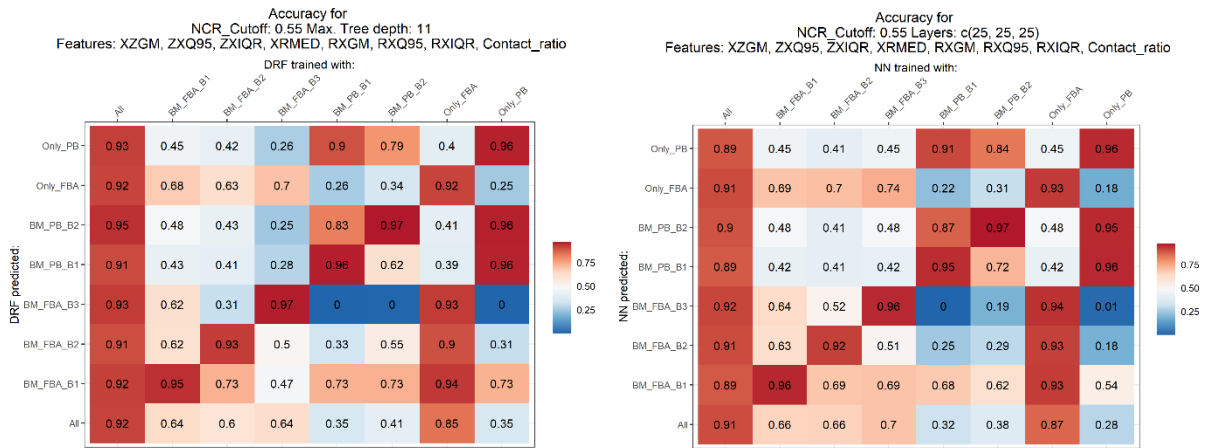
Figure N-1: Exemplary accuracy table for the definition of final feature set, left – winner DRF, right – winner ANN

N.2 Supplement Variation of Required Training Data

Due to the size, the table is located on the CD.

Annex O R-Codes (CD)

All used code can be found on the CD accompanying this thesis.

Table O-1: R scripts and apps used in this work

Folder	Script name	Chapter Reference	Details
CO/Input data		6.1	Contains raw input data for CO
CO/	CO1_Feature_ selection.R	6.1.2	Feature selection algorithm for Experiment CO1
CO/	CO2_Feature_ selection.R	6.1.2	Feature selection algorithm for Experiment CO2
CO/	CO_kmeans	6.1.4	k-means analysis for CO
CO/	CO_DRF_Varimp	6.1.4	DRF classification for feature analysis for CO
GN/Input		6.2	Contains raw input data for GN
GN/	Gneiss.R	6.2	FCR evaluation of Experiment GN.
GR/Input			Contains Raw input data for GR
GR/	Analysis GR.rmd	6.3	Force and FCR evaluation of GR; spatial CR analysis.
Case Study/Input		6.4	Contains pre-processed raw cutting force data
Case Study/	CS_RockAIMD.rmd	6.4	Markdown file for case study; incorporates main parts of the analysis.
Case Study/	CS_sidescript_ANN.R	6.4	Supplement for the case study; variation of hyperparameters to identify a suitable set for case study.
Case Study/	CS_sidescript_DRF.R	6.4	Supplement for the case study; variation of hyperparameters to identify suitable set for case study
RockAI_RockAI_View er/	ui.R / server.R	6.4	App that visualises the results of the case study, also accessible under: https://brunanza.shinyapps.io/RockModel VieweR/
App_CutAnalyst/	app.R	7.1.5 / Annex G	App to efficiently assess large amounts of raw cutting data and correct/reject the data. Folder contains sample dataset.

Annex P   Supplements Rock Mechanical Tests (CD)

The supplementary data are located on the accompanying CD. The structure of the data is explained in the following table. The results are in German.

Table P-1: Data structure of supplementary rock property data

Folder Name	Experiment	Comments
CO	CO	Consists datasheets for the used concrete mixtures for Zone 1, 2, and 3.
GR	GR	Consists of datasheet for the used granite.
GN_FBA	GN FBA	Gneiss and fluorite were analysed together. Folder consists of individual results of each performed *UCS* and *BTS* test as well as a photographic documentation of the samples
PB	PB	Folder consists of individual results of each performed *UCS* and *BTS* test as well as a photographic documentation of the samples.